DOCTORAL THESIS
2015

COMPLEX DYNAMICS OF DELAY-COUPLED SEMICONDUCTOR LASERS: FUNDAMENTALS AND APPLICATIONS
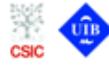
Javier Porte Parera

DOCTORAL THESIS
2015

Doctoral Program of Physics

COMPLEX DYNAMICS OF DELAY-COUPLED SEMICONDUCTOR LASERS: FUNDAMENTALS AND APPLICATIONS

Javier Porte Parera

Thesis Supervisor: Ingo Fischer

Thesis Co-Supervisor: Miguel Cornelles Soriano

Doctor by the Universitat de les Illes Balears

COMPLEX DYNAMICS OF DELAY-COUPLED SEMICONDUCTOR LASERS: FUNDAMENTALS AND APPLICATIONS

Javier Porte Parera
Tesi realitzada a l'Institut de Física Interdisciplinària i Sistemes Complexos (IFISC)
i presentada a la Universitat de les Illes Balears (UIB)

PhD Thesis

Director: Prof. Ingo Fischer
Co-Director: Dr. Miguel Cornelles Soriano

This document was typeset with LaTeX 2_ε

El Professor Ingo Fischer, Científic Titular del Consell Superior d'Investigacions Científiques i el Doctor Miguel Cornelles Soriano, Contractat Postdoctoral CAIB

FAN CONSTAR

que aquesta tesi doctoral ha estat realitzada pel Sr. *Javier Porte Parera* sota la seva direcció a l'Institut de Física Interdisciplinària i Sistemes Complexos (UIB-CSIC) i, per a donar-ne constància, firmen la mateixa.

Palma, 27 de juliol del 2015

Ingo Fischer
Director

Miguel Cornelles Soriano
Director

Javier Porte Parera
Doctorand

Resum

La present tesi està dedicada a l'estudi dels làsers de semiconductor sotmesos a realimentació i a acoblament òptics amb retard. Les complexes propietats dinàmiques i espectrals d'aquests sistemes han sigut investigades emprant les actuals tecnologies de detecció en l'àmbit de les telecomunicacions. Mitjançant aquestes eines, hem sigut capaços de caracterizar experimentalment propietats dels nostres sistemes fins aleshores desconegudes. Durant aquest treball, ambdós tipus de resultats, fonamentals i aplicats, són presentats pels diferents experiments que hem realitzat.

La primera part de la tesi se centra en el sistema d'un làser sotmès a realimentació òptica amb retard. El problema de la caracterització de la dinàmica s'aborda des de la perspectiva de les escales de temps del sistema, relacionant els règims dinàmics amb les freqüències característiques del làser amb realimentació òptica. Hem trobat empíricament que els quocients entre aquestes freqüències característiques determina completament la dinàmica resultant, el que constitueix un enfocament independent de qualsevol model que es pot utilitzar, al mateix temps, per testejar la validesa dels models numèrics que tinguin la intenció d'explicar el comportament dinàmic d'aquests làsers. A més, la validesa general del nostre enfocament s'ha confirmat mitjançant la seva aplicació a làsers de característiques diferents.
Les propietats específiques de la dinàmica d'aquest sistema també s'han caracteritzat a partir de la funció d'autocorrelació de la intensitat. Per aquest propòsit, l'autocorrelació experimental es compara amb l'autocorrelació obtinguda a partir del model per a un oscil·lador lineal estocàstic amb retard. La relació entre els paràmetres del model i els paràmetres del sistema experimental s'analitzen i discuteixen juntament amb els límits de validesa d'aquest enfocament.

En la segona part, hem estudiat diferents sistemes de dos làsers acoblats amb retard. El fenomen de sincronització del caos és explorat en dues configuracions diferents: una configuració d'acoblament unidireccional on el senyal del làser amb realimentació retardada també està acoblat òpticament a un segon làser, i un esquema bidireccional de dos làsers acoblats mútuament amb realimentació pròpia. A la primera configuració, hem estudiat bàsicament la relació entre la consistència de la dinàmica i la possibilitat de sincronitzar el segon làser. En aquest últim esquema, la robustesa de l'estat sincronitzat es caracteritza en funció del desajustament en els paràmetres i de l'efecte del soroll.
A la pràctica, utilitzam el coneixement adquirit en els experiments de sincronització per implementar un protocol d'intercanvi de clau segura a través d'un canal públic en

l'esquema d'acoblament bidireccional. A més de demostrar experimentalment la possibilitat d'implementar aquest protocol, analitzam els seus avantatges i debilitats.

Finalment, presentam una implementació fotònica d'un sistema dinàmic que experimenta dos temps de retard diferents depenent de l'estat del sistema. En aquest sistema experimental hem estudiat les característiques espectrals promitjades en el temps, així com també les condicions necessàries perquè la dinàmica ocorri en estats separats. També hem investigat la intensitat i la dinàmica dels espectres òptics en temps real per demostrar l'existència i estudiar les propietats d'aquesta dinàmica on el retard depèn de l'estat del sistema. Curiosament, propietats qualitativament similars es poden trobar a partir d'un model numèric adequat d'aquest sistema.

En resum, al llarg d'aquesta tesi s'han presentat resultats d'àmbits fonamental i aplicat en el camp de làsers de semiconductor acoblats òpticament amb retard. La fenomenologia presentada és de potencial utilitat en una varietat d'aplicacions que van des de la computació de reservoris basada en sistemes fotònics fins a les comunicacions amb senyals caòtiques. A més, els avenços de caire fonamental poden ser potencialment aplicats a altres classes de sistemes dinàmics més enllà dels làsers de semiconductor.

Abstract

The present thesis is devoted to the study of semiconductor lasers subject to delayed optical feedback and coupling. The complex spectral and dynamical properties of these systems have been investigated using state-of-the-art telecommunications detection technologies. With such tools, we have been able to experimentally characterize previously unknown features in our delay-coupled systems. Along this work, both fundamental and applied results are presented for the different experiments investigated.

The first part of the thesis is focusing on the system of the single delayed feedback laser. The problem of feedback characterization is approached from a time scale perspective, relating the dynamical regimes to the characteristic frequencies of the delayed feedback laser. We have empirically found that the ratios of these characteristic frequencies completely determine the dynamical behavior. This constitutes a model independent approach that can be used, for example, to test the validity of numerical models that aim at explaining the dynamical behavior of these lasers. Furthermore, the general extent of our approach is validated by measuring various laser diodes with distinct characteristics. Specific properties of the dynamics of the single laser with feedback system have also been characterized by means of the intensity autocorrelation function. For this purpose, the experimental autocorrelation is compared with the autocorrelation obtained from a model of a stochastic linear oscillator with delay. The relation between the model parameters and the experimental system parameters is analyzed and discussed together with the limits of validity of this approach.

In the second part, systems with two delay-coupled lasers are studied. The phenomenon of chaos synchronization is explored in two different configurations: a unidirectional coupling configuration where the delayed feedback laser signal is optically coupled to a second laser, and a bidirectional scheme of two mutually coupled lasers with self-feedback. In the first configuration, the relation between the consistency of the dynamics and the synchronizability with the second laser is studied. In the latter scheme, the robustness of the synchronized state is characterized against detuning in parameters and noise.
The knowledge gained in the synchronization experiments is used to implement a classical public-channel secure-key exchange protocol in the bidirectional coupling scheme. This protocol is demonstrated experimentally, and its advantages and weaknesses are analyzed.

Finally, we present a practical photonic implementation of a dynamical system expe-

riencing two different delay times depending on the state of the system. The stationary spectral characteristics of this experimental system are studied and the conditions for the dynamics to occur in separated states are highlighted. We have also investigated the real-time intensity and optical spectrum dynamics to demonstrate the existence and properties of state-dependent delay dynamics. Qualitatively similar properties can be found from a proper numerical model of this system.

Altogether, we have presented fundamental and applied aspects of semiconductor lasers optically coupled with delay. The presented phenomenology is of immediate potential use for a variety of applications that range from photonics-based reservoir computing to chaos communications. In addition, the presented fundamental insights can potentially be extended to other classes of dynamical systems.

List of Publications

Regular articles:

1. Jordi Tiana-Alsina, Konstantin Hicke, Xavier Porte, Miguel C. Soriano, Maria C. Torrent, Jordi García-Ojalvo, and Ingo Fischer. *"Zero-lag synchronization and bubbling in delay-coupled lasers."* Phys. Rev. E **85**, 026209 (2012)

2. Daniel Brunner, Xavier Porte, Miguel C. Soriano, and Ingo Fischer. *"Real-time frequency dynamics and high-resolution spectra of a semiconductor laser with delayed feedback."* Scientific Reports **2**, 00732 (2012)

3. Konstantin Hicke, Xavier Porte, and Ingo Fischer. *"Characterizing the deterministic nature of individual power dropouts in semiconductor lasers subject to delayed feedback."* Phys. Rev. E **88**, 052904 (2013)

4. Xavier Porte, Miguel C. Soriano, and Ingo Fischer. *"Similarity properties in the dynamics of delayed-feedback semiconductor lasers."* Phys. Rev. A **89**, 023822 (2014)

5. Xavier Porte, Otti D'Huys, Thomas Jüngling, Daniel Brunner, Miguel C. Soriano, and Ingo Fischer. *"Autocorrelation properties of chaotic delay dynamical systems: A study on semiconductor lasers."* Phys. Rev. E **90**, 052911 (2014)

6. Jade Martínez-Llinàs, Xavier Porte, Miguel C. Soriano, Pere Colet, and Ingo Fischer. *"Dynamical properties induced by state-dependent delays in photonic systems."* Nature Communications **6**, 7425 (2015)

Preprints (in press):

1. Daniel Brunner, Miguel C. Soriano, Xavier Porte, and Ingo Fischer. *"Experimental phase-space tomography of semiconductor laser dynamics"* Physical Review Letters (accepted)

Contents

Chapter 1

Introduction

1.1 Motivation

Since the demonstration by Heinrich Rudolf Hertz in 1887 that electromagnetic waves can propagate in free space[1], many inventions have been made that have resulted in a revolution in the way we humans communicate. Through the 20th century, telecommunications have undergone profound changes resulting in a globally connected world with the messages traveling at the speed of light. Different milestones have contributed to the global spread of information, like the radio or the optical fibers. An unprecedented number of signals travel nowadays encoded as binary digits across the planet connecting the humanity under a huge heterogeneously composed network of networks, *the Internet*.

Nowadays, a variety of applications are incrementing Internet traffic: e-mails, video-calls, banking transactions, voting, multimedia cloud services, etc., and the corresponding traffic will further significantly increase in the foreseeable future. Moreover, an increasing number of devices are joining this global *connectome*[2]. Devices like laptops, tablets and especially smartphones are connected in a number that already exceeds the sum of all past existent devices. Indeed, the next step in this global infrastructure is expected to be even bigger, the transition towards what is known as the *Internet of Things*. A concept that promises linking everyday "real world" objects like buildings or vehicles to the previously software oriented devices by means of (wireless) sensor networks, control systems, and automation.

In this scenario, **Photonics** is playing a central role. For already more than three decades, global telecommunications rely on the backbone of photonics technologies using light to create, transmit, and display most of the digital information that is generated. Photonics technologies are offering two exclusive advantages to global telecommunications. Firstly, the development of cheap, fast and efficient emitters and receivers: the semiconductor-based **laser diodes** and **photodiodes**. On the other hand, the possibility to transmit the huge amount of data using semiconductor lasers at the speed of light and with low losses via **optical fibers**. Single-mode silica fibers typical transmission

---

[1]Theorized by James Clerk Maxwell's electromagnetic theory of light in 1873.
[2]Name used in analogy to the map of neural connections in the human brain.

capacities are in the range of 100 Gbit/s, only limited by nonlinear effects [1] [3].

In spite of their high transmission capacity, the growing demands of global telecommunications in combination with the chances to embrace new fields of application trigger more research in photonics. Some of the new applications may come from the variety of **nonlinear properties** of the photonic devices. The study of these properties have brought improvements in already existing applications and have opened the door to completely new applications, like the possibility to build all-optical computers [2,3].

In this wide panorama, our work focuses on a particular subset of the nonlinear phenomena in photonics devices: the effect of delayed optical feedback and coupling on the emission dynamics of semiconductor lasers. Traditionally considered as a nuisance in applications like telecommunications or optical-data storage [4], the sensitivity of these devices to external perturbations offer promising opportunities when seen under the perspective of new applications. Decades after the first reports of feedback instabilities, there exists a renewed interest in delayed feedback effects due to novel scientific and technological insights. Moreover, we now have the possibility to detect and study in full bandwidth the resulting characteristics. The capabilities to control the variety of complex dynamics further increases the chances to put semiconductor lasers with delayed feedback in the center of a number of future photonic applications [5].

In this thesis, phenomena due to delayed optical feedback in semiconductor lasers are revisited with new findings that dramatically simplify the zoo of complex dynamics known up to this moment. A deeper understanding of the origin (and tailoring) of the feedback induced instabilities could provide a new perspective on the dynamical regimes induced by optical feedback and could prove very useful for applications. The key idea is to exploit the knowledge gained on the interdependencies between the parameters and the laser operating conditions that determine the feedback regimes to tailor the system to various application needs.

Also, the nonlinear phenomenon of chaos synchronization in delay-coupled semiconductor lasers, is studied in this thesis with the application to secure-communications in mind. In the particular objective is to find the ideal experimental conditions for good identical synchronization between two coupled lasers and implement a secure-key distribution scheme. The interest in this particular application becomes clear in the context of a global and ubiquitously connected world. Concepts like security and privacy of telecommunications do no longer belong to a reduced number of privileged participants, but to the whole community of connected users. Privacy is without doubt a universal right, and everyone should be able to use this right if he or she wants to. Therefore, satisfactory solutions to achieve privacy in a globally connected world are an important subject of research.

1.2   Semiconductor Laser Devices

The importance that semiconductor lasers (SL) have in global telecommunications have already been mentioned. Nevertheless, actual semiconductor-based laser diodes have

---

[3]The low-loss transmission window encompasses up to several tens of terahertz potential bandwidth.

evolved considerably since their origins at three different laboratories in 1962 [6–9]. First bulk semiconductor homostructure devices only allowed for pulsed operation at liquid nitrogen temperatures. The practical innovations towards room-temperature CW operation are associated with the introduction of double heterostructure and quantum well active media, enormously enhancing the efficiency of the light confinement and amplification in the SL.

Today, SL are small and efficient devices regularly used in a variety of applications like optical data storage, metrology, spectroscopy, material processing, biophotonics, pumping of other lasers and optical telecommunications. In particular, its application to long-distance optical data transmission as a high-speed light source has permitted the world-wide optical fiber communication networks. At present, quantum well lasers are acknowledged as a standard for optical communications, with satisfactorily low operating currents. The main features of SL that have led to their impressive development and their ubiquitous application in many fields are:

- A wall-plug efficiency up to more than 60%.

- Small dimensions, typical volumes range in size from 100 μm^3 to 1 mm^3.

- Fast internal time scales that allow for high frequency modulations up to tens of GHz.

- Narrow spectral linewidth. The SL used for telecommunications typically exhibit optical linewidths of few tens to hundreds of Megahertz.

- Diversity of structures and properties. Modern epitaxy techniques allow individual atomic layers growth and lateral structuring, tailoring with great precision the physical properties and the device structure.

- Low costs per laser and possibility of integration in photonic integrated circuits.

All types of lasers share the same conceptual design, and SL are no exception. They are constituted of two basic ingredients: an **active medium** and a **resonant cavity**. The active medium amplifies the light by stimulated emission of radiation once the pumping has created a population inversion. The resonator shapes the optical modes and couples the coherent light out. In the paradigmatic example of SL, the thin depletion region of the diode's pn junction acts as the active medium and the resonator is of the Fabry-Perot type, with the cleaved facets of the semiconductor crystal acting as the reflectors. Depending on the semiconductor alloy used as gain medium, the laser will emit in different wavelengths that range from UV to near infrared.

SL have also evolved in terms of different structures of the gain material. From bulk to quantum well, and from quantum well to quantum dashes and dots and to quantum cascade lasers. Quantum dot lasers (QDL) are a relatively new kind of semiconductor laser made from an ensemble of nano-sized crystals grown inside the semiconductor active region. These crystals, referred as dots to highlight its discrete volume, are the

laser light emitters. QDL are considered the natural evolution of state-of-the-art quantum well lasers for many applications. In particular, fields like telecommunications, spectroscopy, or medical diagnosis could benefit from their enhanced properties (higher potential modulation bandwidths, typically higher characteristic temperatures, etc...). Quantum cascade lasers (QCL) [10, 11] are the most distinct devices in terms of their operating principle. It makes use of engineered inter sub-band transitions in carefully designed QW layer structures do not involve electron-hole recombinations. The electrons are injected in the upper band and coherent radiation is emitted upon carrier radiative relaxation to lower bands (engineered quantum states) within the conduction band. QCL have become a SL alternative when the desired frequencies are in the mid-infrared to THz range.

SL also come in a variety of distinct resonator structures. Laser cavities that differ from the Fabry-Perot type have interesting properties for particular applications. Some examples are useful to illustrate different possible laser cavities. The ring laser structure is present in many types of lasers, not only in semiconductor lasers. In a ring laser, the cavity has the shape of a ring and light propagates through it in two possible directions: clockwise and counter-clockwise. When both counter-propagating waves co-exist in the ring cavity, they interfere in a pattern that changes with rotations of the laser. Consequently, a widespread application for these lasers is to build gyroscopes [12, 13]. Distributed Bragg reflector (DBR) lasers and distributed feedback (DFB) lasers are semiconductor lasers that have resonator cavities based on the effective reflectivities caused by interference of light when it propagates through their grating structures. In DBR lasers two Bragg gratings are placed at either side of the cavity acting as mirrors. In contrast, DFB lasers are lasers where the whole cavity consists of a periodic structure. This periodic structure is usually obtained by modifications of the refractive index combined with a phase shift element in the middle of the cavity. Both laser structures (DBR and DFB) exhibit single-mode operation and are widely used in telecommunications. Finally, vertical-cavity surface-emitting laser (VCSEL) structure have the particularity that emits light perpendicularly to the semiconductor wafer surface. The VCSELs have two epitaxially grown Bragg reflectors placed below and above the thin active medium layer. VCSELs are versatile devices that allow for fast modulation rates, single-mode emission, and easy collimation into an optical fiber. These conditions make them very suitable for data-communications uses. Furthermore, thousands of these VCSELs are fabricated on a single wafer. In fact, the coincidental vertical direction for the growth and for the emission eases their operation as laser arrays, where they can achieve combined emission powers in the order of watts.

Discrete-Mode Laser-Diodes present an etched-ridge Fabry-Perot structure that has been designed for longitudinal-modes selection. Those lasers are the chosen devices in the majority of the experiments that have been implemented in the present thesis. The particularity of their design ensures single-longitudinal mode operation for a wide bias currents range and the typical moderately-high powers related to edge emitter devices. Additional information on the experimental characterization of these devices can be found in appendix A.

1.3 Nonlinear Dynamics of Semiconductor Lasers

A particularly interesting dynamical property of SL is their nonlinear response to perturbations, which is manifested in a pronounced sensitivity to, e.g., noise, variations in the injection current, external optical injection or delayed optical feedback. Even small amounts of re-injected light can destabilize the SL emission [14–16] and cause its dynamics to exhibit chaotic behavior. For applications in which stable emission is needed, even the reflections from the facet of any coupled fiber[4] can give rise to destabilizing feedback. Such instabilities are usually prevented via the introduction of optical isolators to shield the laser diode from feedback. The problem is that this measure implies additional costs and is detrimental in the design of compact and miniaturized photonic integrated circuits. These instability problems were one of the first questions that were addressed in the study of the nonlinear properties of SL subject to delayed optical feedback [17].

Next, a different point of view was adopted and feedback effects gained interest from the perspective of nonlinear dynamics (NLD) community. The different dynamical regimes of a delay-coupled SL depend directly on the pump current and on the feedback parameters. The main feedback parameters are the amount of light re-injected in the cavity (feedback rate), the length of the external cavity (EC) and the feedback phase. A SL subject to delayed optical feedback or coupling may exhibit many characteristic high-dimensional NLD phenomena, including hyper-chaotic regimes [18, 19] and chaos synchronization when delay-coupled to other SL [20]. Moreover, since the highly complex dynamics generated in delay-coupled lasers are used in applications as diverse as chaotic secure communications [21], ultrafast random bit sequence generation [22], rainbow refractometry [23], neuroinspired computation and ultrafast all-optical signal processing [24, 25], a proper experimental and theoretical characterization and understanding is extremely desirable. It is clear that the reliability and flexibility of these practical applications will benefit from the fundamental study of the dynamical properties of these delay systems.

The importance of SL subject to delayed optical feedback even goes beyond the particular interest in laser dynamics and or their photonics related applications. SL are well-controlled and tunable experimental systems in which we can study very accurately delay-induced phenomena. Therefore, SL subject to delayed optical feedback are excellent testbed examples of delay-coupled systems in general, being of fundamental importance in a variety of fields. Some examples of these fields are chaos control [26], neuroscience [27], traffic dynamics [28], population dynamics [29], gene regulatory networks [30, 31], generic models [32, 33], and encrypted communications [21]. The whole range of possible applications of SL adds even more interest to the study of NLD phenomena in SL.

To understand the origin of the nonlinear phenomena in SL we must take into account two distinct SL material properties. First, the fact that many SL can be described as **Class B lasers**. To be considered class B lasers, SL must fulfill some assumptions like, e.g., single mode emission or no spatial extension. This classification of lasers imply

---

[4]Commercial telecommunications lasers are fiber pigtailed.

that the typical electric field and carriers inversion have decay rates much slower than the decay rate of the medium polarization. In class B lasers, periodic solutions, known as relaxation oscillations, are possible in which the laser energy oscillates between inversion and optical field. Such oscillations can be undamped through external parameters modulation or by delayed feedback.

The key property to understand the sensitivity of SL to delayed optical feedback and/or external parameter modulation is the linewidth enhancement factor (α). It represents the typically strong amplitude-phase coupling of the electromagnetic field and the laser medium [34]. This nonlinear effect is caused by the carrier induced variations in the real and imaginary parts of the semiconductor material susceptibility, $\chi(n) = \chi_r(n) + i\chi_i(n)$. This means that any small amplitude perturbation caused by spontaneous emission (inherently present in SL), bias injection modulation or by delayed optical feedback will cause a perturbation in the phase of the field. The linewidth enhancement factor (α parameter) is defined as [35]:

$$\alpha = -\frac{d(\chi_r(n))/dn}{d(\chi_i(n))/dn} \tag{1.1}$$

where $d(\chi_r(n))/dn$ and $d(\chi_i(n))/dn$ are the respective derivatives of the real and imaginary parts of the susceptibility with the carrier inversion. The particularities of lasing transitions in the semiconductor medium, which occur between two partially filled energy bands and not between discrete energy levels, gives rise to larger values of α in SL in contrast with other types of lasers, like gas lasers, where $\alpha = 0$. The inter-band transitions lead to a strong amplitude-phase coupling of the electromagnetic field in the laser medium and to the fast characteristic time scales of the SL. α is one of the fundamental parameters important for the dynamics of SL and is typically the most pronounced intrinsic nonlinearity in these kind of lasers.

The α parameter is also the origin for an anomalous broadening of the semiconductor laser's linewidth, first explained by Henry in 1982 [35], giving rise to an enhancement of the laser linewidth by a factor of $1 + \alpha^2$. It is also important for the modulation response of the SL, because the amplitude-phase coupling due to α is the cause of significant frequency chirp for high-bandwidth modulations.

1.3.1   Delayed Optical Feedback Effects on the Emission of Semiconductor Lasers

The simplest configuration of delayed optical feedback is sketched in Figure 1.1. It basically compromises the laser diode, the light propagating channel, and a mirror. The laser diode emits in continuous wave under unperturbed operating conditions. The mirror redirects a fraction κ_f of the laser's emitted optical field into the laser cavity again after a time τ_f. The channel is considered linear and only marginally affects the properties of the propagating light. In experimental implementations of this scheme, the channel can be formed by air or by an optical fiber.

Even small amounts of reinjected light, < -50 dB [36], may affect the laser emission. Slightly higher feedback levels are already related with the destabilization of the laser
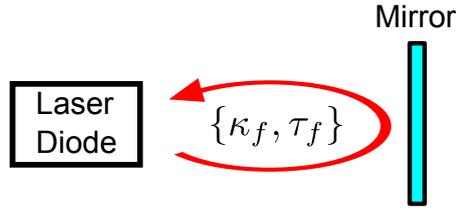
Figure 1.1: Schematic representation of the feedback phenomenon components. A fraction, κ_f, of the light emitted by the laser diode is fed back with a certain delay τ_f.

emission and the corresponding drastic increase of the emission linewidth. In technological applications of semiconductor lasers, the role of the mirror can be played by a variety of elements like, e.g., the fiber connections in telecommunications systems. In many cases, reflections will originate at distances from the laser diode that can be considered long when compared with the characteristic laser intensity dynamics time scales. This case is usually known as *long-cavity feedback* regime.

The first and most straightforward consequence of delayed feedback that can be measured in SL is its effect on the output power. It is well known that polarization-maintained optical feedback typically reduces the laser's threshold[5]. This threshold reduction is due to the photons being re-injected into the laser cavity, which reduce the total losses and cause the lasing regime to set on at lower currents than in the solitary laser case. In consequence, under constant biasing, the output power is usually higher when delayed feedback is present.

Figure 1.2 displays two different power-current characteristics of the same laser under different experimental conditions. The blue curve corresponds to the case of the laser without feedback. In contrast, the orange line, with a reduced threshold current, corresponds to the case of the laser subject to delayed optical feedback.

The first identifiable feature is the distinct slopes that both curves have above threshold. This difference is related to the change in external differential quantum efficiency (η_d) due to the reinjection of light and the corresponding change in balance of the output facet reflectivity.

The laser used in this measurement has high power emission from one laser facet (the output facet) and low power emission from the other facet. This asymmetry in the power emission is engineered by asymmetric coating of the laser facets: one facet with high-reflection (HR) coating (typical reflectivities larger than 90 %) and a facet with anti-reflection (AR) coating (typical reflectivities smaller than 10 %). These different coatings lead to asymmetries of carrier density and optical field along the laser cavity of the solitary laser. Our laser is fiber-pigtailed to the AR coated facet side of the laser and the external cavity mirror is consequently connected to this facet. Once the delayed optical feedback is active, a substantial decrease in the slope of the power-current curve can be found, even leading to that both curves, with and without optical feedback, cross for a certain value of the injection current. This value is referred to as the cross

---

[5]It is important to specify the type of feedback at this point. Neither incoherent feedback nor polarization-rotated feedback typically cause a reduction of the lasing threshold
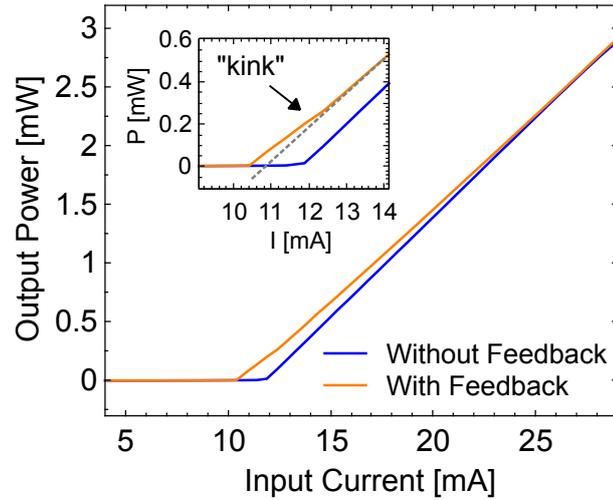
Figure 1.2: Power-current characteristics of a single-mode laser under different operation conditions: in solitary emission (blue line) and when subject to delayed optical feedback (orange line). The temperature of the laser is set to 22 °C. The inset is a magnification of the region around the two distinct laser thresholds.

over point [37]. The reason of the less steep slope is not that the laser's output power decreases in the presence of optical feedback, but that there is a change in the laser's cavity power balance caused by an increase in the effective power reflectivity on the AR-coated facet.

Another difference between both curves is the kink close to the solitary laser threshold in the feedback case (region highlighted at the Figure 1.2 inset). This loss of linearity in the power-current characteristics above threshold, not present in the solitary laser case, can be related with dynamical instabilities of the output power [16]. The characteristic frequencies these low-frequency fluctuations exhibit are significantly lower than other laser characteristic frequencies as, e.g., the relaxation oscillation frequencies, the laser internal round trip frequency, and the external cavity round trip frequency. These fluctuations occur close to the solitary laser threshold for moderate to strong feedback conditions.

As explained in the previous section, the linewidth enhancement factor (α) plays a crucial role in the destabilization of the laser emission via delayed optical feedback. This parameter acts as the coupling mechanism between light intensity and spectral emission properties. In consequence, any intensity fluctuation in the laser's emission will be fed back by the delay line, amplified by the gain medium, and coupled to the optical frequency via α. Figure 1.3 represents the influence of delayed optical feedback on the optical spectrum of a single-mode laser diode.

Figure 1.3a presents the experimental optical spectra with and without feedback as detected from a grating optical spectrum analyzer (resolution 0.05 nm). This 10 nanometer scale permits to identify that this laser emits in a single-longitudinal mode under both conditions. It can be observed that the delayed feedback spectrum is asymmetri-
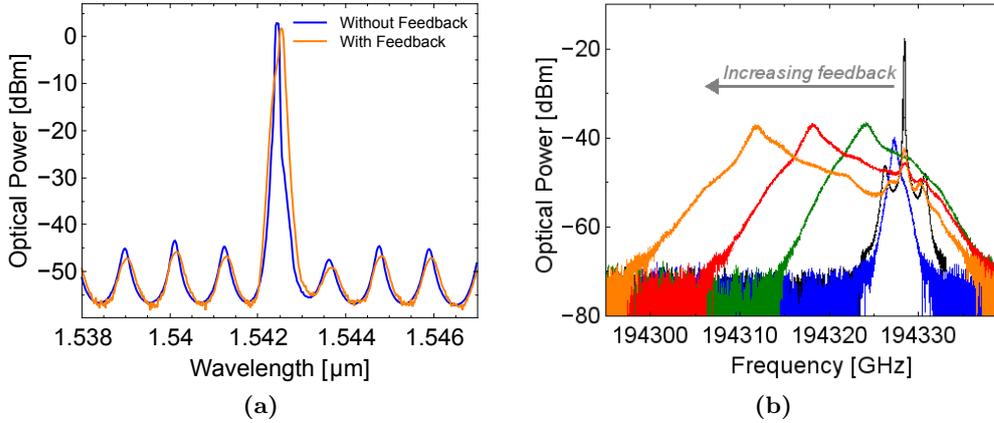
Figure 1.3: Impact of delayed optical feedback on the linewidth of a laser diode. Panel (a) plots the spectra measured with a grating spectrometer. In panel (b) the phenomenon of coherence collapse is shown in high resolution. The arrow indicates the broadening direction of the optical spectrum when the feedback strength increases.

cally broadened towards higher wavelengths. Nevertheless, it is hard to resolve further particular effects on the laser's linewidth from this plot. Indeed, one feature that can be recognized is the emission level in the side-modes of the laser diode resonator cavity with a side-mode suppression ratio larger than 40 dB. This is a cavity with a separation between the cavity modes of 1.2 nm (that corresponds to the resonance conditions).

A more highly resolved view of the feedback effects on the laser's linewidth are displayed in Figure 1.3b, where the spectra have been measured with a high-resolution optical spectrum analyzer [38] (resolution 10 MHz). The different spectra correspond to different feedback strengths. The black curve plots the solitary laser spectrum. The higher the value of the feedback strength (the lighter the curve color), the broader becomes the optical spectrum, particularly broadening towards lower frequencies. For the highest feedback conditions (orange curve) in this particular device, the broadening of the spectrum already covers more than 20 GHz. This is a well known phenomenon frequently referred in literature as *coherence collapse* [39].

The multi-GHz broadening of the optical spectrum coincides with the appearance of sub-nanosecond fluctuations in the output intensity. Figure 1.4 illustrates the impact of delayed optical feedback on both emission characteristics of semiconductor lasers. Figures 1.4b and 1.4d plot the intensity time traces corresponding to two illustrative conditions. The solitary emission is depicted in panels 1.4a and 1.4b. Here, the optical linewidth is narrow ($\leq$ 1MHz) and the relaxation oscillation sidebands are clearly identifiable as the only signature of dynamics reflected in the optical domain. The intensity shows small fluctuations around a constant value, which are the combination of spontaneous emission amplification (relaxations oscillations) and detection noise. In contrast, in panels 1.4c and 1.4d, the behavior under delayed optical feedback is illustrated. The optical spectrum experiences a dramatic broadening, expanding its linewidth from MHz
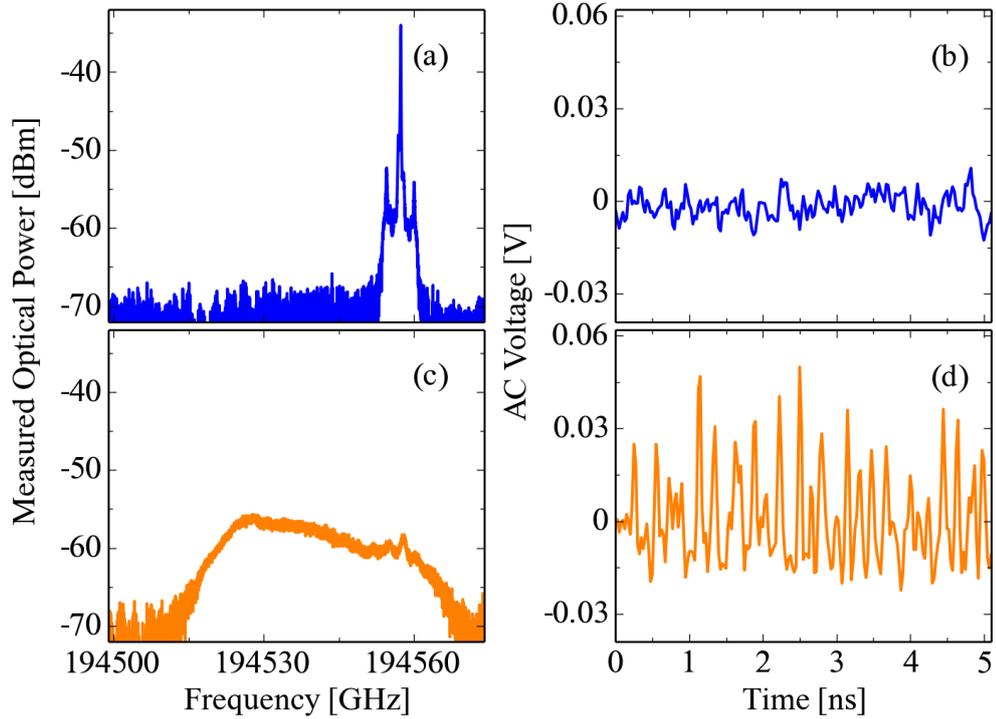
Figure 1.4: Fingerprint of the coherence collapse phenomenon on the intensity dynamics. The optical spectra depicted in panels (a) and (c) correspond to the solitary laser and the delayed feedback laser scenarios respectively. The corresponding AC-coupled (no DC voltage component) time traces are plotted in panels (b) and (d). The tens of GHz linewidth collapse is reflected in fast and chaotic oscillations of the corresponding time trace.

to tens of GHz. The intensity dynamics experiences the corresponding expected destabilization, with chaotic pulsations on sub-ns time scale. Detection bandwidth plays a fundamental role in the study of the intensity dynamics of this system. The fast intensity pulsations, that remained mostly unresolved for a long time, can now be characterized in detail due to multi-GHz scopes in combination with fast photodetectors.

The last characterization tool that we will illustrate is the RF power spectrum. The presence of sub-nanosecond chaotic pulsations will have the direct consequence of broadening the RF bandwidth up to multiple GHz.

Figure 1.5 depicts the fingerprint of the delayed feedback on the RF power spectrum. In a multiple GHz scale (panel 1.5a) it can be seen that the spectrum broadens from roughly 2 GHz to a spectrum flattened by the multi-GHz hyperchaos signature. The relaxation oscillations frequency are clearly visible in the solitary laser conditions (highest power frequency in the black curve). In the two distinct values of the feedback strength (green and red lines represent successively higher feedback strengths) the maxima peaks broaden and shift towards higher frequencies.

Figure 1.5b is an illustration of the fingerprint of the delay time in the laser spectrum
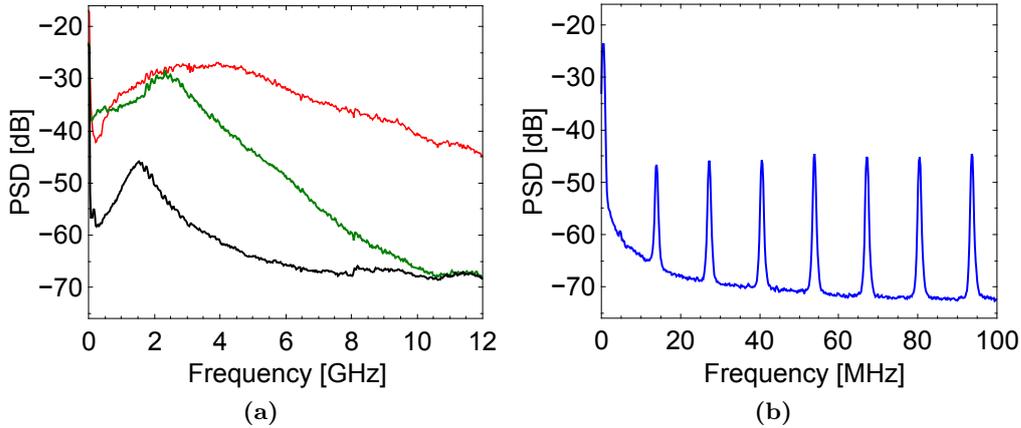
Figure 1.5: Evolution of the RF power spectral density (PSD) under delayed optical feedback. Panel (a) shows the PSD over a 12 GHz frequency span for increasing feedback conditions. The solitary laser emission (black line) and two successively higher values of the feedback strength (green and red lines) are depicted. Panel (b) depicts a zoom of the first 100 MHz in a feedback scenario where the signature of the inverse delay time is clearly recognizable. The external-cavity frequency resonances are clearly visible as equidistant peaks separated by 13.43 MHz.

for such long external cavity feedbacks. The inverse of the external-cavity roundtrip time is clearly recognizable as resonance peaks in the RF power spectrum. These peaks are separated in frequency a distance corresponding to the inverse of the light flight time in the external cavity, here 13.43 MHz ($\tau_{\mathrm{f}} \simeq 74.5$ ns).

1.4 Chaos Synchronization in Optically-Coupled Semiconductor Lasers

In section 1.1 we discussed the central role of photonics in nowadays telecommunications. Indeed, it would be desirable if this physical layer that sustains the global connectome, could be employed to realize extra security and privacy needed in the present.

In our days, privacy of communications is assured via software-based cryptography [40]. The actual paradigm is the public-key cryptography, an approach mostly based on algorithmic procedures for asymmetric ciphering. It is beyond the scope of this introduction to enter into the details of the specific methods used to encrypt and decrypt the data using algorithmic-based public-key cryptography, but we will give a brief overview of the advantages and possible risks. The obvious advantage in comparison with the methods prior to public-key cryptography is the applicability to today's widely connected world. Indeed, this approach has hugely helped to the democratization of encrypted communications.

The standard cryptosystem in this respect is known as the RSA (after MIT professors Ravi, Shamir, and Adleman) [41]. The reason why this software based cryptosystem is considered relatively secure and has become a standard is related to the *mathematical*

difficulty to break it. The security of this algorithm relies on the difficulty to decompose very large numbers into its prime factors. The best known algorithms associated with the prime numbers factorization face a complexity that grows exponentially with the size of the integer number to factorize. The "security rule" is actually quite simple, the bigger the number used, the more secure the communications is.

However, a change in the complexity of factoring big numbers could undermine the security of most encryption systems. This threat could come either from the world of mathematics in the form of some advanced algorithm for the factorization[6] or from the world or physics in the form of, e.g., the quantum computer approach [42].

Therefore, *hardware-based encryption* of the information via the physical layer represents an attractive option for the security enhancement of today's algorithmic security schemes. Photonics systems, given their privileged position as the backbone of modern global telecommunications, provide a realistic chance to implement this possibility. Among the possible options of photonics-based secure communications schemes, in the present work we implement a secure-key protocol based on identical chaos synchronization between two delay-coupled SL. Advantages and limitations will be extensively discussed in the chapter devoted to this topic.

Chaos synchronization is the natural evolution in the NLD framework of the classical synchronization phenomenon, already discovered in the mid 1660's by Christiaan Huygens. The key idea behind the synchronization phenomenon is the subtle nature of the coupling between the synchronized systems. The coupling should not drive the system with higher intensity than the intrinsic dynamics of the system [43].

In the specific topic of chaos synchronization, the pioneering work by Fujisaka and Yamada [44] was soon followed by Pikovski's idea of synchronization of chaotic attractors [45], and by Afraimovich's first demonstration [46]. Finally, the concept was experimentally demonstrated in the beginning of the 1990's by Pecora and Carroll under convenient coupling conditions [47–49].

Chaos synchronization was numerically demonstrated for SL by Winful and Rahman already in 1990 [50]. However, robust experimental synchronization between all-optical chaotic SL required more time. Two optically-coupled semiconductor lasers exhibited synchronized dynamics in the sub-nanosecond time scale for weak to moderate coupling rates and long delay times in [20, 51]. Figure 1.6 illustrates an exemplary scenario of identical chaos synchronization between two optically-coupled SL in experiments.

The original concept of chaos synchronization in SL contemplated perfect synchronization conditions by means of coupling of identical laser units. In this type of system, the information is secured by means of hiding it within (or nonlinearly mixing it with) the noise-like output of the chaotic emitter. This idea is only successful if the receiver is able to exactly extract the deterministic chaotic waveform from the mixed message-dynamics information. This mechanism was coined *chaos-pass-filtering* [51] and had the additional advantage that an hypothetic eavesdropper could only extract the message

---

[6]In fact, there exist no mathematical limitation to the possibility of finding a simplification method that would lower down the complexity to factorize prime numbers and convert an exponentially difficult problem into a polynomially difficult problem.
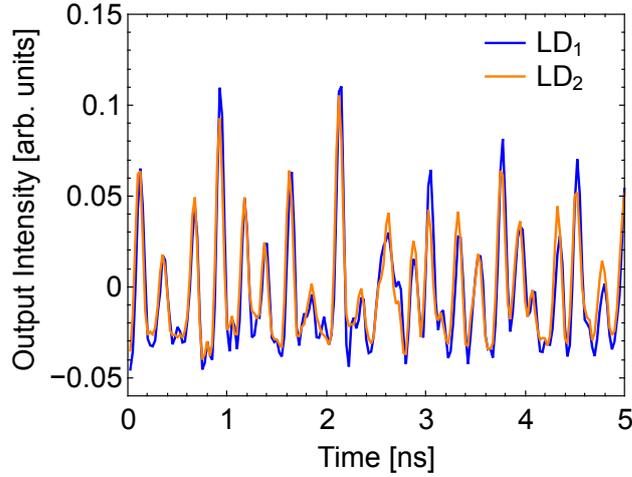
Figure 1.6: Example of identical chaos synchronization between two delay-coupled lasers in experiments. The fast sub-ns chaotic pulsations are well synchronized up to the level of detection noise.

with an identical laser. It is obvious that the difficulty for the eavesdropper to find an identical device is enhanced with respect to that of the emitter and receiver, that may have shared this information beforehand.

The first proposed schemes of optical chaos cryptography involved solid-state lasers and fiber ring lasers [52, 53]. Using semiconductor lasers delayed-coupling is a very advantageous mechanism to achieve chaos cryptography, because SL coupled in such a way typically display high-dimensional chaotic dynamics, with hundreds of positive Lyapunov exponents. Consequently, intensive research on SL systems with feedback has been carried out to demonstrate that photonics-based chaos cryptography is possible in their synchronized hyperchaotic regime [54, 55].

However, there is a drawback in the proposed schemes, identical chaos synchronization is difficult to achieve in experiments. Indeed, the unavoidable mismatches present in real systems (that can be very small but nevertheless significant in the context of NLD) and a variety of noise sources typically degrade the synchronization quality and might induce frequent failures in the explained scheme.

The approach we follow in this thesis to overcome this problem is via a particular key-distribution protocol. This scheme relies on identical synchronization (therefore it needs at least very similar units), but exchanges only a key between both units, not the full message. Therefore we can afford loosing some bits due to mismatches and due to noise-induced desynchronization events and still exchange those secure synchronized bits between the two coupled units. We will demonstrate that our proposed scheme is robust against desynchronization events and, therefore, suitable for field technological applications, where parameter mismatches between the lasers and noise in the communication channels are unavoidable.

1.5   Outline of this Thesis

In the present thesis, the reader will find a study on the dynamics of semiconductor lasers optically coupled with delay. The thesis can be divided into three conceptually different parts. In the first part, centered around the system of a single laser subject to delayed feedback, different aspects of the dynamical behavior of this system are characterized in detail. In the second part, our attention shifts from the single laser system to a system of two delay-coupled lasers. The phenomenon of chaos synchronization is studied in this context and, for the specific case of identical synchronization, it is used to implement a secure communications scheme. The third part is devoted to the study of a novel system of a single laser with two cavities of different length. A more detailed chapter-oriented outline is provide in the following:

- In **Chapter 2**, the dynamics of a semiconductor laser subject to delayed optical feedback is studied in detail. The problem of feedback-induced instabilities is approached from a time scale perspective, relating the dynamical regimes with the characteristic frequencies of the delayed feedback system. The empirical finding that the ratios of these characteristic frequencies completely determine the dynamics constitutes a model independent approach to the characterization of these systems that can be used, for example, to test the validity of numerical models intended to explain the dynamical behavior of these lasers. The general validity of our approach is validated in comparison with other laser diodes with distinct characteristics.

- **Chapter 3** is devoted to the characterization of specific properties of the dynamics by means of the shape of the intensity autocorrelation function. For this purpose, the experimental autocorrelation is compared with the autocorrelation obtained from a model of a linear stochastic oscillator with delay. The relation between the model parameters and the experimental system parameters is analyzed and discussed together with the limits of validity of this approach.

- In **Chapter 4**, the chaos synchronization phenomenon is explored in two configurations: an unidirectional coupling configuration where the delayed feedback configuration presented in the previous chapters is extended via an optically coupled response laser, and a bidirectional coupling scheme of two mutually coupled lasers with self-feedback. In the first configuration, the relation between dynamics and synchronization is studied. In the latter scheme, the robustness of the synchronized state is characterized against detuning in parameters and noise.

- In **Chapter 5**, the knowledge gained in the synchronization experiments is used to implement a classical public-channel secure-key exchange protocol in the bidirectional coupling scheme. This protocol is demonstrated experimentally, and its advantages and weaknesses are analyzed.

- In **Chapter 6**, we discuss a system consisting in a semiconductor laser with filtered feedback from two delay cavities. Such system displays a dynamical regime

dominated by state-dependent delay dynamics, where the system switches in a self-organized fashion between two well-separated delays determined by the state of the system itself.

- The last chapter is devoted to present some **Concluding Remarks**. Therefore, the main results of this thesis are summarized. In addition, we also propose some perspectives for future investigations and discuss possible directions of the delay-coupled semiconductor lasers field.

Chapter 2

Semiconductor Lasers Subject to Delayed Optical Feedback: Similarity Properties in the Dynamics

2.1   Introduction

Early after the experimental demonstration of the first semiconductor laser [6] it was reported that delayed optical feedback[1] can induce instabilities in the emission of semiconductor lasers [14–16]. This phenomenon originally represented a nuisance in the performance of laser diodes because even low amounts of feedback dramatically reduced the coherence and the stability of the emission of these lasers [39, 56, 57]. Therefore, it became important to understand semiconductor lasers with delayed optical feedback and their dynamics in order to avoid or control the feedback issues. For many years the most accepted classification of dynamical regimes in delayed feedback lasers has been due to Tkach and Chraplyvy on the sample of a DFB laser subject to feedback from a distant mirror [36]. This classification established a rigid map of states in dependence of the feedback strength and the distance to the reflecting mirror, two fundamental parameters in delay-coupled lasers. However, only limited understanding of the fundamental mechanisms that cause feedback instabilities are obtained from such classifications.

Indeed, the feedback regimes require a redefinition under a more physics related perspective. For this purpose, here a concept related to the property of synchronizability of chaotic dynamics is utilized.

---

[1]In the context of this thesis, the expression *delayed optical feedback* always refers to light coupled back into the cavity of the laser diode maintaining the polarization orientation.

2.1.1   Strong and Weak Chaos Regimes

In the last decades, a number of studies have addressed the topic of chaos synchronization in delay-coupled systems. A fundamental property, namely *chaos strength*, has been introduced in relation with the Lyapunov spectrum of delay-coupled nonlinear oscillators [58–60]. The formal definition addresses the stability of chaos synchronization in delay-coupled networks where the coupling delay times are much longer than the characteristic time scales of the uncoupled systems. In particular, **strong chaos** and **weak chaos** refer to different scaling behaviors of the maximum Lyapunov exponent within the synchronization manifold.

For strong chaos, the maximum Lyapunov exponent is independent of the delay time and its magnitude is comparable to the inverse of the characteristic time scales of the uncoupled systems, therefore the synchronization will be unstable already on the fastest time scales. For weak chaos, the maximum Lyapunov exponent is comparable to the inverse of the delay time. Hence, the trajectories of the coupled units will separate on the time scale of the long delay time and synchronization can be stable. The oscillator is capable to synchronize its instantaneous emission with its delayed feedback field (or with a different laser's field) if it is emitting in the weak chaos regime. On the contrary, if the oscillator is emitting in strong chaos, it will not be able to synchronize its emission with any other in-coupled field. This defines two different dynamical regimes for delay-coupled nonlinear oscillators: one regime where synchronization is possible and stable (weak chaos), and another regime where synchronization is not possible because it is fundamentally unstable (strong chaos).

In the scenarios of delayed feedback and delay-coupled SL, our aim is to unveil the relations between these important chaos regimes and the dynamics as measured in experiments. Therefore, the interest in this property goes beyond the scope of this chapter and is also addressed in chapter 4.

2.1.2   Chapter Outline

The results presented in this chapter constitute a novel perspective on the consequences of delayed optical feedback on the dynamics of semiconductor lasers. The old problem of feedback characterization has been approached from a time scale perspective, drawing a scenario where the dynamical regimes have a meaningful relation with the characteristic frequencies of the delay-coupled system. These frequencies will be completely characterized from direct experimental measurements in quantum well single mode SL. The dynamics changes correspondingly with the changes of the ratios of these characteristic frequencies. This empirical finding constitutes a model independent approach that can be used to test the validity of numerical models that intend to explain the dynamical behavior of these lasers. The good agreement of our approach with the paradigmatic rate equations model for a quantum-well single-mode SL subject to delayed feedback [61] is demonstrated in section 2.7. The final part of the chapter is devoted to discuss the applicability of this approach to quantum dot lasers, i.e., SL with different gain material than quantum well lasers. These results extend the validity of our model-independent

redefinition of dynamical regimes in delayed FB lasers.

2.1.3 Contributions to the Work in the Present Chapter

A significant part of the results presented in this chapter has been published as: X. Porte, M. C. Soriano, and I. Fischer, "Similarity properties in the dynamics of delayed-feedback semiconductor lasers", *Physical Review A*, **89**, 023822 (2014). The work on the similarity properties in QD lasers has been published in the conference proceedings of the *24th International Semiconductor Laser Conference* as: Xavier Porte, Miguel C. Soriano, Stefan Breuer, Lukas Drzewietski, Wolfgang Elsäßer, and Ingo Fischer, "Scaling Properties of the Dynamics of Semiconductor Lasers in External Cavities" (2014).

The planning and execution of the experiments in quantum well lasers have been done by me under the supervision of Miguel C. Soriano and I. Fischer. Numerical simulations were performed by Miguel C. Soriano. The experiments on quantum dot lasers have been executed at the Technical University of Darmstadt (Semiconductor Optics Group laboratories) by me in collaboration with Lukas Drzewietski and Stefan Breuer. The planning of the quantum dot experiments and posterior discussion of the results have been done together in collaboration with Lukas Drzewietski, Stefan Breuer, Wolfgang Elsäßer, Miguel C. Soriano and Ingo Fischer.

2.2 Experimental Methods

2.2.1 Semiconductor Lasers

In the first part of the chapter, experimental results using two quantum-well semiconductor lasers are presented. These lasers are a discrete-mode laser diode (DM) [62] and a distributed-feedback laser diode (DFB) [34]. Both lasers are single longitudinal-mode emitters in absence of feedback, with side-mode suppression ratios larger than 40 dB. The threshold current of the DM laser is $I_{\text{th}} = 12.08$ mA at a temperature of 22 ℃. The threshold current of the DFB laser is $I_{\text{th}} = 7.72$ mA at a temperature of 21 ℃. The emission wavelengths of these two lasers are around 1550 nm. Under the previously mentioned operating conditions, the DM laser emits with a frequency of 194327.8GHz and the DFB laser emits with a frequency of 194524.7GHz.

The linewidth enhancement factor (α parameter) is a parameter closely related to the sensitivity of a semiconductor laser to delayed optical feedback. We have characterized the α parameter of these lasers using the Henning-Collins method [63]. The α parameters obtained for the DM and the DFB lasers are $\simeq 1.9$ and $\simeq 3.2$, respectively.

In the last section, the validity of the presented approach is tested for a device with different gain material and cavity structures, a quantum dot (QD) laser diode with a Fabry-Perot resonator cavity. This device has a gain medium composed of three independently grown populations of quantum dots. The emission wavelength of the different populations ground states (GS) are $\lambda_{\text{GS1}} \simeq 1273$ nm, $\lambda_{\text{GS2}} \simeq 1249$ nm, and $\lambda_{\text{GS3}} \simeq 1226$ nm. Within this potentially broad bandwidth, the Fabry-Perot cavity structure allows

the emission in different, equally spaced, longitudinal modes. The threshold current for the selected operating temperature (18 °C) is $I_{th} = 92.56$ mA.

2.2.2   Feedback Experiments in Fiber-Based Setups

Most experimental setups employed in this thesis are fiber-based. Only in some cases the laser will be free-space mounted and the connection to the rest of the fiber setup will be made via a coupling stage.

Fiber-based feedback setups have some advantages with respect to the traditionally used free-space setups. These advantages include among others: higher mechanical stability, accessibility to long/very-long external cavities and availability of many standard telecommunications components. In contrast, the control of the polarization of light propagating through the optical fibers needs to be taken care of in these setups. Inherent birefringence in optical fibers can be compensated for using an in-line polarization controller. In addition, birefringence is affected by modifications in stress along the fiber or variations of the ambient temperature. The experience acquired during the experiments under laboratory conditions demonstrates that these phenomena and their effects can be kept under control.
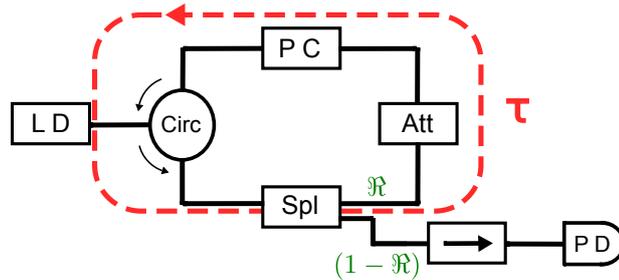
Figure 2.1: Scheme of our typical experimental setup to study feedback dynamics. LD: laser diode, Circ: optical circulator, PC: polarization controller; Att: optical attenuator, Spl: one by two intensity splitter with $\Re$ and (1-$\Re$) splitting ratios, →: optical isolator, and PD: photodiode.

From the possible different configurations to implement delayed optical feedback using fiber-based setups, we have chosen the single-pass fiber-loop. Figure 2.1 depicts this particular scheme of experimental setup, realized by employing standard telecommunication components. The dashed red line encloses the external cavity of round trip time τ defined by twice the length of the laser's fiber pigtail plus the fiber components loop. Such a fiber-optic external cavity has characteristic round-trip times of ~ 100 ns.

A variety of fiber-based elements allows to accurately control the different experimental parameters, and the fiber-loop configuration ensures that none of the components is crossed more than once during the optical path (obvious exception to this rule is the circulator that encloses the loop). This avoids additional losses, consequence of passing twice through each component. All fiber connectors are FC/APC connectors (ferrule connectors with an angled physical contact), reducing considerably back-reflections from the connections between components by ~ 65 dB.

By means of measuring the relative losses through the successive elements in the external cavity, a maximum value of the feedback strength σ_{max} can be estimated. The maximum feedback strength, i.e., the proportion of intensity reflected back to the laser diode cavity for the depicted setup is 54%. From this maximum value, the feedback strength σ can be attenuated by more than 30 dB using the in-line attenuator. The attenuation and the feedback rate are related via the following expression:

$$Attenuation[dB] = -20 \log_{10} \left(\frac{\sigma}{\sigma_{max}} \right). \tag{2.1}$$

Thus, any axis plotting the feedback attenuation will depend logarithmically on the proportion of power fed back into the laser diode cavity.

2.2.3 Acquisition Conditions

The time-dependent intensities have been detected using a 12.5 GHz bandwidth AC-coupled photodetector and a 16 GHz analog bandwidth oscilloscope. The time traces sampling frequency is 40 GSamples/s and their typical recorded time interval is over 100μs. The optical spectra at 1550 nm have been recorded using a Brillouin scattering-based high-resolution optical spectrum analyzer with 10 MHz optical resolution. A more flexible but less precise diffraction grating optical spectrum analyzer has been used to detect the emission of the QD laser around 1220 nm. This instrument has a broad tuning range from 600 nm to 1750 nm with a maximum resolution of 50 pm.

2.3 Characteristic Frequencies of Delayed Feedback Lasers

The approach followed in this chapter implies the experimental determination of the characteristic time scales present in semiconductor lasers when subject to delayed optical feedback. These time scales correspond to the frequencies that constitute the complex spectral characteristics of these lasers. Moreover, it is of major importance to know this information for the characterization of possible operating conditions. Three fundamental frequencies have been identified to determine the resulting feedback dynamics, and are therefore studied in this section. Two of them can be directly determined from the optical spectrum. The other one, too small to be accurately resolved in the optical spectrum (since with very long external cavities), has been characterized via the intensity power spectrum.

Figure 2.2 shows the dependence of the optical spectra on the feedback strength for the DM laser. The figure is made of stacked optical spectra for different values of the attenuation. Each one of the 48 color-coded horizontal lines corresponds to an experimentally recorded optical spectrum for a given attenuation value. The increase in attenuation reduces the feedback strength, that has its maximum at 0dB of attenuation. The injection current has been kept constant at $1.5I_{\text{th}}$ for all the recorded spectra. The solitary emission optical frequency, denoted with a solid line, has been shifted to 0GHz.
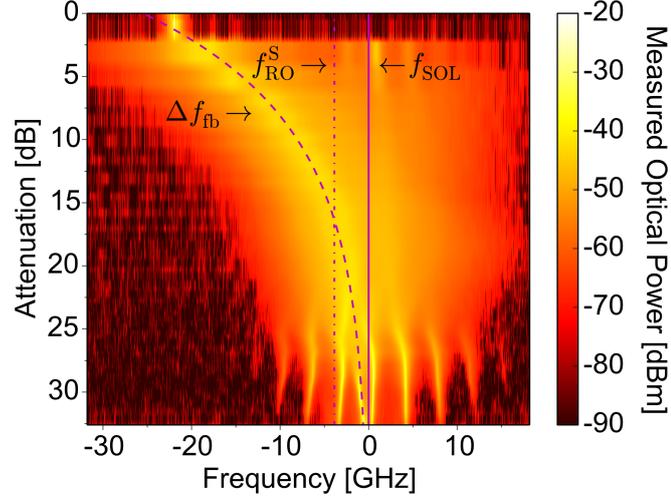
Figure 2.2: Color-coded optical spectra versus the feedback attenuation. The important frequencies are highlighted with different lines in the figure, i.e., a solid line denotes the solitary laser emission frequency, f_{SOL}. The dashed-dotted line marks the solitary relaxation oscillations frequency, f_{RO}^S. Finally, the dashed curve indicates the feedback-induced frequency shift, Δf_{fb}.

The increase in feedback strength tends to enhance the dynamical bandwidth. The broadened optical spectra extend towards the lower frequencies direction due to the positive sign of the α parameter. Only at the strongest feedback conditions, the spectrum collapses again to a narrow linewidth state. This transition, the occurrence of which strongly depends on the α parameter, will be explained in more detail later in this chapter. The dashed line indicates the maximum of the bandwidth enhanced spectrum, here named Δf_{fb}, which shifts with the feedback attenuation. This is the first characteristic frequency that can be directly determined from the optical spectrum. The logarithmic dependence of Δf_{fb} on attenuation indicates (following Eq. 2.1) a linear relation between this frequency and the feedback strength in experiments, which is in good agreement with the predicted dependence in rate-equations based models of a laser with feedback.

The dashed-dotted line (parallel to the solitary laser frequency line) at $\simeq 4$ GHz denotes the second characteristic frequency, the relaxation oscillations frequency for the solitary laser f_{RO}^S. This frequency is strongly undamped for feedback attenuations larger than 25dB, and does not shift significantly with attenuation. In fact, f_{RO} mainly depends on the pump current. Figure 2.3 shows the clear square root dependence of this frequency with the excess pump current ($\frac{I}{I_{th}} - 1$). Therefore, the relaxation oscillations frequency is the second relevant frequency of the system which we can directly characterize from the optical or the power spectrum.

The last frequency that has an important role in the dynamics of the system is the inverse of the delay time. It appears as a consequence of coupling the laser diode to the external cavity. For such long fiber-based cavities, this frequency is of the order of few MHz, and it is better characterized via the intensity power spectrum. Figure
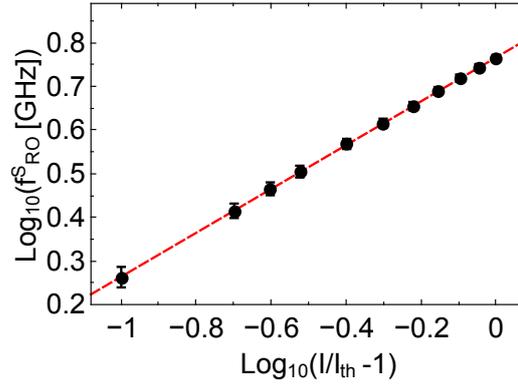
Figure 2.3: Experimentally determined relaxation oscillations frequency (for the solitary laser) as a function of the excess pump current. The slope of the linear fit (dashed red line) is 0.5 ± 0.01, indicating a very good agreement with the square root expected dependence.

2.4 illustrates the power spectrum of the DM laser subject to feedback. The broad bandwidth extending beyond 9 GHz at -10 dB indicates chaotic dynamics under these operating conditions.
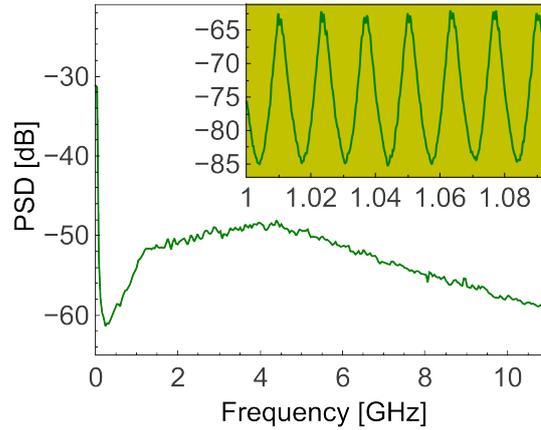
Figure 2.4: Power spectrum of the DM laser subject to delayed optical feedback for a bias current of $I = 1.1 I_{th}$ and the highest feedback strength $\sigma_{max} = 0.54$. The inset magnifies the power spectrum at 1 GHz. The resonances of the external cavity frequency modulate the power spectrum with the external cavity frequency, $f_{EC} = 13.32 \pm 0.01$ MHz.

The inset in Fig. 2.4 depicts a zoom at 1 GHz of the power spectrum[2]. A modulation with a frequency spacing equal to the inverse of the external cavity roundtrip time is clearly visible. This resonances structure extends all along the power spectrum. For this particular external cavity length the frequency corresponds to $f_{EC} = 13.32 \pm 0.01$ MHz, corresponding to $L_{ext} = 15.49 \pm 0.01$ m. A longer cavity would result in even closer

---

[2]The power levels of the inset and the main panel do not coincide because the data have been detected with different resolution bandwidths.

external cavity modes.

The figures in this section demonstrate that the main frequencies of feedback lasers can be directly determined in experiments. The influence of f_{RO} and f_{EC} on the dynamics has been recognized in earlier works. Here, we include Δf_{fb} as the third key frequency in the determination of the dynamical regime, as it will be explained in detail.

2.3.1   Autocorrelation Function of the Intensity Dynamics

In laser systems with optical feedback, the time scales may differ by several orders of magnitude. Nowadays, state of the art technologies offer the possibility to detect and record these relevant time scales from the intensity dynamics. The acquisition conditions for the time series depicted in this thesis include a sampling time of 25ps (16GHz analog bandwidth) and a recorded time interval over 100μs. This means that the acquired time series always comprise more than 500 repetitions of the delay time. Thus, the time scales related to f_{RO} and f_{EC} are present (with enough statistics) in the recorded time series and, in consequence, we can analyze them in detail.
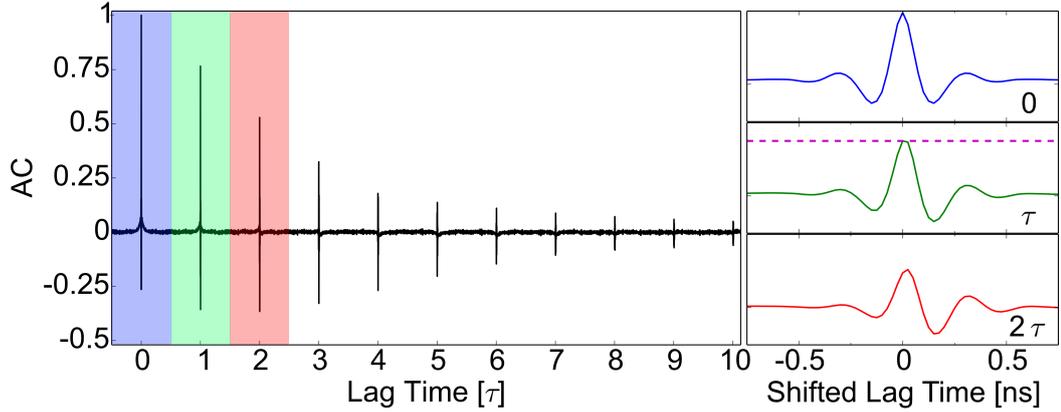
Figure 2.5: Autocorrelation function (AC) of the intensity dynamics showing the successive laser response echoes at multiples of the delay time for a bias current of $1.08 I_{\mathrm{th}}$ and a feedback attenuation of 1.9 dB. The three panels on the right-hand side depict zooms centered at the central AC peak (0), the first (τ) and the second (2τ) delay echoes, respectively. The dashed magenta line in the right-central panel indicates the height of the AC at this first delay echo. The delay time is $\tau = 75.25 \pm 0.025$ns.

A commonly used approach to analyze the characteristic time scales of a delayed feedback system is to calculate the autocorrelation function of the recorded intensity (AC) [64, 65]. Figure 2.5 illustrates the intensity dynamics AC of a delayed feedback laser. The normalized AC is averaged, here, over the whole time series:

$$\mathrm{AC}(k) = \frac{\langle I(t+k)I^*(t)\rangle}{\langle |I|^2(t)\rangle}, \tag{2.2}$$

where I represents the detected intensity of the optical field ($I = E^*E$) and k is the lag time.

The features of the AC function around time shifts of delay-time size (τ) are high-lighted on the three right hand side panels in Fig. 2.5. Each panel shows an oscillatory structure of frequency and decay similar to those of the relaxation oscillations, but affected by the chaoticity of the dynamics. The region around τ (from now on referred as the *first delay echo*) is of special interest because it illustrates the nonlinear transformation of the delayed feedback signal by the laser [65]. In particular, the AC peak height of the first delay echo (indicated with a dashed magenta line in Fig. 2.5) is a good indicator for the weak and strong chaos regimes in SL (see sections 2.4.1 and 4.3), and it will be named from now on as the *dynamics signature*.

2.4 Invariant Dynamics Signature

The heights of the AC at successive delay echoes depend on the bias current and the feedback strength. The dependence on these two parameters is characterized here in order to explore the different possible dynamical regimes and their transitions by means of the AC height at the first delay echo. Figure 2.6 depicts the maximum AC height at the first delay echo versus variations in feedback strength and bias current. The plotted data cover injection currents in the range from $1.1I_{\text{th}}$ to $1.5I_{\text{th}}$ (four different symbols) and for attenuations up to 25dB. Lower attenuations are depicted on the right hand side (high feedback strengths), and higher attenuations are depicted on the left hand side (low feedback strengths). There exists a dependence on the attenuation that is clearly repeated for every current. Nevertheless, the different currents result in different dependencies.
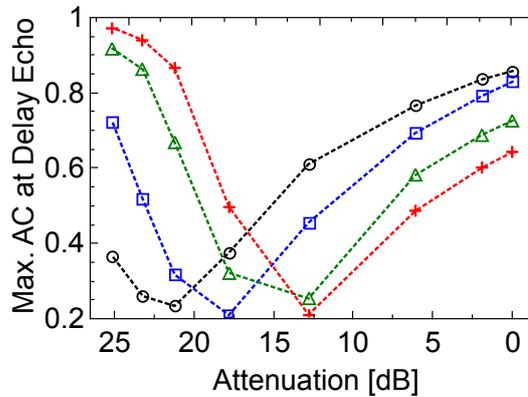
Figure 2.6: Maximum AC height at the first delay echo versus attenuation for four different bias currents: circles (I=13 mA), squares (I=14 mA), triangles (I=16 mA), and crosses (I=18 mA). The solitary laser threshold is $I_{\text{th}} = 12.08$ mA.

It is clear from Figs. 2.2, 2.3 and 2.4 that the characteristic time scales depend on the operating conditions and the feedback parameters. Figure 2.2 illustrates the feedback induced frequency shift Δf_{fb} dependence on the attenuation, while Fig. 2.3 shows that the experimentally measured f_{RO} exhibits a square root dependence on the injection

current. Therefore, each bias current condition in Fig. 2.6 has a different f_{RO} and, in consequence, a different ratio $f_{RO}/\Delta f_{fb}$.

If the ratio $f_{RO}/\Delta f_{fb}$ is to be kept constant, the increase in f_{RO} for increasing bias currents can be compensated for by changing the Δf_{fb} correspondingly, i.e., rescaling the attenuation axis in accordance. The result of keeping the variations between those two characteristic time scales constant is plotted in Fig. 2.7. The same dependence is found when the data is plotted versus a rescaled version of the attenuation. The set of curves corresponding to different injection currents collapse onto the same curve, which is a sign of similarity properties. Suddenly, the different AC heights follow a unique non-monotonous dependence on the feedback strength, exhibiting a clear minimum for intermediate feedback strengths. The transitions from high correlation regions to the low correlation region (intermediate attenuations) can be attributed to the emergence of strong chaos [60, 66]. The motivation behind this rescaling is to keep the measurement independent from the variations between characteristic time scales, as long as their ratios are kept constant.
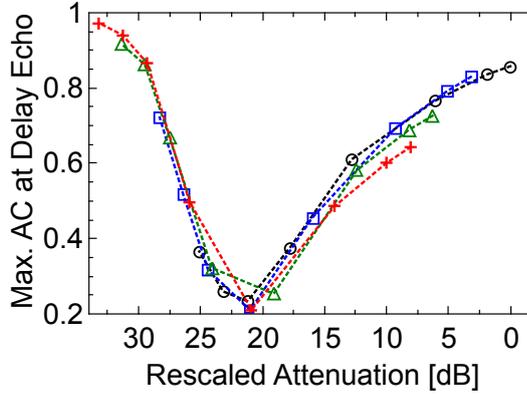
Figure 2.7: Maximum AC height at the first delay echo versus the rescaled attenuation for four different bias currents: circles (I=13 mA), squares (I=14 mA), triangles (I=16 mA), and crosses (I=18 mA). The AC heights corresponding to different currents collapse to a single curve when plotted versus the rescaled attenuation (detailed explanation in the text).

The rescaled version of the attenuation is obtained starting from the expression already introduced in Eq. 2.1. We choose the AC curve at $2I_{\text{th}}$ as a reference and rescale the feedback attenuation for the other currents such that the ratios $f_{RO}/\Delta f_{fb}$ correspond. Thus, the attenuation axis is modified in order to compensate for the variation of f_{RO}. As shown in Fig. 2.3, f_{RO} scales proportionally to the square root of the bias current above threshold for this laser diode[3]. This is the scaling that is compensated for by shifting the attenuation axis. After rescaling, all currents (except $2I_{\text{th}}$) have points with negative attenuation values. In order to keep the attenuation axis positive valued for all currents, the following expression of the rescaled attenuation also includes an offset $A_S[dB]$ equal for all curves:

---

[3]The same square-root dependence with the bias current is predicted from rate equations models of single mode quantum well SL

$$Rescaled\ Attenuation\ (\sigma, I)\ [dB] = A_S \underbrace{-20 \log_{10} \left(\frac{\sigma}{\sigma_{max}} \right)}_{\text{Attenuation}} +20 \log_{10} \left(\sqrt{\frac{I}{I_{th}} - 1} \right).$$

(2.3)

2.4.1 Physical Mechanism for Weak and Strong Chaos

As it was explained in the previous section, once the attenuation is rescaled the dynamics exhibits similarity properties. The AC heights become invariant under appropriate transformation of feedback strength taking into account the corresponding bias current. All data collapse onto a single U-shaped curve, with particularly low values of the AC heights for intermediate attenuations.
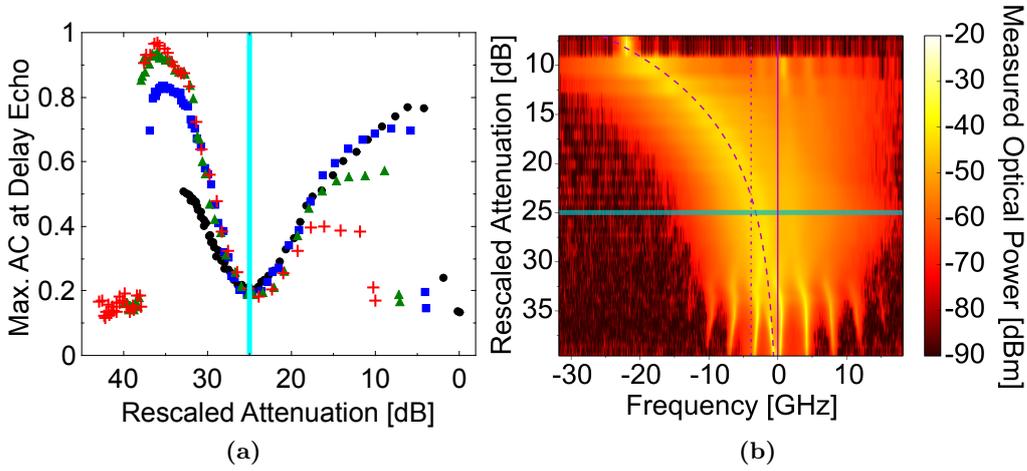
Figure 2.8: (a) maximum AC height at the first delay echo as a function of the rescaled feedback attenuation for four operating currents of the DM laser. The pump currents correspond to $1.1 I_{th}$ (circle), $1.25 I_{th}$ (square), $1.5 I_{th}$ (triangle), and $2 I_{th}$ (cross), respectively. (b) exemplary evolution of the optical spectra versus the feedback strength for a bias current of $1.5\ I_{th}$. The solitary emission optical frequency (solid magenta line) has been shifted to 0 GHz, and the f_{RO} (dashed-dotted line) has been measured independently to be $\simeq 4$ GHz for this bias current. The dashed curve represents the evolution of Δf_{fb} with the rescaled attenuation. The meaning of the cyan lines in both panels is explained in the text.

Altogether, the physical mechanism behind the shape of the AC heights has not yet been clarified. To find the answer, we compare the rescaled AC heights curves with the optical spectral information in Fig. 2.8. Figure 2.8a depicts the maximum AC height at the first delay echo as a function of the rescaled feedback attenuation. Figure 2.8b contains the spectral data already introduced in Fig. 2.2, although here it is plotted against the rescaled attenuation. The set of data depicted in Fig. 2.8 extends the validity of our approach to higher injection currents ($2 I_{th}$) and a larger range of feedback strengths at the expense of having a lower signal-to-noise ratio (SNR) for detection.

In Fig. 2.8a, a cyan vertical line illustrates the rescaled attenuation for which the AC heights have their common minimum. This cyan line is also plotted in Fig. 2.8b (an horizontal line in this case) at the same rescaled attenuation value. Remarkably, the AC height is minimum in the region in which Δf_{fb} (dashed magenta curve) approaches f_{RO} (dashed-dotted magenta line) in Fig. 2.8b. The strong nonlinear interactions resulting from the mixing of these two characteristic frequencies is identifiable in the broadening of the optical spectrum at both sides of the solitary laser frequency. Consequently, the nonlinear mixing of Δf_{fb} and f_{RO} can be considered as the physical mechanism leading to the appearance of a region of strong chaos, i.e. low AC heights, in semiconductor lasers subject to delayed optical feedback. The U-shaped region around the AC heights minimum at intermediate attenuations in Fig. 2.8a is the consequence of this nonlinear mixing between Δf_{fb} and f_{RO}.

Various regions with well differentiated AC heights can be identified in Fig. 2.8a. These regions have corresponding spectral characteristics easy to distinguish in Fig. 2.8b. Below the maximum rescaled attenuation the laser exhibits stable emission in its solitary frequency (shifted to 0GHz), that corresponds to the drop in AC heights beyond 38dB. A slight increase of the feedback strength from this point causes undamping of the relaxation oscillations [67–69], subsequently entering the weak chaos (high correlations) regime. Further increase of the feedback strength causes the transitions towards strong chaos for intermediate attenuations. A second region of weak chaos appears for increasing feedback. Finally, for the strongest feedback conditions, also in Fig. 2.8b, the laser emission becomes stable again exhibiting emission in the high-gain modes region.

Furthermore, in order to prove the general validity of our approach, data from another laser is provided. Both panels in Fig. 2.9 show data from a different laser diode, i.e., the DM laser has been replaced by a distributed-feedback (DFB) laser diode, keeping the rest of the experimental setup unchanged.

Identical conclusions can be drawn from the combined data of the DFB laser. The AC heights fall under the same invariant curve when plotted against the rescaled attenuation. The common minimum in the AC heights (denoted with a cyan line in both panels) again corresponds to the region of maximum nonlinear mixing between the two characteristic frequencies: Δf_{fb} (dashed magenta curve) and f_{RO} (dashed-dotted magenta line).

The abscissas in panels 2.8a and 2.9a extend almost 10 dB more than in Fig. 2.7, because smaller and larger values for the feedback strength are explored. Interestingly, one can observe deviations of the correlation values from the invariant behavior for low feedback strengths. These deviations are completely explained by the different signal-to-noise ratios (SNR) at different bias currents, affecting the experimentally determined values.

A detailed characterization of the SNR impact demonstrates that the effect limiting the heights of the AC for weak feedback values is their respective SNR, and not a deviation from the invariant dynamics. The experimental data with the highest AC value (0.96) at the first delay echo of Fig. 2.8a has been selected. This experimental condition corresponds to the current with the highest SNR, $2I_{\text{th}}$. Fig. 2.10 depicts the AC signature when white noise is externally added to a given experimental time series.
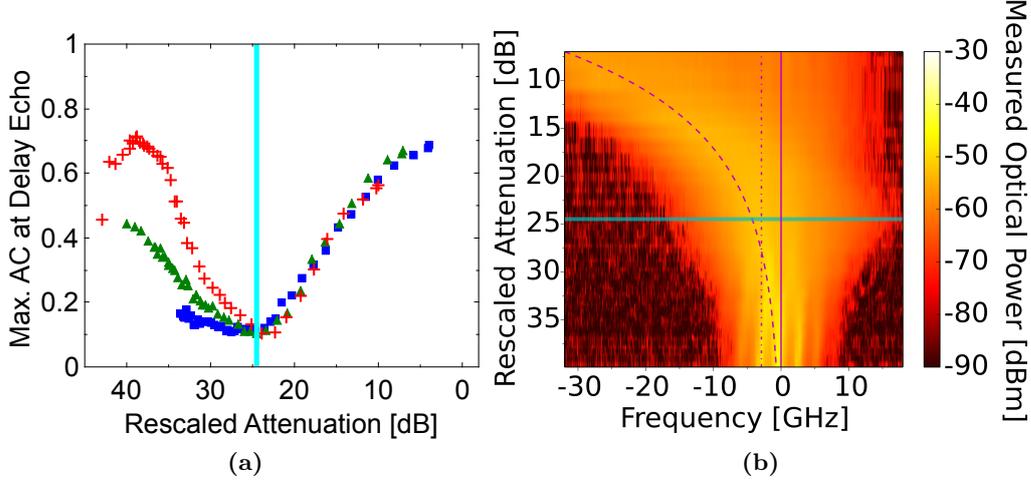
Figure 2.9: (a) maximum AC height at the first delay echo as a function of the rescaled feedback attenuation for (a) three operating currents of the DFB laser. The pump currents correspond to $1.25I_{\text{th}}$ (square), $1.5I_{\text{th}}$ (triangle), and $2I_{\text{th}}$ (cross), respectively. Panel (b) depicts the evolution of the optical spectra versus the feedback strength also for the DFB laser. The corresponding bias current is $1.5\ I_{\text{th}}$ in both lasers. The solitary emission optical frequency (solid magenta line) has been shifted to 0 GHz, and its corresponding f_{RO} (dashed-dotted line) has been measured independently to be $\simeq 2.8$ GHz. The evolution of Δf_{fb} with the rescaled attenuation is represented by a dashed curve. The meaning of the cyan lines in both panels is explained in the text.
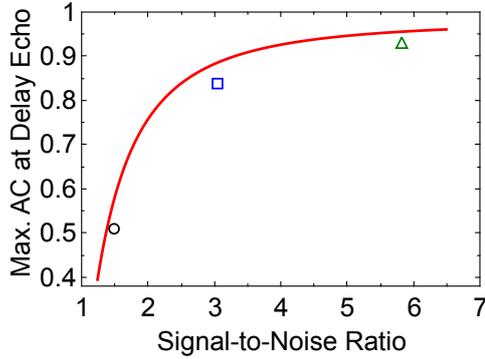
Figure 2.10: Dependence of the maximum of the first delay echo on the SNR (solid line). The original time series corresponds to the conditions with the highest AC at delay echo for the DM laser: bias current of $2I_{\text{th}}$ and 26 dB feedback attenuation. The different symbols depict the maxima of the first delay echo for the other pump currents under weak feedback conditions: $1.1I_{\text{th}}$ (circle), $1.25I_{\text{th}}$ (square), and $1.5I_{\text{th}}$ (triangle).

The addition of noise is associated with a drop in correlation to values below 0.4. For comparison, the different higher AC signatures for the other currents have also been plotted. The dependence given by the SNR influence is in good agreement with the experimental findings within a margin of error below 5%.

Remarkably, there are also deviations for high feedback strengths in panel 2.8a. These

deviations have been verified to be due to the onset of alternations between chaotic dynamics and stable emission. The highly averaged picture captured by the AC is the reason why our dynamics signature is pulled down in such conditions of alternating dynamics. This effect is prominent in the DM laser due to the low α parameter of this laser (~ 2). Another particularity caused by the low α value of the DM laser is that, for the strongest feedback conditions, the emission becomes stable and narrow linewidth again. In fact, the points at the extreme left and right sides in panel 2.8a, showing correlations lower than 0.2, correspond to stable emission in different spectral regions. For high feedback strengths, the dynamics gets trapped in the high-gain modes region, and in the solitary emission mode for very low feedback strengths. The normalized AC mostly reflects intensity and detection noise under both conditions. In contrast to the DM laser, the DFB laser with a higher α parameter (~ 3) does not exhibit stable emission in the scanned parameters range.

2.5   Full Rescaling of the Dynamics

The so far considered rescaling only accounts for the dependence of the dynamics signature on bias current and feedback strength. Exploring the similarity properties of this delay system further, the delay characteristic frequency ($f_{EC} = 1/\tau$) should play a crucial role as well. Therefore, keeping the ratio of the relaxation oscillations and the external cavity frequencies constant, i.e. f_{RO}/f_{EC}, in addition to the condition $f_{RO}/\Delta f_{fb}$, fully equivalent dynamics should be obtained. This is correspondingly illustrated with the schematic drawing in Fig. 2.11.
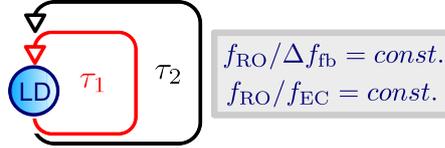
Figure 2.11: Schematics depicting the change in delay time. The indicated ratios between characteristic frequencies must be kept constant to completely rescale the dynamics.

In order to test the previous arguments, the experiment is performed for two delay times, namely τ_1 and τ_2, where $\tau_2 > \tau_1$. The length of the external optical cavity is extended by adding 5 meters of fiber. The delay time is consequently increased from $\tau_1 = 75.18$ns to $\tau_2 = 99.95$ns, corresponding to a scaling factor of $\beta = \frac{\tau_1}{\tau_2} = 0.75$. For these two cases the pump current of $I_1 = 2I_{th}$ is compared to a pump current of $I_2 = 1.566I_{th}$, respectively, such that f_{RO}/f_{EC} remains equal. The different bias currents imply that the amplitudes rescale correspondingly, in addition to the rescaling in time.

The similarity of the dynamics after a change in the delay time is illustrated in Figure 2.12, where the AC is shown for the rescaled delay time and current. Remarkably, not only the maximum AC height at delay echoes is invariant, as shown in panel (a), but the time-rescaled AC function around the delay times, as depicted in panels (b) and (c). The curves correspond to the same condition with minimum AC height at -14 dB
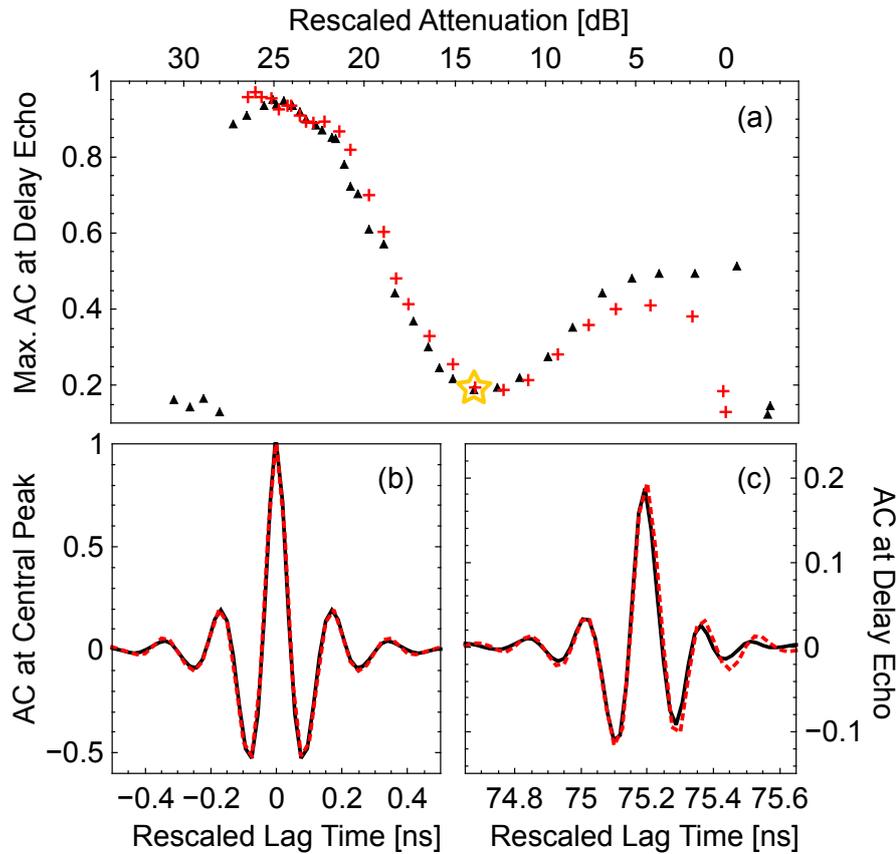
Figure 2.12: (a) AC height at the first delay echo for two different dynamical conditions. Crosses and triangles correspond to $2I_{\text{th}}$, $\tau_1 = 75.18$ns and to $1.566I_{\text{th}}$, $\tau_2 = 99.95$ns, respectively. (b) full AC around the central peak and (c) the first delay echo for a particular rescaled attenuation (indicated with a star) in panel (a). In panels (b) and (c), the dashed lines correspond to $2I_{\text{th}}$, $\tau_1 = 75.18$ns and the solid lines correspond to $1.566I_{\text{th}}$, $\tau_2 = 99.95$ns. Each curve in the lower panels corresponds to the rescaled attenuation with the minimum of each respective AC height in panel (b). The time axis is rescaled by $\Delta t' = \frac{\tau_1}{\tau_2}\Delta t$ for the solid lines in panels (b) and (c).

in Fig. 2.12, indicated with a star. Thus, this verifies that the whole time-rescaled AC functions correspond.

   This result is of high relevance, since it means that dynamics of delayed feedback SL can be scaled in amplitude and time. A particular dynamics that is observed for a certain delay time, can be simply slowed down or accelerated by changing delay time, feedback attenuation and pump parameter appropriately. By this, the dynamical properties can be adjusted and tailored according to the requirements of applications.

2.6   Dynamical Regimes

To gain further insights into the similarity properties of the feedback dynamics we discuss some significant examples. The particular regimes are selected according to their position along the characteristic U-shaped AC heights curve. In section 2.6.1, the regime with high AC values under weak FB conditions is depicted. Section 2.6.2 illustrates the regime of the lowest AC height values at intermediate FB strengths. Finally, in section 2.6.3, the high-correlation dynamics corresponding to the highest FB strengths are depicted.

2.6.1   Low Feedback Strengths

The first illustrated regime corresponds to the weakest FB conditions, in the onset region of the dynamical instabilities. Figure 2.13a indicates with a star the characteristic high dynamics signature for this regime. The rescaled attenuations corresponding to these low values of FB strength are around 30 dB and, in the selected example, the bias current is I=18 mA ($\simeq 1.5I_{\text{th}}$). These conditions correspond to the undamped relaxation oscillations (URO) dynamics [69], occurring just after the transition from stable to unstable emission.

Figure 2.13b shows the optical spectrum, in which some characteristic frequencies are present. The highest intensity peak corresponds to the solitary laser mode. The frequency peak at its immediate left side corresponds to the feedback induced frequency shift (Δf_{fb}). Moreover, one can observe other side peaks that are shifted by multiples of the relaxation oscillations (f_{RO}). This weak feedback regime is defined by Δf_{fb} being (significantly) smaller than the solitary relaxation oscillations frequency (f_{RO}). This condition is fulfilled for different feedback strengths depending on the specific value of the α parameter because the growth of Δf_{fb} increases with α.

The AC is depicted in Fig. 2.13c for an interval of 10τ. It becomes clearer now why in this regime the AC height potentially has its maximum values. The overall AC decay along multiple delay echoes is very small and the system contains, in average, persistent τ-fedback memory of its past states. The inset in Fig. 2.13c depicts the AC oscillations around the first delay echo. These oscillations are the signature of the undamped relaxation oscillations in the AC, they have a frequency mainly dominated by the relaxation oscillations frequency visible in the optical spectrum. In the broader view of the AC, a particular lobe structure modulates the AC envelope amplitudes for multiple delay echoes. This modulation is related to the interplay between the different frequencies that influence the dynamics. Only a slight modification of any of the feedback parameters can significantly modify the lobes structure, but their influence on the AC height will be much minor.

Finally, Figure 2.13d illustrates the spatio-temporal representation [70–72] of the intensity dynamics. In this two-dimensional representation, the delay time is plotted as a pseudo-space variable. Here, the abscissa denotes the time offset in a delay window of length τ. Meanwhile the vertical axis denotes the ordinal of the current delay window. From such a representation in delay-coupled systems, much information can be extracted from long time series, specially if the plotted dynamics is irregular or chaotic. In our
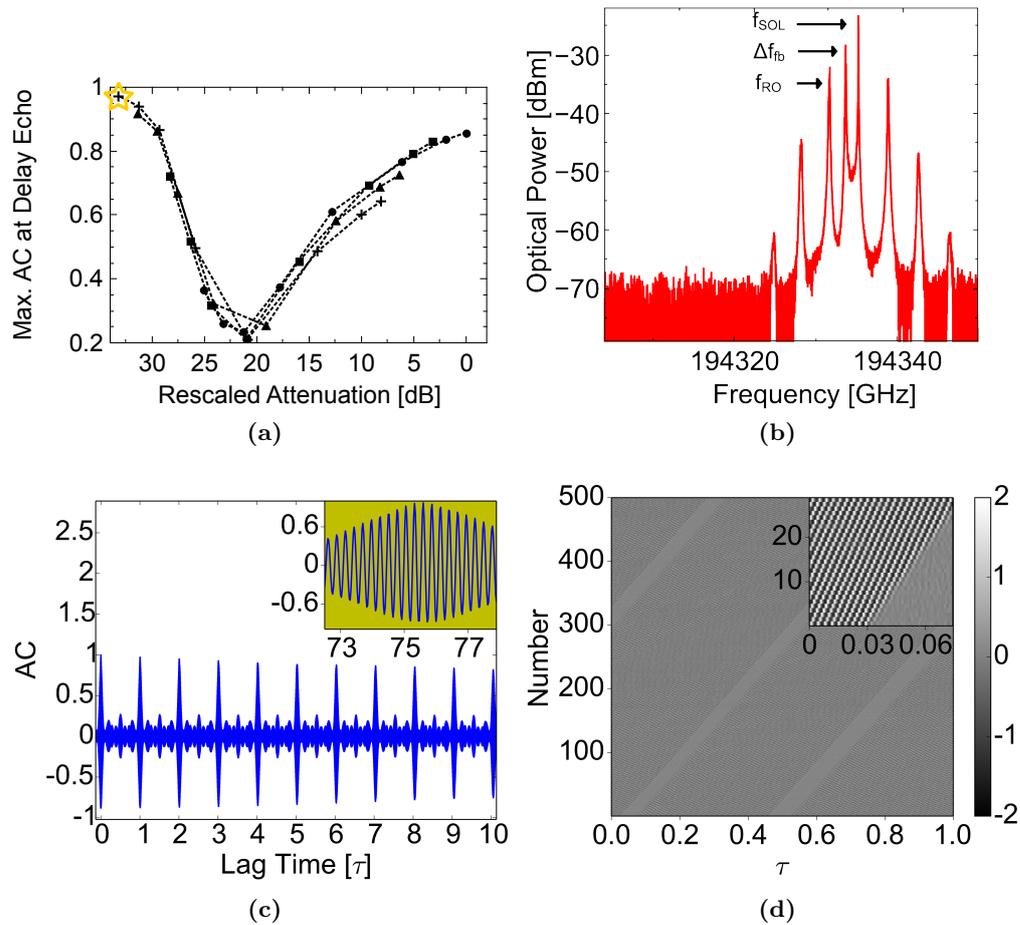
Figure 2.13: Characteristics for low FB strength dynamics at bias current and rescaled attenuation of I=18 mA and 31 dB, respectively. The star in panel (a) indicates the AC height value for this experimental conditions. The other panels depict (b) the optical spectrum, (c) the AC (with inset at the first delay echo), and (d) the spatio-temporal representation of the real-time intensity (with inset for magnification).

case, already at first glance the high correlation that the dynamics has with τ becomes apparent. For a time window of 500τ (more than 30 μs), two distinct and separated dynamics regions coexist. These two dynamics are a stable emission dynamics and an oscillatory state. The region magnified in the inset allows identifying the clear oscillations of constant frequency f_{RO} that characterize the oscillatory region. The coexistence of these two regions resembles the phenomenon of chimera states. This is an hybrid type of dynamics where two states coexist for a homogeneous system, i.e., an ordered state and a dynamical state. Chimera type of dynamics has been previously demonstrated in optical systems [73] and in delay-coupled electronic oscillators [74] among other types of systems.

2.6.2   Intermediate Feedback Strengths

In this section, the particular region in the AC heights curve of the concave U-shaped minimum is discussed. The star in panel 2.14a indicates the position along the AC heights curves of the selected minimum. The rescaled attenuations corresponding to this low-correlation conditions are in the range $\{18 - 25\}$ dB, and the highlighted data point corresponds to a bias current of I=16 mA ($\simeq 1.3 I_{\text{th}}$). This intermediate feedback region represents the paradigmatic strong chaos regime, associated with the dynamics signature approaching a minimum. As explained in section 2.4.1, the nonlinear mixing between Δf_{fb} and f_{RO} is enhanced in this region. This feature can be identified in panel 2.14b, with a broad spectrum covering more than 20GHz at -20dB height, and a decaying spectral power of $\simeq 2$ dB/GHz. Even more, the extended view of the AC in panel 2.14c clearly illustrates the fast fading memory of the dynamics at successive delay echoes for these experimental conditions. The AC height at the first delay echo is below 0.3, as visible in the inset.

It is important to mention that low AC values only indicate strong chaos in this intermediate feedback region. In Figure 2.8a, the extreme values show similarly low AC values for the DM laser. As it has already been explained, these points reflect the transition of the dynamics towards CW emission. Nevertheless, these points can easily be distinguished from strong chaos with similarly low correlations via the corresponding time series. Panel 2.14d shows the spatio-temporal representation of the current strong chaos conditions. One can still recognize structures, which however decorrelate quickly.

2.6.3   High Feedback Strengths

Finally, the strong FB conditions are depicted in Fig. 2.15.

Figure 2.15a illustrates the typical high correlations of the data with rescaled attenuations close to 0dB. The bias current of the point highlighted with a star is I=13 mA ($\simeq 1.1 I_{\text{th}}$). For such low current, the laser exhibits low-frequency fluctuations (LFF). The paradigmatic LFF dynamics is characterized by irregularly distributed dropouts in the intensity dynamics. The characteristic LFF power dropouts are clearly distinguishable in Fig. 2.15d as dark horizontal lines that last for τ and repeat irregularly every $\sim 20\tau$. The low amplitude of these intensity dropouts and their characteristic frequencies, almost three orders of magnitude slower than the picosecond pulsations of the underlying chaotic dynamics, triggered a lot of interest in this phenomenon. However, despite being widely studied in the past [18, 75–80], this dynamics still gives rise to new insights nowadays [81, 82].

The optical spectrum in panel 2.15b shows a two-peaked structure with a distance of ~ 20GHz between the broad peaks. The highest peak, on the left side, corresponds to the spectral signature of the maximum feedback-induced frequency shift (Δf_{fb}), while the peak on the right side of the spectrum is the signature of the dynamics in the region of the solitary laser mode.

The high values of correlation (e.g., inset in panel 2.15c) indicate that the high FB strength conditions correspond to the weak chaos regime. The long-term propagation
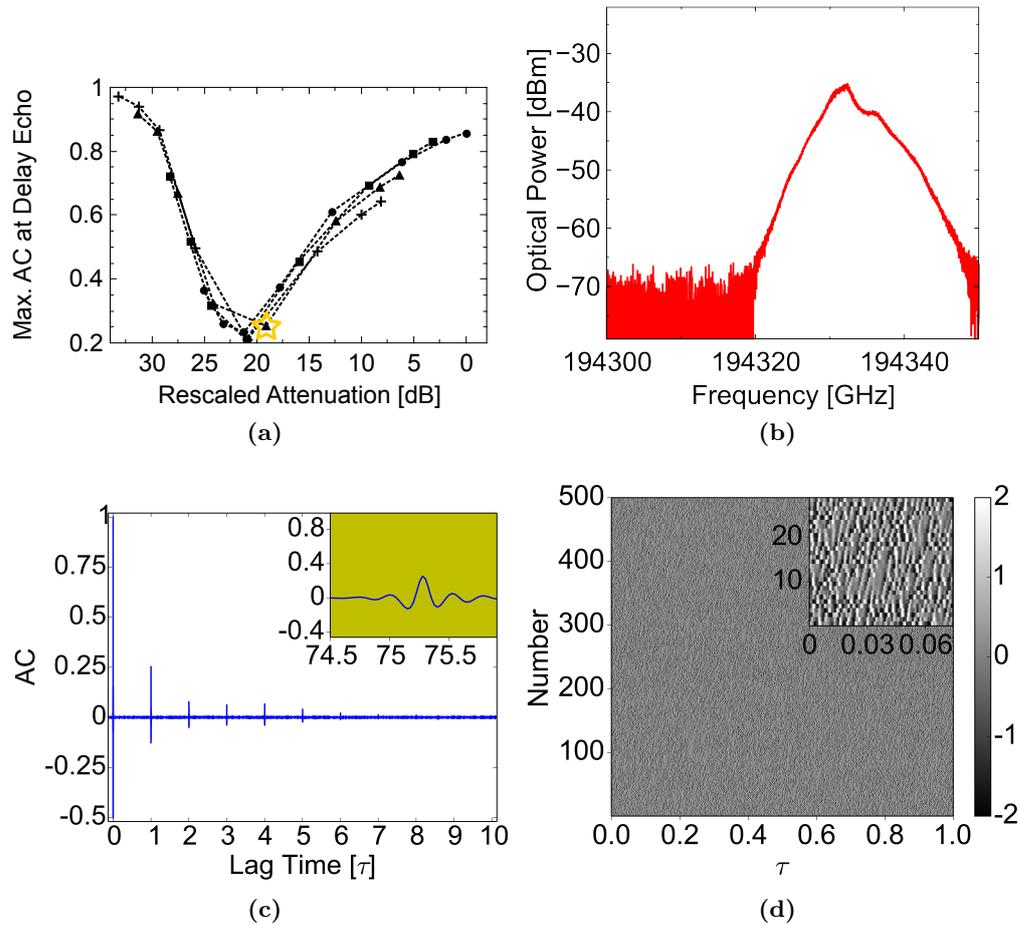
Figure 2.14: Exemplary dynamics at intermediate FB strengths. The bias current is I=16mA and the rescaled attenuation is 19dB. Panel (a) shows the AC height curves. The AC height for the current experimental conditions is indicated with a star. The other panels depict (b) the optical spectrum, (c) the AC (with inset at the first delay echo), and (d) the spatio-temporal representation of the intensity time series (with inset for magnification).

of vertical structures visible in the spatio-temporal representation (inset in panel 2.15d) supports this interpretation.

2.7   Comparison with Numerical Modelling

All previous results have been obtained in experiments using quantum well single mode laser diodes. Even though our approach is model-independent, it is of major interest to test if numerical models can reproduce its results. Only those numerical models able to reproduce the observed similarity properties in the chaotic dynamics are suitable to study the dynamics of our delayed feedback lasers. A semiconductor laser subject to
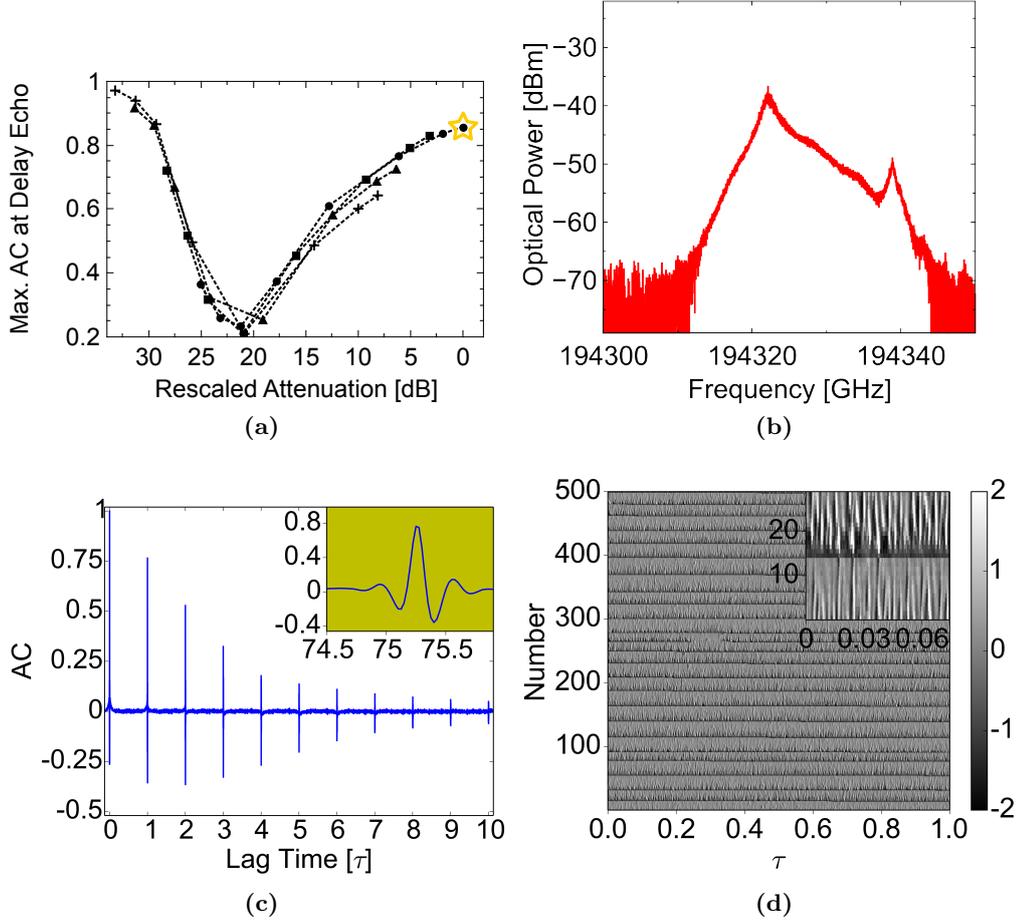
Figure 2.15: High FB strength dynamics at bias current and rescaled attenuation of I=13 mA and 0 dB, respectively. Panel (a) depicts the AC heights at the first delay echo, with a star indicating the AC height value for this specific experimental conditions. The other panels show the (b) optical spectrum, (c) AC (with inset at the first delay echo), and (d) space-time representation of the intensity time series (with inset for magnification).

moderate optical feedback can in many cases be described by the Lang-Kobayashi (LK) rate equations as follows [61, 76, 83],

$$\dot{E}(t) = \frac{1 + \mathrm{i}\,\alpha}{2}\,G_{\mathrm{N}}\,n(t)\,E(t) + \kappa E(t - \tau)e^{-\mathrm{i}\omega_0\tau}\,, \tag{2.4}$$

$$\dot{n}(t) = p_{exc}\,J_{\mathrm{th}} - \gamma\,n(t) - \left[\Gamma + G_{\mathrm{N}}\,n(t)\right]|E(t)|^2\,, \tag{2.5}$$

where E and n are the complex electric field amplitude and the carrier number above threshold, respectively. The feedback parameters are the delay time τ and the feedback rate κ. The excess pump current over threshold is $p_{exc} = (\frac{J}{J_{\mathrm{th}}} - 1)$. The laser parameters in Eqs. (2.4) and (2.5) are the linewidth enhancement factor (α), the

differential optical gain ($G_{\mathrm{N}} = 2.142 \cdot 10^4$ s^{-1}), and the laser solitary frequency (ω_0). The pump threshold current in units of the electron charge is $J_{\mathrm{th}} = 1.552 \cdot 10^{17}$ s^{-1}, $\gamma = 0.909 \cdot 10^9$ s^{-1} is the carrier decay rate, and $\Gamma = 0.357 \cdot 10^{12}$ s^{-1} is the cavity decay rate. Parameter values have been chosen according to [76, 83], except for $\alpha = 3$, $\tau = 10$ ns^{-1}. The feedback rate κ has been varied in the range $\{1 \ldots 100\}$ ns^{-1}. In this model, the relaxation oscillations frequency is given by $f_{RO} = \frac{1}{2\pi}\sqrt{G_{\mathrm{N}} p_{exc} J_{th}}$ and the maximum feedback-induced frequency shift (position of the high gain external cavity mode) is $\Delta f_{fb} = \alpha \kappa / 2\pi$ [56, 84].
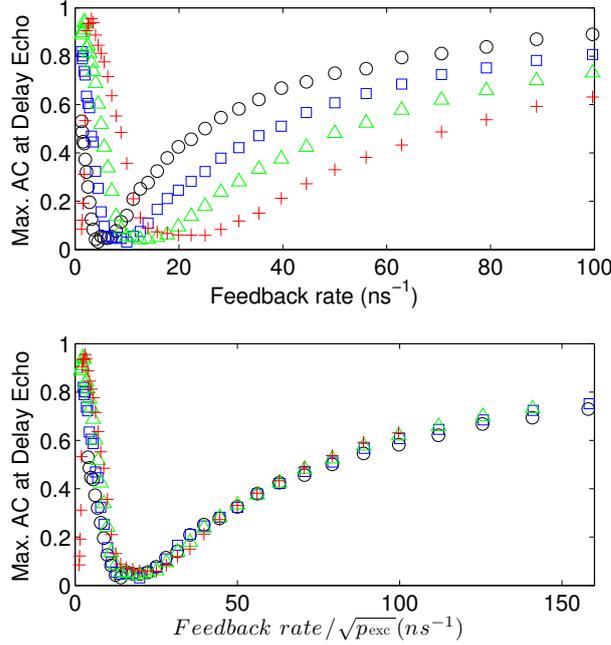
Figure 2.16: Maximum of the first autocorrelation peak as a function of the feedback attenuation for three different operating currents: $1.1 I_{\mathrm{th}}$ (circle), $1.25 I_{\mathrm{th}}$ (square), $1.5 I_{\mathrm{th}}$ (triangle), and $2 I_{\mathrm{th}}$ (cross) respectively. In the lower panel, the feedback rate has been scaled as $\sqrt{p_{exc}}$. Figure courtesy of Miguel C. Soriano.

Fig. 2.16 depicts the numerical results for the height of the first AC peak for different pump currents. The results for the AC heights become pump current independent when the feedback rate κ is rescaled by $\sqrt{p_{exc}}$, as shown in the lower panel. This similarity results are in good agreement with the rescaling found in the experiments in, e.g., Fig. 2.7.

Following the model expressions for the characteristic frequencies scaling with the system parameters, the condition for the AC heights rescaling corresponds to $f_{RO}/\Delta f_{fb} \sim \sqrt{p_{exc}}/\kappa$. Indeed, the generic expression for the full scaling of the dynamics requires the extension including the external cavity frequency. Therefore, keeping the ratio of the relaxation oscillations and the external cavity frequencies constant, i.e. $f_{RO}/f_{EC} \sim$

$\tau\sqrt{p_{exc}} = const.$, in addition to the condition $f_{RO}/\Delta f_{fb} \sim \tau\sqrt{p_{exc}} = const.$, equivalent dynamics are obtained. The following similarity property for the autocorrelation function comprises the previous findings,

$$\text{AC}\big(\Delta t;\ \tau,\ p_{exc},\ \kappa\big) \cong \text{AC}\big(\beta\Delta t;\ \beta\tau,\ \frac{p_{exc}}{\beta^2},\ \frac{\kappa}{\beta}\big),$$

In order to also corroborate the physical mechanism behind the emergence of strong chaos found in experiments, the numerical optical spectra of the laser with feedback have also been computed. The different panels in Figure 2.17 show the optical spectra as a function of the feedback strength in dB (0 dB corresponds to maximum feedback), where each panel corresponds to a different pump current. The different dynamical regions and transitions observed in this figure are very similar to the experimentally observed ones for the DFB laser in Fig. 2.9b. For increasing feedback (always starting from the bottom of each panel), the laser exhibits a transition from stable emission to undamped relaxation oscillations like in the experiments. Further increasing the feedback, the frequency bands corresponding to the relaxation oscillations and its higher harmonics start to nonlinearly mix with Δf_{fb}, until they can no longer be distinguished.

The minimum in the AC height curves (horizontal magenta line in each panel of Fig. 2.17) occurs just after the onset of the strong mixing of the characteristic frequencies. In particular, the minimum AC height at delay echo occurs when Δf_{fb} (dashed curve) approaches the corresponding relaxation oscillations frequency of the solitary laser. Interestingly, all spectra show a characteristic extension on the left and right hand sides for feedback strengths centered at the minimum AC height. This signature of the strong nonlinear mixing of frequencies is common to all currents.

2.8   Similarity Properties in Quantum Dot Lasers

The main goal of this section is to test the validity of the rescaling approach in quantum dot (QD) lasers, i.e. SL with a different gain material. These lasers constitute a relatively new kind of SL that have attracted a lot of attention. The reason is that QD based lasers have many properties that differ from those of their QW counterparts (see section 1.2). Consequently, it is interesting to devote the following paragraphs to introduce the main properties and characteristics of QD based lasers.

2.8.1   Brief Introduction to Quantum Dot Lasers Particularities

QD lasers are made from an ensemble of nano-sized crystals grown inside the semiconductor active region. These crystals, referred as dots to highlight its discrete volume, are the light emitters. QD lasers are considered the natural evolution of state-of-the-art quantum well lasers for many applications. Fields like telecommunications, spectroscopy, or medical diagnosis could benefit from their enhanced properties.

The idea that a 0-dimensional active region in SL could improve their temperature stability is already three decades old [85]. Later predictions pointed in the direction of
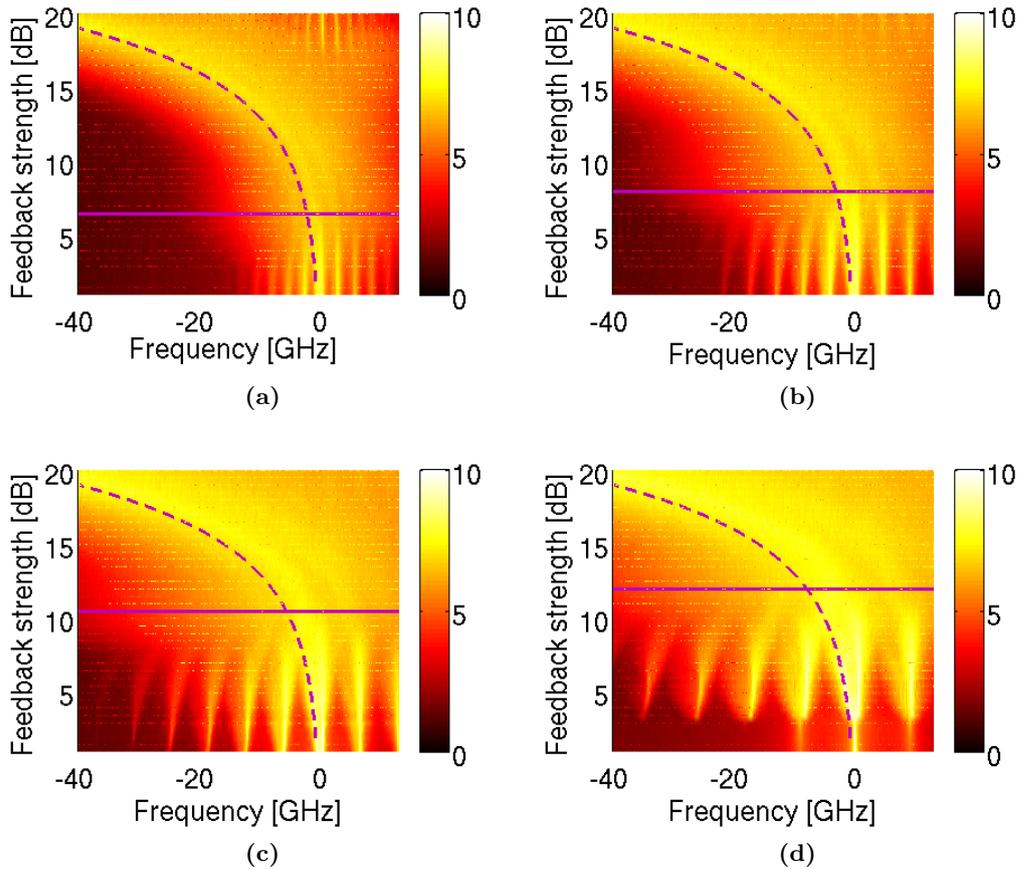
Figure 2.17: Color-coded power spectral density of the numerically calculated optical spectra versus feedback strength in dB (i.e. attenuation) for four different excess pump currents: (a) $p_{exc} = 0.1$, (b) $p_{exc} = 0.25$, (c) $p_{exc} = 0.5$, and (d) $p_{exc} = 1$. The horizontal solid lines indicate the feedback for which the AC height is minimum at each current, and the dashed curves depict the position of Δf_{fb}. Figure courtesy of Miguel C. Soriano.

power saving due to the lasing threshold reduction [86]. It was a long way from these predictions until the first demonstration of real quantum dots lasing was reported in 1994 [87,88]. Superior lasing characteristics than its quantum well counterparts were finally achieved in 1997 by Bimberg et al. [89] by increasing the density of the quantum dot structures. Nowadays QD lasers emitting at 1.3μm are typically constituted by several layers of self-assembled InAs dots (following the Stranski-Krastanov growth process) grown on top of a GaAs substrate [90]. The diversity of sizes and positions in the self-assembled ensemble of QD cause an important inhomogeneous broadening in the emission of these lasers. Other important properties that have also been reported for these lasers are high modulation bandwidths capabilities with low relative intensity noise [91–93], and simultaneous lasing at the QD discrete ground (GS) and excited (ES) states [94].

Another intriguing property that QD laser devices typically show is a low sensitivity to optical feedback [95–97]. Different reasons have been related with the cause of this robustness against optical feedback, like their characteristic low values of the α parameter or the high values of their relaxation oscillations damping [98, 99]. In spite of that, complex dynamics induced by optical feedback have been reported in QD lasers. Particularly interesting examples are the antiphase dynamics between GS and ES [100, 101], and the feedback impact on the balance between the emission states [101, 102].

2.8.2 Invariant Dynamics Signature in Quantum-Dot Lasers

The main idea of this section is to test the validity of the presented rescaling approach in QD lasers. In consequence, we have reproduced the scaling experiments with the QD laser already introduced in the methods section. Figure 2.18 depicts the maximum height of the AC at the first delay echo versus the rescaled attenuation for different bias currents at a temperature of 18 ℃. The selected bias currents are $1.25I_{\text{th}}$, $1.4I_{\text{th}}$, and $1.75I_{\text{th}}$.
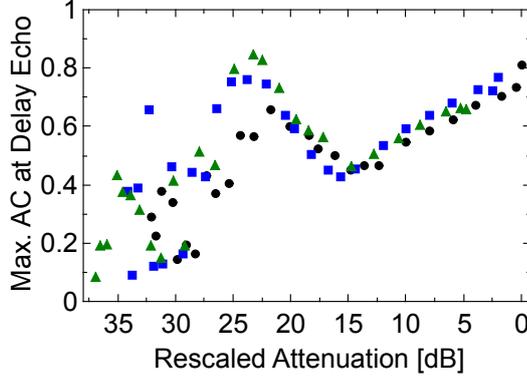
Figure 2.18: Maximum of the first autocorrelation peak as a function of the rescaled attenuation for three different operating currents: $1.25I_{\text{th}}$ (circle), $1.4I_{\text{th}}$ (square), and $1.75I_{\text{th}}$ (triangle) respectively.

Analogously to the results in section 2.4, our dynamics measurement (the AC height at the first delay echo) shows similarity properties when it is plotted such that the ratio $f_{RO}/\Delta f_{fb}$ is kept constant. The points corresponding to the three different bias currents follow one invariant curve from the highest feedback strengths until approximately 23dB. We find the presence of similar regimes than in the scenario with the QW lasers (DM and DFB lasers): a regime of weak chaos indicated by high correlations in the low feedback strengths region, followed by a potential regime of strong chaos denoted by low correlations when the feedback strength is further increased, and a rise in the correlation values when the dynamics enter in the weak chaos regime again at high feedback strengths. Certainly, here the low correlations for the strong chaos regime are not as low as in the QW lasers scenario. Possible explanations could be related with a small value of the α parameter [103] or with the multi mode nature of the dynamics for this particular device. Further studies with single mode QD lasers are required in order to

gain further insights in this particular question.

There is another important difference to highlight between the AC height curves of the QD laser and those previously shown for the QW lasers (sections 2.4 and 2.4.1). In Fig. 2.18, the similarity properties seem to be valid up to a certain value of the rescaled attenuation (approx. 23dB). Below this point (in the lower feedback strengths direction), the AC heights are scattered and do not drop as happens in the QW lasers scenario. In order to gain further insights in what is affecting the dynamics at different attenuations, the optical spectrum information is helpful.
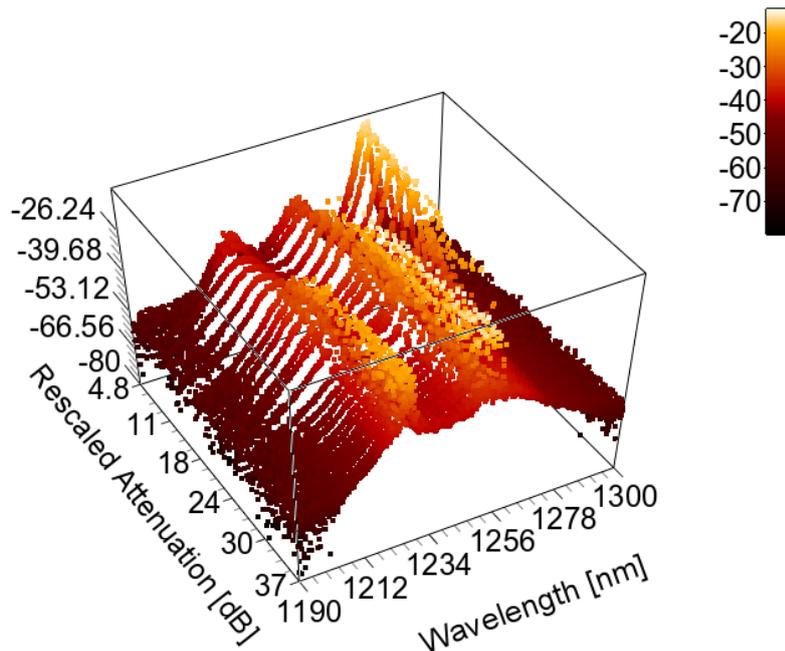
Figure 2.19: Optical spectra for a bias current of $1.75I_{\text{th}}$ versus the rescaled feedback attenuation. The measured optical power is color-coded in dBm.

Figure 2.19 shows the evolution of the optical spectrum versus the rescaled attenuation. The 27 plotted optical spectra correspond to the same experimental conditions of Fig. 2.18 for the bias current of $1.75I_{\text{th}}$. The optical spectrum evolves from emission in GS2 and GS3 to emission in GS1 by increasing the FB strength. The comparison with Fig. 2.18 indicates that the rescaling is fulfilled when the emission is centered in GS1. When the two higher energy ground states dominate the emission, the dynamics no longer shows similarity properties. Further detailed studies are needed to understand the additional factors that come into play when the QD laser is emitting in more than one state.

Furthermore, another consequence of the broad multi state lasing induced bandwidth is the high variability in the AC heights at low feedback strengths. Many different dynamical behaviors can be present in the simultaneous multi mode and multi state

combined emissions of GS2 and GS3. This variety of possible dynamics, that range from stable emission to pulsed operation, result in the different characteristic AC heights observed in Fig. 2.18.

2.9   Discussion and Summary

We have shown in experiments and simulations that the dynamics of a laser with delayed feedback shows similarity properties. For a certain change of pump currents, if delay time and feedback strength are adjusted in accordance, the ratio between the total number of external cavity modes and the maximum feedback-induced frequency shift also remains constant. For different feedback strengths, pump parameters and delay times, equivalent dynamics are observed, when keeping the ratios $f_{RO}/\Delta f_{fb}$ and f_{RO}/f_{EC} constant.

Three different lasers have been used in the experiments described in this chapter, all of them showing similarity properties. In the QD laser, the rescaling is fulfilled for a significant part of the rescaled attenuation range, only failing at low feedback strengths when the laser emits in different higher energy ground states.

The maximum AC height at the first delay echo (our dynamics signature) has been used as a consistency indicator of the laser response to its own delayed signal. In essence, the similarity properties consist in the collapse of all measured data on a single curve when the feedback strength parameter is rescaled appropriately. This behavior demonstrates invariance with respect to parameter changes that keep the time scales ratio constant. This similarity property of the AC height proves that the transitions between different dynamical regimes are not directly linked to an absolute feedback strength or pump current, as traditionally considered [36, 104], but rather to the interplay between these two parameters via their associated characteristic time scales. An intriguing consequence of these results is that in order to characterize the dynamical properties of semiconductor lasers subject to delayed optical feedback, one can reduce the amount of measurements in parameter space significantly. The whole process would consist in characterizing the dependence once, either on feedback strength or pump current, while keeping the other parameter constant. Any feedback condition could be deduced from other values of the parameters simply keeping the ratios between characteristic time scales constant. It is worth noting that the similar AC height for different currents can be achieved for the same delay time as long as the system can still be considered to be in the very long cavity limit.

It has also been shown that the drop in AC height at intermediate feedback strengths is caused by the strong nonlinear mixing of f_{RO} and Δf_{fb}. In fact, this intermediate strong chaos region separates two weak chaos regions at low and high feedback strengths. In addition of demonstrating the presence of weak and strong chaos regimes in delayed FB lasers, our approach goes beyond the strong limitations of the analytic derivation of the strong and weak chaos theory. Those limitations include: long external cavity, neglected carrier dynamics, and low feedback strengths. The experimental results are valid far beyond the mentioned limitations.

If the delay time is included in the rescaling process, the full autocorrelation func-

tion can be rescaled accordingly. Therefore, a particular dynamics observed for a certain delay time, can be simply slowed down or accelerated by changing delay time, feedback attenuation and pump parameter appropriately. The dynamical properties can therefore be adjusted and tailored for the particular needs of applications. This constitutes a powerful tool to extend the applicability ranges of laser dynamics. Of course, the limitations to our dynamics rescaling approach come from those laser parameters that cannot be compensated for, like for example the α parameter. However, it is worth mentioning that even for a given laser, α is not a fixed constant, but it can be tuned [105] within certain limits.

Particular regions of the invariant AC heights curve have also been analyzed to illustrate some specific dynamics in detail. A paradigmatic dynamical regime is the LFF dynamics, typically associated with low currents and strong feedback scenarios. Under the similarity perspective, this dynamics constitutes a nice example of the weak chaos regime at high feedback strengths.

The rescaling approach has been confirmed for the Lang-Kobayashi model, validating the suitability of this model to reproduce the dynamics found in the experiments with real lasers. The same approach can be used to efficiently perform model verification in models to describe QD lasers, where proper rate equation models are still under debate.

Altogether, the rescaling methodology and the similarity properties found in the delayed feedback induced dynamics constitute a device- and model-independent powerful approach to characterize and tailor laser dynamics over large ranges of bias currents and feedback strengths.

Chapter 3

Properties of the Autocorrelation Function of a Laser with Feedback

3.1   Introduction

Among the variety of phenomena that delayed coupling can induce in semiconductor lasers, some of the most intriguing examples are high-dimensional chaos and chaos synchronization [19,83]. The fundamental nonlinear nature of the coupling process is at the origin of these complex behaviors. A detailed study of such phenomena requires knowledge on complexity indicators, e.g., the Lyapunov spectrum, correlation dimensions, or entropy. However, these are often hard to obtain from experimental data because of inherent noise sources and, in the particular case of delay-coupled systems, the high dimensionality of the system. On the contrary, one of the most accessible measurements in experiments, the autocorrelation function (AC), has a nontrivial relation with the nonlinear properties of the system (exception made of some particular cases [106,107]).

In this thesis, the autocorrelation function (AC) of the intensity time series has already been used to study the weak and strong chaos regimes in the dynamics of delayed feedback SL. The AC of an intensity time series clearly shows the fingerprint of the delay time in these lasers, as shown in section 2.3. Structures composed by damped oscillations are present at successive multiples of the delay time. The maximum height of the AC around the first multiple of the delay time (first delay echo) has been used as the signature of the dynamics complexity, namely the dynamics signature. Different bias currents, feedback strengths or delay times result in distinct decays of the overall AC and, therefore, in different heights at the first delay echo. Interestingly, a fundamental similarity appears when the dynamics signature is plotted such that the ratios between the characteristic time scales are kept constant. All previously disperse values of the dynamics signature collapse on the same invariant curve, where distinguishable strong chaos (low correlations) and weak chaos (high correlations) regimes are depicted. This approach is confirmed for a large variety of feedback strengths, pump parameters and delay times.

In this chapter, we introduce a model of a stochastic linear oscillator with delay and

compare its analytically obtained AC to the experimentally observed AC. We investigate which characteristic features of the experimentally observed AC can be explained by this simple linear model. We find that in a wide range of dynamical regimes the experimentally observed AC can be well approximated by this model.

3.1.1   Chapter Outline

In the present chapter, the full shape of the AC will be used to characterize specific properties of the dynamics. For this purpose, the experimental AC is compared with the AC obtained from a model of a linear stochastic oscillator with delay.

In order to compare both AC, the experimental delay time must be precisely known. In section 3.2, the method used to obtain the round-trip time of the light in the external cavity is introduced. The advantage of this method is that its results do not depend on the dynamics of the system.

Section 3.3 is devoted to the introduction of the linear model (LM) and its analytic expression of the AC. The LM AC is explicitly compared with the experimental AC in section 3.4. Accordingly, the experimental AC is fitted with the analytical expressions of the model AC for different operating conditions. The limits of validity of the comparison between model AC and experimental AC are discussed by means of the fit error in section 3.5.

Finally, in section 3.6 the relation between the model parameters and the experimental system parameters is analyzed and discussed.

3.1.2   Contributions to the Work in the Present Chapter

The major part of the results presented in this chapter has been published as: X. Porte, O. D'Huys, T. Jüngling, D. Brunner, M. C. Soriano, and I. Fischer, "Autocorrelation properties of chaotic delay dynamical systems: A study on semiconductor lasers", *Physical Review E*, **90**, 052911 (2014).

The theoretical analysis of the linear stochastic model was developed by Otti D'Huys. The planning and execution of the experiments have been done by me under the supervision of Daniel Brunner, Miguel C. Soriano and I. Fischer. All authors contributed to the discussion of the results.

3.2   Experimental Methods

Figure 3.1 depicts the schematic view of the setup used for the experiments described in this chapter. Most of the components employed in this setup, as well as the acquisition conditions correspond to those introduced in detail in section 2.2. The SL used in this chapter is the DM laser already used in section 2.2.1.

In this version of the setup, the previous coupler has been substituted by a two by two coupler. The second input allows for the determination of the external cavity delay time by measuring the round-trip time of injected light pulses. This constitutes an essential measurement for the proper comparison between model and experiments.
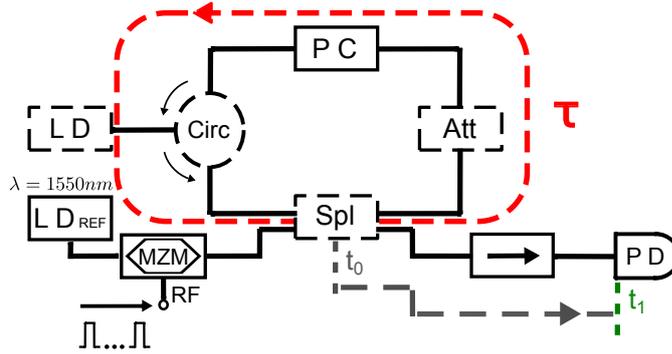
Figure 3.1: Schematic view of the experimental setup. LD: laser diode, LR: reference laser diode, Circ: optical circulator, PC: polarization controller; Att: optical attenuator, Spl: two by two intensity splitter, →: optical isolator, and PD: photodiode.

3.2.1 Experimental Technique to Determine the Delay Time

The external cavity round trip time is measured via the injection of a train of short light pulses. The measured delay time corresponds to the time separation between successive reflections in the external cavity of each light pulse.

A CW reference laser (LR) and a 20 GHz bandwidth Mach-Zender (MZ) intensity modulator are combined to generate the light pulses. The LR emits a constant output with narrow linewidth around 1550 nm and has been fine tuned from the DM laser wavelength such that the minimum amount of light from the reference laser is coupled into the DM laser cavity. The MZ modulator is DC biased to low transmission. Then light pulses are generated by increasing the transmission of the MZ modulator via a voltage pulse. The square wave voltage pulse is generated with a 12 GSamples/s arbitrary waveform generator. Each pulse has a duration of 10 ns, and the temporal separation between the generated pulses is 500 ns. Therefore, each pulse travels multiple times through the external cavity before the next pulse is injected. The acquired waveform has been averaged, triggering to the rising edge of each pulse.

The injected pulse and the first reflection are shown in Figure 3.2. The first pulse arrives to the photodetector with a lag $t_0 + t_1$. The next pulse (that has traveled once through the external cavity) arrives to the photodetector with a time lag of $t_0 + t_1 + \tau$. Thus, the difference between the arrival of the two pulses gives us the delay time τ. The measured external cavity roundtrip time is $\tau = 75.25 \pm 0.025$ ns.

3.3 Autocorrelation Function of a Linear Stochastic Delay Model

In this section, a linear model to describe the AC of a delayed feedback laser is presented. This model does not intend to properly reflect the equations of motion of a SL subject to delayed optical feedback. But characteristic emergent properties of the underlying complex dynamics are taken into consideration in the model.
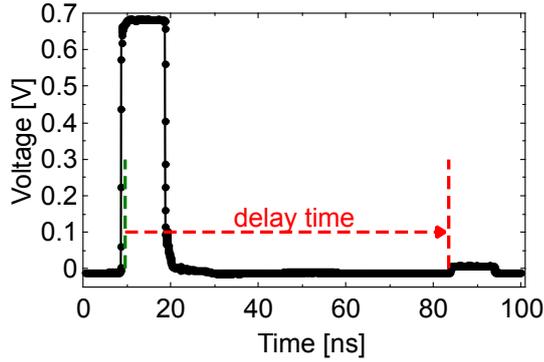
Figure 3.2: Oscilloscope time trace of the delay time measurement. The depicted square pulses correspond to the injected pulse and to the first reflection. The distance between the pulses rising edges corresponds to the delay time of 75.25 ± 0.025 ns.

The model considers the following simple linear stochastic oscillator with delayed feedback

$$\dot{x}(t) = (-\alpha + i\omega)x(t) + \beta e^{-i\phi}x(t-\tau) + \xi(t) , \qquad (3.1)$$

with $x \in \mathbb{C}$. The parameters ω and α (with $\alpha > 0$) represent the characteristic frequency and damping of the oscillator, respectively.

Without delay, the model corresponds to an harmonic oscillator, with solutions that decay exponentially as $\cos(\omega t)e^{-\alpha t}$. The main idea behind this model is to extend the linear response theory to the fully developed chaotic regime. When time scale separation is possible, it is a common procedure to consider the fast complex drive signals as noise [108]. The delay term is linearly added to the harmonic oscillator. The feedback strength is denoted by β and the feedback phase by $-\phi$. In the context of the current theoretical analysis, we require that the conditions for weak feedback ($\beta < \alpha$) and long delay ($\tau \gg \max(\alpha^{-1}, \beta^{-1}, \omega^{-1})$) are fulfilled. The complex drive signal of the delayed feedback laser is composed by fast chaotic trajectories. This high bandwidth dynamics is in the model approximated by a white noise $\xi(t)$ term (with $\langle \xi(t)\xi(t')\rangle = 2D\delta(t-t')$). In comparison with the experimental system, the variable $x(t)$ is associated with the time-dependent intensity of the laser. The parameters ω and α can be respectively associated to the relaxation oscillations frequency and damping.

The four panels of Fig. 3.3 illustrate the suitability of a white noise term to approximate the high bandwidth chaotic dynamics from an experimental viewpoint. Each panel depicts two experimental intensity power spectra for a given bias current, one corresponding to the solitary laser and the other to the delayed feedback laser emission. The increase in bandwidth caused by delayed optical feedback is obvious for all depicted bias currents, resulting in an almost flat power spectral shape. Even for the two lower currents, where the spectra are not entirely flat, the -10 dB bandwidth has increased beyond 10 GHz, which is more than twice the solitary emission bandwidth.
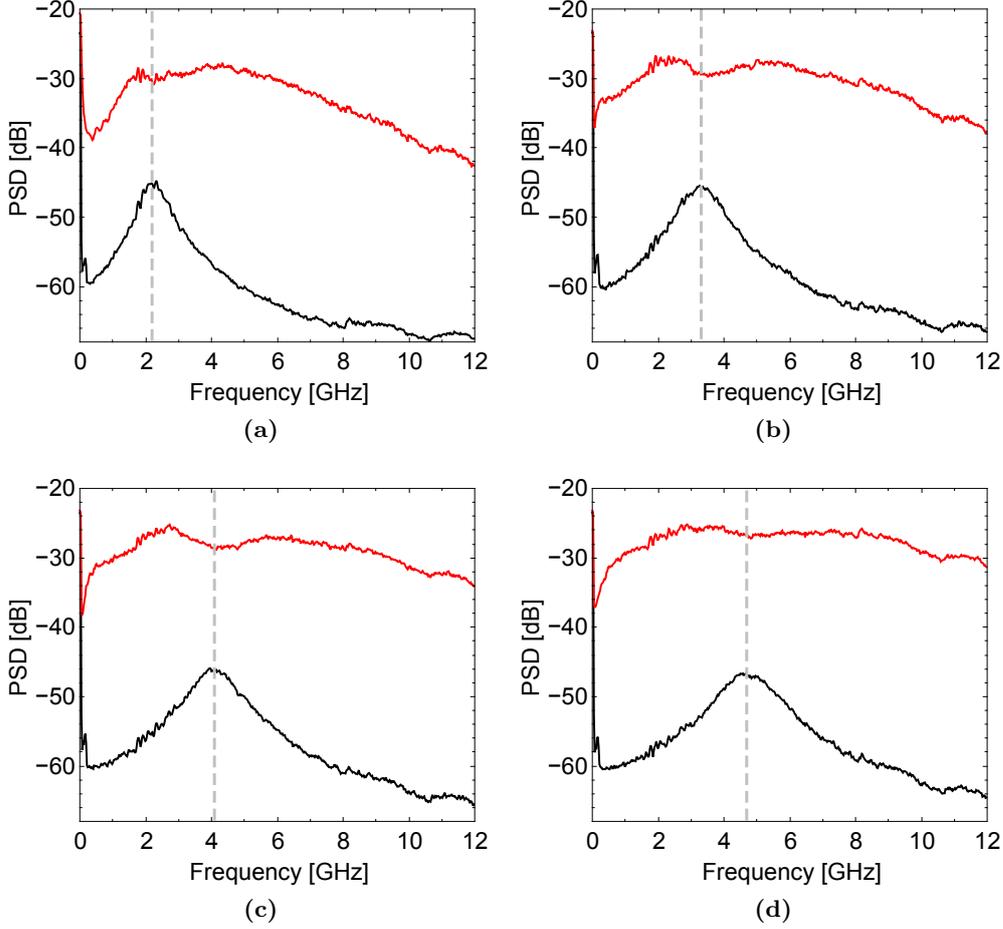
Figure 3.3: Intensity power spectra of the DM laser with (red) and without delayed optical feedback (black). The bias current corresponding to each of the four panels are (a) 14mA, (b) 16mA, (c) 18mA, and (d) 20mA. The threshold current is $I = 12.08mA$. The dashed vertical lines indicate the relaxation oscillations frequency at each current.

For the model in Eq. 3.1, it is possible to analytically calculate the AC if the time scales of the delay time and of the oscillator parameters are separable. The experimental conditions have been chosen such that adapt to this model requirement and the comparison of both will reflect the properties behind the clearly separated autocorrelation signatures (e.g. in Fig. 2.5).

The expression of the autocorrelation function of the variable $x(t)$ is

$$r(k) = \frac{\langle x(t+k)x^*(t) \rangle}{\langle |x|^2(t) \rangle} .$$

The shapes of the AC delay echoes can be explicitly calculated for consecutive windows of length τ. A detailed derivation of the model's analytic AC equations can be

found in [109]. The AC shape for the first interval $[0, \tau[$ is

$$r_0(k) = e^{(-\Lambda + i\omega)k} + \gamma e^{(\Lambda + i\omega)(k - \tau)} \,. \tag{3.2}$$

The two terms in Eq. 3.2 represent clearly separated peaks due to the large value of the delay time τ. Close to the origin ($k \approx 0$) the second term is approximately zero, the same is true for the first term for $k \to \tau$. The AC central and first delay peaks are modulated with the characteristic frequency ω. The envelope of the AC $|r_0(k)|$ decays (and increases) exponentially with Λ for $k \approx 0$ and $k \to \tau$, respectively. This decay/growth rate is given by

$$\Lambda = \sqrt{\alpha^2 - \beta^2} \,. \tag{3.3}$$

The decay therefore depends on the real part α of the characteristic dynamics and on the magnitude β of the feedback. The amplitude of the first delay peak is proportional to the factor γ, given by

$$\gamma = \frac{\beta e^{-i\phi}}{\Lambda + \alpha} \,. \tag{3.4}$$

The first delay echo at $k = \tau$ has a phase shift equal to the feedback phase $-\phi$.

In the interval $[\tau, 2\tau[$ the autocorrelation follows the solution

$$r_1(k) = \gamma^{*-1} e^{(-\Lambda + i\omega)(k - \tau)} + \gamma^2 e^{(\Lambda + i\omega)(k - 2\tau)} + \left(\gamma - \gamma^{*-1} \right) e^{(-\alpha + i\omega)(k - \tau)} \,. \tag{3.5}$$

Thus, the first delay echo is asymmetric, with the right side broadened with respect to the left side. Moreover, the highest peak position is not at $k = \tau$, but is slightly shifted to longer lag times. The magnitude of this shift depends on the model parameters, as will be explained in section 3.6.1.

The AC can be calculated in the consecutive delay intervals, $[n\tau, (n + 1)\tau[$, giving the following general expression

$$r_n(k) = \gamma^{*-n} e^{(-\Lambda + i\omega)(k - n\tau)} + \gamma^{n+1} e^{(\Lambda + i\omega)(k - (n+1)\tau)} +$$
$$\left(\gamma^n \sum_{m=0}^{n} \frac{\left(\gamma^{-1} \beta e^{-i\phi} (k - n\tau) \right)^m}{m!} - \gamma^{*-n} \sum_{m=0}^{n} \frac{\left(\gamma^* \beta e^{-i\phi} (k - n\tau) \right)^m}{m!} \right) e^{(-\alpha + i\omega)(k - n\tau)} \,. \tag{3.6}$$

The modulation of the nth peak still corresponds to the characteristic frequency ω. Each delay peak is more asymmetrically broadened than the previous one, and the maxima are shifted further away from $k = n\tau$. Interestingly, multiple characteristic features observed in the experimental AC of chaotic feedback lasers are also depicted by this simple linear model, e.g., the frequency, damping, shift and broadening of the delay echoes. Nevertheless, some nonlinear properties are reflected in the model via the noisy drive .

3.4 Comparison of the Autocorrelation Functions of the Laser and the Linear Model

The suitability of the LM to describe the measured intensity AC is tested by means of fitting the analytic expressions of the AC to the experimental data.

Equation 3.2 represents the analytic solution of the AC in the interval $[0, \tau[$. This expression from the model is fitted to the experimental data using a least-squares method. It is important to note that all model parameters are present in the expression of $r_0(k)$. Consequently, all the information needed to compare the model AC with the experimental AC can be extracted simply from the fit in the interval $[0, \tau[$. From the right side of the central peak, in the interval $[0, \frac{\tau}{10}]$, the parameters Λ and ω are extracted. From the left side of the first delay echo peak, in the interval $[\tau - \frac{\tau}{10}, \tau]$, the parameters β and ϕ are extracted. The window size of $\frac{\tau}{10}$ has been chosen because it covers the AC oscillations (either at the right side of the central peak or at the left side of the first delay echo) for most of the experimental conditions.

Figure 3.4 shows the comparison between experimental AC and the LM analytic expressions for three different FB strengths. The bias current was chosen to be 16 mA for constant in all panels. The plotted data corresponds only to one bias current. This is to illustrate the characteristic behavior found for other currents in this laser. Furthermore, as it has already been demonstrated in chapter 2, the scenarios explained for this current can be translated to other bias currents by properly rescaling the experimental parameters. The top panels (3.4a, 3.4b, and 3.4c) correspond to 27.5 dB of rescaled attenuation[1]. Panels 3.4d, 3.4e, and 3.4f (set of panels with green curves) correspond to 19.1 dB of rescaled attenuation. Finally, panels 3.4g, 3.4h, and 3.4i (with orange curves) correspond to a rescaled attenuation of 6.3 dB. The solid lines and the dashed lines in every panel depict the experimental AC and the fitted analytic curves, respectively. The set of panels on the left side depict the central AC peak, while the central panels and those on the right side respectively depict the AC at first and second delay echoes, respectively.

The model AC accurately reproduces the experimental AC for low feedback strength conditions (panels 3.4a, 3.4b, and 3.4c). The fact that only the first interval $[0, \tau[$ has been used for the fit further supports the validity of the model to reproduce the full first, second and successive AC delay echoes. The quality of the fit suggests that this approach captures dominant features of the time series corresponding to linear response properties. Therefore, this approach allows for an appropriate description of the complex dynamics as well as qualitative and even quantitative insight into physical properties of the system, as it will be further explained in section 3.6.

However, not all experimental conditions are fitted by the model with equal accuracy. For the intermediate FB conditions (with the model AC highlighted in green) the feedback regimes corresponds to strong chaos (for a more detailed explanation see section 2.1.1). More specifically, this experimental condition corresponds to the minimum of the AC invariant curve in Figure 2.7. The central peak is very well fitted. However,

---

[1]For the complete definition of rescaled attenuation, see chapter 2
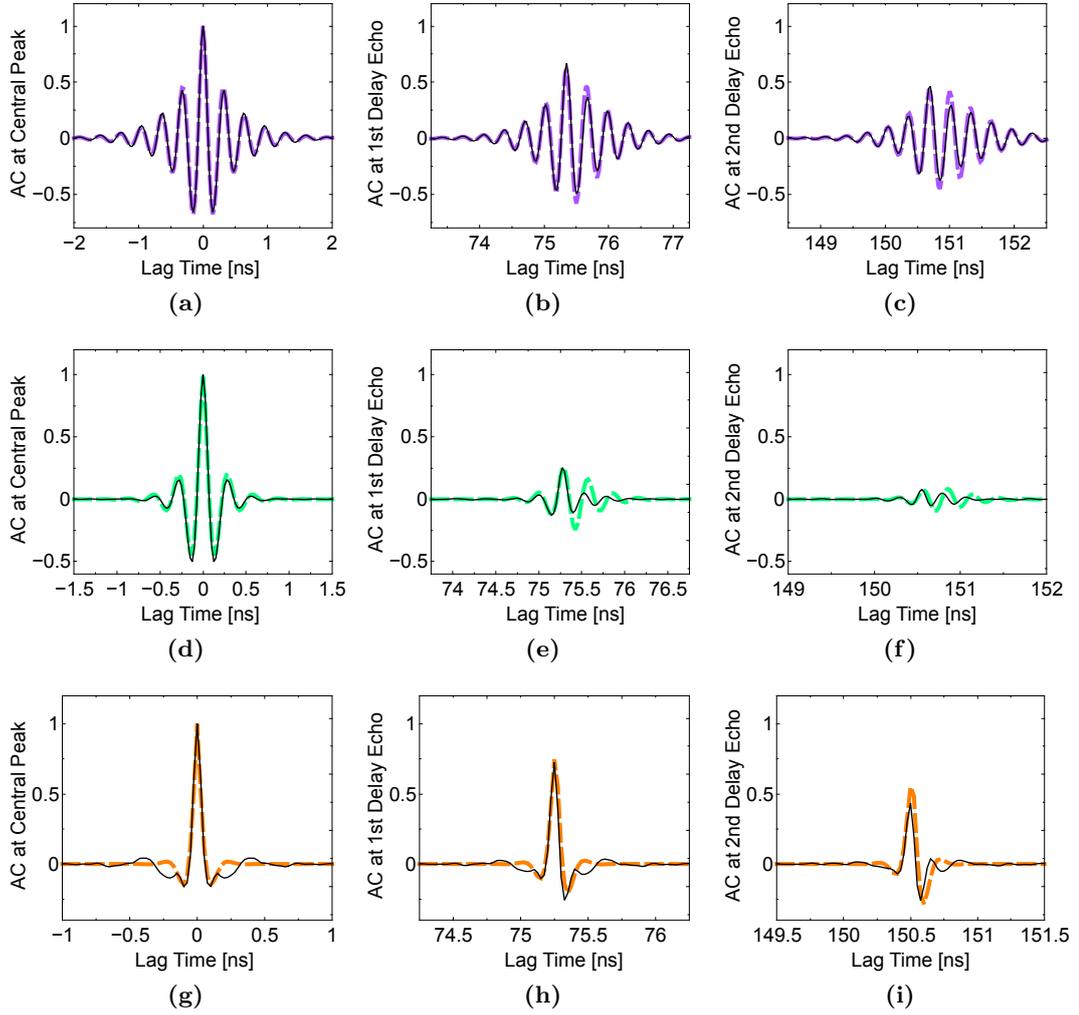
Figure 3.4: Experimental AC (solid lines) and their corresponding fitted curves (dashed lines). Panels (a), (b) and (c) respectively depict the central peak, the first and the second delay echoes for a current of 16 mA and a rescaled attenuation of 27.5 dB. Panels (d), (e) and (f) depict the central peak, first and second delay echoes for a current of 16 mA and a rescaled attenuation of 19.1 dB. Finally, panels (g), (h) and (i) depict the identical information for the same bias current and a rescaled attenuation of 6.3 dB.

the experimental AC modulation on the right side of the first and second delay echoes present a clear excess of damping when compared to the model prediction.

For the highest FB strength conditions (panels 3.4g, 3.4h, and 3.4i), both the global AC decay and the phase of the modulation at successive delay echoes seem to be well fitted. The global AC decay among successive delay echoes is small, as expected for experimental conditions in a regime of weak chaos. Nevertheless, the peak modulation frequency seems to be erroneously fitted. The model only contains one frequency, mean-

while the experimental AC seems to be composed of at least two different interfering frequencies (as deduced from the inspection of the AC peaks). Additional analysis must be performed in order to gain further insights on the origin of the described fit errors.

3.5 Limits of Validity of the Linear Approximation

The experimental AC shape varies with the operating conditions and with the feedback parameters. The potential applicability of the presented model to different experimental conditions requires the quantitative evaluation of its suitability to reproduce the AC of real lasers. In this section, the error resulting from the fit process is numerically evaluated and discussed.

We quantify the quality of the AC fit using the least-squares error:

$$\Delta = \frac{1}{\max(y_i)} \sqrt{\frac{\sum_{i=1}^{n}[y_i - f_i(\bar{a})]^2}{n}} \, ,$$

where f and y respectively represent the data of the model and the experimental autocorrelations. The set of parameters obtained from the fit is denoted by $\bar{a}$. Errors have been calculated independently for the different delay echoes, in windows centered around each peak structure. The widths n of the integration windows were chosen as ten times the inverse of the decay rate Λ of the central envelope. This integration window includes all the significant oscillations around each AC peak structure, but makes sure that the windows corresponding to different delay echoes never overlap. Finally, given the diversity in AC maxima, the errors have been normalized by the maximum height of the AC at their correspondent peak structure.

Figure 3.5 depicts the normalized fit error Δ for the central peak and the successive two first delay echoes of the 16 mA exemplary bias current. In the three panels of Fig. 3.5 the accuracy of the fit degrades with increasing feedback strength. Another visible effect, that could be partly related to our fit procedure, is that the fit error is systematically larger at the first delay echo than at the central peak (and at the second delay echo than at the first one). Furthermore, the fit errors depicted in panels 3.5b and 3.5c show clear maxima at intermediate values of the rescaled attenuations (with the maximum at 19.1 dB). These maxima appear in the region of strong chaos, at the conditions of maximum nonlinear mixing between characteristic frequencies as described in section 2.4.1. Inspecting again panels 3.4d, 3.4e, and 3.4f, one can observe that the experimental AC is well fitted for the central peak structure and the left side of the first and second delay echoes. However, the fit does not reproduce correctly the right sides of these two delay echoes. This disagreement is common for intermediate feedback strengths for all the analyzed bias currents. Moreover, the significant peaks in the fit errors for intermediate feedback strengths suggests that the behavior of the laser deviates the most from linearity around this region, that coincides with the transition region from weak to strong chaos.
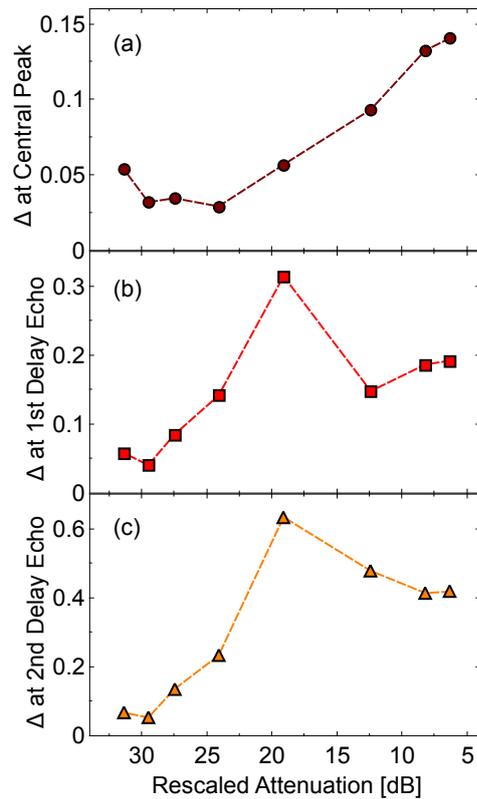
Figure 3.5: Normalized fit error Δ of the experimental AC versus the rescaled attenuation. Panel (a) depicts the fit error for the central peak. Panels (b) and (c) depict Δ in the first and second delay echoes of the AC, respectively.
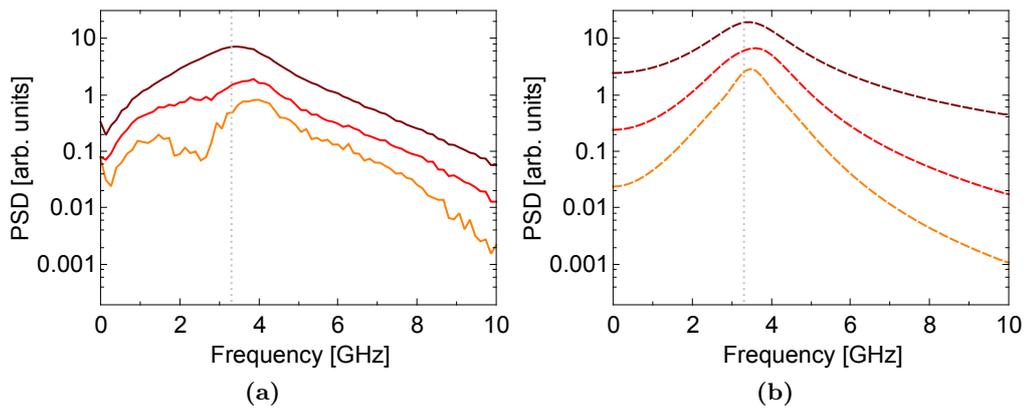
Figure 3.6: Power spectral densities contained in each AC peak of the (a) experimental AC and (b) model AC resulting from the fit. The brown curves depict the PSD of the central peak. The red and orange curves correspond to the first and second delay echoes PSD, respectively. The corresponding rescaled attenuation is 19.1 dB. The vertical dashed line in each panel indicates the relaxation oscillations frequency of the solitary laser for this bias current (16 mA).

The origin of the large error for the intermediate range of feedback strengths is illustrated in Fig. 3.6, where the power spectral densities (PSD) contained in each AC peak are depicted. These PSD are calculated from the Fast-Fourier transform (FFT) amplitudes of the different experimental AC peaks in panel 3.6a and model AC peaks in panel 3.6b. The discrepancy between linear model and experimental AC originates from the fact that multiple dominant frequencies are actually present in a delayed feedback laser system. This becomes evident in the bimodality exhibited at the PSD of the first and second delay echoes, a signature of the coexistence of two distinct frequencies that compete in the feedback dynamics. In contrast, the PSD calculated from the model never exhibit a second frequency because only one frequency, ω, appears in the analytic solutions of the LM.

(a) (b)
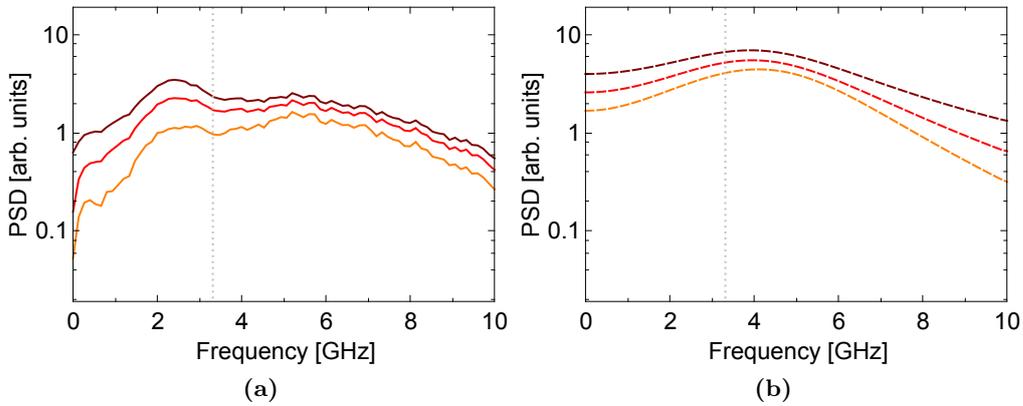
Figure 3.7: Power spectral densities contained in each AC peak of the (a) experimental AC and (b) fitted AC from the model. The brown curves depicts the PSD of the central peak. The red and orange curves correspond to the first and second delay echoes PSD, respectively. The corresponding rescaled attenuation is 6.3 dB. The vertical dashed lines indicate the relaxation oscillations frequency of the solitary laser for this bias current (16 mA).

An additional illustration of this multiple frequency caused misfit can be observed from the detailed inspection of the fit for the highest feedback conditions. Figure 3.7 depicts the PSD for the FB strength of 6.3 dB. As expected for a higher feedback strength scenario, the PSD are flatter and with a higher frequency bandwidth. Here, the bimodal spectra are present in all three peaks of the experimental AC. On the contrary (and coinciding with panel 3.6b), the model PSD has only a single frequency peak, shifted approximately 1 GHz away from the relaxation oscillations frequency of the solitary laser. The fitted frequency approximately corresponds to the higher frequency in the experimental AC, as can also be deduced from the direct inspection of panels 3.4g, 3.4h, and 3.4i. Despite the failure to properly fit the oscillations frequency, the model correctly reproduces other characteristics from the experimental AC, like the decay and the phase at the successive delay echoes.

Altogether, the presented analysis on the quality of the fit further supports the application of this procedure to extract the LM parameters from the various bias and

feedback conditions that we can address in our experiment.

3.6   Parameters Extraction from the Fit of the Autocorrelation Function

In this section, the parameter of the analytic expressions of the model are extracted from the fits to the AC of the SL at different experimental conditions. From the right side of the central peak, the parameters of the damping (Λ) and the frequency (ω) are extracted. Once these two parameters are known, from the left side of the first delay echo the modulus of the feedback strength (β) and the phase (ϕ) are extracted.
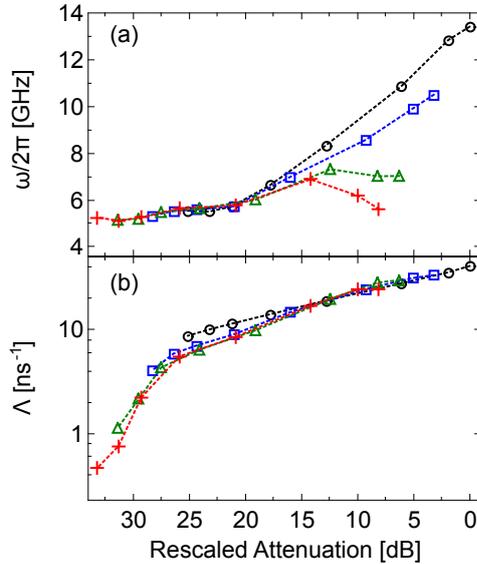
Figure 3.8: Plot of the rescaled parameters fitted from the right side of the central peak. Panel (a) depicts internal frequency $[\frac{\omega}{2\pi}]$. Panel (b) depicts the decay (including the effect of the FB term) $[\Lambda]$. The different bias currents are associated with each curve as follows: circles (I = 13mA), squares (I = 14mA), triangles (I = 16mA), and crosses (I = 18mA).

In Figure 3.8 the extracted model parameters of the central peak are plotted versus the rescaled feedback attenuation. The extracted parameter values are also rescaled together with attenuation. The parameters ω and Λ, with units of ns^{-1}, have been rescaled dividing by a factor $\sqrt{\frac{I}{I_{th}} - 1}$. The rescaled parameter curves for different bias currents collapse onto each other, indicating that the linear model correctly fits the self-similar AC curves.

The extracted frequency $\frac{\omega}{2\pi}$ approximately corresponds to the dominant frequency component in the radio-frequency spectral density of the laser, as pointed out in Figs. 3.6 and 3.7. In fact, it approaches the relaxation oscillation frequency for high values of the rescaled attenuations. The increase in feedback strength results in an enlargement of the dynamical bandwidth for most conditions [36, 39]. As a consequence, the decay

of the central peak of the AC is faster, which is reflected in a higher damping Λ.
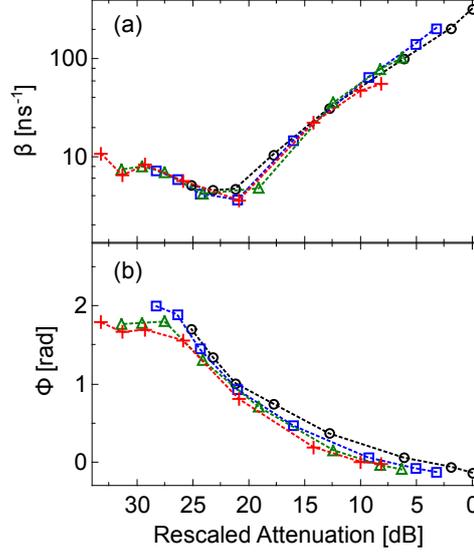
Figure 3.9: Plot of the rescaled parameters fitted from the right side of the central peak. Panel (a) depicts the feedback strength [β]. Panel (b) depicts the feedback phase [ϕ]. The different injection currents are associated with each curve as follows: circles (I = 13mA), squares (I = 14mA), triangles (I = 16mA), and crosses (I = 18mA).

Figure 3.9 depicts the parameters, β and ϕ. The latter parameter is related to the shift in position of the AC maximum at first delay echo. The extracted phase and the corresponding shift in the position of the AC maximum with respect to the delay time decreases for an increasing feedback strength, as will be explained in more detail in section 3.6.1. The linear model's feedback strength β is extracted from the height of this maximum via the second term in Eq. (3.2). However, it does not grow proportional to the AC height, but depends on the ratio β/α as can be deduced from Eq. (3.4). Analogously to Fig. 3.8, these two parameters also exhibit similarity properties when plotted with respect to the rescaled attenuation.

A significant exception to the similarity behavior is found in the plot of the rescaled frequencies ($\frac{\omega}{2\pi}$) in panel 3.8a. The fitted frequencies for different bias currents are found to diverge for intermediate to high feedback strengths. The underlying reason for this effect is the presence of two frequencies in the experimental AC, as has been discussed in section 3.5. Therefore, one can conclude that an extended linear model containing two frequency components with a different damping could overcome this issue for intermediate to strong feedbacks. However, in the context of the present work, the simplest form of the linear model is maintained, because it sufficiently reproduces most of the experimental features and allows for analytic solutions of the AC. Furthermore, the presence of the second dominant frequency does not seem to have a significant influence on the remaining parameters extracted from the fit as can be seen in Figures 3.8b and 3.9.
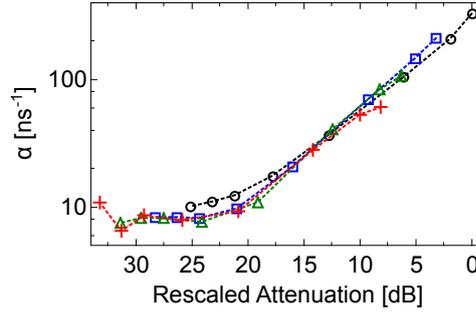
Figure 3.10: Plot of the rescaled internal decay α for different bias currents: circles (I = 13mA), squares (I = 14mA), triangles (I = 16mA), and crosses (I = 18mA).

Finally, the rescaled version of the internal decay parameter is plotted in Fig. 3.10. This model parameter is calculated from two already known other parameters (Λ and β) using Eq. 3.3. The internal decay parameter α can be related to the damping rate of the relaxation oscillations [109, 110]. Similarly to the scenario depicted for Λ, the faster decay of the central peak of the AC for higher feedback strengths is again reflected in higher values of the damping α.

3.6.1   Time Delay Extraction

The delay time is a key parameter to be determined in experimental delay systems [111–119]. If the intensity AC shows peaked structures around multiples of the delay echo, one may ask if the delay time can be precisely obtained from the experimental AC and/or if the linear model is of any help to determine the delay time.
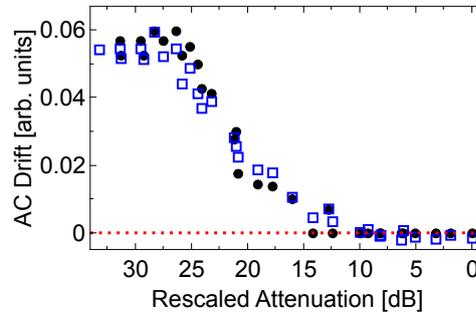
Figure 3.11: Rescaled drift of the maximum AC height at first delay echo respect to the precise delay time (75.25 ns) for the full set of experimental conditions. The dots denote the deviation directly measured from the position of the peak and the squares correspond to the shift predicted from the model extracted parameters, i.e. ϕ/ω. The dashed red line indicates position of the delay time, that has been offset to zero.

Figure 3.11 shows how well the position of the maximum AC height at first delay echo approximates the time delay (see section 3.2 for a description of the method used to extract the delay time with independence of the laser dynamics). The experimentally

determined position (dots in Fig. 3.11) is depicted together with the position calculated from the LM fitted parameters (squares in Fig. 3.11). In a first approximation, the experimentally measured maximum of the first delay echo is only a precise indicator of the delay time for high feedback strengths. In the other cases, its position deviates from the precise delay time. Indeed, this shift is in all cases well approximated by the position of the maximum AC height derived from the LM, that is shifted towards larger delay times an amount equal to ϕ/ω.

From the detailed inspection of the LM expressions, one can deduce that the delay echoes are shifted due to the combination of two different effects: the modulation phase of the delay echoes due to the presence of the coupling phase $-\phi$, and a shift caused by the internal time scale of the system α^{-1}. This latter one corresponds to the shift of the envelope at the delay echoes (it is present even in absence of the internal oscillations). Thus, the analytical expression for the shift of the envelope of the first delay echo can be derived:

$$k_{shift} = \frac{1}{\alpha - \Lambda} \ln \frac{2\alpha}{\Lambda + \alpha} = \frac{1}{2\alpha} \left(1 + \frac{1}{8} \frac{\beta^2}{\alpha^2} + \mathcal{O}(\frac{\beta^4}{\alpha^4}) \right).$$

Interestingly, this shift does not only depend on the internal parameter α, but also on the coupling strength β. However, for sufficiently weak coupling the envelope shift is indeed proportional to the inverse internal damping rate.

From the comparison between both sets of points in Fig. 3.11, one can conclude that the shift of the maxima at first delay echo originates to a large extent from the AC phase shift ϕ. Therefore, the shift of the envelope contributes only little to the shift of the AC peak at the delay echo. As a consequence, the linear model can help in the estimation of the real delay time.

3.7 Summary and Discussion

In this chapter, analytic solutions for the AC of a stochastic LM with delay have been compared to the intensity AC of a SL in the long delay limit. The experimental AC has been approximated by the LM expressions in a wide range of injection currents and feedback strengths, illustrating how the properties of the AC relate to the dynamical regime of the delayed feedback laser.

In a step previous to the comparison of the experimental AC with the LM, the delay time of the fiber-based external cavity has been determined by means of the injection of square pulses of light.

The comparison between experimental data and analytic model expressions has been made via fitting the experimental AC with the analytic solutions in the first delay interval $[0, \tau[$. The fit allows for the extraction of the model parameters that can therefore be related to semiconductor laser parameters, e.g., the relaxation oscillations frequency and damping. Furthermore, it has been shown that the relation of model parameters ϕ/ω precisely reproduces the shift in time of the maximum of the AC at first delay echo.

The model captures the nonlinear properties of the dynamics through the noise term. Consequently, nonlinear mappings or properties like correlation dimension or

Lyapunov spectrum are not properly captured by the model. Nevertheless, the model properly reproduces most of the properties observed in the experimental AC. In fact, the main limitations to fit the experimental AC with the linear model seem to be related to the necessity to include a second frequency in the model. There are two possible physical origins for this second frequency depending on the dynamical regime. For low feedback strengths, it can originate from to the presence of anharmonics of the relaxation frequency in the undamped relaxation oscillations regime. For intermediate and strong feedbacks, it can be due to the competition between the relaxation oscillation frequency and the frequency shift introduced by the feedback, which can be of the same order [109]. The linear model could have easily been extended to multiple characteristic frequencies or colored noise, which would lead to more accurate approximations of the experimental conditions. However, the focus has been kept on the most simple case because analytic expressions for the AC can be obtained for such a model and also because it reproduces most of the observed experimental AC features.

In the context of delay-coupled systems, it has been shown that the AC properties of a single delay-coupled system serve as a predictor to the AC properties of delay-coupled systems [5, 65]. For that reason, if the relationship between AC properties and dynamical regime has a broad validity in nonlinear dynamical systems with delay, the insights obtained by the linear model can also serve as a tool to interpret the dynamical regimes found in delay-coupled systems.

Chapter 4

Chaos Synchronization in Delay-Coupled Semiconductor Lasers

4.1 Introduction

Chaos synchronization (CS) is one of the most prominent phenomena that can emerge from delay-coupled nonlinear systems. This is partly because chaotic dynamics has become the paradigm of unstable and non-predictable behavior in nature. The aperiodic chaotic dynamics is reflected in the divergence of originally nearby phase-space trajectories characterized by a positive Lyapunov exponent. CS is therefore a counterintuitive phenomenon because it implies that two or more chaotic systems follow interrelated (or even identical) phase-space trajectories. Nevertheless, CS has been demonstrated in many systems and the conditions needed for coupled chaotic systems to accomplish it are well studied [47, 48].

Furthermore, CS has evolved into a broad field that comprises a variety of typologies, e.g., generalized, phase, anticipated, identical, or cluster synchronization. The corresponding phenomena, fundamentals and applications have been widely studied in a variety of systems ranging from brain dynamics and neural networks [120–123] to population dynamics [124, 125], electronic circuits [48, 126–129] and lasers [51, 52, 54, 130, 131]. Extensive reviews have been dedicated to the properties of chaos synchronization, see e.g. [132, 133].

In delay-coupled lasers, there have been many works devoted to the study of the CS properties in the aforementioned kinds of synchronization. The synchronization of unidirectionally coupled chaotic SL was demonstrated in seminal works from the numerical [54, 134] and experimental [51, 131] points of view. The previously mentioned types of CS are also are also illustrated in SL, e.g., generalized synchronization [51, 54, 65, 131, 134, 135], identical synchronization either via a an active relay [136, 137] or a passive relay [138–140], leader-laggard synchronization [20], and zero-lag synchronization [141].

In the present chapter, the CS phenomenon is explored in two configurations with

two different objectives in mind. First, we study the relation between consistency of the dynamics and synchronization in a **drive-response configuration**. Second, we demonstrate the existence of the identical synchronization state in a **bidirectional coupling scheme** and we also analyze its robustness. These two different synchronization schemes are schematically illustrated in figures 4.1 and 4.2.

Figure 4.1 depicts the coupling scheme used in our first experiment. This scheme is commonly referred in the literature as an open-loop coupling configuration. In this drive-response configuration, the light of the delayed feedback SL (with feedback strength and feedback delay time κ_f and τ_f, respectively) is coupled into the second SL with a coupling strength κ_c and a coupling delay τ_c (the last parameter does not affect the synchronization quality, it only affects the relative lag between the two coupled laser signals).

Figure 4.1: Scheme of the open loop coupling configuration studied in detail in section 4.3. This setup is an adaptation, originally by Heiligenthal et al [59], of the Abarbanel's original setup for delay-coupled systems. The identical synchronization state existed when the coupling and feedback parameters were identical.

Here, we are interested in the problem of measuring the consistency properties of a laser subject to delayed optical feedback [103]. In this context, *consistency* characterizes the property of whether a similar drive results in a similar response [142]. In our experiment, CS is used as an indirect measurement of consistency. We compare the outputs of the drive and the response lasers when they are injected with the same delayed signal (generated from the drive laser). This method is the analog in delay-coupled systems to the procedure described in [143] (also known as *Abarbanel test*) to test the existence of generalized synchronization. In our experiment, if the response of the drive laser to its own delayed feedback is fully consistent, the response of the replica to the same drive will be consistent as well and both will exhibit complete/identical synchronization.

The second coupling scheme studied in this chapter is illustrated schematically in Fig. 4.2. Here, we are interested in the existence and robustness of the identical synchronization state in this bidirectional coupling configuration. The correct characterization and understanding of those problems is key for applications like secure-key exchange (see chapter 5).

In the bidirectional coupling scheme, the emergence of identical synchronization (under the proper operating conditions) is related to the presence of a relay element between both lasers. The relay can either be active (e.g. a third laser [136]) or passive (e.g. a semitransparent mirror [138]). In our case, it is a passive relay built in a semitransparent mirror configuration as depicted in Fig. 4.2.
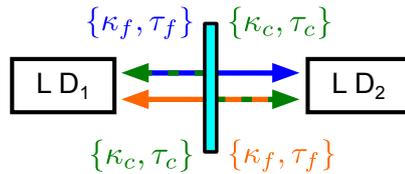
Figure 4.2: Scheme of two semiconductor lasers delay-coupled via a passive relay. In the configuration as depicted, the relay is symmetrically placed between both lasers. The feedback strength is κ_f and the feedback delay time is τ_f. The coupling strength and delay time are κ_c and τ_c, respectively.

4.1.1 Chapter Outline

In this chapter we present the results of our investigations on the synchronization properties of two different coupling scenarios. The description of the experimental setups used to implement the two couplings can be found in the methods section 4.2.

In section 4.3, CS in a unidirectional coupling configuration is used as an indirect method to measure the consistency of the response of a laser to its own delayed optical field. We proceed by measuring and comparing the autocorrelation function (AC) of the drive laser and with the cross-correlation function (CC) of the drive and the response lasers. We find that the AC is a suitable tool to predict under which conditions a SL will synchronize when coupled to other lasers.

The results on the bidirectional coupling configuration are presented in section 4.4. In this section, beyond proving the existence of isochronous CS of the intensity dynamics of both lasers at sub-nanosecond time scales, the stability (i.e. robustness) of this synchronized state is studied in detail. In order to do this, the cross correlation function (CC) is used as an indicator of synchronization. With the help of this indicator, the stability of the synchronized solution is studied under different operating conditions, including the analysis of its dependences with bias current, feedback strengths, and in asymmetric coupling scenarios. In particular, the effect of frequency detuning is analyzed in section 4.4.1 and the effect of noise on the synchronization stability is analyzed in section 4.4.3. Finally, in section 4.5, the results we have presented along this chapter are summarized and their impact for applications of CS is discussed.

4.1.2 Contributions to the Work in the Present Chapter

The first part of the results presented in this chapter, where the open-loop coupling configuration is analyzed, are based on experiments carried out by me. The experiment was suggested by Thomas Jüngling, and the discussion of the results have been done in collaboration with Miguel C. Soriano, Thomas Jüngling, and Ingo Fischer.

The second part of the chapter, devoted to study the bidirectional coupling scheme, includes results already published in: J. Tiana-Alsina, K. Hicke, X. Porte, M. C. Soriano, M. C. Torrent, J. García-Ojalvo, and I. Fischer, "Zero-lag synchronization and bubbling in delay-coupled lasers", *Physical Review E*, **85**, 026209 (2012).

The experiments shown in section 4.4.1 were done by K. Hicke and me. Those experiments shown in section 4.4.3 were mainly done by J. Tiana-Alsina in collaboration

with K. Hicke and me.

4.2   Experimental Methods

The lasers used in this chapter are discrete-mode (DM) lasers. These laser devices have
already been described in section 2.2 and appendix A. The particularity of the employed
devices is that they have been hand-picked from a set of DM lasers that originally
came from the same wafer. This selection has been done with the intention of using
devices with the most similar properties possible for the synchronization experiments.
The analyzed properties are: threshold current, emission frequency, external differential
quantum efficiency, and wavelength-temperature dependence.

4.2.1   Experimental Setups for Synchronization Experiments

The experimental setup used to study the synchronization properties in the open-loop
coupling configuration is depicted in Figure 4.3. This setup has been realized by em-
ploying standard telecommunications fiber components.
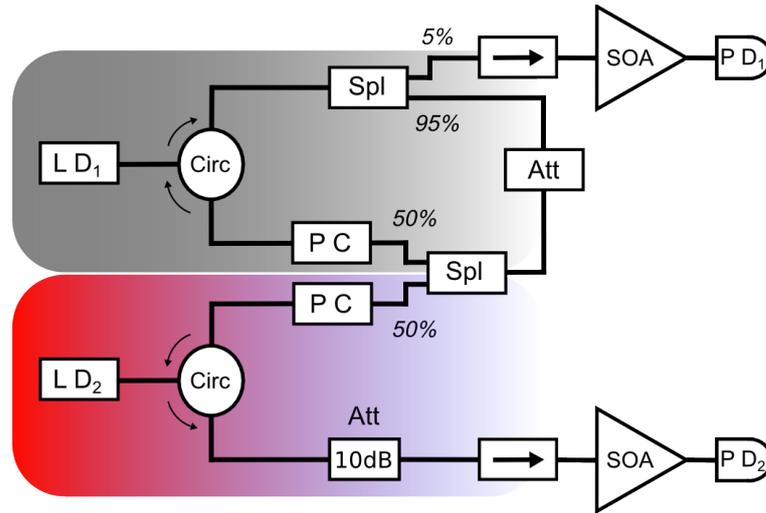
Figure 4.3: Scheme of the experimental setup for the open-loop unidirectional coupling configuration.
LD_1: drive laser diode, LD_2: response laser diode, Circ: optical circulator, PC: polarization controller,
Att: variable optical attenuator, Att[10dB]: fixed 10dB optical attenuator, Spl: one by two intensity split-
ter with indicated intensity splitting ratios, →: optical isolator, SOA: semiconductor optical amplifier,
and PD: photodiode.

The main objective of the experiment with the open-loop coupling setup is to study
the possible relations between the emitted intensities of the delayed feedback laser and
of the injected laser for different operating conditions. The design of the unidirectional
coupling in this setup allows us to scan the coupling-dependence by simply tuning the
attenuator inside the feedback loop. There are two polarization controllers symmetrically
located in order to control the polarization state of the light injected into each laser diode.

The function of the 10 dB attenuator included in the detection path of LD_2 is to equalize the powers arriving to the two SOA, avoiding the asymmetric SNR that would result from the amplification of two signals with different powers. These differences in SNR would cause undesired artifacts in the calculated cross-correlations.

Figure 4.4 depicts the experimental setup used in the two mutually delay-coupled lasers experiment. In this particular coupling configuration, each laser is delay-coupled to the other laser and to itself via delayed feedback. The central element distributing the coupling fields to each laser is a passive relay. The role of the passive relay is played by a semi-transparent mirror-like configuration realized via a single-pass fiber-loop mirror [138–140]. The light coupled back into every laser is a superposition of both optical fields, the self-feedback and the coupling from the other laser. The polarization controllers (PC) control the polarization state of the propagating fields to ensure that we are coupling both lasers via the dominant TE component of the optical field.

In the characterization of the setup we observed that the degree of correlation between both lasers intensities is very sensitive to the PC configurations. However, the total birefringence accumulated along the successive components is reasonably constant within time windows of days (at least in the laboratory controlled conditions) and the configuration of the PCs can be kept fixed during the experiment runs.
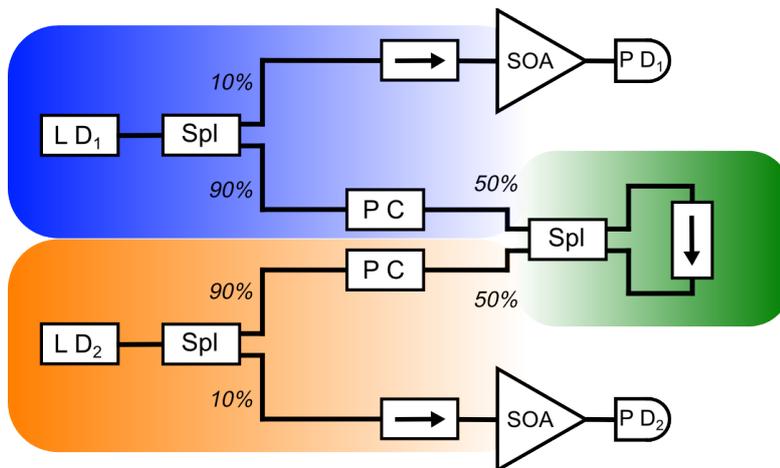
Figure 4.4: Scheme of the experimental setup for the mutually delay-coupled configuration. LD_1 and LD_2: laser diodes, Circ: optical circulator, PC: polarization controller, Spl: intensity splitter with indicated intensity splitting ratios, →: optical isolator, SOA: semiconductor optical amplifier, and PD: photodiode.

The external cavity delay time (τ) is related to the fiber path (l) via $\tau = \frac{l}{v}$, with v being the light propagation velocity in the fibers. Due to the symmetric positioning of the mirror, both external cavity delay times are identical and the synchronization dynamics will occur with zero temporal offset between both lasers.

4.2.2   Cross-Correlation Analysis

We use the normalized CC as a tool to quantify the synchronization between the two coupled lasers in the two coupling configurations studied along this chapter. This mathematical function provides insights on the correlation between the signals of both lasers on different time scales. The better the two lasers are synchronized, the closer the CC value will be to 1.

The CC is computed from the normalized intensity time series in order to avoid contributions from slow or DC offsets and from different amplitudes that can introduce undesired artifacts in the results. For this purpose, each experimental time trace is shifted to zero mean power and normalized by its corresponding standard deviation. It is important to mention that the time-dependent intensities have been detected using an AC-coupled fast photodetector and a 16 GHz analog bandwidth oscilloscope. The formula used to calculate the normalized CC is the following:

$$CC(\Delta t) = \frac{\langle [I_1(t) - \langle I_1 \rangle][I_2(t + \Delta t) - \langle I_2 \rangle] \rangle}{\sqrt{\langle [I_1(t) - \langle I_1 \rangle] \rangle^2 \langle [I_2(t + \Delta t) - \langle I_2 \rangle] \rangle^2}} \tag{4.1}$$

where Δt is the time lag of one time series with respect to the other, I_1 and I_2 are the normalized intensities. The angled brackets indicate the time averaging over t, always performed with time series longer than 50 times the typical external cavity delay time (τ) in our experiments.

4.3   Correlations and Synchronization of Unidirectionally Coupled Lasers in Open-Loop Configuration

In this section, the dynamics of a delayed feedback SL (drive laser) and the dynamics of a unidirectionally coupled second SL (response laser) are compared. This configuration represents the simplest extension of the single laser subject to delayed optical feedback (extensively analyzed in chapters 2 and 3) to a network of two elements where the properties of CS and consistency can be studied.

This coupling scheme may exhibit two possible CS scenarios [144]: identical synchronization and generalized synchronization. A third obvious possibility is the absence of any synchronization between the two coupled units, that may occur e.g. if there are large coupling asymmetries or mismatches between the two coupled systems. Identical CS appears exclusively when the drive and the response lasers share exactly the same characteristics, including the feedback/coupling strengths $\kappa_f = \kappa_c$. This restrictive condition limits the identical synchronization to a very small region in parameters space. Identical synchronization is characterized by equal state variables of the systems, i.e., $x_2(t) = x_1(t - \tau_c + \tau_f)$. This phenomenon is sometimes also referred to as anticipated synchronization [145–147]. In contrast, generalized synchronization can occur even in the presence of significant asymmetries between the two coupled systems[1] or if

---

[1]The nonlinear nature of the systems implies that even small asymmetries can be significant.

the identical synchronization manifold is unstable. In the generalized synchronization scenario, the outputs of the two lasers are not identical. The state variable of the response laser is typically an unknown function of the state variable of the drive laser, i.e., $x_2(t) \simeq \mathcal{F}(x_1(t - \tau_c); t)$.

In our experiment, we use the correlation between the intensities of the two lasers to quantify the degree of synchronization, and compare it to the AC of the drive laser. From now on, we use the term AC to denote the autocorrelation of the intensity of the drive laser (AC_1), and CC to denote the cross-correlation between the drive and the response laser ($CC_{1\rightarrow2}$). We focus on the coefficients of AC and CC that represent the previously described types of CS. The amplitude of $CC(\tau_f - \tau_c)$ (central peak) represents the degree of correlation between the drive and the response lasers to the same delayed feedback signal. Therefore, it is related to the consistency of the response of a single delayed feedback laser via generalized synchronization. Conceptually, the two lasers are two replicas of the same system that are subject to the same drive, a scenario that corresponds to the Abarbanel test [143] in the version for delayed feedback systems as proposed by Heiligenthal and coauthors [59]. The other depicted coefficient is the amplitude of the CC at first delay echo ($CC(-\tau_c)$), which is compared to the amplitude of the AC at first delay echo ($AC(-\tau_f)$) because both coefficients represent the nonlinear transformation of each SL to the delayed feedback/coupling field [148].

Figure 4.5 illustrates the dependences of these AC and CC coefficients on the feedback/coupling attenuation. The two figures depict data from two different pump currents: $I = 1.2I_{th}$ in Fig. 4.5a and $I = 1.5I_{th}$ in Fig. 4.5b. Since the attenuator is situated before the fiber splitter, the feedback and coupling attenuations vary in exactly the same amount of dB. Any possible initial difference between feedback and coupling attenuations (that we have accurately matched) would be reflected in an offset between AC and CC curves on the attenuations axis. The gray squares in both figures depict the AC at first delay echo ($AC(-\tau_f)$). We will not extend in the description of the dependence of this coefficient on the feedback attenuation because it is identical to the dependences already observed and extensively described in chapters 2 and 3. The CC at first delay echo ($CC(-\tau_c)$) is plotted with red triangles. The CC and the AC at first delay echo present the same dependence on the attenuation with very similar amplitudes, which indicates that both lasers are performing the same nonlinear transformation to the delayed feedback field.

The blue circles in Fig. 4.5 depict the CC at central peak. The amplitude of this coefficient represents the level of consistency of the response of the two lasers to the same drive. Certainly, a direct identification of the level of consistency requires the specific knowledge of the sub-Lyapunov exponent [103]. This exponent characterizes the stability of the response of a SL to its delayed feedback. In particular, a negative sub-LE is related to weak chaos, whereas a positive sub-LE results in strong chaos (for an introduction to strong and weak chaos regimes see section 2.1.1). In the context of SL, the properties of weak and strong chaos are directly related to consistency[2]. An inconsistent response of

---

[2]In [103], the exact same optical drive was repeated twice and consistent or inconsistent responses of the laser were found depending on the pump parameter. The authors related the consistency of response
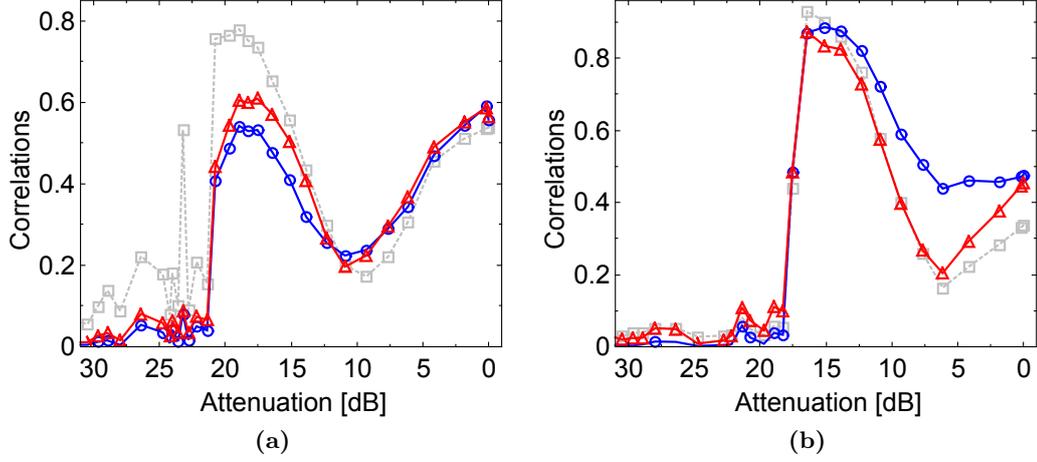
Figure 4.5: Comparison of the CC($-\tau_c + \tau_f$) (blue circles) with the CC($-\tau_c$) (red triangles) for two distinct bias currents in the unidirectional coupling scheme: (a) $I = 1.2I_{th}$, and (b) $I = 1.5I_{th}$. The curve AC($-\tau_f$) (gray squares) is plotted for comparison with the results discussed in chapters 2 and 3.

the laser to its own chaotic delayed signal is referred to as strong chaos, whereas a fully consistent response corresponds to weak chaos. In consequence, the amplitude of the CC peak in our experiment is a direct indicator of the level of consistency of the lasers.

In Fig. 4.5a, all the correlation coefficients closely follow the same dependence on the feedback attenuation with very similar amplitudes. In the context of the results presented in chapter 2, it is clear that the common minima region corresponds to the region of strong nonlinear mixing between the relaxation oscillations frequency (f_{RO}^S) and the maximum feedback induced frequency shift (Δf_{fb}) as it has been extensively discussed in chapter 2. This region on the attenuations axis can now be directly related to strong chaos because it coincides with the minimum region in the amplitude of the central CC peak. Given the coincidence of the amplitudes of the AC at first delay echo and the central CC peak, the dynamical properties of a delayed feedback laser can be used to predict the synchronizability of this laser in a network of delay-coupled lasers. In consequence, the region with low amplitudes of the central CC peak must be avoided in applications that rely on CS between the coupled lasers.

The different panels in Figure 4.6 show the comparison between AC and CC for two different attenuations in Fig. 4.5a (see Figure caption for detailed explanation of the figure contents). To facilitate the comparison, the colors of the curves match with those in Fig. 4.5a. The amplitude of the central CC peak, that corresponds to the level of consistency, is depicted in Fig. 4.6a (attenuation of 0 dB) and in Fig. 4.6b (attenuation of 10.91 dB). In our experimental coupling configuration we have matched the delays, i.e., $\tau_f \simeq \tau_c$. Consequently, the amplitude of this CC peak (CC(0)) reflects the level of consistency. The closer the central peak of the CC is to AC(0) of the drive laser,

---

to weak and strong chaos. This strong form of consistency (when the dynamical system converges towards the same response to an input), is closely related to generalized synchronization.

the more identical dynamics exhibit both lasers. In a perfect identical synchronization scenario the amplitude of this CC peak would be 1 and both correlation measurements would coincide $AC(\Delta t) = CC(\Delta t - \tau_c + \tau_f)$. In this sense, the conditions depicted in Fig. 4.6a presents a higher consistency response than the conditions depicted in Fig. 4.6b. The small asymmetry between the minima in the CC central peaks is probably caused by an initial asymmetry in the feedback and coupling strengths, causing the feedback strength to be slightly higher than the coupling strength.

The AC and the CC at first delay echoes (Figures 4.6c and 4.6d) reflect the nonlinear transformation of the delayed feedback field by the SL. Under this experimental conditions, at $I = 1.2I_{th}$, the AC and the CC at first delay echoes follow similar dependences than the CC at central peak. The difference between the four panels is in the amplitudes of the peaks. Figures 4.6b and 4.6d depict the correlations for the attenuations with the corresponding minima amplitudes, which is reflected in lower amplitudes of the correlations modulations.

The correlations depicted in Figure 4.6 correspond to two different attenuations for the same pump current, $I = 1.2I_{th}$. Under this pumping condition, the synchronization scenario corresponds to generalized synchronization. The amplitude of the central CC peak is never higher than the amplitude of the CC at first delay echo. Interestingly, the synchronization scenario changes for the pump current of $I = 1.5I_{th}$, depicted in Figure 4.5b. Identical synchronization dominates at this injection current, which is reflected in a larger amplitude of the central CC peak than the amplitude of the peaks at first delay echo. It is important to note that the parameter conditions for identical synchronization state are very restrictive. Figure 4.7 depicts exemplary conditions of identical synchronization between drive and response lasers. The amplitude of the central CC peak coefficient is close to 1, which is the unambiguous signature of identically synchronized dynamics.

Different factors may limit the height of the central CC peak at different pump currents and attenuations. Noise is a decisive factor in the limitation of the correlation amplitudes. If the signal has low amplitude at detection, the low SNR will limit the height of our correlation measurements (see section 2.4.1 for a detailed characterization of the effects of SNR on the AC amplitude). This effect is particularly important at low pump currents and intermediate to low feedback attenuations. This is the most probable factor limiting the amplitude of the CC coefficients curves in Fig. 4.5a, but it barely affects the data in Fig. 4.5b. The other main source of noise in our experiment is the inherent laser emission noise (e.g. spontaneous emission). This effect is an important limiting factor of the correlation amplitudes at high feedback strengths and high injection currents. In the context of identical synchronization, the effect of laser emission noise is related to the phenomenon of attractor bubbling, which causes unpredictable episodes of loss of synchronization. Bubbling is introduced and characterized in detail later in this chapter (section 4.4.3).

We have discussed in the context of Figure 4.6 how noise can lower the amplitudes of the correlation peak related with the level of consistency. Nevertheless, the relation between the amplitudes of the CC at central peak and at first delay echo for all the
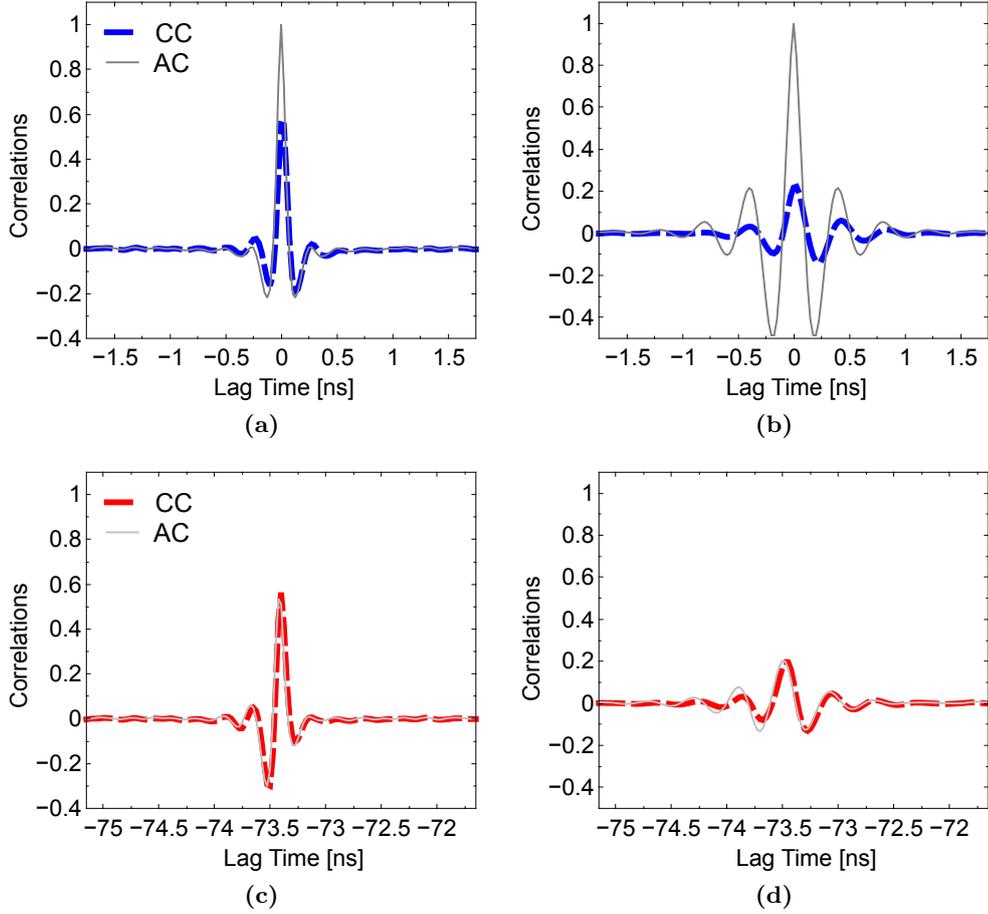
Figure 4.6: Two different points on the AC and CC curves for the injection current of $I = 1.2 I_{th}$. The feedback attenuations of the different selected points correspond to 0 dB in panel (a), and 10.91 dB in panel (b). Panels {(a), (b)}: The dark gray solid curves show to the AC(0) and the dashed blue curves depict the CC($-\tau_c + \tau_f$), i.e., the level of consistency. Panels {(c), (d)}: The light gray solid curves show to the AC($-\tau_f$) and the dashed red curves depict the CC($-\tau_c$), i.e., the nonlinear transformation of the delayed feedback field by the SL.

values on the attenuations axis in Fig. 4.5b suggests that the dynamics is dominated by identical synchronization. This finding is in good agreement with the corresponding results in [103].

At this point, in order to gain insight into the relation between correlation and synchronization, it is desirable to go beyond time averaged correlations and to look at the time-resolved behaviors. The synchronization dynamics is characterized via the calculation of sliding-window correlations. In figure 4.8a and 4.8c we depict time windows of sliding correlations for the two bias conditions and, in panels 4.8b and 4.8d, the histograms of these sliding correlations[3]. The dynamics depicted in Fig. 4.8 correspond

---

[3]The histograms are calculated over 2 MSamples and are normalized such that the integral over the
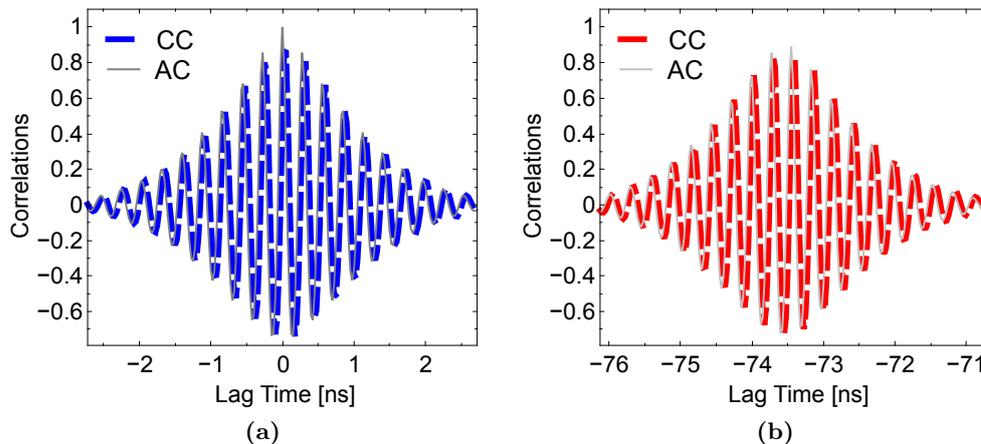
Figure 4.7: Exemplary experimental conditions of identical synchronization in the unidirectional coupling configuration. Panel (a): the blue dashed curve shows the central CC peak $(CC(-\tau_c + \tau_f))$ and the dark gray solid curve shows the $AC(0)$. In panel (b): the red dashed curve depicts the CC at first delay echo $(CC(-\tau_c))$ and the light gray curve shows the AC at first delay echo $(AC(-\tau_f))$. The injection current is $I = 1.5 I_{th}$ and the feedback attenuation corresponds to 15.09 dB.

to different regions in the weak chaos regime.

For the computation of the sliding correlations, the correlation coefficients are calculated over a sliding window of 1 ns width. This sliding window is calculated with a resolution of four sampling steps (0.1 ns). The resulting traces reflect the time-dependent correlation values.

Genuine desynchronization events can be now distinguished from lower-correlation states via significant difference between the sliding central CC peak and the sliding AC peak. The effect of losses of synchronization is visible in Figures 4.8a and 4.8c. Particularly interesting is the situation illustrated in Fig. 4.8a. The three curves suffer from fast episodic drops (not necessarily coincident in time). However, the blue curve (that corresponds to the identical synchronization coefficient) is typically higher than the other two correlation coefficients. The corresponding histograms of the coefficients, depicted in Fig. 4.8b, indicate an interesting feature. While the correlation coefficients at first delay echo have PSD approximately centered at their most probable correlation heights, the central CC peak coefficient (associated to identical synchronization) exhibits a bimodal distribution. The most probable value is at high correlations (as expected for identical synchronization), and the other maximum coincides with the peak of the histogram of the AC at first delay echo. This result indicates that when the identical synchronization state is momentarily lost, the correlation most probably drops to values characteristic of the AC at first delay echo, i.e., of the nonlinear transformation of the delayed feedback signal by the SL. In contrast, the histograms plotted in Figure 4.8d are all peaked around 0.8, indicating the overall high correlations expected for unperturbed identical synchronization. It is clear that this dynamics (undamped relaxation

---

bins is 1. The value for each bin is the corresponding probability.
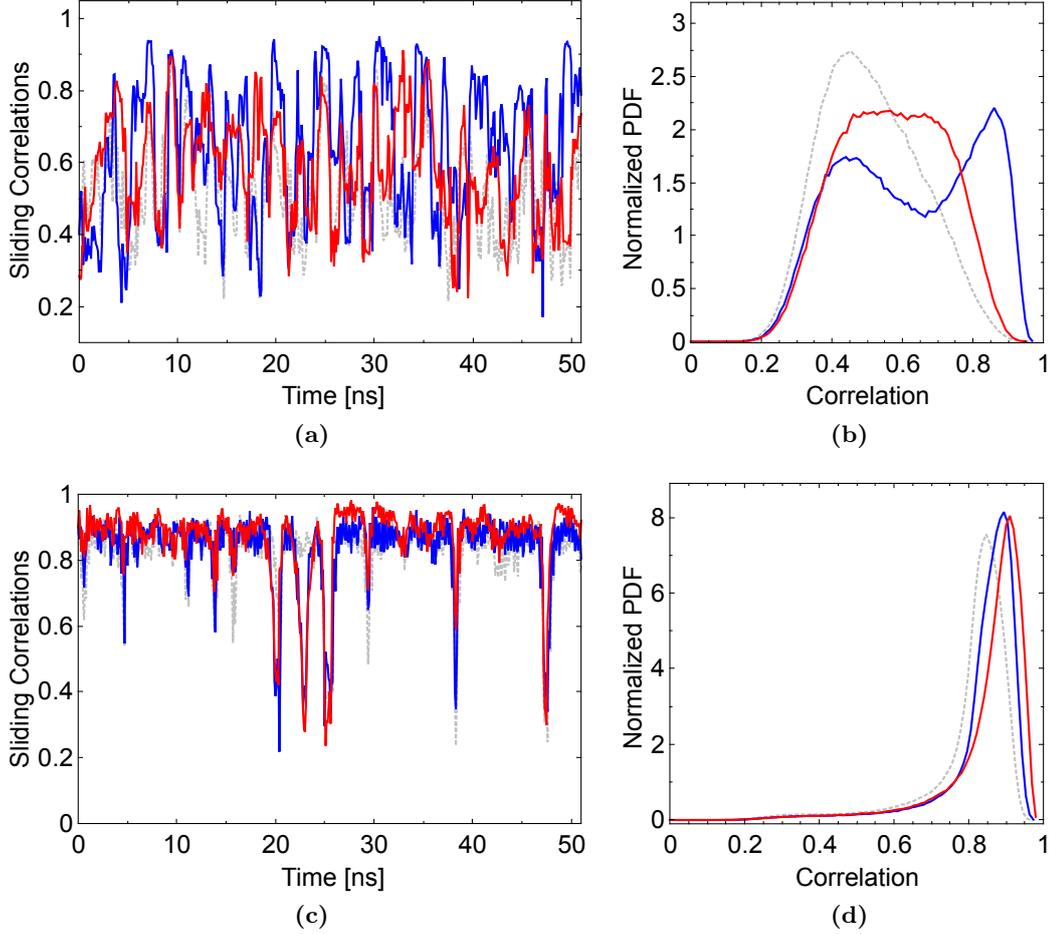
Figure 4.8: Sliding correlations and their corresponding normalized probability density functions (PDF) for the bias current of $I = 1.5I_{th}$ and attenuations of 0 dB (panels (a) and (b)), and 15.09 dB (panels (c) and (d)). The blue, red and gray curves show the sliding functions of $CC(-\tau_c + \tau_f)$, $CC(-\tau_c)$, and $AC(-\tau_f)$, respectively.

oscillations) is more structured than the dynamics corresponding to Fig. 4.8b. Further understanding of the role that play fast desynchronization events in the stability of the identical synchronization state require complementary numerical investigations characterizing the influence of noise and parameter mismatches.

In conclusion, CS has been studied in the context of the consistency testing scheme proposed by Heiligenthal and coauthors in [59]. We have found that in dependence of the pump current, our experimental dynamics exhibit characteristics of generalized synchronization or of identical synchronization. Remarkably, in the generalized synchronization scenario as discussed in our results, the different correlation coefficients follow similar behaviors. Particularly interesting is that the minima coincide for both measurements, the CC and the AC. This finding permits the clear distinction between synchronizable

(weak chaos) and non-synchronizable (strong chaos) scenarios via the knowledge of the AC properties of the single delayed feedback laser. Furthermore, we find that the central CC peak has higher amplitudes than the correlations at first delay echo in the scenario where identical synchronization is dominant. A result that is in good agreement with consistency measurements [103]. Moreover, in a time-resolved characterization of the correlations we have found that the identical synchronization exists even at high feedback strengths, in contrast to what is observed in the averaged picture in Fig. 4.5b. The effect that lowers the average amplitude of the correlation coefficients is the presence of episodic losses of synchronization on a fast time scale.

4.4 Synchronization of Two Mutually-Coupled Semiconductor Lasers with a Passive Relay

In order to characterize the coupling dynamics in the bidirectionally-coupled lasers experiment, the parameter space of each laser has been widely scanned to identify matching operating conditions. The dependence of the emission wavelength or the threshold current on the temperature are illustrated in appendix A. In the current experiment, we take profit from these characterizations to work with the smallest possible mismatches in parameters (e.g., the wavelengths match with a precision better than 0.1 nm). We then study under which conditions identical synchronization can be observed and how robust it is.
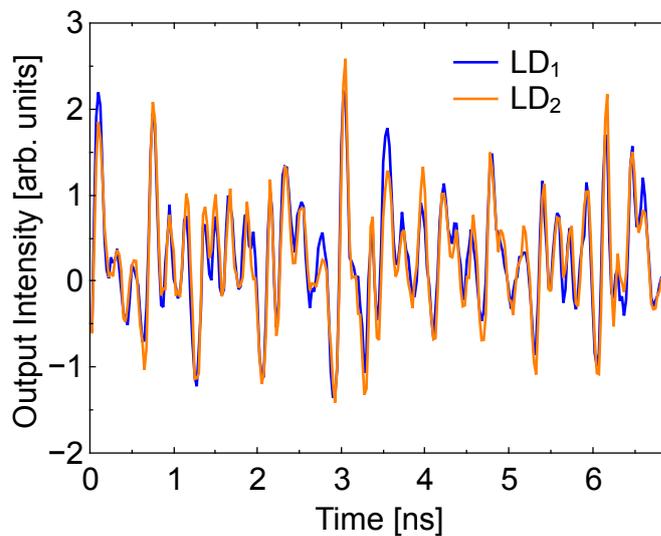
Figure 4.9: Intensity time traces of LD_1 and LD_2. Both lasers are pumped at $I = 1.02I_{th}$. The zero-frequency detuning condition has been achieved by tunning the laser temperatures to 21.08 ° C and 22.00° C, respectively.

In chapter 2 we explained the important role of the relaxation oscillations frequency for the bandwidth of the observed intensity dynamics. For our lasers, these character-

istic frequencies are in the order of a few GHz, smaller than the fast photodiodes and oscilloscope bandwidths. The bandwidth of our detection scheme therefore allow us to resolve the full sub-nanosecond intensity dynamics of the lasers. The intensity dynamics of LD_1 and LD_2 is recorded in two distinct channels of the real-time oscilloscope with a sampling rate of 40 GSamples/s.

Figure 4.9 shows a 7 ns time window of two intensity time traces resolving the sub-nanosecond intensity dynamics of both lasers. Temporal offsets caused by a length difference between the two detection lines have been carefully compensated for. Each intensity time trace has been normalized by subtracting its mean and dividing it by the standard deviation. Therefore, both time traces are centered around zero. We can observe sub-nanosecond chaotic oscillations of the intensity for both lasers. Remarkably, both intensity time traces follow almost identical behavior, demonstrating excellent isochronous synchronization. The observed differences between both time traces are close to the detection noise limit.

A first characterization of the synchronization quality can be obtained from a synchronization plot, i.e., by plotting the normalized output intensity of LD_2 as a function of LD_1. Figure 4.10 depicts 5600 samples covering a time interval of 140 ns. One can observe that the density of points is well-centered around the diagonal.
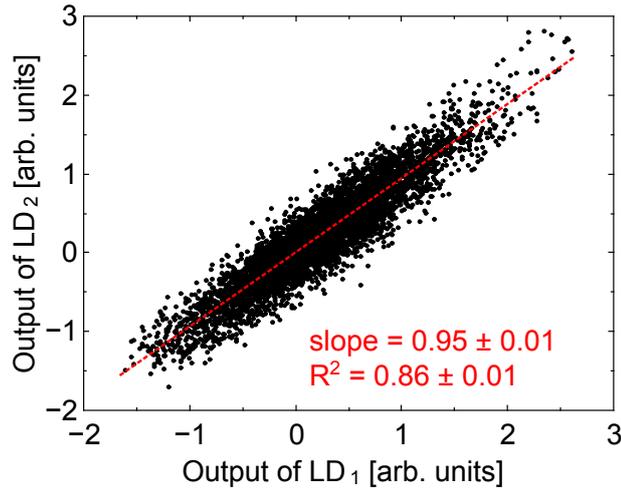
Figure 4.10: Synchronization plot depicting the normalized intensities of LD_1 versus LD_2 of the time series partly shown in figure 4.9.

A linear regression analysis of the distribution of these 5600 points shows that most of the samples are situated along the diagonal line with a regression coefficient of 0.86 ± 0.01. Given the experimental conditions, such correlation properties can be associated with good synchronization.

In section 4.2.2 the cross-correlation was introduced as a key indicator to quantify the quality of the synchronization. In the context of this bidirectional coupling scheme, the CC analysis of the intensity dynamics of both lasers provides important insights into the main time scales of the dynamics and the related physical processes.
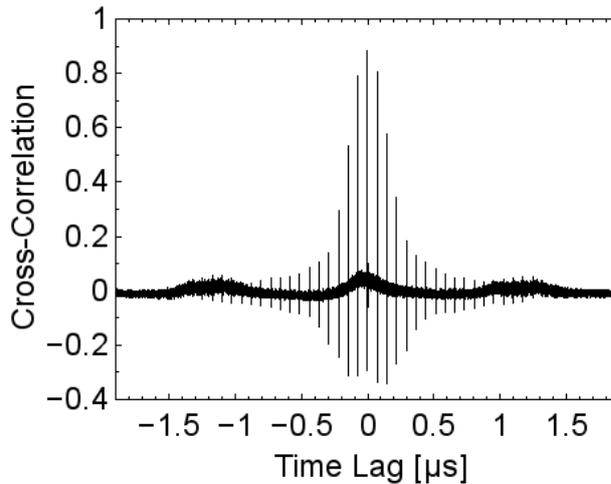
Figure 4.11: Cross-correlation function of the intensity time traces of LD_1 and LD_2. The maximum of the CC occurs at zero-lag and its value is 0.87. Both lasers are pumped at $1.10 I_{th}$ and the laser temperatures are controlled to 21.40° C and 22.00° C, respectively. This corresponds to zero-frequency detuning conditions.

Figure 4.11 depicts the cross-correlation function of the intensity dynamics of LD_1 and LD_2 for an injection current of 13 mA. The dynamics is characterized by LFF behavior under this experimental conditions. Each time trace has a length of 10^6 samples (25 μs). The maximum time lag shown in this figure is of the order of 2 μs to show the behavior of the CC far from the central peak, corresponding to the isochronous synchronization. The first characteristic that can be seen is the decay of the maximum of the CC with the increase of the time-lag. This decaying envelope decreases to almost zero for time-lags larger than 1μs. The coupling time in our delay-coupled system is $\tau = 73.125 \pm 0.025$ns and, therefore, the envelope approaches zero at roughly $\sim 14\ \tau$. This means that there is hardly any correlation between the two time series for lags greater than 14 times the external cavity round trip time. Moreover, one can observe a slightly rising plateau present at positive and negative time-lags close to 1 μs. These times correspond to the characteristic low-frequency fluctuations (LFF) slow time scale ($\sim$ MHz).

Noteworthy, a closer look at the CC central peaks provides valuable information on the fast time scales and on the quality of the synchronization. Panel 4.12a depicts the CC of the two intensity time series partially shown in Fig. 4.9. The time series length used to calculate the CC is $1.6 \cdot 10^5$ samples ($4\mu s$). The different peaks visible at both sides of the central peak are situated at lags that are multiples of the delay time. One can observe that the side peaks are roughly situated at $\tau \simeq 73$ns and $2\tau \simeq 146$ns.

Panels 4.12b, 4.12c, and 4.12d correspond to the magnified CC regions indicated via the corresponding colored braces in panel 4.12a. Panel 4.12c shows the zero-lag central CC peak. Its strong left-right symmetry reflects the symmetric experimental coupling conditions. The structures in panels 4.12b and 4.12d respectively illustrate the delay
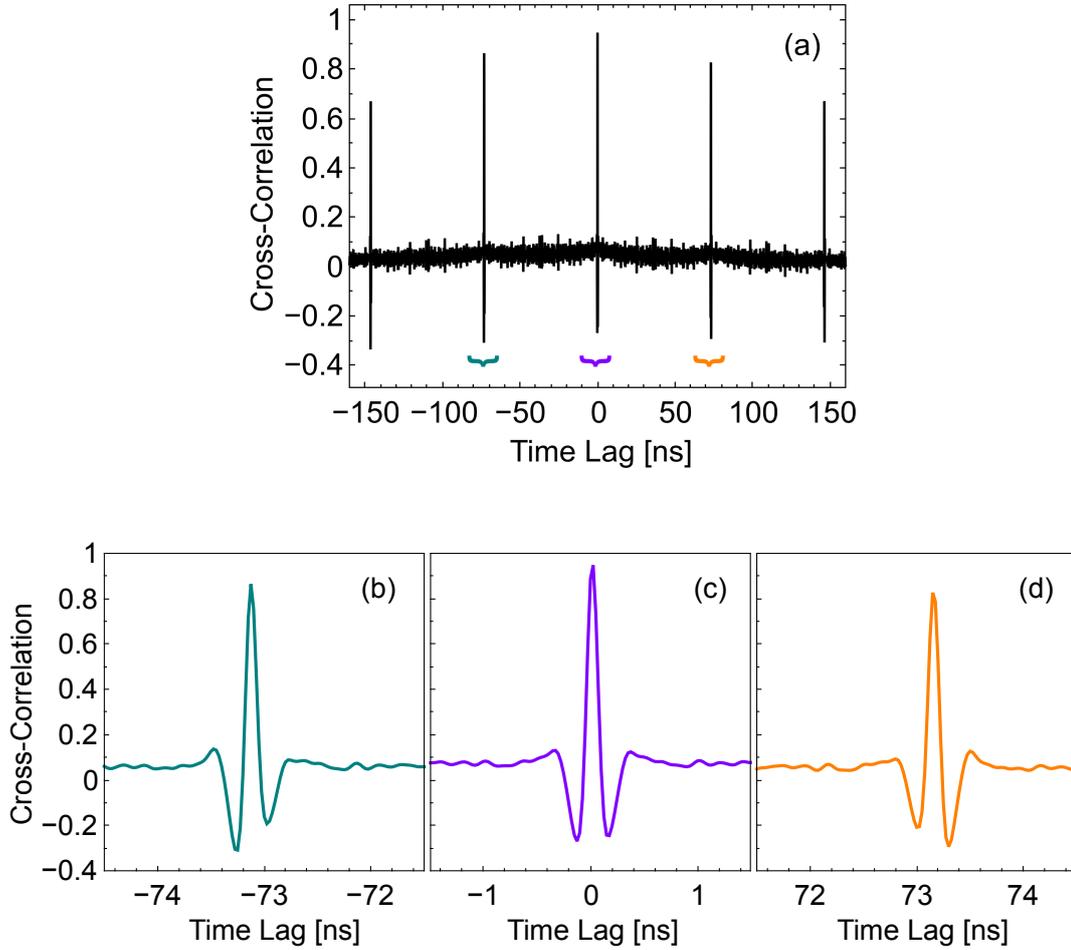
Figure 4.12: Cross-correlation function of the intensity time traces of LD_1 and LD_2. The parameters are the same as in figure 4.10. The CC coefficient at zero-lag is 0.94. The three colored braces indicate the regions around the first delay echoes that are magnified in the lower panels. Panels (a), (b) and (c) respectively depict the $-\tau$, 0, and τ delay echoes.

echoes at $-\tau$ and τ. These recurrent structures of the CC (typical for the majority of delay systems) around multiples of the delay time are no longer individually symmetric, but they are mirror symmetric to the other. The fast decorrelation of each structure reflects the strong damping of the relaxations oscillations in this coupling scenario due to the chaos.

4.4.1   Influence of Spectral Detuning

Up to now, we have demonstrated that identical zero-lag CS can be achieved and is stable for long times in our bidirectional coupling configuration. In addition to these findings, we are interested in studying the robustness of the isochronously synchronized

state towards possible mismatches in the system. Here, the influence of optical frequency detuning on the synchronization dynamics is analyzed. For this purpose, the emission wavelength of one of the lasers is detuned with respect to the emission frequency of the other laser, which is maintained fixed as the reference. The relative detuning in frequency is achieved by changing the temperature of that laser[4].
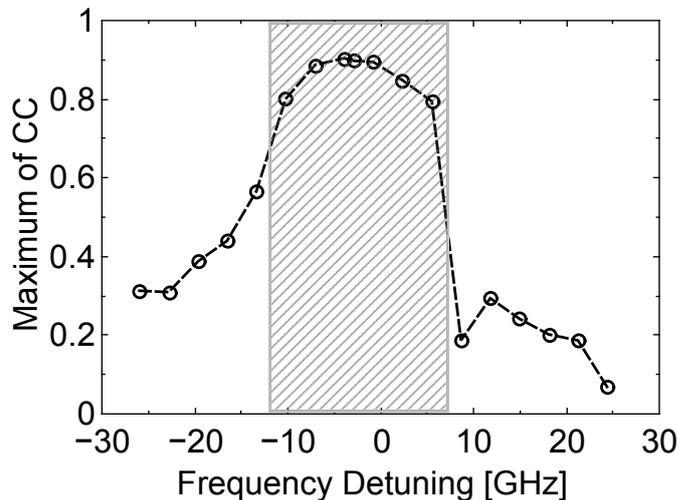
Figure 4.13: Dependence of the CC at zero-lag on the nominal frequency detuning between the solitary lasers. The values correspond to an injection current of $I = 1.02 I_{th}$. The dashed area contains the injection-locking region.

Figure 4.13 depicts the maximum of the CC at zero-lag for the two lasers in dependence of the detuning. The relative frequency detuning is varied by changing the temperature of LD_1 while keeping the temperature of LD_2 fixed. For each step in temperature of $\Delta T = 0.25$ ° C, the CC at zero-lag is measured. We define the detuning to be positive when the detuned laser exhibits a higher solitary emission frequency than its counterpart. The value of the CC at zero-lag is used to establish a threshold for stable synchronization. We identify a region of distinctive good synchronization where the CC value is higher than 0.8. This region, that extends from -11 GHz to 8 GHz in frequency detuning, coincides with the injection-locking region, i.e., the range of frequencies wherein the emission of both lasers lock to one single frequency. For frequency detunings outside of this region, the correlation experiences an abrupt drop. This CC drop is not symmetric for negative and positive detuning values.

The intensity dynamics of the lasers exhibit different behavior in the different detuning regions. Inside the locking region (Fig. 4.14a), the two intensity time traces exhibit high correlation of the characteristic sub-nanosecond chaotic fluctuations. In contrast, in the large detuning region (Fig. 4.14b), the time traces are not synchronized, their fast chaotic fluctuations show long periods of completely uncorrelated behaviors. A more detailed investigation on the influence of spectral detuning can be found in [149].

---

[4]The wavelength versus temperature dependence is explored in the appendix A
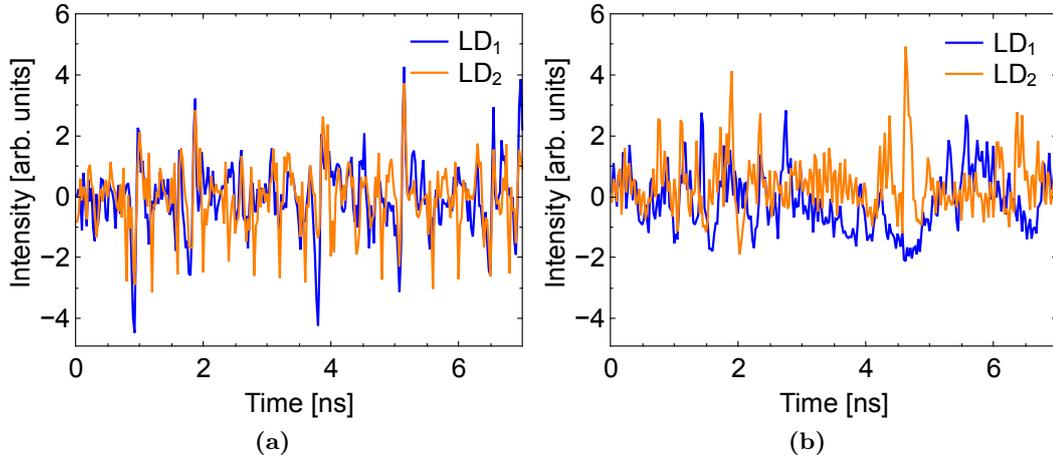
Figure 4.14: Experimental time traces for detuning values (a) inside and (b) outside the injection-locking region. The respective detuning values are -0.78 GHz and -25.95 GHz.

4.4.2   Isochronous Synchronization Regime

After we have analyzed the effects of the detuning in optical frequencies, we investigate the role of the injection current on the synchronization of the mutually delay-coupled lasers. For this experiment, the laser temperatures have been chosen to realize zero-frequency detuning conditions at each different bias current. The careful selection of the lasers implies very similar threshold currents and $\lambda(I, T)$ characteristics. Therefore, we modify the injection current equally in both lasers to account for the symmetric situation in this measurement.
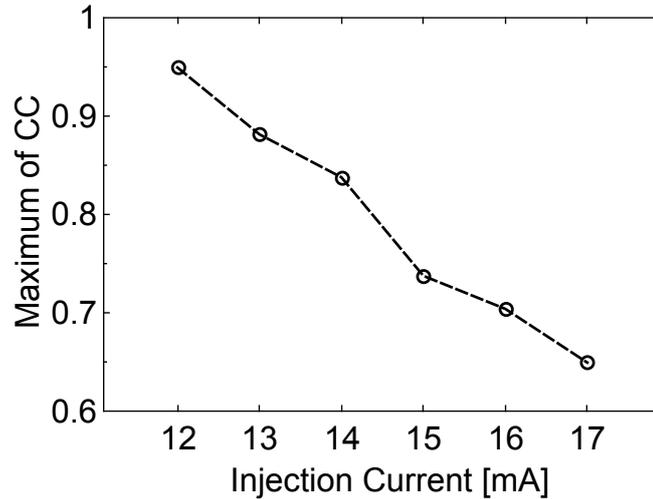
Figure 4.15: Dependence of the zero-lag CC coefficient on the bias current. The bias current is scanned from $I = 1.02 I_{th}$ to $I = 1.45 I_{th}$. The values correspond to the zero-frequency detuning region.

Figure 4.15 depicts the zero-lag CC coefficient for different bias currents. It can be observed that this coefficient decreases monotonously with the increase of the injection current. This monotonous decay is not obvious to explain since it covers two different dynamical regimes. The bias currents up to 14 mA result in dynamical behaviors in the LFF regime. Increasing the pump currents result in a transition towards the fully-developed coherence collapse regime, without identifiable low-frequency structures.

One possible origin of the decay in the zero-lag CC coefficient is an increase of desynchronization events for higher bias currents. This is discussed in detail in the following section. Therefore, our goal is to study the emergence of desynchronization events in the zero-frequency detuning scenario.

4.4.3 Noise-Induced Desynchronization Events: Bubbling

So far, we have shown the dependence of correlations related to isochronous synchronization on frequency detuning and injection current. We will now investigate the robustness of isochronous synchronization for the zero-frequency detuning case. From theoretical studies [150, 151] we know that synchronization is usually characterized by transversal stability of the attractor of the coupled system. However, transversal stability is not enough to characterize the synchronization behavior. Invariant manifolds within the chaotic attractor can become transversally unstable. When in the vicinity of these invariant manifolds, noise can induce excursions away from the synchronization manifold. We identify these noise-driven desynchronization events as bubbling events. The saddle point solutions of the two delay-coupled lasers with a passive relay represent the transversely unstable solutions [151].

Figure 4.16a depicts the time traces of LD_1 and LD_2 pumped at 12 mA for zero-frequency detuning conditions. The time trace of LD_1 has been shifted up to visualize both time traces. The two lasers exhibit LFF dynamics with apparently well synchronized behavior, even though their intensities are not fully resolved in this figure. The desynchronization events can be investigated by calculating the intensity difference between time traces [151]. In order to distinguish real desynchronization events in the chaotic trajectory from noise in the detection we perform an analysis summing the intensity difference over finite time intervals. Equation 4.2 defines the procedure to calculate the integrated intensity difference time trace:

$$\Delta I(t) = \sum_{k=t-\frac{\Delta s}{2}}^{t+\frac{\Delta s}{2}} \frac{|I_1(k) - I_2(k)|}{\Delta s \langle |I_1(k)| + |I_2(k)| \rangle_{\Delta s}}, \tag{4.2}$$

where Δs is the averaged time interval and the brackets represent the mean value over this interval. Consequently, Eq. 4.2 represents the sum of the normalized intensity difference over the chosen time interval. This sum is calculated at each time step of the corresponding intensity time traces.

The resulting integrated intensity difference is depicted in Fig. 4.16b for $\Delta s = 4$ ns. The integration over Δs allows for the identification of the major desynchronization
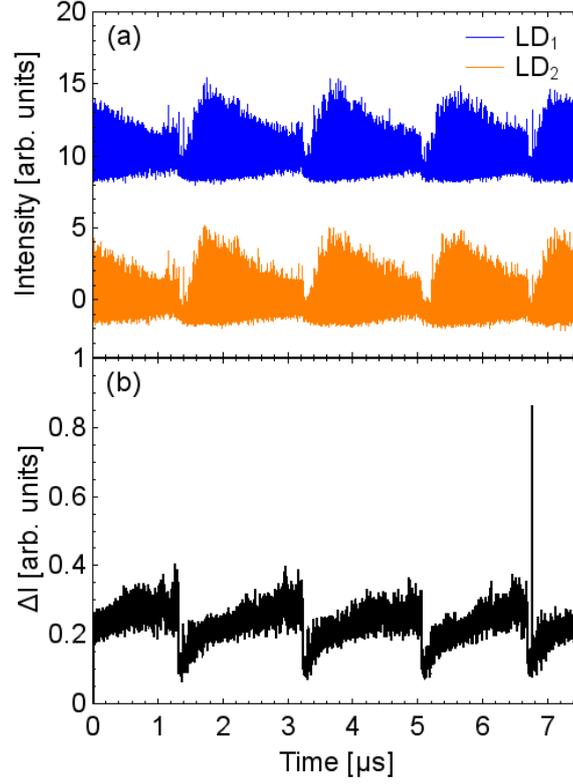
Figure 4.16: (a) Intensity time traces and (b) Integrated intensity difference, ΔI, of LD_1 and LD_2 pumped at $I = 1.02 I_{th}$ (12 mA). Temperature of LD_1 is 21.08 ° C and temperature of LD_2 is 22.00 ° C.

events highlighting them from the rest of the well synchronized time series. We can then distinguish real desynchronizations from detention noise dominated decorrelation. In Figure 4.16b, the integrated intensity difference ΔI follows regular oscillations that resemble the underlying LFF structures. After each dropout takes place, ΔI shows a minimum and smoothly increases during the next LFF cycle. This behavior was also observed in other experimental studies and the low absolute levels of ΔI indicate synchronized behavior. [152]. In addition, the presented data shows one large peak with a clearly differentiated height from the baseline variations. This event, that appears at ∼6700 ns, coincides in time with one characteristic LFF intensity dropout and, due to its high ΔI value, can be classified as a real desynchronization event.

Interestingly, the presence of desynchronization events (those regions where ΔI values approach to 1) raises in proportion when the bias current is increased. Figure 4.17 illustrates this effect by depicting data at 13 mA. Figure 4.17a depicts the time traces of LD_1 and LD_2 for a pump current of 13 mA. Similarly to panel 4.16a, the time trace of LD_1 has been shifted up to visualize both time traces. Figure 4.17b depicts the corresponding 7500 ns window of the integrated difference time trace for $\Delta s = 4$ns. Under this higher bias current conditions, five abrupt high ΔI peaks are clearly distinguishable
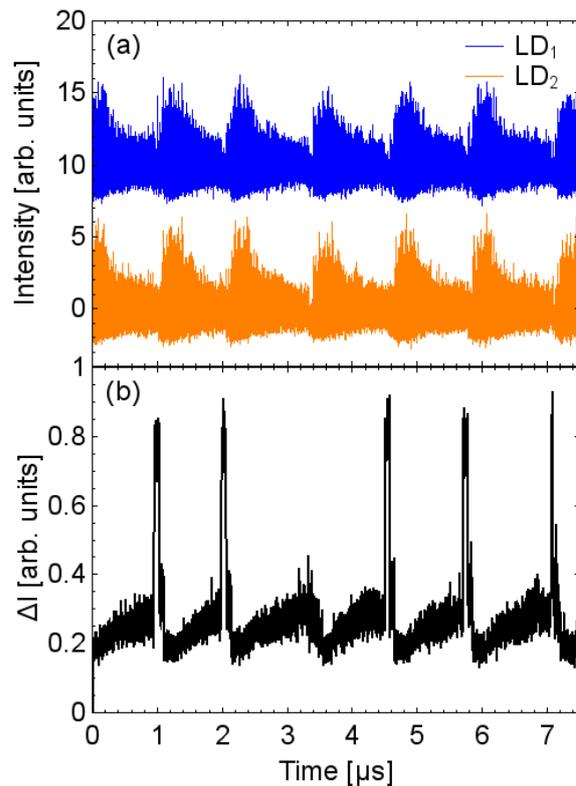
Figure 4.17: (a) Intensity time traces and (b) Integrated intensity difference, ΔI, of LD_1 and LD_2 pumped at $I = 1.10 I_{th}$ (13 mA). Temperature of LD_1 is 21.40 ° C and temperature of LD_2 is 22.00 ° C.

in Fig. 4.17b. From the direct comparison of this trace and the intensity time traces of the lasers (Fig. 4.17a), it is evident that these peaks are again related to the LFF characteristic intensity dropouts. Therefore, in LFF dynamics (under zero-frequency detuning conditions) the desynchronization events are related to the power dropouts.

Remarkably, not all the dropouts at this bias current have an associated abrupt increase in ΔI. In panel 4.17a, there is a dropout around 3300 ns that has no corresponding change in its integrated intensity difference in panel 4.17b. This observation implies that, despite their frequency decreases for increasing bias currents, there still exist some LFF dropouts that have no desynchronization events associated with them. Figure 4.18 illustrates the time traces of LD_1 and LD_2 near different dropout regions for the same data plotted in Fig. 4.17. Panel 4.18a depicts the LFF dropout without loss in synchronization. In contrast, panel 4.18b shows a typical LFF dropout with an associated desynchronization event. In the latter panel, it can be observed that the time trace of LD_2 shows an intensity dropout. After one delay time ($\tau \simeq 73.1$ ns), LD_1 experiences the dropout too and isochronous synchronization is recovered. As both time traces are uncorrelated for a time interval τ, the integrated intensity difference ΔI correspondingly grows during this period of time, as it is observed in panel 4.17b.
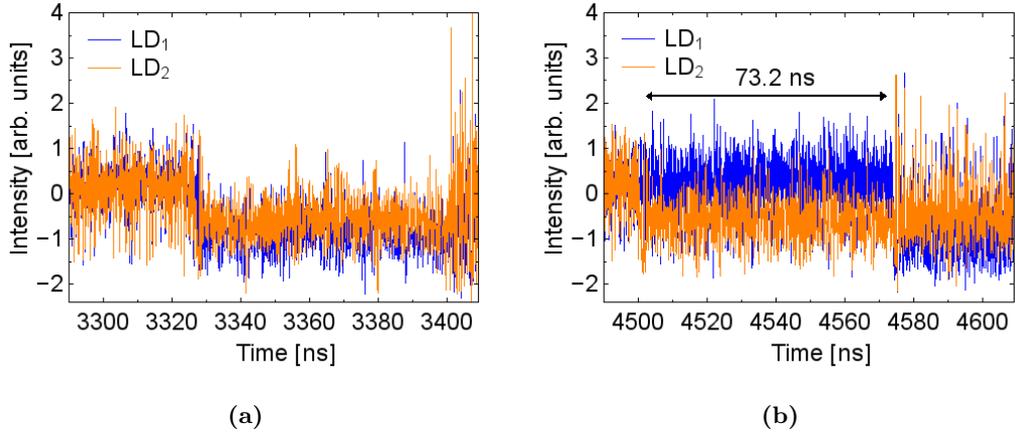
Figure 4.18: (a) Experimental LFF dropout without loss of isochronous synchronization. (b) Experimental LFF dropout with loss of isochronous synchronization. The duration of the desynchronization event corresponds to the delay time, $\tau \simeq 73.1$ns. The data in both panels correspond to different instants in the same time trace. The injection current is 13 mA ($1.10 I_{th}$) and temperatures of LD1 and LD2 are 21.40 ° C and 22.00 ° C, respectively.
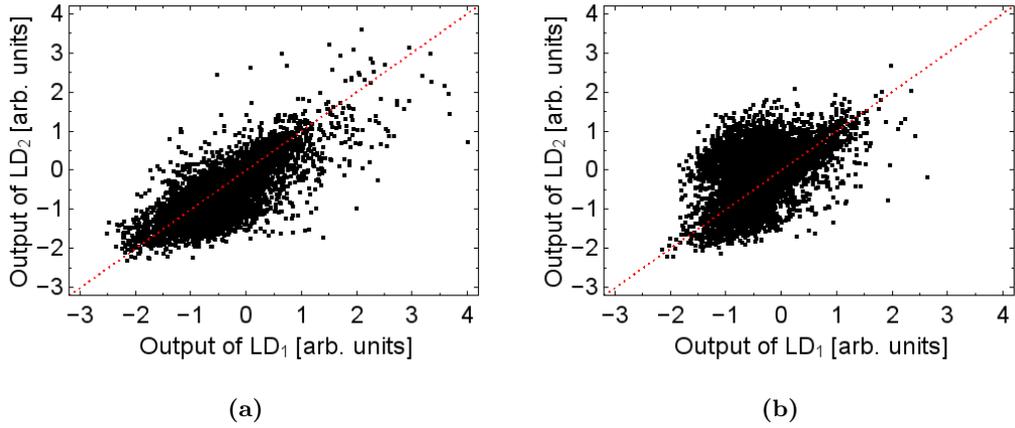
Figure 4.19: Synchronization plots depicting the normalized intensity of LD_1 versus intensity of LD_2 of the time series shown in figure 4.18 for the cases of: (a) dropout without loss of isochronous synchronization (regression coefficient of $\sim$0.57), and (b) dropout with loss of isochronous synchronization (regression coefficient of $\sim$0.18).

Figure 4.19 shows the synchronization plots corresponding to the data depicted in Fig. 4.18. Each figure is composed of 5600 points of the time trace of LD_2 versus the time trace of LD_1. Panel 4.19a corresponds to a dropout where both time traces drop simultaneously, while panel 4.19b corresponds to a dropout with loss of correlation between the time traces during the dropout. The red dotted lines drawn in both panels are guides to the eye that indicate the identical synchronization conditions. We observe that

in panel 4.19a both intensity time traces fall approximately on the diagonal, exhibiting a moderate correlation value ($\sim$0.57). In contrast, the correlation between both intensity time traces in panel 4.19b is much lower ($\sim$0.18).

Different physical mechanisms lead to the synchronous and to the τ-lagged dropouts. We know that two identically synchronized lasers in a symmetric coupling-configuration with relay follow identical dynamical trajectories to that of a equivalent single delayed feedback laser. Therefore, it is reasonable to consider that the isochronous dropouts have been caused by the underlying deterministic chaotic dynamics. In contrast, we cannot determine the origin from those dropouts that occur first at one laser and, one delay time after, at the other laser (they can either have deterministic or stochastic origin). Only a fraction of the power dropouts are associated with a loss of synchronization, and this fraction increases with the injection current as it is illustrated with Figures 4.16 and 4.17. We take profit of identical synchronization together with an event based analysis of the desynchronization events to demonstrate the possibility of determining the deterministic nature of specific events in the dynamics of a semiconductor laser subject to time-delayed optical feedback in the LFF regime [82].

Certainly, a detailed study on this subject goes beyond the scope of this chapter. Further detailed information can be found in the following publication: K. Hicke, X. Porte, and I. Fischer, "Characterizing the deterministic nature of individual power dropouts in semiconductor lasers subject to delayed optical feedback", *Physical Review E*, **88**, 052904 (2013).

The complete picture of desynchronization events in our delay-coupled system implies a further analysis of bubbling for higher injection currents. The low-frequency fluctuations can be observed in our delay-coupled lasers for bias currents up to 14 mA. As we have already shown, in this dynamical regime bubbling mostly occurs during power dropouts. Moreover, the characteristic time of the desynchronization intervals is close to the external cavity delay time τ. The main difference between the three injection currents analyzed in the LFF regime is that the characteristic inter-dropout time interval decreases as the injection current is increased.

For pump currents above 14 mA, in the fully developed coherence collapse regime, we find that the fingerprint of desynchronization events appears much more frequently. Panel 4.20a illustrates that the broadband chaotic dynamics at 15 mA does no longer reflect identifiable dropouts. The conclusion that can be drawn from the careful inspection of those intensity time traces in combination with the intensity difference ΔI depicted in panel 4.20b is that desynchronization events become much more frequent in the coherence collapse regime. Furthermore, the typical duration of such events is also shorter.

Figure 4.21 depicts a closer view to one representative desynchronization event in the coherence collapse regime. We can see that both time traces follow good synchronized behavior until 5.5 ns, when they desynchronize for approximately 3 ns. After this interval they re-synchronize again. This 3 ns desynchronization window is much shorter than the characteristic desynchronization intervals in the LFF regime (of the order of $\tau \simeq 73.1$ns). Furthermore, another particularity of the desynchronization events in coherence collapse
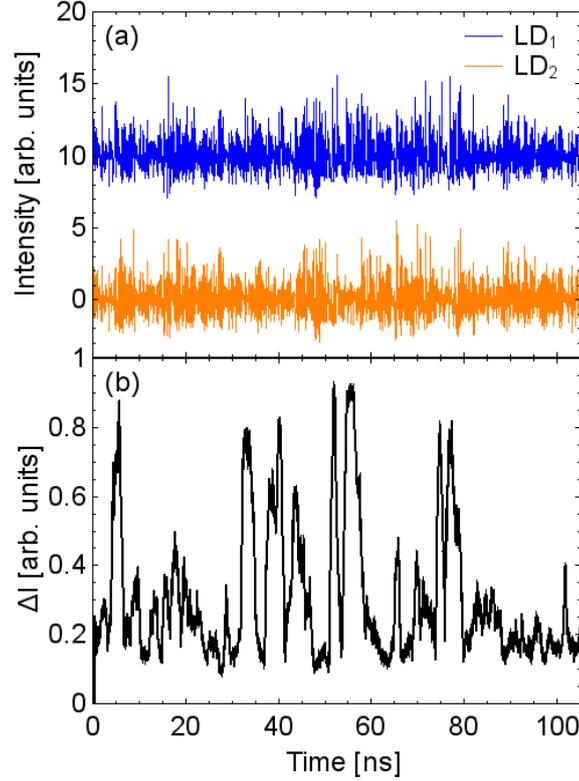
Figure 4.20: (a) Intensity time traces and (b) Integrated intensity difference, ΔI, of LD_1 and LD_2 pumped at $I = 1.27 I_{th}$ (15 mA). Here, Δs has been set to 1 ns, in contrast with the 4 ns used in the LFF regime dynamics. Temperature of LD_1 is 21.37 ° C and temperature of LD_2 is 22.00 ° C.

regime is that their characteristic inter-events time decreases down to sub-ns. These particularities characterize the synchronization in the coherence collapse regime as fast alternations between periods of well synchronized behavior and short desynchronization intervals.

In order to quantify the synchronization robustness as a function of the injection current, we have analyzed the integrated intensity difference ΔI for different injection currents in the zero-detuning scenario. Figure 4.22 depicts the dependence of the probability density function (PDF) of ΔI for different injection currents. For the first three values of the bias current, both lasers exhibit intensity time traces in the LFF regime, while in the latter three currents both lasers operate in the fully developed coherence collapse regime. The distributions for the LFF dynamics cases are peaked with significant heights at low values of ΔI. In contrast, the distributions corresponding to coherence collapse dynamics tend to shift towards higher values of ΔI (which means worse average synchronization) and become broader as the bias current increases. This behavior is complementary to the previously obtained tendency of the cross-correlation coefficient at zero-lag shown Fig. 4.15, where this coefficient decreases monotonously
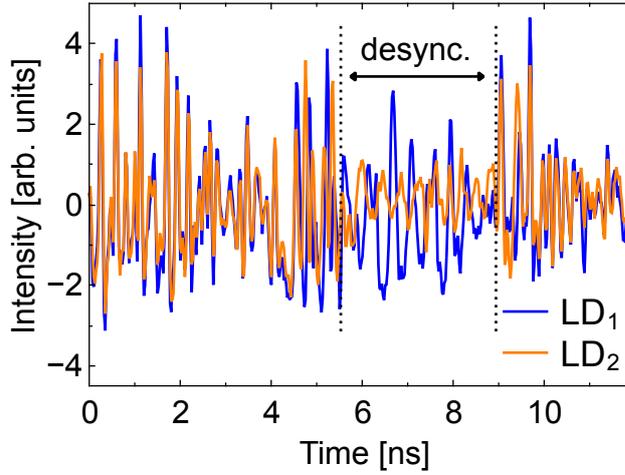
Figure 4.21: Exemplary desynchronization event in coherence collapse. The characteristic desynchronization duration time for this operating conditions is of the order of a few nanoseconds, much shorter than in LFF regime. The injection current is $I = 1.27I_{th}$ (15 mA) and temperatures of LD_1 and LD_2 are 21.37 ° C and 22.00 ° C, respectively.
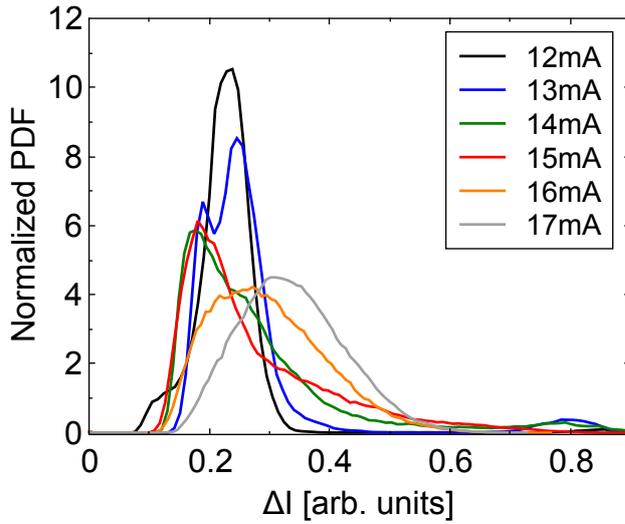
Figure 4.22: Normalized probability density functions of the integrated intensity difference ΔI for the zero-detuning conditions at different bias currents. The time series length used to calculate those histograms is of $20\mu s$.

with the increase of the injection current. Nevertheless, the maxima of the histograms remain in the low side of ΔI for the currents up to 15 mA, meaning that the time the systems are synchronized remains significant.

4.5   Summary and Discussion

In this chapter, different aspects of synchronization between delay-coupled chaotic systems have been studied. Two distinct coupling configurations that involve two SL each are investigated. In both scenarios the SL are coupled via their optical fields. In order to quantify the synchronization, we have mainly used the cross-correlation function (CC) of the intensity time traces of both lasers.

In the first part, an open-loop coupling configuration is used to study the interrelation between the intensity dynamics of a delayed feedback laser and its synchronization to a second laser. The phenomenon of CS in the unidirectional coupling configuration is therefore used to measure the degree of consistency of the delayed feedback laser. We have found that in dependence of the pump current, our experimental dynamics exhibit characteristics of generalized synchronization or of identical synchronization.

We have demonstrated that the cross-correlation values between the delay-coupled response and drive lasers follow a similar dependence than the AC of the delayed feedback drive laser. In particular, it is remarkable the coincidence in the position on the attenuation axis of the maximum nonlinear mixing region for the AC and the CC coefficients. The resulting AC dependences on distinct parameters can be extrapolated to synchronization dependences (strong and weak chaos) in delay-coupled lasers. An interesting aspect of this result is that it has been obtained for non-identical (but very similar) coupled systems, meaning that our approach is valid even if small asymmetries and/or mismatches are present.

Consistency is a key ingredient for the implementation of neuroinspired information processing systems like reservoir computing. Our results in the identical synchronization scenario are directly related to consistency properties and are in good agreement with previous consistency measurements [103]. In addition, we have shown in a time-resolved characterization of the correlations that identical synchronization exists (for short periods of time) even at high feedback strengths, in contrast to what is observed in the averaged cross-correlation coefficients.

In the second experiment, we have investigated the synchronization properties of a system of two delay-coupled SL with a passive relay. The coupling and the feedback originate from the same fiber-loop mirror. We have reported sub-nanosecond chaotic oscillations with isochronously synchronized identical dynamics. We have measured the CC characteristics for two different scenarios. Namely, an asymmetric scenario where both lasers are detuned with respect to each other in their optical frequencies, and a symmetric scenario (with zero-frequency detuning). In the latter scenario, the robustness of the identical synchronization state is studied as a function of the pump current (that is equal for both lasers in every measurement).

In the frequency detuning experiment, both lasers exhibit good synchronization characteristics inside a certain injection-locking region. We have demonstrated that the maximum CC coefficient for detuning values beyond the locking range decays drastically. However, there is an asymmetry for the CC in the limits of the locking range for positive and negative detuning values. This asymmetry could be caused by the way the

emission frequencies are detuned. The procedure in the present experiment is to detune the frequency of only one of the lasers by changing its temperature. As we discuss in detail in appendix A, a change in temperature also causes a modification in the laser threshold current and, consequently, influences the emission power of the detuned laser. In principle, a change in the emission frequency of the detuned laser where the power would be maintained could avoid this asymmetry in the locking range, i.e., every change in temperature at the detuned laser should be followed by a change in the injection current to maintain the power unchanged. Thus, to prove this ideas will require further detailed investigations.

In the zero-frequency detuning experiment, the evolution of the zero-lag CC coefficient is studied with respect to the injection current. For low injection currents, the CC coefficient is very high, indicating high quality of the identical synchronization state in the LFF dynamics. A time-resolved analysis of the synchronization at low injection currents reveals the simultaneity between desynchronization events and power dropouts (in the LFF regime). Interestingly, only a fraction of the power dropouts are associated with a loss of synchronization, and this fraction increases with the injection current. We know that two identically synchronized lasers in a symmetric coupling-configuration with relay follow identical dynamical trajectories to that of a equivalent single delayed feedback laser. We take profit of this fact together with the individualized analysis of the desynchronization events to demonstrate the possibility of determining the deterministic nature of specific events in the dynamics of a semiconductor laser subject to time-delayed optical feedback [82]. Specifically, we study on an individual event basis the power dropouts in the LFF regime, identifying an upper fraction of those events that likely have deterministic origin (and this fraction decreases with the injection current).

The dependence of the zero-lag CC coefficient with respect to the injection current is studied. We have observed a decrease of this coefficient for increasing values of the injection current (see Fig. 4.15). An accurate analysis of the robustness of the synchronization has given us a possible explanation for this behavior. We have observed how desynchronization events can be observed during power dropouts in the LFF dynamics. However, when the injection current is increased, the dynamics of the coupled system evolves towards the coherence collapse regime. This significant transition of the dynamical behavior occurs between the currents of 14 mA and 15 mA, but it is not clearly reflected in the maxima of the CC at zero-lag. The temporal characteristic structure of the LFF regime can no longer be identified beyond 14 mA, and the desynchronization events become more frequent in time (even though shorter in duration) as it is depicted in Fig. 4.20. Here, the plot of the average desynchronization depicted in Fig. 4.22 presents complementary behavior with respect to the CC, i.e., when the CC at zero-lag increases, the mean average desynchronization decreases and vice versa (see Fig. 4.22 and Fig. 4.15). In our high-coupling strengths scenario, we relate the overall synchronization quality with the occurrence of desynchronization events attributed to the bubbling phenomenon [153]. The noise-induced instability differentiate bubbling from other well known sources of desynchronization caused by the loss of stability of the chaotic attractor itself [151]. Examples are the transverse instability occurring for

rather small coupling strengths or the scenario of blow-out bifurcations, present when there is a mismatch in parameters [149, 154].

The characterization of bubbling in the mutually delay-coupled system is not complete. It would be interesting to more accurately study the nature of bubbling in the coherence collapse regime. The influence of frequency detuning on the robustness of synchronization is also an open question. Furthermore, the characterization of synchronization robustness under zero-detuning conditions is essential to find the optimal conditions for chaos communications. If two coupled lasers are modulated in current, the synchronization between both lasers can be momentarily lost either due to power differences in the modulation or by noise-induced instabilities. The study of the noise-induced losses is fundamental because they might lead to a significant increase of the BER, if the protocol does not take them into account. The results presented in this chapter suggest that there is no dynamical regime that totally avoids bubbling and, consequently, bubbling is a problem inherent to delay-coupled systems in the presence of a passive relay. Moreover, the occurrence of bubbling events cannot be predicted because it is a noise-induced phenomenon. This has direct implications in chaos communications systems that rely on identical chaos synchronization, that must implement communication protocols robust against bubbling. This point will be discussed in detail in chapter 5.

Further investigations on the setup of two mutually-coupled semiconductor lasers with a passive relay could focus on different aspects of the setup. For example, the variation of the ratio between the mutually-coupling and the self-coupling strengths or the study of the effects of a mismatch between the delay times for both lasers. These variations have already been studied from numerical and analytical points of view [149, 154]. These works showed interesting behaviors like the suppression of coupling-induced instabilities for small delay mismatches away from simple commensurate ratios [152, 154], or the increase of bubbling under coupling mismatch conditions.

Chapter 5

Bidirectional Secure Key Exchange using Chaotic Semiconductor Lasers

5.1 Introduction

Privacy and security of communications is a fundamental topic of everyday importance in, e.g., digital money transactions or personal identifications on the Internet (see section 1.1 for a more extended discussion). Nowadays, privacy of communications is mainly guaranteed via software-based cryptography [40]. Two different approaches roughly divide the software-based cryptosystems in *symmetric* and *asymmetric* cryptociphers.

In the category of symmetric cryptociphers we can find those systems that use the same key for ciphering and for deciphering a message. An example of this approach is the one-time pad first proposed by Gilbert Vernam [155] and demonstrated to be absolutely secure by Claude E. Shannon [156]. In essence, this kind of systems can be thought of as a safe in which the message is locked by Alice[1] with a key. In a correct implementation, the key must be at least as long as the message itself. A copy of this key is used by Bob to unlock the safe and recover the message. Thus, it is essential for Alice and Bob to possess the common secret key. This key must be shared in some way, which is actually the weakness of this approach.

The other cryptosystem paradigm, the public-key cryptography, comes in to solve the problem of key sharing. This approach is mainly based on asymmetric algorithmic procedures for ciphering and deciphering the messages [157]. When it was first proposed by Diffie and Hellman in 1976, it represented a radical break with any other previous cryptosystem [40]. The reason is that instead of trying to maintain the key in secrecy, this approach suggested to publicly share the encrypting information. The asymmetry of the process originates from the decryption side.

---

[1]We use here the names *Alice* and *Bob* for the sender and the receiver, respectively. These names are commonly used in literature. Similarly, we name *Eve* to the hypothetical eavesdropping adversary.

Figure 5.1: Scheme of Public-Key Exchange Cryptosystem.

The basic scheme for such cryptosystems is represented in Figure 5.1. We illustrate the algorithm with the example of Alice to send Bob a message:

1. Alice generates a public-key and store it in a trusted public server (*Certification Authority*). Actually, all the users of this communications system must independently generate their own public-keys and store them in the trusted public server.

2. They also generate a corresponding private-key that, as its name indicates, is not shared.

3. Alice takes Bob's public-key, encrypts the message with it, and sends the message to Bob.

4. Bob receives the message (encrypted with Bob's public-key) and decrypts it with his own private-key.

The use of two distinct keys for encryption and decryption defines this cryptosystem. In a simplistic approximation, this system can be thought of as a mailbox (one for each user) in which anybody can insert a letter. But only the legitimate owner of the mailbox can recover the stored letters, because only he or she has the key needed to open the mailbox. The crucial idea is that it must be (computationally) easy to encrypt a message with the public-keys, but very difficult to decrypt the ciphered message without the knowledge of the private-key.

Beyond the concept, the implementation of such cryptosystem requires two additional elements, namely a mathematical object that fulfills the explained asymmetric ciphering and a trustful infrastructure that can take care of the public-keys management.

In any secure communication, the users need to know the public-keys of their counterparts in order to cipher the messages with them. If the exchange of public-keys is done in private, an eavesdropper (Eve) could perfectly intercept the public-key and exchange it for one created by herself. Then, she could easily decrypt all eavesdropped communications with her own private-key. This is the reason why *Certification Authorities* are needed. These authorities verify that the public-key do indeed correspond to their legitimate users. If the users trust the certification authority, they can obtain from it the other user's public-keys and cipher their messages with them.

The first public-key exchange implementation with appropriate mathematical functions was developed at the Massachusetts Institute of Technology in 1978. It is named *RSA* after its creators (Ravi, Shamir, and Adleman), and it remains widely used today [41]. The reason why this software-based cryptosystem is still considered safe is

related to the *mathematical complexity* to break it. It uses mathematical objects called one-way functions, i.e., it is very easy to encrypt the message with the public-key, but fundamentally difficult to decrypt it without the corresponding private-key.

The security of the RSA algorithm relies on the computational difficulty to decompose very large numbers into its prime factors. In essence, the private-key of Alice (or Bob) consists of two prime numbers that can only be found by factoring its product, i.e., the public-key. The "security rule" is actually quite simple, the bigger the number used as public key, the more secure the communications are because it requires more time to find out the prime numbers that compose it. The best known algorithms associated with the prime numbers factorization face a complexity that grows exponentially with the size of the integer number to factorize.

In general, for a given key length, symmetrical systems are more secure than their asymmetrical counterparts. The symmetric one-time pad approach is the only secure (at least according to Shannon's information theory) software-based cryptosystem known today. Its obvious main problem resides in secretly sharing the symmetric key. In practical implementations, asymmetrical algorithms are used not so much for encryption (mostly because of their low data rates, not because of their security), but rather for distribution of session keys for symmetrical cryptosystems such as AES (the NIST ciphering standard) [157]. Therefore, public-key cryptosystems are convenient and have thus become very popular over the last 20 years. The security of the communications on the Internet, for example, is largely based on such systems.

However, this cryptosystem suffers from a major flaw, it has not been possible yet to prove whether factorization is fundamentally difficult or not. A change in the complexity of factoring big numbers could undermine the security of public-key cryptosystems and, in consequence, of the most popular actual telecommunications systems. This threat could come either from the world of mathematics in the form of some advanced factorization algorithm or from the world of physics in the form of, e.g., quantum computers [42,158]. Some of the tasks that quantum computers could do with unprecedented efficiency include factoring giant numbers and high-speed searching in large lists. These properties are of fundamental importance for the (lack of) security of the respective state-of-the-art asymmetric and symmetric algorithmic cryptosystems. Therefore, an enhancement of nowadays algorithmic security schemes is highly desirable. In this respect, hardware-based cryptosystems, based on the physical layer of communications, represent an attractive option.

Remarkably, a possible solution to the threat of a quantum computer could come from the quantum world too. Quantum-key distribution is a powerful approach to achieve an absolutely secure cryptosystem [159].

The original (and still very powerful) concept of quantum-key distribution is based on a symmetrical one-time pad protocol [160]. The two counterparts, Alice and Bob, use a quantum channel to transmit a random sequence of quantum bits (also referred as *qbits*) that conform the key. Actually, in most implementations what Alice sends to Bob are individual photons with random polarization states. Bob has a set of two possible bases to measure the polarization state of the photons. He selects one base at random

for each photon and performs the measurement. There exists a degree of uncertainty in those photons measured with the wrong base, consequently Alice and Bob discuss publicly which photons were correctly measured. This represents no drawback from the security perspective because the values of the correctly measured photons are not unveiled. The photons that have been incorrectly measured are discarded from the key. Once the key is built up, the information of the full message is classically encrypted with this key as a one-time pad. It is important to mention that the information carriers are quantum, not the communication channel, that can either be free space or optical fibers.

The strength of quantum cryptography resides in the foundations of Quantum Physics, in particular the axiom stating that measurements in quantum mechanics perturb the system. In other words, by physical principle, Eve cannot take any information from the system without introducing perturbations to the measured states that would reveal her presence[2]. Alice and Bob can check whether there has been eavesdropping on their one-time pad by testing a few of the digits that conform the key. In half of those situations, the qbits intercepted by Eve will be discovered to be uncorrelated from Alice and Bob's.

The possibility to determine if there is eavesdropping in the channel is what confers to quantum cryptography an unprecedented level of security. However, more than three decades after its first conception, it still remains a very challenging technique that requires further development in quantum optics to be competitive at telecommunications standards. Noise and attenuation in the quantum channel are the most significant factors that reduce its efficiency and limit its range and secure-data rate.

Classical Key Distribution Schemes

In the last decade, there have been proposed a number of classical encrypted-key distribution systems that complement the quantum approach as alternatives to the software-based cryptosystems [139, 164–168]. In these classical systems, some physical parameter is randomly modulated by the counterparts to generate a number of possible states. Some of the combinations are ideally non-detectable by eavesdroppers and, consequently, can be used to build the key. The generated key is then used to cipher the messages between the two counterparts.

These systems base their secrecy on the impossibility to fully extract certain physical quantities. Despite of the obvious disadvantage that these systems cannot easily quantify their level of secrecy, unlike the in principle absolutely secure quantum cryptosystems, they present the advantage of an easier implementation mostly based on state-of-the-art optical or electrical telecommunications components. Classical systems present other advantages in front of their quantum counterpart like larger tolerances to noise and longer reachable distances between the two communication partners (Alice and Bob).

The description of some significant examples will be useful to illustrate the state-of-the-art of classical key-distribution systems. Kish [164] proposed a scheme based on the

---

[2]Although the security of the operating principle of quantum-key distribution is assured by the laws of physics, its practical implementations may present loopholes as it has been found in the recent past [161–163].

use of Johnson-noise between electrical resistors to publicly exchange an encrypted key. The physical quantity that defines the state of the channel is the mean-square voltage noise (or current noise amplitude). This system has been demonstrated in a 2000 km range at a bit rate of 0.1 bit/s and with a 99.98 fidelity[3] of the resulting key [169]. Another system, proposed by Scheuer and Yariv [165] considered the possibility to build a private key from the selection of the frequency-dependent mirrors at both ends of an ultralong fiber-laser cavity. This scheme has demonstrated ranges exceeding 200km with potential key establishing rates of hundreds bits per second and fidelities for the generated keys of 99.4% (see e.g. [170–172]). Another photonics-based cryptosystem was proposed by Yoshimura and coauthors [167]. This scheme is based on correlated physical randomness between commonly driven remote optical scramblers. The authors demonstrated the possibility to exchange an encrypted key at a rate of 128 kbit/s through a 120 km optical fiber link. Finally, Kanter, Kopelowitz and Kinzel proposed a scheme based on the phenomenon of chaos synchronization between two bidirectionally-coupled systems [166]. The public-exchange of a key required the use of private commutative filters and the addition of extra nonlinear transformations to the exchanged signals. The complexity of the procedure is rewarded from the security perspective because it maps the task of a passive eavesdropper onto an NP-complete problem, Hilbert's tenth problem.

5.1.1 Chapter Outline

In this chapter we present a cryptosystem based on the symmetric exchange of a secret key between two partners. Our classical key exchange protocol is based on identical chaos synchronization. The key is built up from the synchronized bits occurring between two current-modulated bidirectionally-coupled SL with self-feedback.

The experimental methods particular to this experiment are presented in section 5.2. The protocol followed to generate the secret key is presented in section 5.3.1. The setup used in this experiment is in essence identical to the setup presented in section 4.2, however, in this experiment we have included slight modifications that are detailed in section 5.3.2. The performance of the key exchange protocol is demonstrated in section 5.3.3. Finally, the security and the advantages and limitations of our approach in comparison with the other classical key distribution schemes are extensively discussed in section 5.4.

5.1.2 Contributions to the Work in the Present Chapter

This chapter presents the experimental implementation of a scheme first proposed (and demonstrated numerically) by Vicente, Mirasso and Fischer in [139]. Interestingly, the development of an experimental implementation has faced some exciting and unexpected challenges studied in the time lapse between the original publication and our present results.

---

[3]In this context, fidelity is defined as 1 minus the bit error ratio.

The experiment has been realized by me in collaboration with D. Brunner and M. C. Soriano. In addition, D. Brunner has designed the custom mounts for the laser diodes and has contributed to the setup design and precise delay times measurements. M. C. Soriano and I. Fischer contributed to the original design of the experimental setup and to the characteristics of the modulated bits sequences. D. B., M. C. S. and I. F. have been involved in the improvement of the experiment and in the discussion of the results.

5.2   Experimental Methods

The lasers used in this chapter are discrete-mode (DM) lasers. These laser devices and their characteristics have already been described in section 2.2 and in appendix A. The devices employed in synchronization experiments present the particularity that they have been hand-picked from a set of similar lasers that were originally manufactured on the same semiconductor wafer. This selection process has the intention of using devices with the most similar possible properties for the synchronization experiments (see appendix A). The properties analyzed to determine the similarity between lasers are the threshold current, emission frequency, external differential quantum efficiency, and wavelength-temperature dependence. In particular, the respective threshold currents at zero-frequency detuning conditions are $I_{\text{th}}^{LD_1} = 11.98 \pm 0.01$ mA and $I_{\text{th}}^{LD_2} = 11.83 \pm 0.01$ mA.

It is important to note that there is a difference between the mountings of the devices used in this experiment and those used in chapter 4. We have used devices sub-mounted in packages that will allow us to modulate the DM lasers up to GHz modulation frequencies. Instead of the *butterfly packaged* DM lasers that were used previously, we use *TO-canned* (TO-56 package) DM lasers. The modulation bandwidth allowed by the TO-56 are in the multi-GHz range, meanwhile for the butterfly packaged lasers the 3 dB modulation cut-off is at 400 MHz.

We have designed a custom printed circuit board (PCB) to mount the TO-56 packaged lasers. The role of the PCB is to precisely connect the laser to the external biasing. The output pins of the TO-56 laser package are soldered to the PCB that has an SMA connector directly attached to its output. The SMA output is therefore connected to a bias-tee that couples the DC and the AC biasing contributions. Given that this experiment relies on the direct bias modulation of the lasers, it is required to characterize their response for different modulation frequencies. This characterization will give us the frequency dependence of the combination of Bias-tee, PCB and laser mount.

The modulation response of the two devices used in this experiment is plotted in Figure 5.2. The different curves represent the amplitude of the response at different bias currents. The applied AC modulation has fixed amplitude and a scanning-frequency step of 100 MHz.

Both panels present some important common characteristics. Two regions can be distinguished in the modulation responses of both lasers, i.e., below and above 1 GHz. Below 1 GHz, all curves monotonously decrease in amplitude together. The bandwidth
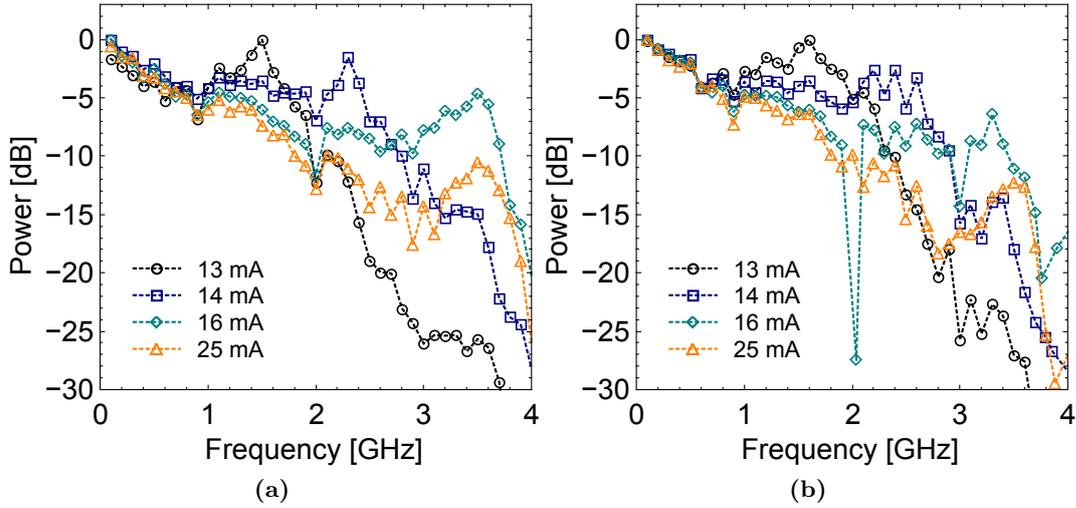
Figure 5.2: Amplitude response to direct bias-current modulation of the TO-56 packaged lasers versus modulation frequency. Panels (a) and (b) respectively depict LD_1 and LD_2, where each laser corresponds to a different communication partner. The different curves in both panels illustrate different laser bias currents. The TO-56 packaged laser diodes are mounted on a custom-designed PCB board and connected to the signal generator through a bias-tee. For modulation, fixed amplitude harmonic signals have been scanned in frequency.

in our experiment arrives up to 500 MHz (maximum data-rate of 1 Gbit/s). Within this frequency region, the amplitude response decreases less than 2.3 dB (0.92 dB are unavoidably caused by the bias tee), therefore representing good operating conditions.

Above 1 GHz, the curves at different bias currents experience different and more ir-regular responses. There even exist some strongly deviating points. Among the different factors that contribute to the difference between these curves, the relaxation oscillation frequencies are the most important one. The characteristic frequency of the relaxation oscillations of these lasers increases proportional to the square root of the bias current respect to threshold, i.e., $\propto \sqrt{I - I_{\text{th}}}$. The bandwidth increase effect caused by larger relaxation oscillations is visible in the response peaks of the bias current curves. How-ever, the presence of standing wave effects (induced by e.g. spurious capacitances) may cause undesired drops in the amplitude response curves. This is an important effect to be considered in modulation schemes that utilize multiple frequencies above 1 GHz.

5.3 Encrypted-Key Distribution Scheme

We implement in experiment a private communications scheme that harnesses the phe-nomenon of identical chaos synchronization between two SL. The lasers are delay-coupled via a semitransparent mirror (see scheme in Figure 4.2). In our scheme, the binary infor-mation is bidirectionally exchanged between both lasers through the common communi-cation channel with delay. The bits sequences are continuously injected into each laser

unit via small AC modulation of its bias current. Since the amplitude of the messages is kept small, the modulation information is hidden within the chaotic carrier (as in the chaos encryption schemes [52–54]). Two combinations of the bits, that leave the identical synchronization state unperturbed, cannot be distinguished from the synchronization error and can be used to publicly negotiate a secure key [173,174]. The scheme is secure as long as only the two communications partners are able to extract the information encoded in the key.

5.3.1   Simultaneous Bidirectional Key Exchange Protocol

In the system we study, the two lasers are identically synchronized in the absence of modulation. Both lasers are then modulated with independent pseudo-random bit sequences. For the scheme to work, the relative *modulation states* in every clock-cycle must determine whether the lasers remain in the identical synchronization state or not. If the bit injected into the two lasers do not coincide (modulation states {-1, 1} and {1, -1}) there will occur a modulation-induced loss of synchronization. In contrast, when the bits do coincide (modulation states {-1, -1} and {1, 1}), the synchronization state is unperturbed. To sum up, at least half of the possible combinations will induce loss of synchronization, meanwhile the rest will not.

In principle, the bits are masked in the chaotic waveform, i.e., the modulation should not be distinguishable from the chaotic waveform[4]. In some instances, the sign of each partner's bits could be guessed from the powers difference if both lasers have been modulated with different states. On the contrary, for identically modulated bits, an eavesdropper cannot identify the relative modulations from the powers difference because it remains zero (the synchronization state has not been perturbed). In consequence, the secure key can be publicly negotiated from the synchronized bits. The combination of both pseudo-random bit sequences will result in identical modulation states half of the times. Therefore, this protocol allows the public exchange of an encrypted key at rates up to half the modulation bit rate, e.g., for our experimental implementation up to 500 Mbit/s (1 Gbit/s pseudo-random bit sequences).

5.3.2   Particularities of the Experimental Setup

Public-key exchange using mutually coupled SL was first proposed in [139]. In the referred work, the feasibility of the protocol was numerically demonstrated. The authors used a rate-equations approach to simulate the mutually coupled SL and evaluate the security of the scheme. However, a number of degrees of freedom like the coupling phases or the spontaneous emission (one of the most prominent noise sources in SL), were simplified or not taken into account in the original reference. In contrast, an experimental implementation of this scheme cannot simply ignore these issues, but must evaluate their impact and even find solutions for some of them. In this section, the adaptations to the scheme and the experimental setup will be explained.

---

[4]In section 5.4 we will explain how this requirement can be relaxed in practical implementations and still be able to reach a sufficient level of security.

Figure 5.3 depicts the setup that we have used in this experiment. It is conceptually identical to the one explained for the bidirectional coupling experiment in chapter 4. However, two modifications have been included here with respect to the one presented in the previous chapter: the use of polarization maintaining (PM) fiber components and the introduction of a length mismatch between the two coupling paths.
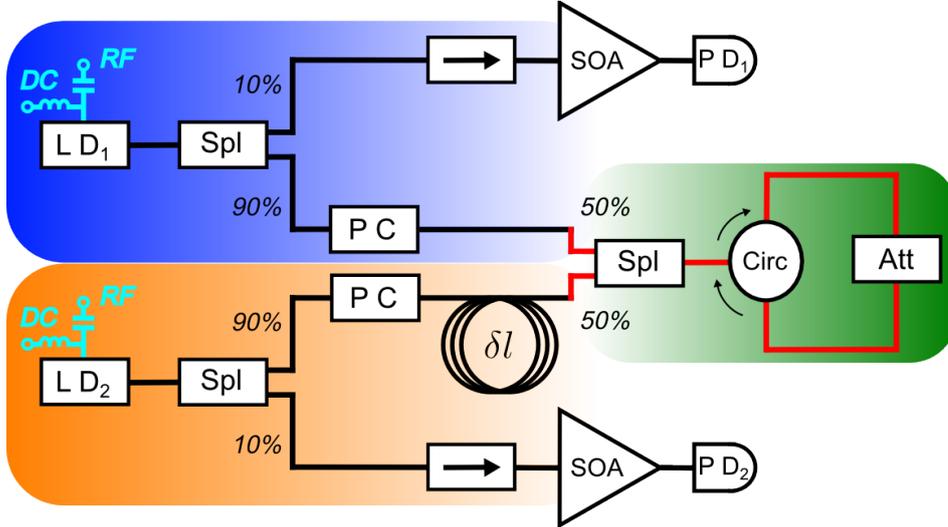
Figure 5.3: Scheme of the experimental setup for the SKE experiment. LD_1 and LD_2: laser diodes, Circ: optical circulator, PC: polarization controller; Att: variable optical attenuator, δl: fiber extension (2 meters), Spl: one by two intensity splitter with indicated intensity splitting ratios, $\rightarrow$: optical isolator, SOA: semiconductor optical amplifier, and PD: photodiode. Both lasers are biased through a bias tee with separated DC and RF ports. The red lines in the coupling path represent components with polarization maintaining fiber connections.

In this particular coupling configuration, the semitransparent mirror is not equidistantly placed between both lasers. Indeed, one of the coupling paths has a fiber extension of length δl. We have intentionally included this difference between the coupling paths because it introduces two important advantages. First, the counter-propagating beams arriving at both lasers from the coupling mirror do not interfere coherently. In consequence, possible interferometric effects in the coupled cavity are avoided [175]. These effects, when not controlled, cause variations of the relative coupling phases with consequent presence of periods of destructive interference. This phenomenon results in slow time-scale oscillations of the synchronization quality that could cause high loss of synchronized bits in our public-key exchange protocol. Such phenomenon is not dramatic in well-controlled laboratory conditions, but it is a dramatic nuisance if one desires to implement this scheme in a real technological platform. The scenario with asymmetric coupling delays has a second and more pragmatic advantage, it relaxes the requirements for practical implementations of our SKE scheme. In fact, for asymmetric positioning of the mirror, identical synchronization occurs with a temporal offset given by the difference of the corresponding delay times, $\Delta\tau = \tau_{c_2} - \tau_{c_1}$.

As long as any other detuning in parameters is kept small enough, the stability and
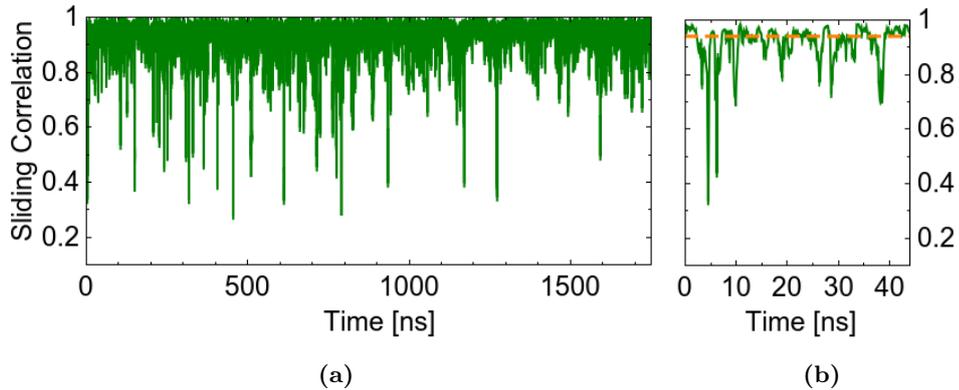
Figure 5.4: (a) Long-term quality of the identical synchronization state in the scenario where the relay is asymmetrically placed. The depicted data corresponds to the sliding cross-correlation in a window of 1.75 μs. The details on its calculation can be found in section 4.3. The bias current is $I = 1.01I_{\text{th}}$. Panel (b) focuses on the time window of the first 40 ns. The dashed horizontal line has been plotted only as a guide to the eye, it indicates a sliding correlation value of 0.95.

overall quality of the identical synchronization state are not affected by the distance between the coupled lasers or by the relative positioning of the mirror [154]. Figure 5.4 illustrates the quality and stability of the identical synchronization state with two intervals of the same sliding cross-correlation time series. The sliding cross-correlation coefficient at the corresponding $\Delta\tau$ is most of the time beyond 0.9 (the time-averaged cross-correlation is 0.949), with sporadic drops to values below 0.8. The persistent high values of the sliding cross-correlation coefficient are better resolved in the magnified time window of Fig. 5.4b. A detailed view of the synchronized dynamics and of the characteristic desynchronization events is shown in Figure 5.5.

The desynchronization events identifiable in Fig. 5.5b can either be induced by short periods of destructive interference between the coupling phases [149] or by attractor bubbling[5]. These effects were not considered in the original numerical demonstration of the scheme [139]. However, even if our coupled system experiences desynchronization events unrelated to the key-exchange protocol itself, but to the mentioned dynamical effects (or even to hypothetical communication disruptions), the generation of a secure-key is still possible. The reason is that Alice and Bob maintain only those states that result in synchronized bits, therefore the only effect of these unpredictable desynchronization events will be that of reducing the rate at which the key is generated. This point is of major importance for the robustness of our public-key exchange protocol.

An additional particularity of this setup resides in the elements that compose the coupling loop. Those elements, represented with red connections, are polarization maintaining (PM) fiber components. The use of PM fiber components in the coupling path facilitates the alignment of the polarizations of the different fields that propagate in the

---

[5]Attractor bubbling phenomenon has already been introduced and extensively characterized in section 4.4.3.
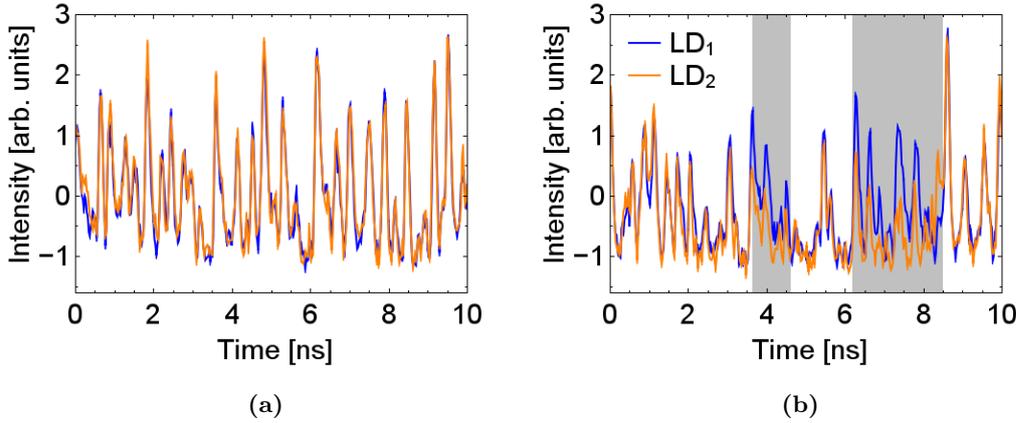
Figure 5.5: Two exemplary intervals of the same time series. The experimental conditions are identical to those of Figure 5.4. Panel (a) shows a window with no desynchronization events. Panel (b) depicts two examples of the characteristic desynchronization events present under this experimental conditions.

coupling cavity. For this purpose, both polarization controllers (PC) are tuned such that the linear polarization state of the field emerging from each laser diode is coupled as a linear polarization state to the 3 dB coupler before the fiber loop mirror. The reason is that this coupler is a fast axis blocked PM component, what allows us to align both incoming fields to the same linear polarization state. The reverse linear-to-linear transformation (when the light propagates back from the 3 dB coupler to the lasers) is automatically fulfilled.

Here again, the control of the polarizations alignment is a perfectly feasible task in laboratory conditions for all the fiber setups presented in this thesis. However, field implementations may suffer of variable environmental conditions and, in consequence, of variations of the polarization state of light. In this sense, the use of PM fibers to build up the fiber-loop mirror has an additional advantage compared to conventional fibers. The power after the coupler (that is a fast axis blocked component) could be monitored by a feedback control loop to compensate for polarization misalignments. Obviously, this implies the substitution of some elements: the 3 dB coupler before the fiber-loop mirror must be a 2-by-2 component (one of the outputs would be used to monitor the average output power) and the polarization controllers should be substituted by electrically tunable ones. These substitutions would have no other impacts on the performance of the setup.

5.3.3 Proof of Concept

Now, we demonstrate experimentally our key exchange scheme. The mutual coupling path among the lasers is the channel used to bidirectionally communicate the bit sequences. The information is encoded by simultaneous modulation of the bias currents of LD_1 and LD_2 at 1 Gbit/s. The modulation consists of two independent pseudo-random

bit sequences of 6000 bits each.

For the correct implementation of our key exchange scheme, the modulations that we apply to both lasers must be properly time shifted. The reason is that both lasers receive the delayed feedback and coupling signals with a mismatch $\Delta\tau$, and they are identically synchronized with this time offset. A time mismatch between the modulations and $\Delta\tau$ will create systematic losses of detection samples from every bit. In consequence, both lasers must receive their modulation signals with a clock skewed by $\Delta\tau$. However, the solution to this problem is nontrivial because this time shift cannot be obtained simply from the detected time traces. The traces depicted on the oscilloscope combine $\Delta\tau$ with other time differences originated in the modulation and detection paths.
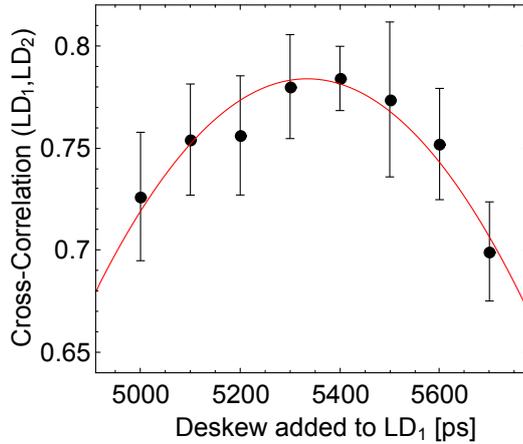
Figure 5.6: Modulation skew measurement using a correlation method. The dots represent the averaged maximum cross-correlation coefficients for different time shifts of the modulations. The red dotted curve is a Gaussian fit to the experimental points.

We have developed a simple method by which we obtain the optimum time shift that synchronizes the clock of the modulation signals to the coupling-delay mismatch. The process consists in modulating the two SL with the same modulation. This modulation sequence is a pseudo-random binary sequence in order to avoid any periodicity. Then, both sequences are relatively skewed until the conditions that maximize their intensities cross-correlation are found. The two copies of the pseudo-random bit sequence will synchronize their arrival to each laser only when their relative time shift is exactly $\Delta\tau$. The cross-correlation between the two lasers decreases otherwise. In particular, we skew one modulation sequence in steps of 100 ps and extract the maximum cross-correlation coefficient. The results of such scan are depicted in Figure 5.6. The values that have been plotted represent only the set of points that are already close to the expected value. Each point is the average of 10 independent measurements and the error bars represent their respective standard deviations. The red curve is a fit of the calculated points that indicates an optimal time shift of 5.35 ns. With this procedure we can fine tune the modulation clock between both lasers, avoiding the systematic loss of a fraction of every bit.

Figure 5.7 illustrates the message decryption process. Figures 5.7a and 5.7b depict two portions of the transmitted messages, that consist in non-return to zero pseudo-random binary sequences. The modulated bits are either 1 or -1, that are conceptually equivalent to modulation with 1 and 0. However, {-1, 1} represents a modulation with zero-mean, which is important in experiments to avoid possible high-pass filtering effects for long chains of bits. The difference between the transmitted messages is plotted in Fig. 5.7c. The appropriate lag $\Delta\tau$ has been added to $m_2(t)$, as previously discussed in this section. Figure 5.7d depicts the reproduction of the messages difference via the subtraction of both SL powers.
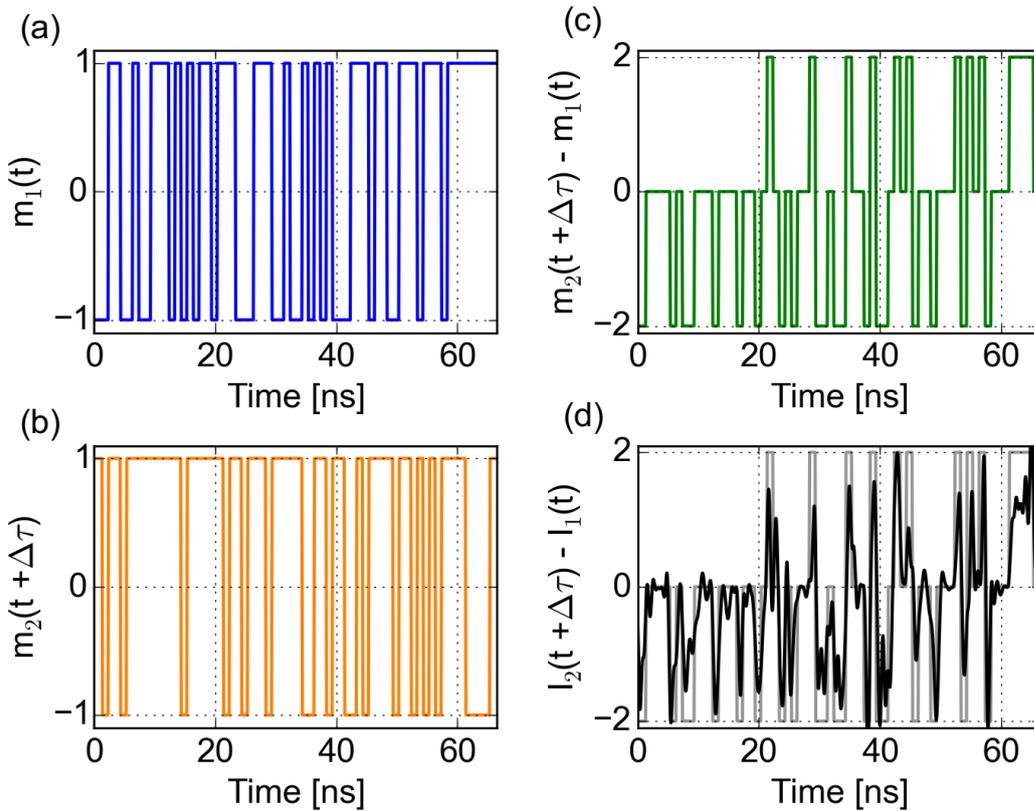
Figure 5.7: secure-key exchange proof of concept. Panels (a) and (b) illustrate the original encoded bit sequence (modulation difference). Panel (c) represents the subtraction of the messages after the appropriate time lag has been compensated for. In panel (d), the modulation difference (gray line) is reproduced by the difference in lasers' powers (black line). The modulation amplitude is $0.08 I_{th}$. The difference in powers has been filtered with a cutoff frequency of 1.2 GHz.

Figure 5.7d is the most fundamental plot to understand our key exchange protocol. We can observe that the combinations of differently modulated bits induce loss of synchronization. In these cases, the sign of the individual bits can be extracted from the power difference. Only those bits that have a modulation difference of zero do not perturb the identically synchronized state. Therefore, the modulations that result in a

zero bit difference can be used to negotiate the secure key.

5.4   Security Analysis of Our Scheme

In every communications system that claims to guarantee privacy of communications, the level of security must be analyzed. Our scheme proposes the exchange of an encrypted key via a fiber optical channel. Fiber-based systems present a number of advantages that facilitate the long-range communications between the partners. However, an eavesdropper may also find eases for tapping the partners' communications. In particular, Eve can split the coupling channel and subtract a fraction of the light coming from each side. We have shown that when both lasers are encoded with the same bit and the intensity differences due to modulation are sufficiently small, Eve cannot extract information on which are the bits that have been sent. In consequence, both partners can agree to discard the bits that are different from each other and keep only the mutually synchronized ones.

For the encryption to be sufficiently strong, it should not be possible to extract information on the bit sign from the time series. From the information theoretical point of view, this is assured if Eve has a probability of 0.5 to correctly guess each bit. In fact, this is the value of probability related with no information leak from the modulated bits.

The key generated in our protocol is encrypted through chaos masking. The effect of the current modulation on the output intensity is small as compared to the amplitude of the chaotic oscillations. Unfortunately, this scheme suffers from a drawback, at least when implemented in experiments. Our key-exchange protocol is meaningful only when the lasers are pulled out of synchronization by means of modulation. In this sense, the modulation amplitude cannot be arbitrarily small, it has a lower boundary. However, as soon as the modulation amplitude is enough to pull the lasers out of synchronization, a fraction of the bits are also statistically identifiable. The amplitude of each bit is still masked inside the chaotic fluctuations, but the sign of the bits (whether the bit is -1 or 1) is partly identifiable from the integral of the bit intensity[6]. Indeed, the concealment of the key decreases gradually with the increase of the modulation amplitude.

Figure 5.8 illustrates with experimental data the information that can be extracted from statistical analysis of the bits. The histograms of the bits integrals (a total of 3000 bits per histogram) are plotted for LD_1 (Fig. 5.8a) and LD_2 (Fig. 5.8b). The integrals of the intensity are evaluated for time windows corresponding to the bit length (in our experiment the duration of each bit is 1 ns). It can be seen that the maxima of the two histograms (in both panels) are clearly separated. If this effect is not compensated for, there exists an information leakage from the individual bits that compromises the encryption of the key. Here, we follow a similar reasoning to when the ideal level of security was discussed. If the histograms corresponding to the bits -1 and 1 would fully overlap, no information could be extracted from the individual bits. The probability for

---

[6]Here, we assume that Eve is able to synchronize her clock with the partners' clock, and consequently extract the maximum amount of statistics from each modulated bit with a matching laser. Of course, this represents a worst-case scenario.

a given bit to be a -1 would be the same than the contrary. Therefore, Eve could extract no information at all from the individual bits amplitude, neither from their integrals.
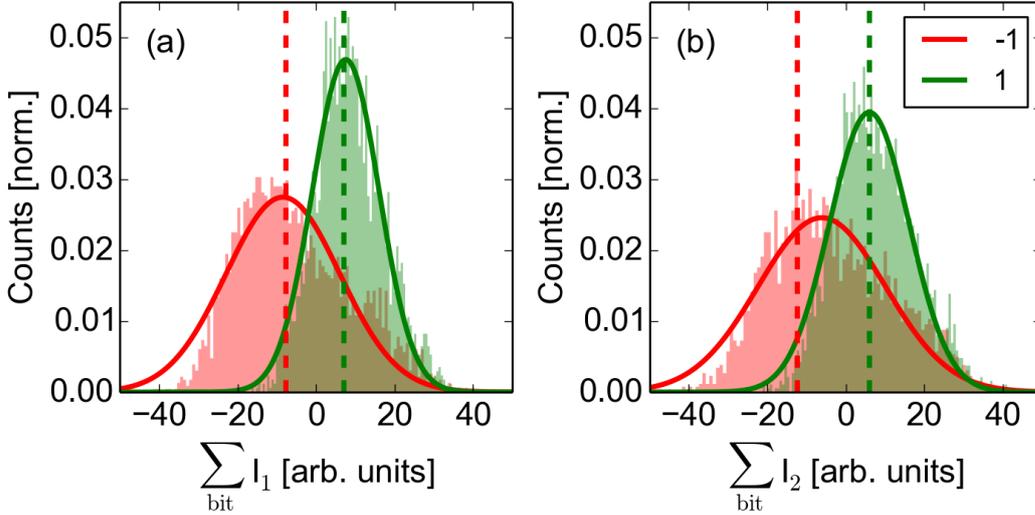
Figure 5.8: Histograms showing the integrals of the modulated bits for (a) LD_1 and (b) LD_2. Here, the bias current is $I = 1.01 I_{\text{th}}$ and the modulation amplitude is $\Delta I = 0.03 I_{\text{th}}$, where I_{th} is the solitary laser threshold. The red curve represents the bit -1 and the green curve the bit 1. Further information on the calculation of these curves can be found in the main text.

To overcome the disadvantage of having partially exposed bits, we can apply a method that has been demonstrated advantageous in other classical key distribution systems. We can use privacy amplification in order to enhance the security of our partially exposed raw key [176]. This method can be applied with effectiveness to systems where the fidelity of the generated raw key is high, which is particularly true in most classical key distribution systems. Here, fidelity refers to 1 minus the fraction of erroneous bits in the raw key [169].

In our particular scheme, we will not use those individual bits that are too exposed. For this purpose, we need to define an upper boundary for the probability of every bit to be correctly identified by Eve. We then sieve only those bits that fulfill our requirement. When this is done, an algorithm for privacy amplification can be used to purify the generated raw key, i.e., the key that is partially exposed. This process always has a cost in terms of encrypted-key generation rate, but allows us to arbitrarily enhance the security of the final key.

In Fig. 5.8, the is normally distributed in a first approximation, although the histograms present many irregularities in their shapes. We have fitted each histogram with a Gaussian distribution in order to smoothen the probability distribution function. The criteria we have chosen here is that the probability in favor of any of the values is never higher than 0.75. This imposes boundaries that are indicated as vertical dashed lines in Figs. 5.8a and 5.8b.

Of course, not all the bits that are inside the probability boundaries will conform the

raw exchanged key, but only those that combine in both lasers to a synchronized state. Again, from the time series we need to determine whether they are synchronized or not. This classification can be done using the synchronization error, as it is usual in chaos communications schemes [177]. Figure 5.9 depicts the accumulated synchronization error that is calculated via the following expression: $\sqrt{\frac{<I_1-I_2>_{bit}^2}{<I_1+I_2>_{bit}^2}}$. This measurement gives us a good contrast between synchronized and unsynchronized bits.
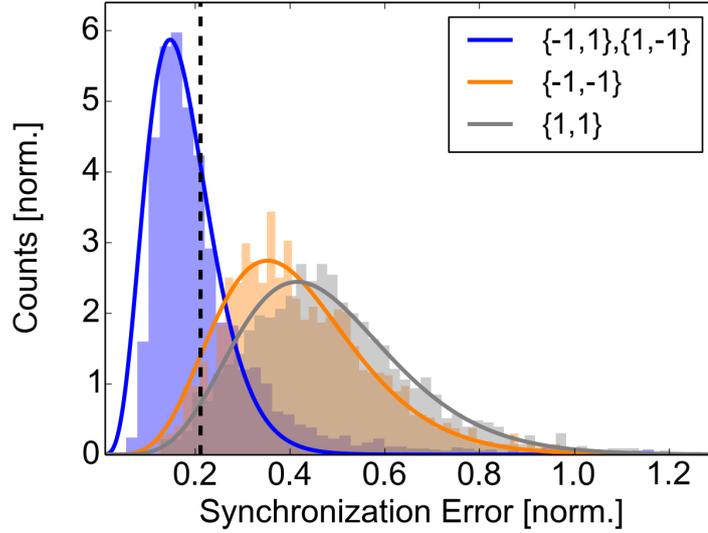
Figure 5.9: Synchronization error between the modulated bits. The bias current is $I = 1.01I_{\text{th}}$ and the modulation amplitude is $\Delta I = 0.03I_{\text{th}}$. The blue curve represents the synchronized bits, meanwhile the orange and the gray curves represent the unsynchronized bits of different sign. Further information on the calculation of these curves can be found in the main text.

In Fig. 5.9, the histogram depicted in blue corresponds to the bits of the synchronized states. The other two histograms correspond to the unsynchronized modulation combinations (detail on the curves indicated in the figure label). It is noteworthy that the data corresponding to the synchronized bits exhibit not only a smaller synchronization error, but also a smaller variance in their distribution than the unsynchronized bits. Here, in order to smoothen the irregularities we have fitted the histograms again. This time we have used a Gamma distribution function to fit the histograms because in the calculation of the synchronization error the intensities are squared. Alternative approaches to smoothen the histograms data could use other functions or varied the bin widths.

We fix a threshold criterion to determine whether the combined bits of both lasers lead to a synchronized state or not. We put the threshold where the unsynchronized states probability distribution functions have half the height of the synchronized states. With this criterion we accept for the key all the bits that have a synchronization error below the vertical dashed line in Fig. 5.9. The ratio of unsynchronized versus synchronized bits inside this region gives us the fidelity of the generated key, that for the data

depicted in Fig. 5.9 is 0.93.

The combination of both criteria as explained in Figs. 5.8 and 5.9 gives us the raw key generated in our scheme under the mentioned experimental conditions. The rate at which this raw key is generated reaches up to 87 Mbit/s. This value represents $\lesssim 20\%$ of the synchronizable bits rate[7]. Under this conditions, the average cross-correlation of the intensity dynamics (without modulation of the bias current) is beyond 0.94. Other experimental conditions give raw key generation rates in the same order of magnitude only if the synchronization quality is similarly good.

We have investigated different bias currents and different amplitudes of modulation ranging from $\{1.01 - 1.5\}I_{\text{th}}$ and $\{0.02 - 0.08\}I_{\text{th}}$, respectively. In our experiment, the highest cross-correlation values were obtained for bias currents close to the solitary laser threshold and high values of the feedback/coupling strength. When the synchronization quality decreases, the raw key bit rate drops rapidly below 50 Mbit/s, e.g., for a cross-correlation coefficient of 0.84, the raw key is already generated at 28 Mbit/s. The reason of this fast deterioration of the performance of our scheme is that the quality of synchronization determines the degree of overlap between the blue and the other curves in Fig. 5.9. The other factor that strongly influences the performance of our scheme is the modulation amplitude. For low modulation amplitudes, the histograms similar to those shown in Fig. 5.8 will strongly overlap and a majority of the bits will be masked in the chaotic waveforms. On the contrary, for high modulation amplitudes, the histograms will separate away from each other and a high number of individual bits will be too exposed to conform the raw key.

A raw key generation rate of 87 Mbit/s is high in comparison with the other classical key generation schemes mentioned in section 5.1. Indeed, it surpasses the state-of-the-art quantum-key distribution cryptosystems [178]. However, this value cannot be considered the rate at which a properly ciphered key is exchanged. The reason is that a part of the bits that conform this key are exposed and its concealment is compromised. Even more, in contrast with the quantum-key distribution systems that can identify whether the distributed key is eavesdropped, we have no mechanisms to find out the exposition of our exchanged key. A fraction of the individually modulated bits will have a probability to be identified up to 0.75, meanwhile the average probability is 0.64. We need privacy amplification [179] in order to enhance the encryption of the raw exchanged key. However, it is important to correct the possible differences in the key retained by Alice and Bob before privacy amplification can be applied (here, the fidelity of the raw key is 0.93). One possibility to correct the errors in the key is to use a procedure known as "information reconciliation" [180] through an authenticated public channel. Other methods to increase the fidelity of the exchanged key could imply particular parameters of our experiment, like reducing the injected bit rate or modifying the modulation scheme.

Following the arguments exposed by Horváth, Kisch and Scheuer in [176], privacy amplification can be applied to classical key distribution schemes with good results as

---

[7]Please note that the key exchange rate must be compared to half the modulation rate, given that only a 50% of the bits will represent synchronizable states.

long as the fidelity of the raw key is sufficiently high. In this work, the authors analyze the effect of privacy amplification on the security of different classical key distribution schemes. The information leak from the raw key can be reduced down to an arbitrarily low value with the simple iterative application of a privacy amplification algorithm. The algorithm used by the authors consists of replacing the original key by a shorter one (with half the length of the original key) whose bits are the product of the XOR operation between couples of successive bits of the original key [181]. By means of this procedure we can target the desired upper bound of Eve's probability to correctly guess the bits of the key. In some of the classical key distribution schemes introduced in section 5.1, the number of iterations of the privacy amplification algorithm are 2 for the Johnson-noise scheme by Kish [164] and 3 for the Scheuer-Yariv's ultra-long fiber laser scheme [165]. In our case, given the average probability of 0.64, it would be enough to iterate three times the privacy amplification algorithm to reduce the probability for Eve below 0.50003 and have a resulting secure key generation rate of 11 Mbit/s.

The analysis of the security of our classical key distribution scheme is not complete if we only consider the information leaked from the bits of the key. Another type of attacks, known as invasive attacks, must also be considered. One example of this type of threat is the so named *man-in-the-middle attack*. In a simplified version, Eve cuts the communication channel and impersonates the legitimate partners. Eve is then receiving the information (with a matching laser) and emitting its own generated bit-sequences, causing the establishment of a non-secure key between both partners. In fact, in this scenario Eve knows an error free version of the key. Security against this attack can be obtained broadcasting the coupling signal in as many public channels as possible [164, 176]. Both legitimate partners can therefore detect any invasive manipulation on the channel signal and discard the related bits if necessary.

5.5   Discussion and Summary

We have experimentally demonstrated a scheme that allows to negotiate an encrypted key through a public channel. The scheme is based on the phenomenon of identical chaos synchronization emerging between two bidirectionally-coupled SL. Both lasers are mutually coupled through a passive relay, that in our experiment is implemented by a fiber-loop mirror. The key is generated from the synchronized bits, that are concealed from eavesdropping through chaos encryption.

The operating principle should work and maintain its exchanged-bits rate no matter the coupling distance between the lasers. The reason is that the relay element shares the coupling between both laser units (constantly feeding both lasers). Once the communication is set and the information from the relay begins to arrive to the partners, the key-build up process begins. The desynchronization-resynchronization time does not depend on the distance to the other laser and is of the order of the high-bandwidth chaotic dynamics. In our laboratory experiment, we have demonstrated raw key exchange rates above the 80 Mbit/s for bit modulations at 1 Gbit/s.

The security aspects of our scheme have been studied. In particular, the possibility

to use privacy amplification indicates that we can always sift a more secure key with a user-defined level of information leakage. Obviously, there exists a trade off between the number of iterations of the privacy amplification algorithm (with a half shortening of the key for each iteration) and the security of the resulting key. Even after reinforcing the exchanged key privacy, this scheme allows us to exchange a private key with high-enough bit rates (11 Mbit/s) to be used as a one-time pad for secure private communications.

Interestingly, some challenges remain to be solved for the field implementation of this scheme. The fact that the bias current modulation is visible in the amplitude of a significant number of the bits is one of the most important challenges, since it causes the requirement of privacy amplification and consequently the loss of a significant part of the raw key bits. A possible solution could come from the use of a phase modulation scheme. This possibility could conceal better the individual bits, leaving the bit rates unaffected or even improving them by means of external electro-optic phase-modulators with modulation bandwidths far beyond the tens of Gigahertz. Therefore, the limitation to the modulation bandwidth would come from the resynchronization time, which is typically shorter than a nanosecond. However, the main technological challenge for this scheme resides in the possibility to extend it to field implementations with long-fiber connections. The use of standard long fiber links represents a nontrivial problem because the signals therein are subjected to amplification, dispersions rectification and routing, what implies unpredictable variations in the propagation delays. The fundamental question is therefore the impact on the quality of the synchronization or even the possibility for this identically synchronized state to exist under such described field conditions. This is a matter of further investigations on the technological side of this system. Besides these technological aspects, the scheme proposed in this chapter has been shown to be robust working over several weeks without extra realignments and it offers a viable solution if a static fiber channel is dedicated to the communication link.

Chapter 6

State-Dependent Delay Dynamics in Semiconductor Lasers

6.1 Introduction

In this thesis, so far we considered systems with a constant delay. There are, however, different classes of delay systems in which the delay time is not constant. For example, in time dependent delay systems an external modulation changes the delay time of the system [182]. Actually, even more intriguing dependences of the delay time can be found in other type of systems. These systems are known as state-dependent delay (SDD) systems. In such systems, there exists a fundamental interrelation between the state of the system and the delay time. The effective delay is intrinsically determined by the state of the system and the latter one depends on the delays active at each time interval. Therefore, in this type of systems the changes in delay times emerge in a self-organized fashion.

A variety of important technological and technical systems can be described with a SDD formalism, some examples are Internet traffic [183], space communication [184], control theory [185], economics [186], turning processes [187], and deep drilling [188]. Furthermore, a number of ecological and biological systems can also be described by this approach, like predator-prey systems [189] or neural systems [190]. Other examples where SDDs play a crucial role are in the dynamical evolution of age-structured biological or physiological processes such as erythropoiesis [191,192] or state-dependent population growth [193]. Given the high number of possible applications, models of dynamical systems with state-dependent delays have found considerable interest in mathematics and control theory. Varied and complex phenomenology has been found in these models although they are demanding to tackle mathematically [184,194,195]. The reason is that state-dependent delays impose challenging problems in the mathematical analysis of the equations, as well as the numerical determination of solutions.

Despite of their relevance and interesting properties, up to today there exist almost no experimental implementations that meet the function of benchmark where to develop the studies in this field. There exist, for example, implementations on Boolean phase

oscillators programmed within a FPGA [196]. However, the state-dependent delay there played mainly the role to vary the effective coupling strengths. Therefore, direct measurement of the SDD dynamics in systems with controllable parameters is interesting and may have relevance for a variety of scientific fields.

Here, we present a real-world photonic implementation of a dynamical system experiencing two different delay times depending on the state of the system. The delay time does not change continuously with the dynamical state, it exhibits discrete jumps between the two delay times. Although this system is conceptually simple, not much is known about their dynamical properties, in particular in the chaotic domain. A simplified scheme of this configuration is depicted in Figure 6.1. It is worth noting that this represents only one of the simplest configurations of many SDD feedback or coupling motifs that can be imagined and realized. Our configuration comprises an oscillator $f(x)$ with its dynamics described by a variable $x(t)$. In dependence of $x(t)$, the state-dependent switch routes the dynamics to either one or another feedback branch with corresponding functions $g_1(x)$ and $g_2(x)$ and delay times τ_1 and τ_2, respectively. The scheme belongs to a class of SDD systems described by:

$$\dot{\mathbf{x}}(t) = f(\mathbf{x}(t)) + \sum_{k=1}^{2} \chi_k(\mathbf{x}(t - \tau_k))g_k(\mathbf{x}(t - \tau_k)), \qquad (6.1)$$

with $\chi_1(\mathbf{x}(t)), \chi_2(\mathbf{x}(t)) \in \{0, 1\}$ and $\chi_1(\mathbf{x}(t)) \cdot \chi_2(\mathbf{x}(t)) = 0$. The functions $\chi_1(\mathbf{x}(t)), \chi_2(\mathbf{x}(t))$ represent here the switch $S(x(t))$. Interestingly, due to the position of the switch, at any moment the oscillator obtains feedback either from branch 1, from branch 2, from both branches or from none of them. The position of the switch, i.e. whether it is situated before or after the delay loops, will determine the accessible dynamical states.
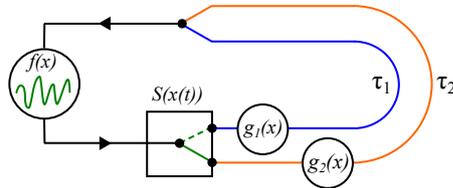
Figure 6.1: Scheme of the state-dependent delayed feedback configuration. An oscillator described by the function $f(x)$ and the dynamical variable $x(t)$ is directed to one or another branch via a switch depending on the state $x(t)$. The two feedback branches are respectively described via functions $g_1(x)$ and $g_2(x)$ and the delay times τ_1 and τ_2.

In this experiment, we replace the usual fiber loop mirror (see experimental setups presented in chapters from 2 to 4) with fixed delay by two feedback loops with mutually exclusive spectral reflection properties. Both loops have different lengths that result in different delay times, τ_1 and τ_2. Those delays are long compared to the characteristic dynamical time scales of the laser. We act on the spectral characteristic of the state[1]. The

---

[1]It is preferable to act on the spectral characteristic of the state rather than its amplitude, since amplitude nonlinearities are related to only very small relative changes of the delay times.

spectral characteristics are associated to the amplitude dynamics through the amplitude-phase coupling (the α parameter [35]). In this sense, the use of spectrally selective mirrors is a very convenient and flexible mechanism to choose different delay loops depending on the corresponding optical spectrum of the laser emission. Such system has recently attracted the interest of different research groups. Słowiński, Krauskopf and Wieczorek theoretically studied their relative equilibria structure and stability [197, 198]. In a recent experiment, the combination of the two frequency-selective feedback loops was investigated in terms of controlling the frequency oscillations of the laser light [199].

6.1.1 Chapter Outline

In section 6.2, the experimental setup and the characteristics of our implementation of SDD are presented. In particular, those related with the filters positioning and characterisation. The experimental results are presented in section 6.3. This section is divided in three parts. In the first part, the stationary spectral characteristics of this experimental system are studied and the conditions for the dynamics to occur in separated filters are highlighted. In the latter two parts, the real-time intensity and optical spectrum dynamics in each filter are investigated. From the aforementioned analysis, the existence and characteristics of state-dependent delay dynamics are demonstrated.

The experimental results are compared to numerical modeling in section 6.4. The model that is explored depicts qualitatively the same properties than the experimental system. In particular, the statistics of the residence times at each filter, analyzed in detail in section 6.5, are found to have similar behaviors.

6.1.2 Contributions to the Work in the Present Chapter

A large part of the results presented in this chapter have been published as: J. Martínez-Llinàs, X. Porte, M. C. Soriano, P. Colet, and I. Fischer, "Dynamical properties induced by state-dependent delays in photonic systems", *Nat. Commun.* **6**, 7425, (2015).

The state-dependent delay configuration was originally designed by I. Fischer. The planning and execution of the experiments have been done by me under the supervision of M. C. Soriano and I. Fischer. The theoretical analysis and numerical simulations were performed by J. Martínez-Llinás and supervised by P. Colet. All previously mentioned authors have been involved in the discussion of the results.

The experimental detection of the optical frequency dynamics presented in this chapter has been implemented by me following the method originally developed by D. Brunner and published as: D. Brunner, X. Porte, M. C. Soriano, and I. Fischer, "Real-time frequency dynamics and high-resolution spectra of a semiconductor laser with delayed feedback". *Sci. Rep.* **2**, 732; DOI:10.1038/srep00732 (2012).

6.2 Experimental Methods

In this experiment, we have employed a discrete-mode (DM) quantum-well semiconductor laser emitting at 1543 nm with a threshold current of $I_{th} = 12.00$ mA. With and

without external optical feedback, the laser exhibits single-longitudinal mode behavior
with a side-mode suppression ratio larger than 35 dB and a longitudinal mode separation
of 150 GHz. The temperature and current of the laser are stabilized to an accuracy of
0.01 K and 0.01 mA, respectively. Further information on this type of laser devices can
be found in section 2.2.
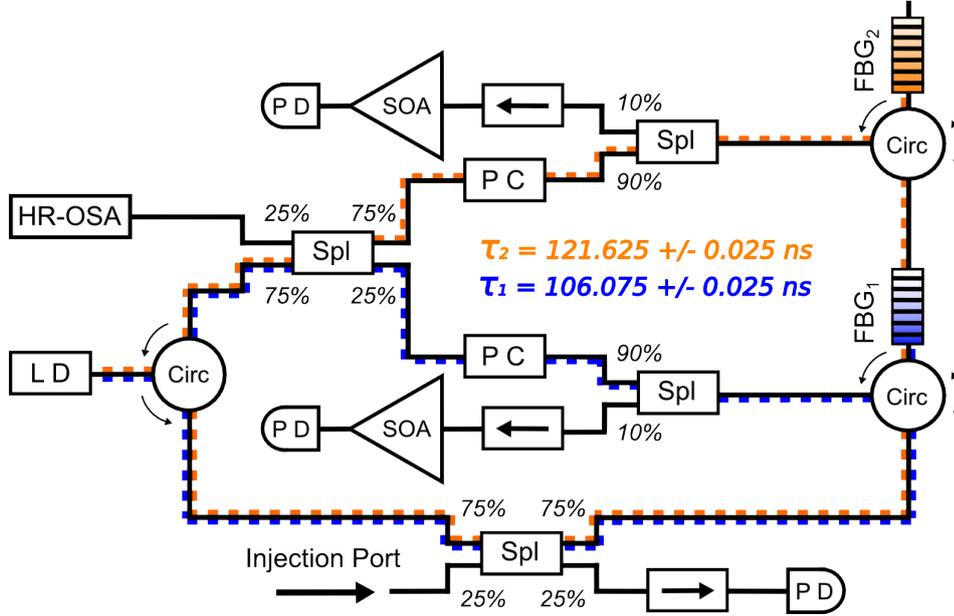
Figure 6.2: Scheme of the experimental setup for the state-dependent delays experiment. LD: laser
diode, Circ: optical circulator, PC: polarization controller, Spl: one/two by two intensity splitter with
indicated intensity splitting ratios, →: optical isolator, FBG: fiber Bragg gratings, SOA: semiconductor
optical amplifier, PD: photodiode, and HR-OSA: high-resolution optical spectrum analyzer.

Figure 6.2 depicts the experimental setup, that has been implemented employing
standard telecommunications components. The laser is subject to delayed optical feed-
back from two distinct cavities. Each feedback cavity contains an independent fiber-
loop mirror closed by a fiber Bragg grating (FBG) that acts as the frequency-selective
reflector. Therefore, both feedback paths have different lengths with disjunct spectral
reflection ranges. About 75% of the light from FBG_2 and 25% of the light from FBG_1
are merged and fed back to the laser diode, resulting in an effective ratio of feedback
strengths of 4.38 dB. The light propagates linearly through the delay loops, while the
laser represents the nonlinear element in this experiment. The polarization controllers
are used to independently align the polarization for each feedback cavity.

The experimental setup design allows for direct detection of the light reflected from
each individual FBG, besides of the light emitted by the LD. About 10% of the light
reflected from each FBG is coupled out for detection. Therefore, two semiconductor
optical amplifiers (SOA) are needed to amplify the light reflected from each FBG before
detection. The measurements of the dynamics are performed using a 13 GHz bandwidth
detector for the total intensity dynamics and two 20 GHz detectors for the filtered

dynamics. The dynamics is recorded using a 16 GHz analog bandwidth oscilloscope with a sampling rate of 40 GS/s.

The two FBG filters are grating structures of 1 mm length photo-imprinted in standard single-mode fiber (SMF28). Their maximum reflectivities are typically $> 90\%$ and the measured reflection bandwidths are 4.63 ± 0.02 GHz and 5.69 ± 0.02 GHz for FBG_1 and FBG_2, respectively. In the present experiment, the reflection bandwidths of the FBG, their spectral positions and relative amplitudes have been precisely measured with the combination of a super-luminescent diode and a high-resolution optical spectrum analyzer (that corresponds to the element labeled as HR-OSA in the setup depicted in Fig. 6.2) with 10 MHz resolution [38]. Figure 6.3 depicts the position of the FBGs in the present experiment. An important advantage of employing FBGs is that they allow for tuning of their reflection frequencies without essential modification of any of their other characteristics, like reflectivity and reflection bandwidth. For this purpose, both FBGs have been fixed to independent translation stages in order to tune them to the desired reflection frequencies by means of stress. The frequency dependence on length changes is $\delta f/\delta L = 1.1 \pm 0.1$ GHz/μm, and the maximum tuning range is 250 ± 60 GHz. The respective center frequencies of FBG_1 and FBG_2 have been detuned -4 ± 0.01 GHz and -11 ± 0.01 GHz with respect to the solitary laser frequency, that is $f_{LD}^S = 194350$ GHz. Therefore, there is no spectral overlap between the reflection bandwidths of the two FBGs, neither with respect to the f_{LD}^S.
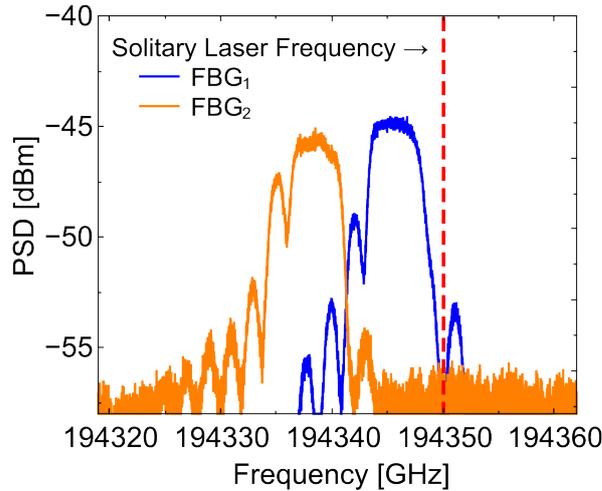
Figure 6.3: Fiber Bragg Gratings. The blue and orange curves respectively represent FBG_1 and FBG_2. The vertical dashed line indicates the emission frequency of the solitary laser, f_{LD}^S.

The injection port has been used to precisely measure the external-cavity round trip times by means of the injection of light pulses. This technique was already described in detail in section 3.2. The only difference present in the actual implementation is that we must detune the emission frequency of the injection laser in order to correctly measure the reflection from each FBG. With this method, we have measured the delay times of the two cavities as $\tau_1 = 106.075 \pm 0.025$ ns and $\tau_2 = 121.625 \pm 0.025$ ns.

6.3   Experimental Results

The combination of the SL (the nonlinear element) with the FBGs acts as the state-dependent switch. First, the results from such combination are discussed in the context of the experiment. Later on, in section 6.4, we will compare the obtained spectral and dynamical features with numerical modeling results.

Optical Spectrum

First, we study the averaged optical spectrum of the laser emission when subject to delayed feedback from the two filtered cavities. Figure 6.4 exhibits the dependence of the optical spectra on the injection current (the parameter that is varied). In this measurement, the injection current is scanned until $1.5I_{\text{th}}$, here only the range close to the solitary laser threshold is shown.
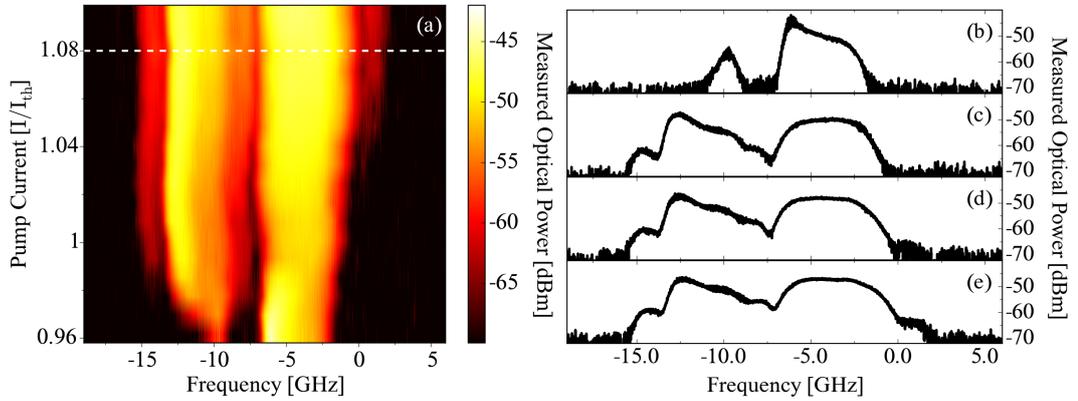
Figure 6.4: Dependence of the optical spectrum on the pump current of the laser. The frequency axis is centered to the value of the solitary laser frequency, $f_{\text{LD}}^{\text{S}} = 194350$ GHz. FBG_1 and FBG_2 are detuned from the solitary laser frequency by -4 ± 0.01GHz and -11 ± 0.01GHz, respectively. The dashed horizontal line in panel (a) indicates the highest current for which the two spectral bands corresponding to the filters are separated by a gap larger than 10 dB. Panels (b) to (e) show representative spectra at different values of the pump current axis: (b) $0.96I_{\text{th}}$, (c) $1.01I_{\text{th}}$, (d) $1.04I_{\text{th}}$ and, (e) $1.07I_{\text{th}}$.

The optical spectra are depicted for pump currents ranging from 4% below the solitary laser threshold to 10% above. The first depicted spectrum is below threshold ($0.96I_{\text{th}}$) because the optical feedback from the external reflectors reduces the threshold current of the laser. The horizontal dashed line in Fig. 6.4a indicates the highest bias current for which we consider the delay dynamics to be state-dependent. For currents below $1.08I_{\text{th}}$, we consider the two filters isolated because there is a spectral gap larger than 10 dB between them. Above $1.08I_{\text{th}}$, this gap gradually disappears and the signatures from the filters cannot be considered spectrally separated anymore. Panels (b) to (e) illustrate some representative points on the pump current axis. We note that

the spectra close to threshold exhibit comparable spectral amplitudes[2] and bandwidths in both filters and, therefore, one can expect that they will contribute similarly to the global dynamics.

Intensity Dynamics

In order to proof whether this system exhibits SDD dynamics or not, the real-time intensity dynamics must be analyzed. The experimental setup has been intentionally designed to allow for direct detection of the light reflected from each individual FBG with independence of the light emitted from the laser. Figure 6.5 depicts the time series of the laser emission and the intensity in the two respective feedback loops for a pump current of $I = 1.01 I_{\text{th}}$.
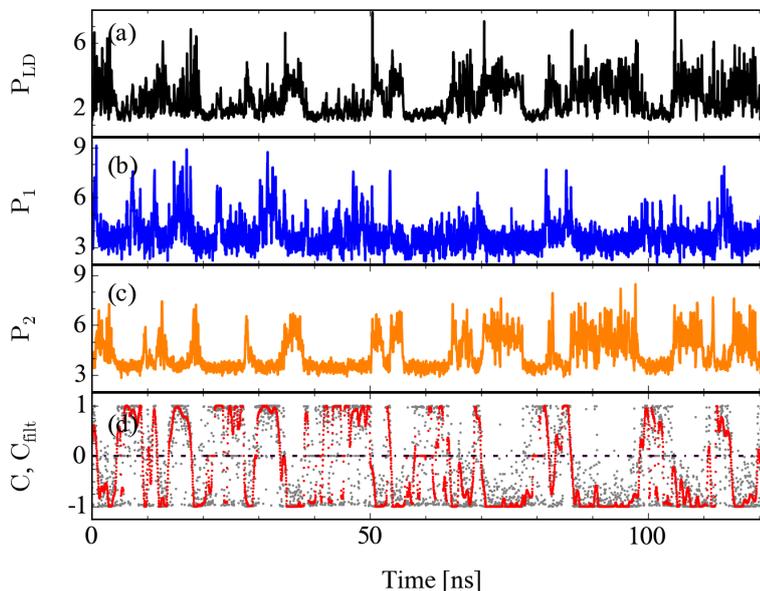
Figure 6.5: Experimental time series for the pump current of $I = 1.01 I_{\text{th}}$. Panel (a) depicts the intensity dynamics emitted by the laser. Panels (b) and (c) respectively show the filter-resolved intensity dynamics for FBG_1 and FBG_2. Two measurements are plotted in panel (d): the contrast function (gray dots) and the contrast function of the 1 GHz low-pass filtered intensity dynamics (red dots). All the intensities have been plotted in arbitrary units.

The total intensity dynamics is depicted in Fig. 6.5a. Panels 6.5b and 6.5c show the filter-resolved dynamics for FBG_1 and FBG_2, respectively. These latter time series demonstrate the state-dependent nature of the dynamics, with alternating periods of emission in the frequency bands corresponding to FBG_1, FBG_2 or in none of both filters resulting in no feedback. Only by visual inspection of these panels it becomes clear the complementary nature of the total dynamics, based on mostly exclusive con-

---

[2]The relative amplitudes of the two spectral components are affected by the coupling ratio of the coupler at which the spectra are measured.

tributions either from FBG$_1$ or FGB$_2$. To quantify this further, the signature of this state-dependent delay dynamics is visualized in Fig. 6.5d using a contrast function. This contrast function is defined as:

$$C(t) = \frac{P_1^*(t) - P_2^*(t)}{P_1^*(t) + P_2^*(t) + \varepsilon},$$

with $P_i^*(t) = \max\left[(P_i(t) - P_{i,o}), 0\right]$, $i = 1, 2$ and ε being infinitesimal. The parameter ε is introduced to avoid indeterminations of the form zero divided by zero, since the powers in both filters can become zero simultaneously. In order to properly define the contrast function, the origin of noise in the detected time series has been characterized. We can clearly attribute the origin of noise to detection noise (originated mainly in the amplification stage at the SOAs), which is symmetric around the actual physical value. Therefore, an offset $P_{i,o}$ can be subtracted from every FBG time series based on the noise characterisation. Fig. 6.5d depicts the contrast functions obtained from the fully resolved (gray dots) and the 1 GHz low-pass filtered (red dots) intensity time traces, respectively. From both time traces of the contrast function, the switches between the states can be clearly recognized. In the contrast function corresponding to the fully resolved intensity time series, one can also see the fluctuations due to the influence of detection noise. Those fluctuations are mostly removed by the low-pass filtering because they do not actually represent switches between states. This is the reason why in Fig. 6.5d the contrast function of the low-pass filtered time series is much smoother.

The dynamics of our system changes when the injection current is increased. Figure 6.6 illustrates the SDD dynamics for two higher injection currents, $I = 1.04I_{\text{th}}$ and $I = 1.07I_{\text{th}}$. The increase of the injection current results in dynamics exhibiting faster transitions between the different filter states, with correspondingly shorter residence times. The contrast functions for these switches show even more distinct switches between the different filter states with similar contribution to the dynamics from both filters.

The pump current limit of $I = 1.08I_{\text{th}}$ discussed in the context of Fig. 6.4 is related to the increase of the bandwidth of the laser dynamics. The increase of the injection current ultimately results in an enhancement of the bandwidth of the laser dynamics, due to the increase of the relaxation oscillations frequency. This resulting spectral overlap causes the loss of a clear distinction between two separate states and therefore establishes a practical limit to our SDD dynamics region.

The switching properties between the two filter states can be further characterized with the calculation of the cross-correlation function. Figure 6.7 depicts the cross-correlation function of P$_1$ and P$_2$ (blue curve) and of the low-pass filtered versions of P$_1$ and P$_2$ (light-red curve). The dashed horizontal lines indicate their corresponding cross-correlation coefficients at the origin. We obtain $C_c = -0.4$ for the unfiltered time traces and $C_{c,f} = -0.65$ for the filtered ones, supporting that the intensity dynamics in the two filters is mostly anti-correlated. One factor limiting the amplitude of the coefficient for the filtered cross-correlation is the time that the system spends at those feedback states where both filters are either simultaneously reflecting or none is reflecting.
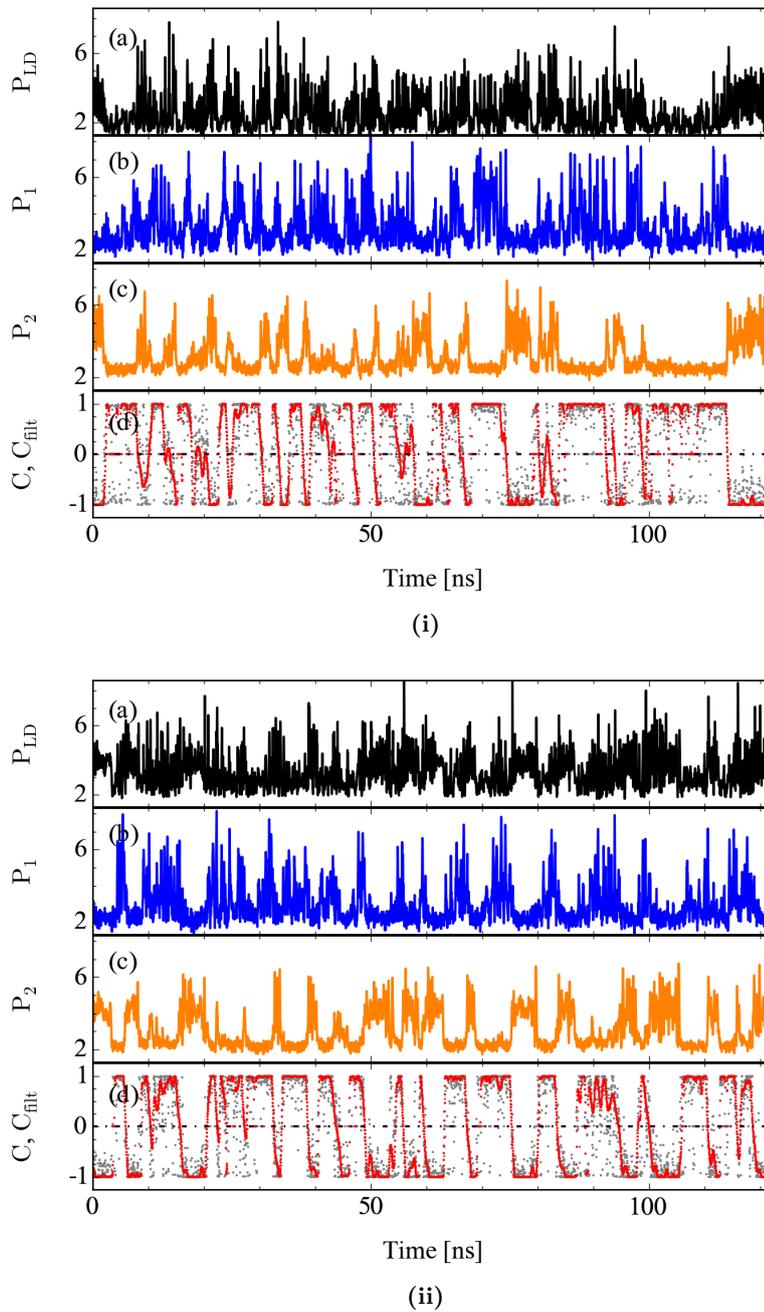
Figure 6.6: Experimental time series for the pump currents of (i) $I = 1.04I_{th}$, and (ii) $I = 1.07I_{th}$. The respective panels correspond to identical measurements: (a) intensity dynamics emitted by the laser, (b) and (c) filter-resolved intensity dynamics for FBG$_1$ and FBG$_2$, respectively, (d) contrast function (gray dots) and contrast function of the 1 GHz low-pass filtered intensity dynamics (red dots). All the intensities are plotted in arbitrary units.
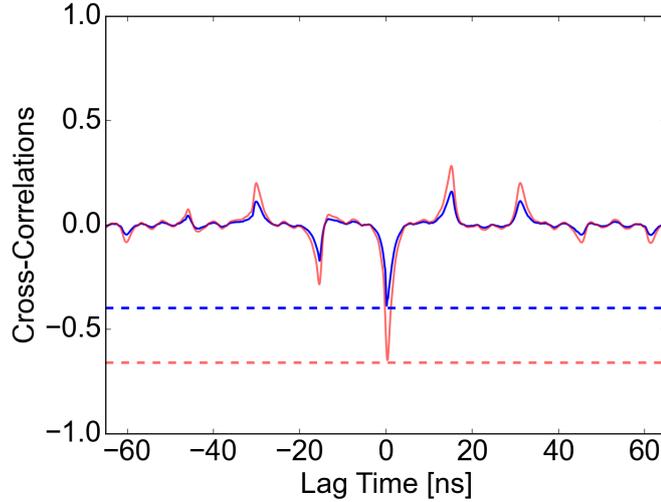
Figure 6.7: Cross-correlation of the signals of both filters for a bias current of $I = 1.07 I_{th}$. The blue curve represents the correlation between P_1 and P_2, while the light-red curve depicts the cross-correlation between the low-pass filtered version of P_1 and P_2. The respective dashed horizontal lines indicate the value of the cross-correlation coefficients at zero-lag.

To sum up, under the conditions described in this section (and due to the chosen geometry), our experimental system belongs to the class of systems described by the state-dependent delay Eq. 6.1.

Optical Frequency Dynamics

The contrast function between both filters has proven to be a useful tool to demonstrate and study SDD dynamics in our experiment. However, this function only contains information of the intensity dynamics. In [200], it was demonstrated that additional valuable information can be extracted from the combination of intensity and frequency dynamics in delayed feedback lasers. The additional physical dimension that provides the real-time measurement of the optical frequency extends the comparison between experiment and numerical modeling. In addition, the use of the optical frequency measurement (with a narrow linewidth optical reference source) for time-averaged spectroscopy allows to extract optical spectra with an unprecedented resolution [200].

The main goal is to study the optical frequency dynamics (from now on only "frequency dynamics") in combination with the intensity dynamics to extract new and valuable information of our SDD system. In order to detect the optical frequency, we use a measurement based on balanced coherent optical detection. Measurements based on coherent detection have their origins in radio communications. In this process (also known as heterodyning), a local carrier mixes with the received RF signal to generate a product term. The product contains a sum and a difference terms of the signal and the local oscillator frequencies. With the help of low pass filtering (that eliminates the sum frequency component), the received RF signal can be demodulated from the difference

term.

In our system, the incoming optical signal corresponds to the laser diode (LD) subject to feedback from two distinct frequency selective cavities, and the local oscillator is a reference CW semiconductor laser (LR). The combination of those two sources occurs in a two-by-two optical coupler. Furthermore, a photodiode (which is a square-law detection device) mixes the signal and the local oscillator. Figure 6.8 depicts the setup used for coherent detection. This scheme reproduces the same experimental system as Fig. 6.2 (grayed out in Fig. 6.8), with additional elements in the detection path. A CW laser diode (with DFB structure) is used as reference stable source to heterodyne with the target optical frequency dynamics. This laser (LR) is directly connected to an optical isolator, suppressing undesired optical feedback and thereby avoiding complex dynamical behavior resulting in artifacts in the heterodyne spectrum. In order to control the correct frequency alignment of LR we have split a part of its light for detection in the HR-OSA. In order to calibrate the respective optical frequencies, the output of LR and LD are combined in a 3 dB coupler (not explicitly drawn in Fig. 6.8, its inputs are indicated with two green labeled ports) before their detection with the HR-OSA. We have set the optical frequency of LR to the solitary emission frequency of LD. The optical polarization of LR is aligned to LD using a polarization controller. This step is of fundamental importance to maximize the power contained in the heterodyne signal.
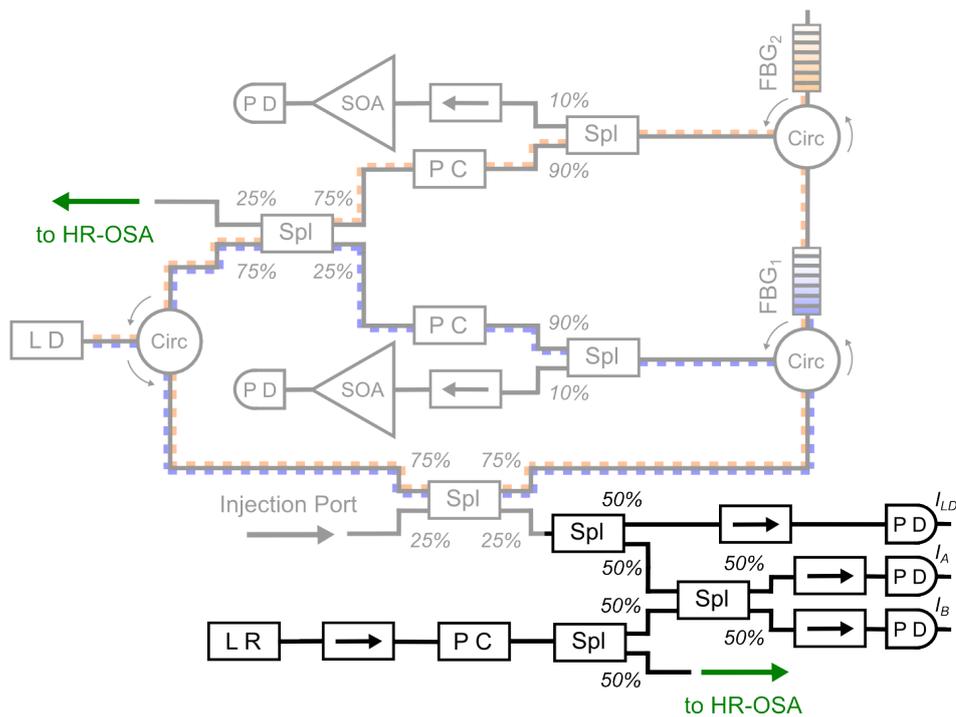
Figure 6.8: The scheme of the experimental setup for the SDDs experiment is similar to the depicted scheme in Fig. 6.2. The novel element in this setup is the laser diode used as reference source (LR).

For the heterodyne detection, the mixing between the signal of interest and LR is

done in a two-by-two optical coupler (with -3 dB coupling ratios). The optical fields emerging from the coupler are detected by two very similar 20 GHz bandwidth photodetectors. These photodetectors are square-law detection devices, therefore the intensities at their two outputs are:

$$I_A(t) = \Re |E_A(t)|^2 = \Re \left| \frac{(E_{LD} + jE_{LR})}{\sqrt{2}} \right|^2,$$ (6.2)

$$I_B(t) = \Re |E_B(t)|^2 = \Re \left| \frac{j(E_{LD} - jE_{LR})}{\sqrt{2}} \right|^2.$$ (6.3)

To derive these equations, we use the expression of the transfer function of a two-by-two optical coupler, which can be found in most books about fiber optic components, e.g. [201]. The term $\Re$ represents the responsivity of the photodiodes and $1/\sqrt{2}$ corresponds to the ratio of the electric field amplitude coupled at each output of the 3 dB optical coupler. The rigorous formulation of Eqs. 6.2 and 6.3 should imply different responsivities for the two photodiodes ($\Re_A$ and $\Re_B$) and different coupling coefficients for the two outputs of the optical coupler ($\sqrt{\epsilon}$ and $\sqrt{1-\epsilon}$). However, the optical coupler and the photodiodes that we use in this measurement have been specifically hand picked from a variety of elements at our disposal due to their strong matching. Therefore, the mismatches between the photodiodes responsivities and the power-coupling coefficients, respectively $\delta\Re$ and $\delta\epsilon$, are very small.

The explicit expressions of the optical fields of both lasers are $E_{LD}(t) = A_{LD}(t)e^{j\omega_{LD}(t)t}$ and $E_{LR}(t) = A_{LR}e^{j\omega_{LR}t}$. Here, we consider ω_{LR} and A_{LR} of our CW reference laser constants during the measurement periods. The arguments in favor of these approximations are twofold: the laser temperature and current are stabilized with fluctuations smaller than the percent, and the influence of the relaxation oscillations in A_{LR} is neglected because of their strong damping. In consequence, equations 6.2 and 6.3 can now be rewritten as:

$$I_A(t) = \frac{1}{2}\Re \left[|A_{LR}|^2 + |A_{LD}(t)|^2 + 2A_{LR}A_{LD}(t)cos(2\pi df_{LD}(t)t) \right],$$ (6.4)

$$I_B(t) = \frac{1}{2}\Re \left[|A_{LR}|^2 + |A_{LD}(t)|^2 - 2A_{LR}A_{LD}(t)cos(2\pi df_{LD}(t)t) \right].$$ (6.5)

Each photodiode intensity contains the two direct detection components ($|A_{LD}(t)|^2$ and $|A_{LR}|^2$) and the heterodyne component. The detected difference frequency, defined as $df_{LD}(t) = f_{LD}(t) - f_{LR}$, is the one related with the optical spectrum of LD. Meanwhile, the sum component $f_{LD}(t) + f_{LR}$ is eliminated (through low-pass filtering) by the RF circuit that follows the photodiode because it still corresponds to the optical domain.

The heterodyne signals are recorded with an analog bandwidth of 16 GHz. In our balanced coherent detection scheme (see Fig. 6.8), we access to the heterodyne component through the subtraction of the output intensities, $I_A(t)$ and $I_B(t)$:

$$\Delta I(t) = 2\Re A_{LR}A_{LD}(t)cos(2\pi df_{LD}(t)t).$$ (6.6)

An additional advantage of this scheme is that significantly improves the signal-to-noise ratio with respect to direct detection as a result of the mixing with the strong reference laser.

The optical spectrum of LD (S_{LD}) can be obtained from the fast Fourier transform (FFT) of Equation 6.6:

$$S_{LD}(f) = \left(\frac{\Delta \tilde{I}(f)}{4\pi \Re A_{LR}} \right) \hat{*} \tilde{A}_{LD}(f), \tag{6.7}$$

where the variable f is the optical frequency, the symbol ~ stands for a Fourier transformation of the corresponding variable, and the symbol $\hat{*}$ depicts a deconvolution.

As proof of concept, in Figure 6.9 we compare the optical spectrum obtained using the FFT of a long time window with the optical spectrum recorded with the HR-OSA. The time traces for the heterodyne measurement were recorded at a sampling rate of 40 GSamples/s and with a total length of 8 MSamples (i.e. 200 μs). The maximum spectral resolution with this method is determined by the signal detection bandwidth (16 GHz) and the recorded samples length (8 MSamples), resulting in a theoretical limit of 2.5 kHz in our measurement. In practice, the (narrow) linewidth of the CW reference laser is what physically limits the frequency resolution of our optical detection technique, in our case $\lesssim$ 1 MHz. It is worth noting that this value is one order of magnitude smaller than the resolution of the HR-OSA.
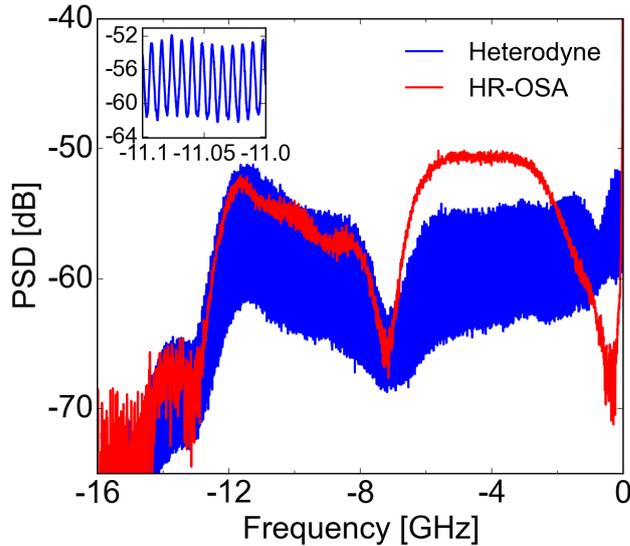
Figure 6.9: Comparison of the optical spectrum detected with two different techniques. The blue trace corresponds to the heterodyne technique and the red trace corresponds to the spectrum obtained with the HR-OSA. The inset illustrates the modes of the filtered external cavities in a zoom of the heterodyne spectrum. The bias current for the depicted conditions is $I = 1.03 I_{\text{th}}$.

In Fig. 6.9, the blue and the red traces respectively depict the time averaged heterodyne spectrum and spectrum recorded with the HR-OSA. The abscissa depicts the

frequency detuning in GHz respect to the solitary emission frequency of LD. Both spectra are plotted on a logarithmic axis. The logarithmic expression of the heterodyne spectrum has a different offset in dB with respect to the spectrum detected with the HR-OSA. We have subtracted this bias to match the power spectral densities around the filter FBG_2. However, there is a mismatch in powers visible around FBG_1. This mismatch is due to the difference in detection powers between both filters signals at the HR-OSA port, and coincides in magnitude with the expected 4.38 dB resulting from the different coupling ratios of the 25/75 coupler (see Fig. 6.8).

Given the high resolution of our measurement technique, we can access the individual modes of the filtered external cavities. The inset in Fig. 6.9 illustrates those modes in a zoom of the heterodyne spectrum. It is important to note that the heterodyne spectrum has been convoluted with a 1 MHz sliding average filter in order to smoothen the fast noisy fluctuations around the modes. With dependence on the region that is inspected, we can resolve the modes corresponding to FBG_1 or the modes corresponding to FBG_2. Interestingly, the measurement of the modes frequency separation in each filter gives different results, that correspond to the inverse of the delay time at the corresponding cavity. The modes in the spectral region of FBG_1 are separated $\Delta f = 9.44 \pm 0.01$ MHz, that corresponds to an external cavity delay time of $\tau_1 = 105.9 \pm 0.1$ ns. Meanwhile those modes in the expected frequency region of FBG_2 are separated $\Delta f = 8.23 \pm 0.01$ MHz, corresponding to an external cavity delay time of $\tau_2 = 121.5 \pm 0.1$ ns. In both cases the obtained result coincides (within the resolution of the measurement) with the directly measured delay times.

By means of this heterodyne detection approach, it is also possible to extract the dynamics of the laser frequency. In order to obtain the frequency dynamics of LD we use a sliding version of Eq. 6.7:

$$S_{LD,t'}(f) = \left(\frac{\Delta \tilde{I}_{t'}(f)}{4\pi \Re A_{LR}} \right) \circledast \tilde{A}_{LD,t'}(f). \qquad (6.8)$$

In Equation 6.8, the FFT is calculated on data windows of fixed size Δt centered at successive times t'. An optical snapshot spectrum is calculated for each time window of length Δt. Due to the nature of the sliding FFT (sFFT), temporal and spectral resolution cannot be chosen independently, since spectral resolution is given by $\Delta \nu = \frac{1}{2\Delta t}$. We chose $\Delta t = 1$ ns, allowing for a resolution of $\Delta \nu = 0.5$ GHz.

Figure 6.10 depicts together the intensity dynamics and the frequency dynamics of LD for the two pump currents already illustrated in Fig. 6.6. The full spectrogram of the frequency dynamics is shown in panels (b) for both pump currents. This plot gives us the information on how the SDD dynamics behaves in the frequency domain, with fast switchings between FBGs of characteristic times shorter than any of the two delay times. Moreover, the simultaneous plot of the filter-resolved intensity dynamics of FBG_2 (Fig. 6.10a) and the frequency dynamics (Fig. 6.10b) validates the latter through the comparison of the time windows when FBG_2 is active with those periods when the frequency dynamics occurs at the spectral region of FBG_2.
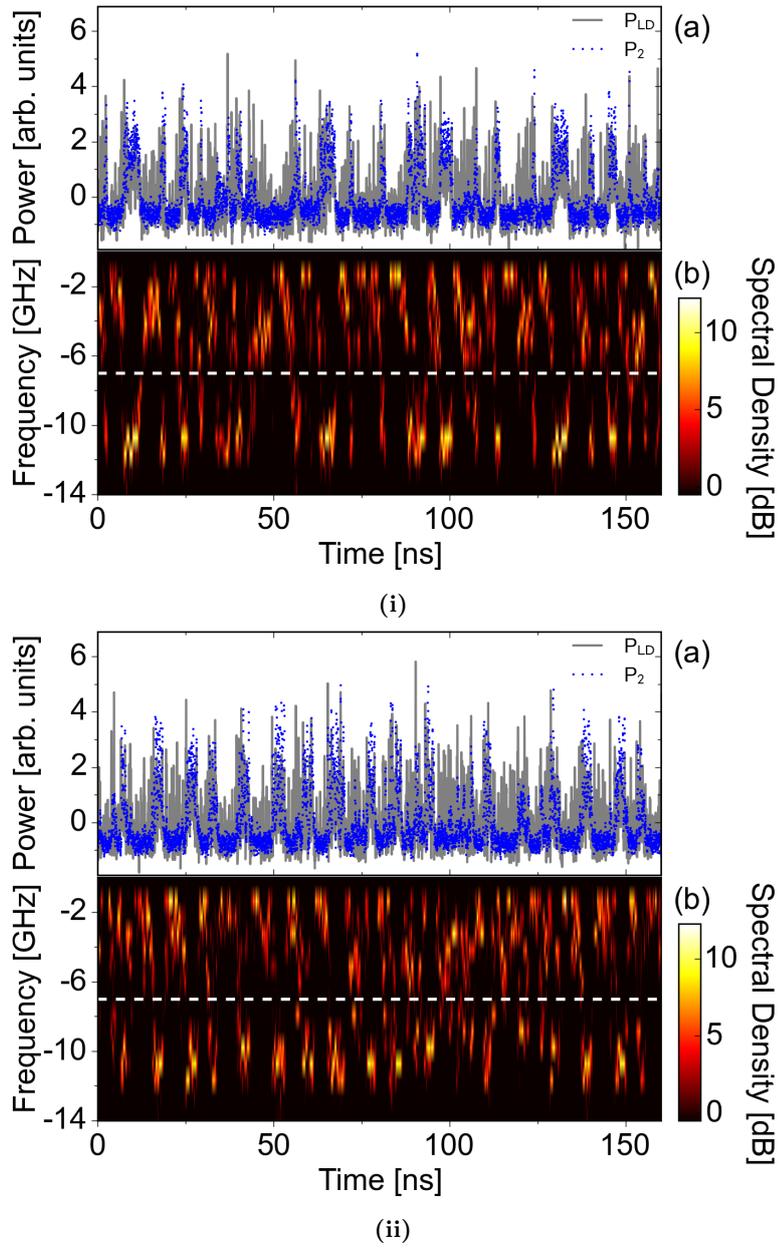
Figure 6.10: Experimental intensity and frequency time series for the pump currents of (i) $I = 1.04I_{th}$, and (ii) $I = 1.07I_{th}$. The respective panels (a) and (b) correspond to identical measurements in both experimental conditions. In panel (a) the intensity dynamics emitted by the laser is plotted in gray and the filter-resolved intensity dynamics of FBG$_2$ is plotted in blue. The full spectrogram of the frequency dynamics is depicted in panel (b). The horizontal dashed line indicates the position of the dip between both filters. The intensities have been plotted in arbitrary units and the power spectral density is color-coded in dB scale.

Consistently with the time averaged picture, the spectrogram of the frequency dynamics exhibits particularly low activity in the spectral region between the filters. At any moment the spectral width is in the order of GHz, reflecting the bandwidth of the irregular nanosecond intensity pulsations. In accordance with this spectral bandwidth, many filtered external cavity modes contribute to the real-time optical spectra at each time. Altogether, the joint extraction of the intensity and the frequency dynamics represents a proper tool towards an accurate reconstruction of the evolution of our SDD system's complex dynamics.

6.4   Numerical Modeling

In this section, we introduce a model for a semiconductor laser subject to feedback from 2 frequency selective external cavities, and compare its properties with the experiments. The model is based on the Lang-Kobayashi [61] model already introduced in section 2.7. The dynamics is analyzed through an extended version of this model which consists of $2 + 2$ equations in its simplest form. The first two equations are for the slowly varying complex amplitude of the electric field $E(t)$ and the carrier number $N(t)$, respectively. The equation of the electric field is expressed in the reference frame of the solitary laser frequency. The equations are:

$$
\begin{aligned}
\dot{E}(t) &= \frac{1 + i\alpha}{2}[G(N, E) - \gamma]E(t) + \sum_{k=1}^{m} \kappa_k e^{i\varphi_k} F_k(t - \tau_k) \\
\dot{N}(t) &= \frac{I}{e} - \gamma_n N(t) - G(N, E)|E(t)|^2,
\end{aligned}
\tag{6.9}
$$

where $F_k(t)$ is the slowly varying complex amplitude of the filtered electric field that is fed back to the laser after spectral filtering from filter k, $\gamma = 0.2\ \mathrm{ps}^{-1}$ is the photon decay rate, $\gamma_n = 1\ \mathrm{ns}^{-1}$ is the decay rate for the carriers, α is the linewidth enhancement factor, I is the injection current, e is the electron charge and τ_k, κ_k and φ_k are the feedback delay time, the feedback strength and the accumulated phase of filter k, respectively. The phases are set to $\varphi_k = 0$ because in the long-cavity limit, as considered here, the phases do not play a significant role [5]. The Lang-Kobayashi approach is valid for a single longitudinal mode of the internal cavity. As we already remarked in section 6.2, this model limitation is fulfilled in the experiment. We consider a nonlinear gain $G(N, E) = g\frac{N(t) - N_0}{1 + s|E(t)|^2}$, where $g = 1.5 \cdot 10^{-8}\ \mathrm{ps}^{-1}$ is the differential gain coefficient, $N_0 = 1.8 \cdot 10^8$ the carrier number at transparency and $s = 10^{-7}$ the gain saturation coefficient. We define the dimensionless carrier number as $n = (N - N_0)g/\gamma - 1$. The threshold current of the solitary laser, $I_{th} = e\gamma_n (N_0 + \gamma/g)$, is 30.98 mA.

For ease of analytic and numerical tractability, we consider Lorentzian linear filters [202, 203]. The respective center frequency and half width at half-maximum of these filters are Ω_k and Λ_k. Then, the extended Lang Kobayashi equations (6.9) are completed with 2 equations, one for each filter,

$$
\dot{F}_k(t) = \Lambda_k E(t) + (i\Omega_k - \Lambda_k)F_k(t), \quad k = 1, 2.
\tag{6.10}
$$

This simple model approach allows for qualitative comparison with the experiments and for a detailed study of the underlying mechanisms that result in SDD dynamics. We can chose parameters similar to the experiment, which give rise to similar physical conditions and dynamical behavior. However, we do not expect a precise quantitative agreement between theory and experiment because the Lorentzian filter profile does not reflect the detailed filter characteristics of the Fiber Bragg gratings.

The numerical simulations of (6.9)-(6.10) have been performed for a set of parameter values that mimic the experimental conditions. We consider a laser with a linewidth enhancement factor of $\alpha = 3$ and two cavities with $\kappa_1 = \kappa_2 = 40$ ns^{-1}, $\Lambda_1/(2\pi) = \Lambda_2/(2\pi) = 0.5$ GHz, $\tau_1 = 106.075$ ns, $\tau_2 = 121.625$ ns, $\Omega_1/(2\pi) = -5$ GHz and $\Omega_2/(2\pi) = -15$ GHz, for several values of the injection current.

The relative equilibria of the system (6.9)-(6.10) are external modes of the the filtered feedback cavity, or filtered cavity modes (FCMs). Those modes represent rotating wave solutions with constant frequency, carrier number and field amplitude. They can be calculated analytically and their position and properties depend on laser and filter parameters, as detailed in the methods section of reference [204]. As an example, Figure 6.11 shows the FCMs in the (ω_i, n) plane. This structure of modes and anti-modes represents the skeleton that vertebrates evolution of the dynamics.
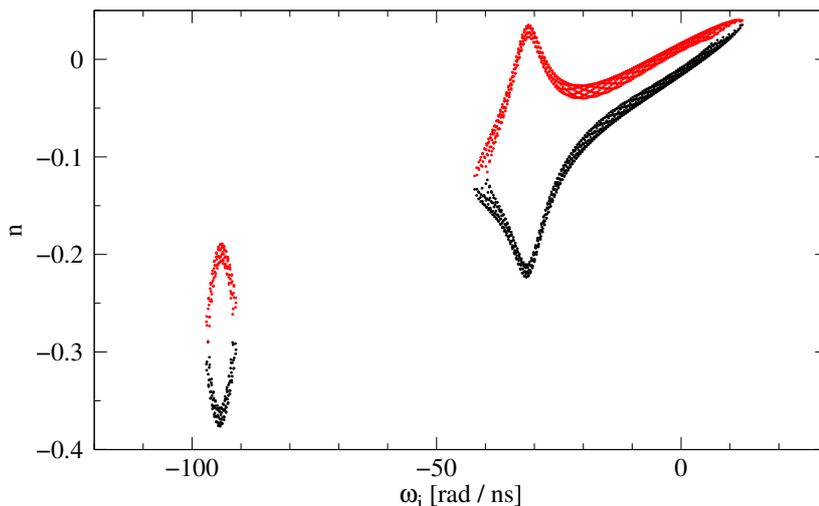
Figure 6.11: Filtered cavity modes in the (ω_i, n) plane. These points represent the relative equilibria solutions of the system of (6.9)-(6.10) with two filters. The black and red points illustrate the modes and the anti-modes, respectively. The parameters are $\alpha = 3$, $I = 0.99 I_{\text{th}}$, $\Omega_1/(2\pi) = -5$ GHz, $\Omega_2/(2\pi) = -15$ GHz, $\kappa_1 = \kappa_2 = 40$ ns^{-1}. Figure courtesy of J. Martínez-Llinàs.

Remarkably, the parameters that match the experimental conditions represent optimal conditions to exhibit SDD dynamics also in the model. As shown in Fig. 6.11, two separated islands of modes (one for each filter) are obtained for these parameter values. Similarly to the experimental system, here the parameter explored to characterize the dynamics is the injection current. For injection currents sufficiently below

threshold, $I/I_{\text{th}} < 0.99$ the system gets trapped at the most stable FCM, with lowest n and frequency close to the center frequency of the more detuned filter[3]. It is worth noting that for large delays the switching regime can start even below the solitary laser threshold. For injection currents close to the solitary laser threshold, in the interval $I/I_{\text{th}} = 0.99 - 1.1$, the system exhibits switching dynamics between the two islands of FCMs. These two separated regions correspond to the two solitary filters with different delay times. Despite of the tails of the Lorentzian filter functions, the FCMs of the system with two filters lie very close to the FCMs of the corresponding system with a single filtered feedback. One can therefore conclude that the dynamics indeed will exhibit state-dependent delay properties.
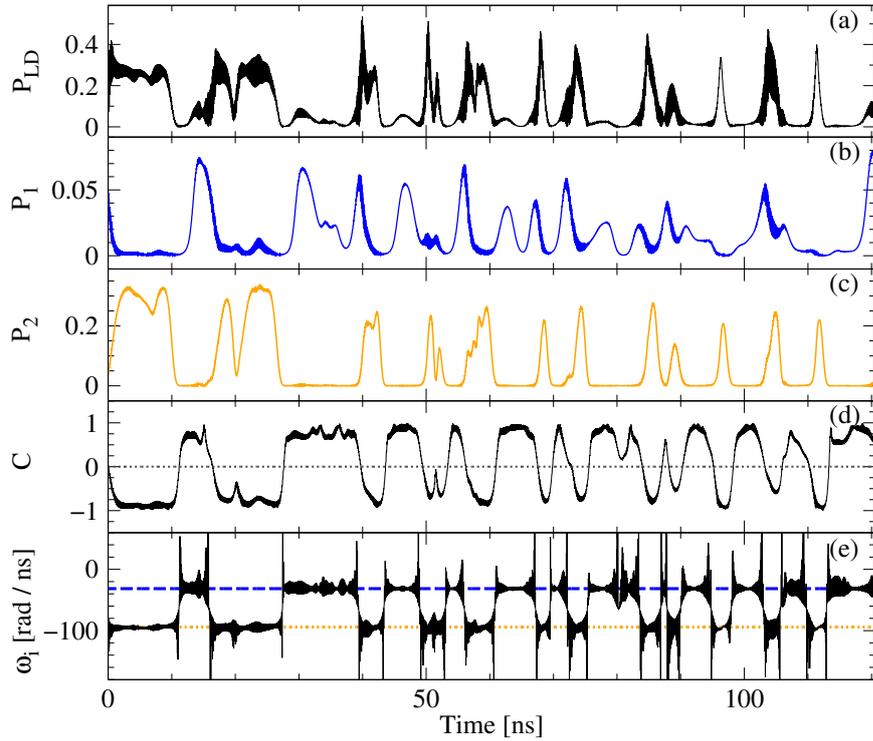
Figure 6.12: Numerical time traces for the same parameters as in Fig. 6.11: (a) intensity of the electric field, (b) $P_1(t) = |F_1(t)|^2$, (c) $P_2(t) = |F_2(t)|^2$, (d) filter contrast and (e) instantaneous optical angular frequency of the electric field. In the last panel, the dashed lines indicate Ω_1 (blue) and Ω_2 (orange). Figure courtesy of J. Martínez-Llinàs.

Figure 6.12 shows an example of the dynamical behavior when both filters are active. The intensity of the electric field is plotted in Fig. 6.12a, the intensity of the filtered fields, $P_1(t) = |F_1(t)|^2$ and $P_2(t) = |F_2(t)|^2$, are respectively plotted in Figs. 6.12b and 6.12c. Similarly to the experimental figures showing different examples of the dynamics, the filter contrast is plotted here in Figure 6.12d. In Fig. 6.12e, the corresponding in-

---

[3]The scenario described here neglects the role of noise in the simulations. The effect of adding noise is to lower the threshold at which we have switching between the filters.

stantaneous optical angular frequency (relative to the solitary laser frequency) is shown as a function of time. The jumps between filters can be compared with the corresponding periods of activity of each filter by eye. The center frequencies of the two filters are plotted as dashed lines to illustrate the time intervals in which the trajectories oscillate around the relative equilibria of each filter. The time intervals during which the trajectories are concentrated in one of the filters are typically shorter than the delay times. Please note that the time-dependent spectrograms depicted in Fig. 6.10 contain information complementary to the one plotted in the instantaneous frequency here.

For injection currents $I/I_{\mathrm{th}} > 1.1$, the dynamical evolution of the system converges to a global chaotic attractor, in which distinct jumps between the two different filters can no longer be identified. The range of currents in which state-dependent delay dynamics is found in numerical simulations has proven to be robust against changes in the parameter values [204].

6.5 Switching Characteristics

Once we have demonstrated in experiments and in simulations the existence of regimes where the dynamics can exhibit state-dependent delay switching, it becomes interesting to further characterize those switchings. The time intervals during which the trajectories are concentrated in one of the filters are always shorter than the delay times, but additional insights imply detailed characterization of the switching statistics.

Figure 6.13 depicts the experimental residence time distributions at each filter for different bias currents. State-dependent switching is present in all the bias currents depicted in Fig. 6.13. The residence times have been extracted from the contrast function for 195 μs long time traces (with a sampling time of 0.1 ns) after filtering with a cutoff frequency of 1 GHz. This filtering removes the fastest noisy oscillations, unrelated to switches in delay states. In all panels one can recognize that the residence-time distributions in this irregular switching regime show a maximum of switchings on fast time scales of few nanoseconds or less. Nevertheless, for lower bias currents the system exhibits higher typical residence times than for higher bias currents. Moreover, the residence-time distributions approximately exhibit exponential tails that decay faster for higher bias currents.

In Fig. 6.14, we compare the residence time distributions of experiment and modeling for two different pump currents, corresponding to $1.0I_{\mathrm{th}}$ and $1.1I_{\mathrm{th}}$. The experimental results exhibited in panels (b) and (d) correspond to the respective curves in Fig. 6.13. Remarkably, the most interesting insight from the comparison between experiment and modeling is that the residence time distributions exhibit a similar decay. Another important similarity is that the residence times longer than the difference between the two delay times ($\tau_2 - \tau_1 \sim 15$ ns) are very rare. The reason is that a switching between both filters (with two different delay times) can either be caused by the dynamics within one filter state, or by a previous filter jump being fed back into the laser. Perturbations related with filter jumps will cause with high probability a change in the filter state, and therefore in the delay. Equation 6.1 predicts that these induced events will occur in
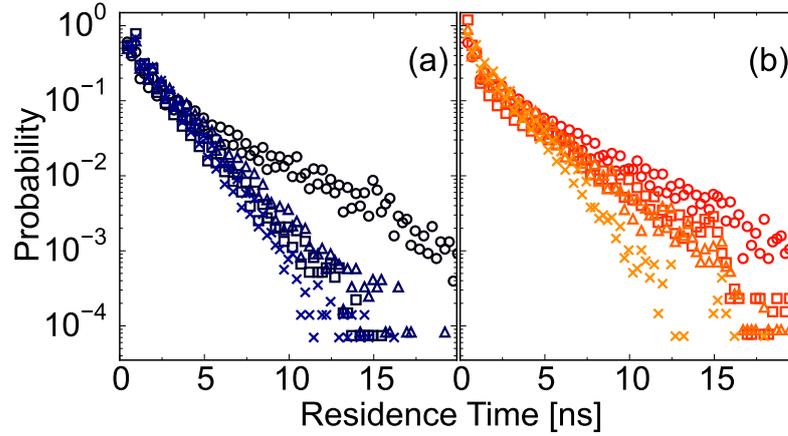
Figure 6.13: Residence-time distributions of different experimental bias currents. The residence-time distributions in the filter states corresponding to the two delays are depicted in (a) for FBG_1 and in (b) for FBG_2. Circles correspond to $1.0I_{th}$, squares to $1.04I_{th}$, triangles to $1.07I_{th}$, and crosses to $1.1I_{th}$.

intervals smaller than the difference in delay times, setting aside the spontaneous jumps as less relevant phenomena.
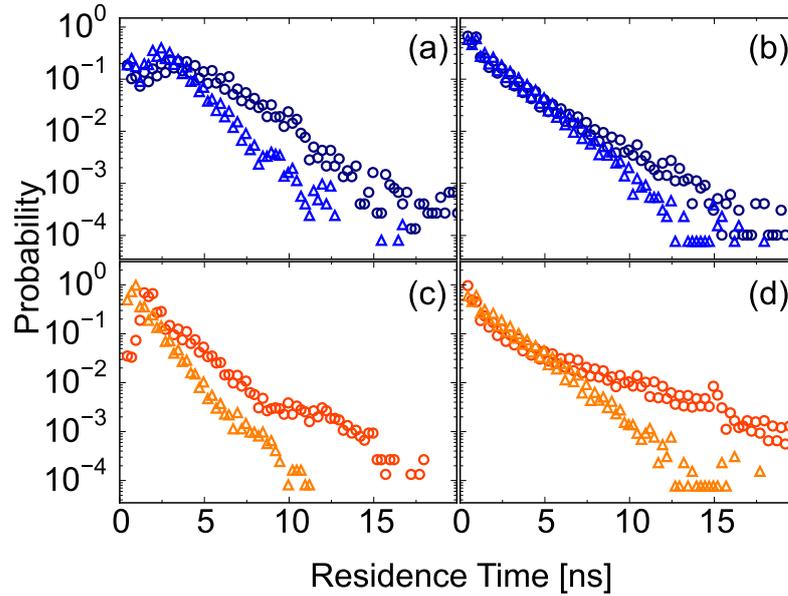
Figure 6.14: Residence-time distributions. Numerical, (a) and (c), and experimental, (b) and (d), residence-time distributions in the states corresponding to the two delays of τ_1 and τ_2. Circles correspond to $1.0I_{th}$ and crosses to $1.1I_{th}$. Panels (a) and (b) show the residence times in filter state 1 while (c) and (d) correspond to filter state 2.

6.6 Summary and Discussion

In this chapter, we have introduced a SL with feedback from two delay cavities that displays a dynamical regime dominated by SDD dynamics. In this regime the system switches in a self-organized fashion between two well-separated delays determined by the state of the system itself.

In the experiment, the two delays are implemented as two fiber delay loops of different length. Each fiber-loop mirror is enclosed by a frequency selective Bragg filter. In this system, the state-dependent delay dynamics results from the interplay between the laser bandwidth, the central frequencies and the bandwidths of the filters. In particular, the two filters must reflect disjunct frequency bands, i.e., the overlap between the filters has to be sufficiently small in order to clearly distinguish the two states. Therefore, the frequency of the optical field (that is associated to the state of the system) determines which of the two delays is active at a given time interval. Our system represents a well-controllable and reconfigurable experimental platform built from standard telecommunications components in which the dynamics can be precisely measured.

In order to gain further insight into the properties of this system, a suitable numerical model has been introduced and studied. The model consists of a rate-equations description of a semiconductor laser subject to feedback from two frequency selective external cavities. The filters selected in the model are Lorentzian-type filters. From the modeling results presented in section 6.4 (see [204] for a more complete derivation and characterization of the model), we can conclude that the phase space states of each filter in the model are analogous to those appearing in a semiconductor laser with a single delayed feedback (structures of modes and anti-modes). However, there will exist SDD dynamics in two separated regions of the phase space only as long as the filters characteristics fulfill the following requirements: the combination of filters bandwidth and central frequencies separation must result in a filtered cavity modes structure basically located in two separated regions in phase space.

The relative intensity difference of both filters (also referred as contrast function) has been shown to be a suitable quantifier to identify SDD dynamics. Both in numerics and experiments, SDD dynamics has been identified close to the laser threshold when the delay times are chosen such that the longer delay corresponds to the more detuned filter. Once the filter positions and the feedback strengths have been calibrated, the observed dynamics are tailored by using the bias current. The dynamics varies as the pump current is increased. When the bias current is below the solitary laser threshold, there exist time intervals in which the feedback is mainly coming only from one of the two filters. From the model perspective, these time intervals of feedback from a single filter correspond to trajectories in phase space which remain around the filtered cavity modes associated to a given delay loop. The observation of SDD dynamics requires not too frequent jumps between the regions in phase space associated to the two delay loops, as occurs for values close and slightly above the solitary laser threshold. In this sense, the increase of the bias current leads to more frequent jumps (with the consequent increase of the dynamics bandwidth) and causes mixing of the dynamics of the two states.

In our study we have complemented the intensity dynamics with a measurement of the frequency dynamics. This additional variable not only serves to confirm the SDD nature of the dynamics, but represents a necessary tool to comprehend how the dynamics self-organizes in different delay states. Further understanding of the mechanisms governing this self-organization will drive future investigations.

Our approach represents a prototypical study of state-dependent dynamics. Overall, it is a flexible platform that allows for a detailed experimental and theoretical exploration of SDD systems and their possible applications. In fact, it opens major opportunities to investigate different classes of SDD systems with different mathematical backgrounds. These other systems could be implemented by varying the filters positions or by increasing the number of filters. Another possibility would be to extend this system from discrete delays to continuous dependences of the delay. A possible implementation of this approach could use continuously chirped Fiber Bragg gratings.

The self-organized erratic switching between different delay states can be exploited in technological applications. In particular, control systems and encryption systems could benefit from such switching. In chapter 5, an encrypted-key exchange protocol that utilizes chaos synchronization between delay-coupled systems was introduced. In such system, the irregular switching of conditions is necessary to enhance the security of the encrypted key [166]. Irregular jumps between states induced by SDD dynamics could play this role without the need of externally controlled switching. From a control systems perspective, the self-organized switching between different delay loops potentially performing different transformations provides new possibilities. This approach allows the use of different control loops for multiple possible states or the implementation of a control-loop dependence on how far the system is from a target state.

The work presented in this chapter represents the demonstration of SDD dynamics in our system and its first characterization. Further work is required to convert SL into an ubiquitous platform to test and tailor different classes of SDD dynamics, a phenomenology of potential interest for a variety of applications.

Chapter 7

Concluding Remarks

In the present thesis, we have investigated the complex dynamics generated in semiconductor lasers when subject to delayed optical feedback or coupling, a topic situated at the crossroads between photonics and nonlinear dynamics. From the applications perspective, semiconductor lasers are particularly attractive because in more than half century of existence, they have found applications in a huge variety of fields. Thus, they have become ideal testbed platforms for the study of many nonlinear dynamics concepts and their application through photonics.

An important milestone of the present thesis has been the innovation in the methodology used to characterize delay-coupled systems. In particular, the novel use of standard techniques or well known phenomena to detect particular features of our systems. To mention two examples, the implementation of a heterodyning technique to enable the real-time detection of the optical frequency of a chaotic emitting laser and the use of zero-lag synchronization in delay-coupled lasers to detect the signature of determinism in particular dynamical events of the chaotic time series of a single delayed feedback laser.

This thesis is focused on the dynamical behavior of delay-coupled lasers from an experimental point of view. First, we have studied the dynamics of the system built from the the most basic configuration, a single laser with delayed optical feedback. It is known since decades that this system exhibits a large variety of dynamical behaviors (depending on its operating conditions) that range from CW emission to fully developed chaotic dynamics. The detection of those dynamics using state-of-the-art telecommunications technologies enabled us to experimentally characterize previously unknown features. In particular, we have unveiled simple relationships between the characteristic time scales of this system and the parameters that determine the biasing and feedback conditions. These relationships define the dynamical regime of the laser.

The dynamics has been found to exhibit similarity properties as long as the combination of system parameters leave the ratios between the characteristic time scales constant. We have therefore developed a simple rationale to rescale the observed dynamics to different absolute conditions, but always maintaining the ratios between them constant. Any targeted dynamics can be decelerated or accelerated by modifying the

feedback and pump parameters in such a way that the characteristic time scales relations are kept unaltered. This opens the possibility to apply this approach in applications where specific dynamics are required, but that face particular time-scale constraints.

Furthermore, this approach has been found valid for devices with different cavity structures and different gain media. The only limitation is that the external coupling needs to be classified as long cavity feedback, i.e., the time-scale related to the external cavity roundtrip time must be much larger than the time scale related to the relaxation oscillations frequency. Given that our approach has demonstrated broad validity with independence of modelling, it actually represents an excellent tool to validate the suitability of specific models to predict the dynamics of the corresponding laser devices. As an example, numerical simulations with a rate-equations based model of a single-mode laser with optical feedback confirm the scaling properties, at least within the range of validity of the model.

Semiconductor lasers, when subject to delayed optical feedback, can exhibit pronounced nonlinear dynamics. The effects of feedback and coupling on intrinsic laser properties, like the relaxation oscillations frequency and damping, are usually not known and are not easy to determine. We have found that the autocorrelation function, which is a linear measurement on the intensity time series, provides information on those properties when it is compared to the analytic expressions of the autocorrelation function of a stochastic model of a linear oscillator with delay. The physical motivation behind this model is to consider that the laser system can under some circumstances be approximated as a damped linear oscillator, and to emulate all the dynamics and spectral complex behavior caused by the delayed feedback as white noise. The fit of the experimental autocorrelation function (for a variety of experimental conditions) allows to extract model parameters that can be related to laser parameters. Obviously, the model only captures the linear properties of the dynamics. Still, the insights obtained from the comparison between the linear model and the delayed feedback laser can serve as a tool to interpret the dynamical regimes found in delay-coupled systems.

Second, we have studied the dynamics of coupled laser systems. In a unidirectional coupling scheme (open-loop configuration), we have studied the interrelation between intensity dynamics autocorrelation of the delayed feedback drive laser and its synchronization to the response laser. We have demonstrated that the characteristic trend followed by the magnitude of the τ-lagged autocorrelation coefficient is replicated in the identical synchronization coefficient of the response laser. This result suggests that consistency properties of the single delayed feedback laser can be used to predict fairly well the synchronization behavior in delay-coupling configurations.

Next, we studied the phenomenon of isochronous identical synchronization in a system of two mutually coupled lasers with self-feedback. This phenomenon is of particular interest for us due to the implications it has for the key-exchange protocol we explore in this thesis. That is why we have fundamentally characterized the feasibility of the isochronous identical synchronization and its robustness before implementing any practical application. The frequency detuning has been explored as an important coupling asymmetry, since identical synchronization is only possible inside the frequency locking

region. Under the zero-frequency detuning conditions, the robustness of the identical synchronization solution has been investigated for different pumping conditions.

If all the system asymmetries were reduced to a minimum, the two mutually coupled lasers with a passive relay should behave identically, their dynamics should correspond to that of a laser with delayed feedback. Nevertheless, effects related to the dynamical regime like strong or weak chaos and the influence of noise distort the synchronized state. In this sense, noise can induce transient desynchronization periods, also called bubbling events, that we have found to be unavoidable in the experimental implementation of this type of coupling configuration. Different dynamical regimes (explored through the bias current parameter in our experiment) present different levels of influence of bubbling. The existence of bubbling has important implications for applications in chaos communications.

From the application point of view, the phenomenon of identical chaos synchronization emerging between two mutually-coupled semiconductor lasers through a passive relay has been used to experimentally demonstrate a scheme that allows to negotiate an encrypted key through a public channel. This key is generated from the synchronized bits, that are concealed from eavesdropping through chaos encryption.

The key is generated at a rate that is independent (in principle) of the coupling distance between both lasers since the information is continuously fed into every laser from the passive relay element. This feature represents an advantage with respect to other classical key-distribution systems that rely in sharing information between two units placed at the extremes of the communication channel, and therefore the information needs to travel an amount of time proportional to the length of the communication channel for every bit generated.

We have also investigated the security aspects related to our scheme. In particular, the possibility to use privacy amplification to sift a more secure key with a user-defined level of information leakage. This process has an impact on the length of the exchanged key. The more iterations of the privacy amplification algorithm we do, the shorter will be the length of the final key. Even after reinforcing the key privacy so that Eve has a probability below 0.50003 to correctly identify the exchanged bits, we are able to experimentally exchange a private key at 11 Mbit/s, a high enough bit rate to be used as a one-time pad for secure private communications.

In the last line of research presented in this thesis, we have studied the fundamental properties of a semiconductor laser with feedback from two delay cavities that displays a dynamical regime dominated by state-dependent dynamics. In this regime the system switches in a self-organized fashion between two well-separated delays determined by the state of the system itself. Our system is the first experimental and optical implementation of such kind of systems. It represents a well-controllable and reconfigurable experimental platform built from standard telecommunications components in which the dynamics can be precisely measured.

The insights gained from the experimental implementation of this system can be complemented by means of the comparison with a suitable numerical model. The model consists in a rate-equations description of a semiconductor laser subject to feedback

from two frequency selective external cavities, where the frequency selective elements are Lorentzian-type filters. Similarly to what we observed in the experiment, the combination of filters bandwidth and central frequencies separation must result in a filtered cavity modes structure basically located in two separated regions in phase space.

In the laser system with two mutually exclusive external cavities, once the filters positioning and the feedback strengths have been calibrated, the observed dynamics are tailored by using the bias current, both in experiment and numerics. The dynamics varies as the pump current is increased. The limits in pump current and filters detuning for which we can obtain state-dependent delay dynamics are explored.

The system that we have setup offers a platform to study state-dependent delay dynamics. Overall, the detailed experimental and theoretical exploration of this systems opens the path to possible future applications in the many fields where state-dependent equations can be used to describe the resulting dynamics. Furthermore, the self-organized erratic switching between different delay states can be exploited in technological applications. In particular, control systems and encryption systems could benefit from such switching. The irregular switching of conditions is necessary to enhance the security of the encrypted key in secure-communications systems, where irregular jumps between states induced by SDD dynamics could play this role without the need of externally controlled switching. This system offers many possibilities to be extended towards filters with different characteristics or by increasing the number of filters, i.e., increasing the number of delay states.

Altogether, we have gained new fundamental insights in the different systems with delay-coupled interactions studied along this thesis that are useful for many applications. As an example, the finding that the dynamical properties of a laser subject to delayed optical feedback can be adjusted and tailored (slowed down or accelerated) by appropriately changing the delay time, feedback attenuation, and pump parameter is of high relevance for applications like photonic information processing. Furthermore, our fundamental insights related to consistency and to the properties of weak and strong chaos in delay-coupled lasers (e.g. the identification of the physical mechanism that generates strong chaos in semiconductor lasers) are very useful to clarify which dynamical regimes will be best to achieve high values of synchronization in systems of delay-coupled semiconductor lasers. Thus, we have profited from those results to select the optimal synchronization conditions in a system of two mutually-coupled lasers with a passive relay. The high values of synchronization have enabled the implementation of an encrypted-key exchange scheme.

In conclusion, along this thesis, fundamental and applied results in the field of semiconductor lasers optically coupled with delay have been presented. We have put special emphasis on emerging complex behaviors like state-dependent delay dynamics, deterministic chaos and synchronization, demonstrating the flexibility of SL to access different dynamical regimes and to accurately control their parameter conditions. The research in photonics technology in the last decade indicates the decided evolution towards large-scale photonic integration of components with complex functionalities and hybridization with other platforms, like silicon and graphene. It is reasonable to predict that these

steps will naturally build bridges between the photonic systems and the community of complex networks. In this scenario to come, SL are in a privileged position regarding the networks of delay-coupled elements. Those devices are ideal candidates to serve as test-bed systems to study a variety of phenomena like, e.g., the role of the network topology, the emergence of collective behavior in large networks, the role of diversity between the coupled nodes, or the presence of extreme events. The insights gained with SL can potentially be applied to other fields in which delay-coupled networks play a role, like communication networks, critical infrastructure, biology, neuroscience, or economics. Thus, offering many possibilities of symbiosis between complex photonics and these other fields of science.

Appendix A

Experimental Aspects

The majority of results presented in this thesis are of experimental nature. This appendix is intended to give further insight into the properties of the elements that compose our experimental setups: the semiconductor lasers and the optical fibers. We motivate why we choose certain components, by linking them to the role they play in the experiment.

In the first section, we introduce the most frequently used laser sources in our experiments and explain the particular features exhibited by these SL. The criteria for the selection of the lasers in the experiments that involve chaos synchronization are explained. In the next two sections, we explain the optical fiber components, the detection devices and different measurements we perform with them. Finally, we list the components and instruments used in the different experiments.

First of all, before introducing the individual elements in our setup, the laboratory environment deserves attention. Our laboratory has been shielded against external electromagnetic waves by a surrounding Faraday cage, in order to shield the experiment from wireless and radio frequencies which are in the same frequency range than the SL typical relaxation oscillations dynamics (GHz range). These external fields could cause undesired modulations and perturbations in the recorded measurements. This perturbations would be particularly sensitive in experiments that involve synchronization phenomena.

A.1   Laser Sources

In the different experiments presented along this thesis, we have used a variety of laser sources. As an example, we used three different types of lasers to test the validity of the fundamental insights found on the dynamics of delayed feedback SL in chapter 2.

One of the main interests of the present thesis relies in the exploration of synchronization of two mutually-coupled semiconductor lasers. Synchronization can only be obtained if both SL are similar, typically matching in parameters by few percent. One way to achieve almost identical properties and internal dimensions is to choose them from the same semiconductor wafer. The SL used for our synchronization experiments have been hand-selected to match. The chosen lasers exhibit single-mode emission and

narrow linewidth. The lasers have been manufactured by *Eblana Photonics*[1]. The type of lasers we use is named Discrete Mode Laser Diode (DMLD) [62]. They have a particular device structure based on a Fabry-Perot (FP) cavity with a small number of etched structures along the laser cavity. These etched structures change the refractive index in the cavity manipulating the FP cavity loss spectrum, resulting in a suppression of all cavity modes except one.

Our DMLD are either butterfly or TO-56 packaged. The butterfly packaged devices are mounted via modules that have an integrated temperature controller (TEC) with a peltier element and a thermistor to set and control the laser working temperature. The mounting of the TO-56 packaged lasers is described in 5.2. Both packagings are pigtailed with a single-mode fiber (SMF) with angled end connector (FC/APC). The laser current and temperature are controlled (Thorlabs PRO8000) with an accuracy of ± 0.01 mA and ± 0.01 C. Another characteristic of the laser packages is the absence of optical isolators at the laser output. Commercial telecommunications SL packages typically have such an optical isolator at the output to avoid back reflections that could destabilize the CW emission. Obviously, since we will use these particular devices for optical coupling purposes, optical isolators are not desired.

Basic Laser Characterization

The lasers used for the synchronization experiments in chapters 4 and 5 are very similar. We have characterized the following parameters in order to select the most similar devices: optical frequency, lasing threshold, and external differential quantum efficiency.

Here, we illustrate how close these devices are giving further details on the dependence of the emission wavelength on injection current and temperature.
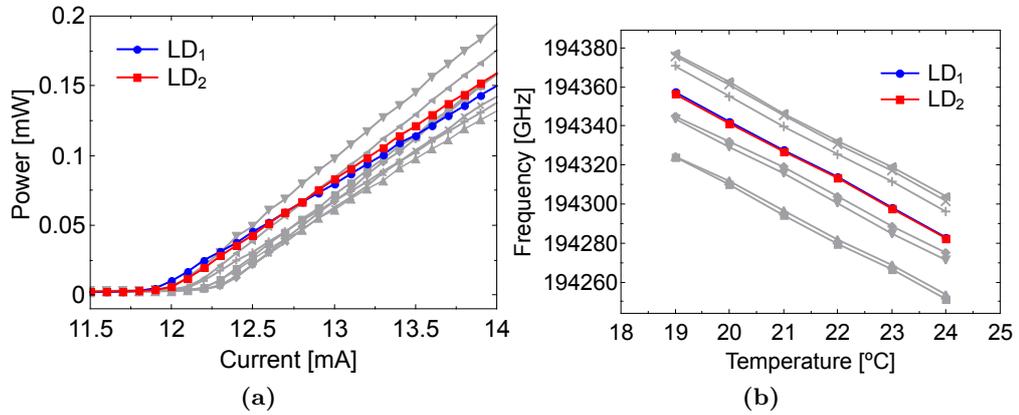
Figure A.1: Experimental optical spectrum of two DM laser diodes in zero-frequency detuning conditions.

When we refer to the experimental conditions of zero-frequency detuning, we are

---

[1]Specific reference to components and instruments is listed in section A.4

referring to a situation exemplary depicted in Figure A.2 Figure A.2 depicts an experimental spectrum of a DM laser diode at $I = 1.25I_{\text{th}}$.
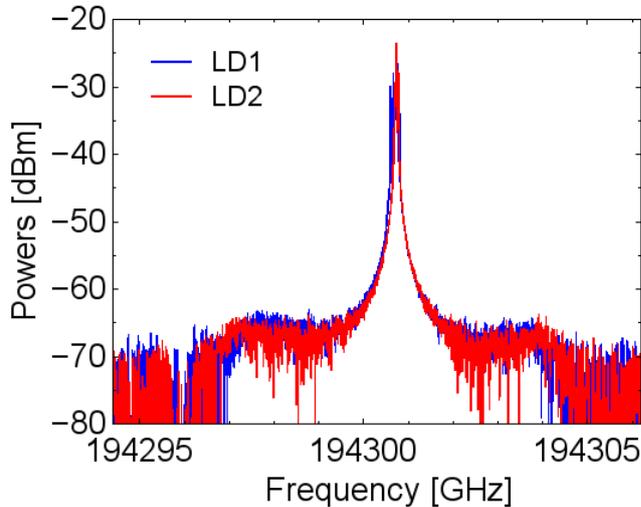
Figure A.2: Experimental optical spectrum of two DM laser diodes in zero-frequency detuning conditions.

The two different quantum well semiconductor lasers are single longitudinal-mode lasers in absence of feedback. The discrete-mode (DM) laser diode emits at 1543 nm [62], and the distributed feedback (DFB) laser emitting at 1541 nm for the standard conditions of temperature in that they are typically operated. Without external feedback, both lasers emit in single-longitudinal mode with side-mode suppression ratios of more than 40 dB and respective longitudinal mode separations of 150 GHz and 142 GHz. The **linewidth enhancement factor** of $\alpha \sim 2$ for the DM laser and of ~ 3 for the DFB laser using the Henning-Collins approach [63].

A.2 Feedback Experiments in Fiber-Based Setups

All experimental setups employed here are fiber-based with similar components to those that compose the setup in Figure A.3. This section aims to provide information of the fiber-based devices we use in our experiments.

Our setups are mostly composed of SMF components, specified for 1550 nm with a tolerance of ± 40 nm. This wavelength corresponds to optical communication wavelengths, the so called third window. It is the mostly used wavelength range for long-range telecommunications, because it is the one that implies lowest losses. All components are chosen in this window: laser sources, fiber components, and detectors. The fibers have FC/APC connectors, i. e. the input and output ends of the fiber are cleaved at an 8 °angle, which minimizes undesired back-reflections from fiber connections. Particular
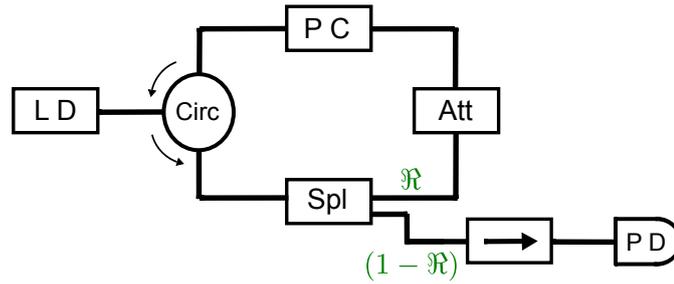
Figure A.3: Scheme of the experimental setup. LD: laser diode, Circ: optical circulator, PC: polarization controller; Att: optical attenuator, Spl: one by two intensity splitter with $\Re$ and (1-$\Re$) splitting ratios, →: optical isolator, and PD: photodiode.

fiber components we use in the experiments are couplers, polarizers, isolators, circulators, polarization controllers, interferometers, and bragg-gratings. Our fiber **couplers** have two input fibers and two output fibers like the one depicted in figure A.4:
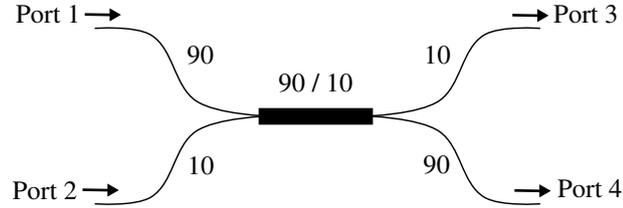
Figure A.4: Schematic picture of a fiber coupler.

Light from one input exits at both opposite outputs with a proportion that depends on the coupling percentage. The fiber coupler depicted in fig. A.4 is a 90/10 coupler. The light from anyone of the inputs is split in a proportion of 90 to 10 at the opposite two outputs. Note that the couplers do not have a predefined directionality. One of the most common methods for manufacturing fiber couplers can be fabricated fusing both fiber cores at the contact point. This causes a coupling of the mode from the mode that is propagating into the fiber to the other fibers in contact.
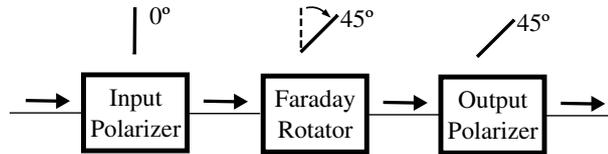
Figure A.5: Schematic picture of the internal parts of a fiber optical isolator.

Figure A.5 depicts the schematic structure of a fiber-based **isolator**. We can see that fiber isolators are composed by two polarizers and one Faraday rotator. Light injected in the forward direction is linearly polarized, shifted 45 °after the Faraday rotator and

passes through the second polarizer without loss. The light propagating in the reverse direction is isolated due to the 90 °shift respect to the input polarizer.

An **optical circulator** is another device that is based on the nonreciprocal polarization of an optical signal by Faraday effect. A basic optical circulator is a three-terminal device as illustrated in Figure ... . where terminal 1 is the input port and terminal 2 is the output port, while the reflected signal back into terminal 2 will be redirected to terminal 3 instead of terminal 1. Optical circulators have many applications in optical communication systems and optical instrumentations for redirecting optical signals. One example is the use with **fiber Bragg gratings**.
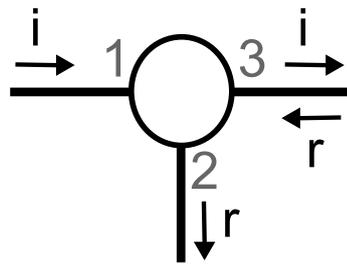
Figure A.6: Schematic picture of a fiber optic circulator.

One particularity of fiber-based setups is the importance to control the polarization of the propagating light. The polarization inside the fibers is changed by the birefringence, which is induced by stress and temperature changes. For this reason we use fiber polarization controllers in our setup. Fiber polarization controllers (Thorlabs FPC560) are designed to perform controlled polarization changes. They utilize stress induced birefringence to change the polarization state of the light. Figure A.7 shows an schematic view of a FPC. The number of loops in the three paddles are 1, 2 and 1 respectively. This configuration allows for modifying the polarization to any state. The $\lambda/2$ plate can either change the orientation of linearly polarized light or exchange the handedness of circularly polarized light. The $\lambda/4$ plates interchange linearly to circularly polarized light and vice versa. To be able to change from any polarization state of light to any other we need to align the fast axis of the fiber properly by adjusting the paddles manually.
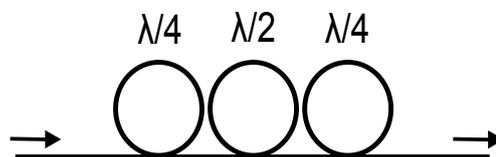
Figure A.7: Schematic picture of a fiber polarization controller (FPC) with three paddles.

A.3   Signal Detection

Semiconductor lasers subject to delayed optical feedback exhibit dynamics on different time scales. For instance, low frequency fluctuations have typical frequencies in the MHz range while the RO frequencies are in the order of GHz. The same wide range of frequencies can be found in the optical spectra. The external cavity modes are typically separated by hundreds of MHz and the laser diode modes are separated by hundreds of GHz. The detection setup has to account for these multiple temporal and spectral scales. Each one of the following devices measures different quantities and covers different ranges:

- The optical power meter (Thorlabs PM30) is used to measure the optical power the SL emits. It is composed by a slow p-i-n-photodiode with sensitivity in the 700-1800 nm window and a power resolution @ 1550 nm of ~ 1 nW.

- The optical spectrum analyzer (Anritsu MS9710C) is a grating spectrometer that measures the optical spectrum of the SL with enough precision (0.1 nm) to resolve the longitudinal modes of the diode cavity, which are separated in our lasers by $\simeq 1.2$ nm. The detection bandwidth of the optical spectrum analyzer (OSA) ranges from 600 to 1750 nm. The optical spectra have been measured with a high-resolution Brillouin Optical Spectrum Analyzer (BOSA) with 10 MHz resolution [38]. The BOSA combines high resolution with a broad scan range. Given that the optical bandwidth of the laser easily increases by more than three orders of magnitude under the influence of optical feedback [39, 200], this combination is essential to detect the interaction between the delayed feedback dynamics and the relaxation oscillations laser dynamics with good accuracy over a wide range of feedback strengths.

- Fast photodiodes (Miteq DR-125G-A) with 13 GHz bandwidth detect the intensity dynamics of the system. The output signal from the photodiodes is electrically amplified before arriving to the oscilloscope or to the electrical spectrum analyzer.

- The electrical spectrum analyzer (Anritsu MS2667C) measures the frequency and amplitude of the signal coming from the photodiode in the frequency domain. The detection bandwidth of the electrical spectrum analyzer (ESA) ranges from 9 kHz to 30 GHz. A DC block at the input of the ESA blocks frequencies ≤ 7 kHz.

- A high bandwidth oscilloscope (LeCroy SDA816Zi) detects the output signal from the photodiode in the time domain. The oscilloscope bandwidth is 16 GHz and we can measure simultaneously 4 channels at a sampling rate of 40 GS/s.

A.4   List of Instruments and Components

In this section we present the detailed references to the components and instruments used in the experiments:

1. Eblana EP1550-DM-BAK-001: DM Laser Diode

2. Toptica LD-1550-0050-DFB-1: DFB Laser Diode

3. Covega SOA-7345: Semiconductor Optical Amplifier

4. Thorlabs SLD1550S-A2: Super-Luminescent Diode

5. Thorlabs LM14S2: Butterfly Mount

6. Thorlabs PRO8000: LD Controller

7. Newport 8016: Modular LD Controller

8. Absys C-WD-AL-XX-H-2210-35-AP/AP: Fiber Coupler with XX% coupling ratio

9. FCIR-55-222-LLL-1: Polarization Insensitive Fiber Optic Circulator

10. Absys PII-55-P-D-2-22-LL-1: Fiber isolator

11. Thorlabs FPC560: Fiber Polarization Controller

12. Fibrepro PC1100: In-Line Polarization Controller

13. Eigenlight 420 WDM: Optical Attenuator / Power Monitor

14. EO-Space AZ-5K5-20-PFA-PFA-UV: (Lithium Niobate) Electro-Optic Intensity Modulator

15. Thorlabs PM30: Optical Powermeter

16. Anritsu MS9710C: Optical Spectrum Analyzer

17. Aragon Photonics BOSA: High-Resolution Optical Spectrum Analyzer

18. Miteq DR-125G-A / Miteq SCMR-100K20G-30-15-10-FA: Fast Photodiodes

19. Anritsu MS2667C: Electrical Spectrum Analyzer

20. LeCroy SDA816Zi: High Bandwidth Oscilloscope

21. Tektronix AWG7122B: Arbitrary Waveform Generator

22. HP 83623A: Signal Generator / Sweeper

23. Mini-Circuits ZX86-12G-8+: Bias-Tee

Abbreviations

- SL: Semiconductor Laser

- LD: Laser Diode

- LR: Reference Laser Diode

- FC/APC: Ferrule Connector/Angled Physical Contact

- AC: Autocorrelation Function

- FB: Feedback

- NL: Nonlinear

- SNR: Signal-to-Noise Ratio

- LK: Lang-Kobayashi Rate-Equations Model

- LFF: Low-Frequency Fluctuations

- URO: Undamped Relaxation Oscillations

- STD: Space-Time Diagram

- CW: Continuous Wave

- QW: Quantum-Well

- DM: Discrete-Mode (laser)

- DFB: Distributed Feedback (laser)

- QD: Quantum-Dot

- GS: Ground State (in QD lasers)

- ES: Excited State (in QD lasers)

- LM: Linear Model

- FFT: Fast-Fourier Transform

- CS: Chaos Synchronization

- BER: Bit-Error Rate

- FBG: Fiber-Bragg Grating

- SDD: State-Dependent Delay

Bibliography

[1] A. Chraplyvy and R. Tkach, "What is the actual capacity of single-mode fibers in amplified lightwave systems?," *IEEE Photonics Technology Letters*, vol. 5, pp. 666–668, June 1993.

[2] H. J. Caulfield and S. Dolev, "Why future supercomputing requires optics," *Nature Photonics*, vol. 4, pp. 261–263, May 2010.

[3] D. Woods and T. J. Naughton, "Optical computing: Photonic neural networks," *Nature Physics*, vol. 8, pp. 257–259, Apr. 2012.

[4] G. R. Gray, A. T. Ryan, G. P. Agrawal, and E. C. Gage, "Control of Optical-Feedback-Induced Laser Intensity Noise in Optical Data Recording," *Optical Engineering*, vol. 32, p. 739, Apr. 1993.

[5] M. C. Soriano, J. García-Ojalvo, C. R. Mirasso, and I. Fischer, "Complex photonics: Dynamics and applications of delay-coupled semiconductors lasers," *Reviews of Modern Physics*, vol. 85, pp. 421–470, Mar. 2013.

[6] R. Hall, G. Fenner, J. Kingsley, T. Soltys, and R. Carlson, "Coherent Light Emission From GaAs Junctions," *Physical Review Letters*, vol. 9, pp. 366–368, Nov. 1962.

[7] M. I. Nathan, W. P. Dumke, G. Burns, F. H. Dill, and G. Lasher, "Stimulated Emission of Radiation from GaAs p-n Junctions," *Applied Physics Letters*, vol. 1, p. 62, Dec. 1962.

[8] T. M. Quist, R. H. Rediker, R. J. Keyes, W. E. Krag, B. Lax, A. L. McWhorter, and H. J. Zeigler, "Semiconductor Maser of GaAs," *Applied Physics Letters*, vol. 1, p. 91, Dec. 1962.

[9] J. J. Coleman, "The development of the semiconductor laser diode after the first demonstration in 1962," *Semiconductor Science and Technology*, vol. 27, p. 090207, Sept. 2012.

[10] J. Faist, F. Capasso, D. Sivco, C. Sirtori, A. Hutchinson, and A. Cho, "Quantum cascade laser: An intersub-band semiconductor laser operating above liquid nitrogen temperature," *Electronics Letters*, vol. 30, no. 11, p. 865, 1994.

[11] M. S. Vitiello, G. Scalari, B. Williams, and P. De Natale, "Quantum cascade lasers: 20 years of challenges," *Optics Express*, vol. 23, p. 5167, Feb. 2015.

[12] W. M. Macek and D. T. M. Davis, "Rotation rate sensing with traveling-wave ring lasers," *Applied Physics Letters*, vol. 2, p. 67, Nov. 1963.

[13] W. W. Chow, J. Gea-Banacloche, L. M. Pedrotti, V. E. Sanders, W. Schleich, and M. O. Scully, "The ring laser gyro," *Reviews of Modern Physics*, vol. 57, pp. 61–104, Jan. 1985.

[14] R. Broom, "Self modulation at gigahertz frequencies of a diode laser coupled to an external cavity," *Electronics Letters*, vol. 5, no. 23, p. 571, 1969.

[15] R. Broom, E. Mohn, C. Risch, and R. Salathe, "Microwave self-modulation of a diode laser coupled to an external cavity," *IEEE Journal of Quantum Electronics*, vol. 6, pp. 328–334, June 1970.

[16] C. Risch and C. Voumard, "Self-pulsation in the output intensity and spectrum of GaAs-AlGaAs cw diode lasers coupled to a frequency-selective external optical cavity," *Journal of Applied Physics*, vol. 48, p. 2083, Aug. 1977.

[17] T. Heil, I. Fischer, and W. Elsäßer, "Stabilization of feedback-induced instabilities in semiconductor lasers," *Journal of Optics B: Quantum and Semiclassical Optics*, vol. 2, pp. 413–420, June 2000.

[18] J. Môrk, B. Tromborg, and J. Mark, "Chaos in semiconductor lasers with optical feedback: Theory and experiment," *IEEE Journal of Quantum Electronics*, vol. 28, pp. 93–108, Jan. 1992.

[19] I. Fischer, O. Hess, W. Elsäßer, and E. Göbel, "High-Dimensional Chaotic Dynamics of an External Cavity Semiconductor Laser," *Physical Review Letters*, vol. 73, pp. 2188–2191, Oct. 1994.

[20] T. Heil, I. Fischer, W. Elsäßer, J. Mulet, and C. Mirasso, "Chaos Synchronization and Spontaneous Symmetry-Breaking in Symmetrically Delay-Coupled Semiconductor Lasers," *Physical Review Letters*, vol. 86, pp. 795–798, Jan. 2001.

[21] A. Argyris, D. Syvridis, L. Larger, V. Annovazzi-Lodi, P. Colet, I. Fischer, J. García-Ojalvo, C. R. Mirasso, L. Pesquera, and K. A. Shore, "Chaos-based communications at high bit rates using commercial fibre-optic links.," *Nature*, vol. 438, pp. 343–6, Nov. 2005.

[22] A. Uchida, K. Amano, M. Inoue, K. Hirano, S. Naito, H. Someya, I. Oowada, T. Kurashige, M. Shiki, S. Yoshimori, K. Yoshimura, and P. Davis, "Fast physical random bit generation with chaotic semiconductor lasers," *Nature Photonics*, vol. 2, pp. 728–732, Nov. 2008.

[23] M. Peil, I. Fischer, W. Elsäßer, S. Bakic, N. Damaschke, C. Tropea, S. Stry, and J. Sacher, "Rainbow refractometry with a tailored incoherent semiconductor laser source," *Applied Physics Letters*, vol. 89, p. 091106, Aug. 2006.

[24] R. J. Manning, A. D. Ellis, A. J. Poustie, and K. J. Blow, "Semiconductor laser amplifiers for ultrafast all-optical signal processing," *Journal of the Optical Society of America B*, vol. 14, p. 3204, Nov. 1997.

[25] D. Brunner, M. C. Soriano, C. R. Mirasso, and I. Fischer, "Parallel photonic information processing at gigabyte per second data rates using transient states.," *Nature communications*, vol. 4, p. 1364, Jan. 2013.

[26] K. Pyragas, "Continuous control of chaos by self-controlling feedback," *Physics Letters A*, vol. 170, pp. 421–428, Nov. 1992.

[27] G. Stepan, "Delay effects in brain dynamics. Introduction.," *Philosophical transactions. Series A, Mathematical, physical, and engineering sciences*, vol. 367, pp. 1059–62, Mar. 2009.

[28] G. Orosz, R. E. Wilson, R. Szalai, and G. Stépán, "Exciting traffic jams: Nonlinear phenomena behind traffic jam formation on highways," *Physical Review E*, vol. 80, p. 046205, Oct. 2009.

[29] M. C. Mackey and L. Glass, "Oscillation and Chaos in Physiological Control Systems," *Science*, vol. 197, pp. 287–289, 1977.

[30] M. B. Elowitz and S. Leibler, "A synthetic oscillatory network of transcriptional regulators.," *Nature*, vol. 403, pp. 335–8, Jan. 2000.

[31] L. Chen and K. Aihara, "Stability of genetic regulatory networks with time delay," *IEEE Transactions on Circuits and Systems I: Fundamental Theory and Applications*, vol. 49, pp. 602–608, May 2002.

[32] M. Yeung and S. Strogatz, "Time Delay in the Kuramoto Model of Coupled Oscillators," *Physical Review Letters*, vol. 82, pp. 648–651, Jan. 1999.

[33] C. Masoller, A. C. Mart, and D. H. Zanette, "Synchronization in an array of globally coupled maps with delayed interactions," *Physica A: Statistical Mechanics and its Applications*, vol. 325, pp. 186–191, July 2003.

[34] A. Yariv, *Quantum Electronics.* John Wiley & sons, 3 ed., 1989.

[35] C. Henry, "Theory of the linewidth of semiconductor lasers," *IEEE Journal of Quantum Electronics*, vol. 18, pp. 259–264, Feb. 1982.

[36] R. Tkach and A. Chraplyvy, "Regimes of feedback effects in 1.5-μm distributed feedback lasers," *Journal of Lightwave Technology*, vol. 4, no. 11, pp. 1655–1661, 1986.

[37] I. Fischer, "Emission dynamics of semiconductor lasers subject to delayed optical feedback: An experimentalists perspective," in *AIP Conference Proceedings*, vol. 548, pp. 218–237, AIP, Dec. 2000.

[38] A. Villafranca, J. Lazaro, I. Salinas, and I. Garces, "Measurement of the linewidth enhancement factor in DFB lasers using a high-resolution optical spectrum analyzer," *IEEE Photonics Technology Letters*, vol. 17, pp. 2268–2270, Nov. 2005.

[39] D. Lenstra, B. Verbeek, and A. Den Boef, "Coherence collapse in single-mode semiconductor lasers due to optical feedback," *IEEE Journal of Quantum Electronics*, vol. 21, pp. 674–679, June 1985.

[40] S. Singh, *The Code Book: The Secret History of Codes and Code-breaking*. Fourth State, 2000.

[41] R. L. Rivest, A. Shamir, and L. Adleman, "A method for obtaining digital signatures and public-key cryptosystems," *Communications of the ACM*, vol. 21, pp. 120–126, Feb. 1978.

[42] P. Shor, "Algorithms for quantum computation: discrete logarithms and factoring," in *Proceedings 35th Annual Symposium on Foundations of Computer Science*, pp. 124–134, IEEE Comput. Soc. Press, 1994.

[43] A. Pikovsky, M. Rosenblum, and J. Kurths, *Synchronization - A Universal Concept in Nonlinear Sciences*. Nonlinear Science and Fluid Dynamics, Cambridge University Press, 2001.

[44] H. Fujisaka and T. Yamada, "Stability Theory of Synchronized Motion in Coupled-Oscillator Systems," *Progress of Theoretical Physics*, vol. 69, pp. 32–47, Jan. 1983.

[45] A. S. Pikovsky, "On the interaction of strange attractors," *Zeitschrift fr Physik B Condensed Matter*, vol. 55, pp. 149–154, June 1984.

[46] V. S. Afraimovich, N. N. Verichev, and M. I. Rabinovich, "Stochastic synchronization of oscillation in dissipative systems," *Radiophysics and Quantum Electronics*, vol. 29, pp. 795–803, Sept. 1986.

[47] L. Pecora and T. Carroll, "Synchronization in chaotic systems," *Physical Review Letters*, vol. 64, pp. 821–824, Feb. 1990.

[48] L. Pecora and T. Carroll, "Driving systems with chaotic signals," *Physical Review A*, vol. 44, pp. 2374–2383, Aug. 1991.

[49] L. Pecora and T. Carroll, "Synchronization of chaotic systems," *Chaos: An Interdisciplinary Journal of Nonlinear Science*, vol. 25, p. 097611, Sept. 2015.

[50] H. G. Winful and L. Rahman, "Synchronized chaos and spatiotemporal chaos in arrays of coupled lasers," *Physical Review Letters*, vol. 65, pp. 1575–1578, Sept. 1990.

[51] I. Fischer, Y. Liu, and P. Davis, "Synchronization of chaotic semiconductor laser dynamics on subnanosecond time scales and its potential for chaos communication," *Physical Review A*, vol. 62, p. 011801, June 2000.

[52] P. Colet and R. Roy, "Digital communication with synchronized chaotic lasers," *Optics Letters*, vol. 19, p. 2056, Dec. 1994.

[53] G. D. VanWiggeren and R. Roy, "Optical Communication with Chaotic Waveforms," *Physical Review Letters*, vol. 81, pp. 3547–3550, Oct. 1998.

[54] C. Mirasso, P. Colet, and P. Garcia-Fernandez, "Synchronization of chaotic semiconductor lasers: application to encoded communications," *IEEE Photonics Technology Letters*, vol. 8, pp. 299–301, Feb. 1996.

[55] V. Annovazzi-Lodi, S. Donati, and A. Scire, "Synchronization of chaotic injected-laser systems and its application to optical cryptography," *IEEE Journal of Quantum Electronics*, vol. 32, pp. 953–959, June 1996.

[56] C. Henry and R. Kazarinov, "Instability of semiconductor lasers due to optical feedback from distant reflectors," *IEEE Journal of Quantum Electronics*, vol. 22, pp. 294–301, Feb. 1986.

[57] G. Dente, P. Durkin, K. Wilson, and C. Moeller, "Chaos in the coherence collapse of semiconductor lasers," *IEEE Journal of Quantum Electronics*, vol. 24, pp. 2441–2447, Dec. 1988.

[58] S. Lepri, G. Giacomelli, A. Politi, and F. Arecchi, "High-dimensional chaos in delayed dynamical systems," *Physica D: Nonlinear Phenomena*, vol. 70, pp. 235–249, Jan. 1994.

[59] S. Heiligenthal, T. Dahms, S. Yanchuk, T. Jüngling, V. Flunkert, I. Kanter, E. Schöll, and W. Kinzel, "Strong and Weak Chaos in Nonlinear Networks with Time-Delayed Couplings," *Physical Review Letters*, vol. 107, p. 234102, Nov. 2011.

[60] S. Heiligenthal, T. Jüngling, O. D'Huys, D. A. Arroyo-Almanza, M. C. Soriano, I. Fischer, I. Kanter, and W. Kinzel, "Strong and weak chaos in networks of semiconductor lasers with time-delayed couplings," *Physical Review E*, vol. 88, p. 012902, July 2013.

[61] R. Lang and K. Kobayashi, "External optical feedback effects on semiconductor injection laser properties," *IEEE Journal of Quantum Electronics*, vol. 16, pp. 347–355, Mar. 1980.

[62] B. Kelly, R. Phelan, D. Jones, C. Herbert, J. O'Carroll, M. Rensing, J. Wendelboe, C. Watts, A. Kaszubowska-Anandarajah, P. Perry, C. Guignard, L. Barry, and J. O'Gorman, "Discrete mode laser diodes with very narrow linewidth emission," *Electronics Letters*, vol. 43, no. 23, p. 1282, 2007.

[63] I. Henning and J. Collins, "Measurements of the semiconductor laser linewidth broadening factor," *Electronics Letters*, vol. 19, p. 927, Oct. 1983.

[64] M. Sondermann and T. Ackemann, "Correlation properties and drift phenomena in the dynamics of vertical-cavity surface-emitting lasers with optical feedback," vol. 13, no. 7, pp. 4225–4228, 2005.

[65] G. Van der Sande, M. C. Soriano, I. Fischer, and C. R. Mirasso, "Dynamics, correlation scaling, and synchronization behavior in rings of delay-coupled oscillators," *Physical Review E*, vol. 77, p. 055202, May 2008.

[66] X. Porte, M. C. Soriano, and I. Fischer, "Similarity properties in the dynamics of delayed-feedback semiconductor lasers," *Physical Review A*, vol. 89, p. 023822, Feb. 2014.

[67] A. Hohl and A. Gavrielides, "Bifurcation Cascade in a Semiconductor Laser Subject to Optical Feedback," *Physical Review Letters*, vol. 82, pp. 1148–1151, Feb. 1999.

[68] J. Mørk, J. Mark, and B. Tromborg, "Route to chaos and competition between relaxation oscillations for a semiconductor laser with optical feedback," *Physical Review Letters*, vol. 65, pp. 1999–2002, Oct. 1990.

[69] J. Ye, H. Li, and J. McInerney, "Period-doubling route to chaos in a semiconductor laser with weak optical feedback," *Physical Review A*, vol. 47, pp. 2249–2252, Mar. 1993.

[70] F. Arecchi, G. Giacomelli, A. Lapucci, and R. Meucci, "Two-dimensional representation of a delayed dynamical system," *Physical Review A*, vol. 45, pp. R4225–R4228, Apr. 1992.

[71] G. Giacomelli and A. Politi, "Relationship between Delayed and Spatially Extended Dynamical Systems," *Physical Review Letters*, vol. 76, pp. 2686–2689, Apr. 1996.

[72] G. Giacomelli, F. Marino, M. A. Zaks, and S. Yanchuk, "Coarsening in a bistable system with long-delayed feedback," *EPL (Europhysics Letters)*, vol. 99, p. 58005, Sept. 2012.

[73] A. M. Hagerstrom, T. E. Murphy, R. Roy, P. Hövel, I. Omelchenko, and E. Schöll, "Experimental observation of chimeras in coupled-map lattices," *Nature Physics*, vol. 8, pp. 658–661, July 2012.

[74] L. Larger, B. Penkovsky, and Y. Maistrenko, "Virtual Chimera States for Delayed-Feedback Systems," *Physical Review Letters*, vol. 111, p. 054103, Aug. 2013.

[75] J. Mørk, B. Tromborg, and P. Christiansen, "Bistability and low-frequency fluctuations in semiconductor lasers with optical feedback: a theoretical analysis," *IEEE journal of quantum electronics*, 1988.

[76] G. Van Tartwijk, A. Levine, and D. Lenstra, "Sisyphus effect in semiconductor lasers with optical feedback," *IEEE Journal of Selected Topics in Quantum Electronics*, vol. 1, pp. 466–472, June 1995.

[77] I. Fischer, G. van Tartwijk, A. Levine, W. Elsäßer, E. Göbel, and D. Lenstra, "Fast Pulsing and Chaotic Itinerancy with a Drift in the Coherence Collapse of Semiconductor Lasers," *Physical Review Letters*, vol. 76, pp. 220–223, Jan. 1996.

[78] T. Sano, "Antimode dynamics and chaotic itinerancy in the coherence collapse of semiconductor lasers with optical feedback," *Physical Review A*, vol. 50, pp. 2719–2726, Sept. 1994.

[79] A. Hohl, H. J. C. van der Linden, and R. Roy, "Determinism and stochasticity of power-dropout events in semiconductor lasers with optical feedback," *Optics Letters*, vol. 20, p. 2396, Dec. 1995.

[80] T. Heil, I. Fischer, and W. Elsäßer, "Coexistence of low-frequency fluctuations and stable emission on a single high-gain mode in semiconductor lasers with external optical feedback," *Physical Review A*, vol. 58, pp. R2672–R2675, Oct. 1998.

[81] A. Aragoneses, N. Rubido, J. Tiana-Alsina, M. C. Torrent, and C. Masoller, "Distinguishing signatures of determinism and stochasticity in spiking complex systems," *Scientific Reports*, vol. 3, May 2013.

[82] K. Hicke, X. Porte, and I. Fischer, "Characterizing the deterministic nature of individual power dropouts in semiconductor lasers subject to delayed feedback," *Physical Review E*, vol. 88, p. 052904, Nov. 2013.

[83] V. Ahlers, U. Parlitz, and W. Lauterborn, "Hyperchaotic dynamics and synchronization of external-cavity semiconductor lasers," *Physical Review E*, vol. 58, pp. 7208–7213, Dec. 1998.

[84] A. Levine, G. van Tartwijk, D. Lenstra, and T. Erneux, "Diode lasers with optical feedback: Stability of the maximum gain mode," *Physical Review A*, vol. 52, pp. R3436–R3439, Nov. 1995.

[85] Y. Arakawa, "Multidimensional quantum well laser and temperature dependence of its threshold current," *Applied Physics Letters*, vol. 40, p. 939, June 1982.

[86] M. Asada, Y. Miyamoto, and Y. Suematsu, "Gain and the threshold of three-dimensional quantum-box lasers," *IEEE Journal of Quantum Electronics*, vol. 22, pp. 1915–1921, Sept. 1986.

[87] M. Grundmann, U. Richter, V. Ustinov, P. Kop'ev, N. Kirstaedter, D. Bimberg, P. Werner, S. Ruvimov, N. Ledentsov, U. Gösele, Z. Alferov, J. Heydenreich, and M. Maximov, "Low threshold, large T_0 injection laser emission from (InGa)As quantum dots," *Electronics Letters*, vol. 30, pp. 1416–1417, Aug. 1994.

[88] K. Mukai, N. Ohtsuka, M. Sugawara, and S. Yamazaki, "Self-Formed InGaAs Quantum Dots on GaAs Substrates Emitting at 1.3μm," *Japanese Journal of Applied Physics*, vol. 33, pp. L1710–L1712, Dec. 1994.

[89] D. Bimberg, N. Kirstaedter, N. Ledentsov, Z. Alferov, P. Kop'ev, and V. Ustinov, "InGaAs-GaAs quantum-dot lasers," *IEEE Journal of Selected Topics in Quantum Electronics*, vol. 3, pp. 196–205, Apr. 1997.

[90] D. Bimberg, M. Grundmann and N. N. Ledentsov, *Quantum Dot Heterostructures*. New York: Wiley, 1999.

[91] D. Bimberg, "Quantum dot based nanophotonics and nanoelectronics," *Electronics Letters*, vol. 44, no. 3, p. 168, 2008.

[92] K. Lüdge, M. Bormann, E. Malić, P. Hövel, M. Kuntz, D. Bimberg, A. Knorr, and E. Schöll, "Turn-on dynamics and modulation response in semiconductor quantum dot lasers," *Physical Review B*, vol. 78, p. 035316, July 2008.

[93] T. Erneux, E. A. Viktorov, B. Kelleher, D. Goulding, S. P. Hegarty, and G. Huyet, "Optically injected quantum-dot lasers.," *Optics letters*, vol. 35, pp. 937–9, Apr. 2010.

[94] A. Markus, J. X. Chen, C. Paranthoen, A. Fiore, C. Platz, and O. Gauthier-Lafaye, "Simultaneous two-state lasing in quantum-dot lasers," *Applied Physics Letters*, vol. 82, p. 1818, Mar. 2003.

[95] D. O'Brien, S. Hegarty, G. Huyet, J. McInerney, T. Kettler, M. Laemmlin, D. Bimberg, V. Ustinov, A. Zhukov, S. Mikhrin, and A. Kovsh, "Feedback sensitivity of 1.3μm InAsGaAs quantum dot lasers," *Electronics Letters*, vol. 39, no. 25, p. 1819, 2003.

[96] S. Azouigui, B. Dagens, F. Lelarge, J. G. Provost, D. Make, O. Le Gouezigou, A. Accard, A. Martinez, K. Merghem, F. Grillot, O. Dehaese, R. Piron, S. Loualiche, and A. Ramdane, "Optical Feedback Tolerance of Quantum-Dot- and Quantum-Dash-Based Semiconductor Lasers Operating at 1.55μm," *IEEE Journal of Selected Topics in Quantum Electronics*, vol. 15, no. 3, pp. 764–773, 2009.

[97] K. Lüdge (Editor), *Nonlinear Laser Dynamics: From Quantum Dots to Cryptography*. Weinheim: Wiley-VCH Verlag & Co., 2011.

[98] D. O'Brien, S. P. Hegarty, G. Huyet, and A. V. Uskov, "Sensitivity of quantum-dot semiconductor lasers to optical feedback," *Optics Letters*, vol. 29, no. 10, p. 1072, 2004.

[99] B. Lingnau, W. W. Chow, and K. Lüdge, "Amplitude-phase coupling and chirp in quantum-dot lasers: influence of charge carrier scattering dynamics.," *Optics express*, vol. 22, pp. 4867–79, Mar. 2014.

[100] E. A. Viktorov, P. Mandel, I. O'Driscoll, O. Carroll, G. Huyet, J. Houlihan, and Y. Tanguy, "Low-frequency fluctuations in two-state quantum dot lasers," *Optics Letters*, vol. 31, no. 15, p. 2302, 2006.

[101] M. Virte, S. Breuer, M. Sciamanna, and K. Panajotov, "Switching between ground and excited states by optical feedback in a quantum dot laser diode," *Applied Physics Letters*, vol. 105, p. 121109, Sept. 2014.

[102] M. Virte, K. Panajotov, and M. Sciamanna, "Mode Competition Induced by Optical Feedback in Two-Color Quantum Dot Lasers," *IEEE Journal of Quantum Electronics*, vol. 49, pp. 578–585, July 2013.

[103] N. Oliver, T. Jüngling, and I. Fischer, "Consistency Properties of a Chaotic Semiconductor Laser Driven by Optical Feedback," *Physical Review Letters*, vol. 114, p. 123902, Mar. 2015.

[104] K. Petermann, "External optical feedback phenomena in semiconductor lasers," *IEEE Journal of Selected Topics in Quantum Electronics*, vol. 1, pp. 480–489, June 1995.

[105] T. Heil, I. Fischer, and W. Elsäßer, "Influence of amplitude-phase coupling on the dynamics of semiconductor lasers subject to optical feedback," *Physical Review A*, vol. 60, pp. 634–641, July 1999.

[106] B. Dorizzi, "Statistics and dimension of chaos in differential delay systems," *Physical Review A*, vol. 35, no. 1, pp. 328–339, 1987.

[107] V. S. Anishchenko, G. a. Okrokvertskhov, T. E. Vadivasova, and G. I. Strelkova, "Mixing and spectral-correlation properties of chaotic and stochastic systems: numerical and physical experiments," *New Journal of Physics*, vol. 7, pp. 76–76, Mar. 2005.

[108] W. Just, H. Kantz, C. Rödenbeck, and M. Helm, "Stochastic modelling: replacing fast degrees of freedom by noise," *Journal of Physics A: Mathematical and General*, vol. 34, pp. 3199–3213, Apr. 2001.

[109] X. Porte, O. D'Huys, T. Jüngling, D. Brunner, M. C. Soriano, and I. Fischer, "Autocorrelation properties of chaotic delay dynamical systems: A study on semiconductor lasers," *Physical Review E*, vol. 90, p. 052911, Nov. 2014.

[110] J. Cohen, F. Wittgrefe, M. Hoogerland, and J. Woerdman, "Optical spectra of a semiconductor laser with incoherent optical feedback," *IEEE Journal of Quantum Electronics*, vol. 26, pp. 982–990, June 1990.

[111] R. Hegger, M. Bünner, H. Kantz, and A. Giaquinta, "Identifying and Modeling Delay Feedback Systems," *Physical Review Letters*, vol. 81, pp. 558–561, July 1998.

[112] V. S. Udaltsov, J.-P. Goedgebuer, L. Larger, J.-B. Cuenot, P. Levy, and W. T. Rhodes, "Cracking chaos-based encryption systems ruled by nonlinear time delay differential equations," *Physics Letters A*, vol. 308, pp. 54–60, Feb. 2003.

[113] M. Prokhorov, V. Ponomarenko, A. Karavaev, and B. Bezruchko, "Reconstruction of time-delayed feedback systems from time series," *Physica D: Nonlinear Phenomena*, vol. 203, pp. 209–223, Apr. 2005.

[114] M. Siefert, "Practical criterion for delay estimation using random perturbations," *Physical Review E*, vol. 76, p. 026215, Aug. 2007.

[115] D. Rontani, A. Locquet, M. Sciamanna, and D. S. Citrin, "Loss of time-delay signature in the chaotic output of a semiconductor laser with optical feedback," *Optics Letters*, vol. 32, no. 20, p. 2960, 2007.

[116] D. Rontani, A. Locquet, M. Sciamanna, D. S. Citrin, and S. Ortin, "Time-Delay Identification in a Chaotic Semiconductor Laser With Optical Feedback: A Dynamical Point of View," *IEEE Journal of Quantum Electronics*, vol. 45, pp. 879–1891, July 2009.

[117] L. Zunino, M. C. Soriano, I. Fischer, O. A. Rosso, and C. R. Mirasso, "Permutation-information-theory approach to unveil delay dynamics from time-series analysis," *Physical Review E*, vol. 82, p. 046212, Oct. 2010.

[118] J. G. Wu, G. Q. Xia, X. Tang, X. D. Lin, T. Deng, L. Fan, and Z. M. Wu, "Time delay signature concealment of optical feedback induced chaos in an external cavity semiconductor laser.," *Optics express*, vol. 18, pp. 6661–6, Mar. 2010.

[119] R. M. Nguimdo, M. C. Soriano, and P. Colet, "Role of the phase in the identification of delay time in semiconductor lasers with optical feedback.," *Optics letters*, vol. 36, pp. 4332–4, Nov. 2011.

[120] S. Han, C. Kurrer, and Y. Kuramoto, "Dephasing and Bursting in Coupled Neural Oscillators," *Physical Review Letters*, vol. 75, pp. 3190–3193, Oct. 1995.

[121] P. R. Roelfsema, A. K. Engel, P. König, and W. Singer, "Visuomotor integration is associated with zero time-lag synchronization among cortical areas.," *Nature*, vol. 385, pp. 157–61, Jan. 1997.

[122] G. B. Ermentrout and N. Kopell, "Fine structure of neural spiking and synchronization in the presence of conduction delays," *Proceedings of the National Academy of Sciences*, vol. 95, pp. 1259–1264, Feb. 1998.

[123] M. Ciszak, O. Calvo, C. Masoller, C. R. Mirasso, and R. Toral, "Anticipating the Response of Excitable Systems Driven by Random Forcing," *Physical Review Letters*, vol. 90, p. 204102, May 2003.

[124] J. Mulet, C. R. Mirasso, T. Heil, and I. Fischer, "Synchronization scenario of two distant mutually coupled semiconductor lasers," *Journal of Optics B: Quantum and Semiclassical Optics*, vol. 6, pp. 97–105, Jan. 2004.

[125] M. Kim, R. Roy, J. Aron, T. Carr, and I. Schwartz, "Scaling Behavior of Laser Population Dynamics with Time-Delayed Coupling: Theory and Experiment," *Physical Review Letters*, vol. 94, p. 088101, Feb. 2005.

[126] V. S. Anishchenko, T. E. Vadivasova, D. E. Postnov, and M. A. Safonova, "Synchronization of Chaos," *International Journal of Bifurcation and Chaos*, vol. 02, pp. 633–644, Sept. 1992.

[127] C. W. Wu and L. O. Chua, "A Simple Way to Synchronize Chaotic Systems with Applications to Secure Communication Systems," *International Journal of Bifurcation and Chaos*, vol. 03, pp. 1619–1627, Dec. 1993.

[128] J. Heagy, T. Carroll, and L. Pecora, "Synchronous chaos in coupled oscillator systems," *Physical Review E*, vol. 50, pp. 1874–1885, Sept. 1994.

[129] N. F. Rulkov, "Images of synchronized chaos: Experiments with circuits.," *Chaos (Woodbury, N.Y.)*, vol. 6, pp. 262–279, Sept. 1996.

[130] L. Fabiny, P. Colet, R. Roy, and D. Lenstra, "Coherence and phase dynamics of spatially coupled solid-state lasers," *Physical Review A*, vol. 47, pp. 4287–4296, May 1993.

[131] S. Sivaprakasam and K. A. Shore, "Demonstration of optical synchronization of chaotic external-cavity laser diodes," *Optics Letters*, vol. 24, p. 466, Apr. 1999.

[132] L. M. Pecora, T. L. Carroll, G. A. Johnson, D. J. Mar, and J. F. Heagy, "Fundamentals of synchronization in chaotic systems, concepts, and applications.," *Chaos (Woodbury, N.Y.)*, vol. 7, pp. 520–543, Dec. 1997.

[133] S. Boccaletti, J. Kurths, G. Osipov, D. Valladares, and C. Zhou, "The synchronization of chaotic systems," *Physics Reports*, vol. 366, pp. 1–101, Aug. 2002.

[134] C. R. Mirasso, R. Vicente, P. Colet, J. Mulet, and T. Pérez, "Synchronization properties of chaotic semiconductor lasers and applications to encryption," *Comptes Rendus Physique*, vol. 5, pp. 613–622, July 2004.

[135] D. A. Arroyo-Almanza, A. N. Pisarchik, I. Fischer, C. R. Mirasso, and M. C. Soriano, "Spectral properties and synchronization scenarios of two mutually delay-coupled semiconductor lasers," *Optics Communications*, vol. 301-302, pp. 67–73, Aug. 2013.

[136] I. Fischer, R. Vicente, J. Buldú, M. Peil, C. R. Mirasso, M. C. Torrent, and J. García-Ojalvo, "Zero-Lag Long-Range Synchronization via Dynamical Relaying," *Physical Review Letters*, vol. 97, p. 123902, Sept. 2006.

[137] A. Landsman and I. Schwartz, "Complete chaotic synchronization in mutually coupled time-delay systems," *Physical Review E*, vol. 75, p. 026201, Feb. 2007.

[138] E. Klein, N. Gross, M. Rosenbluh, W. Kinzel, L. Khaykovich, and I. Kanter, "Stable isochronal synchronization of mutually coupled chaotic lasers," *Physical Review E*, vol. 73, p. 066214, June 2006.

[139] R. Vicente, C. R. Mirasso, and I. Fischer, "Simultaneous bidirectional message transmission in a chaos-based communication scheme," *Optics Letters*, vol. 32, no. 4, p. 403, 2007.

[140] M. Peil, L. Larger, and I. Fischer, "Versatile and robust chaos synchronization phenomena imposed by delayed shared feedback coupling," *Physical Review E*, vol. 76, p. 045201, Oct. 2007.

[141] V. Flunkert, S. Yanchuk, T. Dahms, and E. Schöll, "Synchronizing Distant Nodes: A Universal Classification of Networks," *Physical Review Letters*, vol. 105, p. 254101, Dec. 2010.

[142] A. Uchida, R. McAllister, and R. Roy, "Consistency of Nonlinear System Response to Complex Drive Signals," *Physical Review Letters*, vol. 93, p. 244102, Dec. 2004.

[143] H. Abarbanel, N. Rulkov, and M. Sushchik, "Generalized synchronization of chaos: The auxiliary system approach.," *Physical review E*, vol. 53, pp. 4528–4535, May 1996.

[144] R. Vicente, T. Pérez, and C. R. Mirasso, "Open-versus closed-loop performance of synchronized chaotic external-cavity semiconductor lasers," *IEEE Journal of Quantum Electronics*, vol. 38, pp. 1197–1204, Sept. 2002.

[145] H. U. Voss, "Anticipating chaotic synchronization," *Physical Review E*, vol. 61, pp. 5115–5119, May 2000.

[146] C. Masoller, "Anticipation in the Synchronization of Chaotic Semiconductor Lasers with Optical Feedback," *Physical Review Letters*, vol. 86, pp. 2782–2785, Mar. 2001.

[147] S. Sivaprakasam, E. Shahverdiev, P. Spencer, and K. Shore, "Experimental Demonstration of Anticipating Synchronization in Chaotic Semiconductor Lasers with Optical Feedback," *Physical Review Letters*, vol. 87, p. 154101, Sept. 2001.

[148] M. C. Soriano, V. Flunkert, and I. Fischer, "Relation between delayed feedback and delay-coupled systems and its application to chaotic lasers.," *Chaos (Woodbury, N.Y.)*, vol. 23, p. 043133, Dec. 2013.

[149] K. Hicke, "Synchronization and application of delay-coupled semiconductor lasers," *PhD Thesis*, 2014.

[150] S. C. Venkataramani, B. R. Hunt, E. Ott, D. J. Gauthier, and J. C. Bienfang, "Transitions to Bubbling of Chaotic Systems," *Physical Review Letters*, vol. 77, pp. 5361–5364, Dec. 1996.

[151] V. Flunkert, O. D'Huys, J. Danckaert, I. Fischer, and E. Schöll, "Bubbling in delay-coupled lasers," *Physical Review E*, vol. 79, p. 065201, June 2009.

[152] A. Englert, W. Kinzel, Y. Aviad, M. Butkovski, I. Reidler, M. Zigzag, I. Kanter, and M. Rosenbluh, "Zero Lag Synchronization of Chaotic Systems with Time Delayed Couplings," *Physical Review Letters*, vol. 104, p. 114102, Mar. 2010.

[153] J. Tiana-Alsina, K. Hicke, X. Porte, M. C. Soriano, M. C. Torrent, J. Garcia-Ojalvo, and I. Fischer, "Zero-lag synchronization and bubbling in delay-coupled lasers," *Physical Review E*, vol. 85, p. 026209, Feb. 2012.

[154] K. Hicke, O. D'Huys, V. Flunkert, E. Schöll, J. Danckaert, and I. Fischer, "Mismatch and synchronization: Influence of asymmetries in systems of two delay-coupled lasers," *Physical Review E*, vol. 83, p. 056211, May 2011.

[155] G. S. Vernam, "Cipher Printing Telegraph Systems For Secret Wire and Radio Telegraphic Communications," *Transactions of the American Institute of Electrical Engineers*, vol. XLV, pp. 295–301, Jan. 1926.

[156] C. E. Shannon, "Communication Theory of Secrecy Systems*," *Bell System Technical Journal*, vol. 28, pp. 656–715, Oct. 1949.

[157] D. R. Stinson, *Cryptography: Theory and Practice*. CRC Press Book, 3 ed., 2006.

[158] D. Deutsch, "Quantum Theory, the Church-Turing Principle and the Universal Quantum Computer," *Proceedings of the Royal Society A: Mathematical, Physical and Engineering Sciences*, vol. 400, pp. 97–117, July 1985.

[159] N. Gisin, G. Ribordy, W. Tittel, and H. Zbinden, "Quantum cryptography," *Reviews of Modern Physics*, vol. 74, pp. 145–195, Mar. 2002.

[160] C. H. Bennett and G. Brassard, "Quantum Cryptography: Public-Key Distribution and Coin Tossing," in *Proceedings of the IEEE International Conference on Computers, Systems and Signal Processing*, (Bangalore (India)), pp. 175–179, 1984.

[161] Y. Zhao, C. H. F. Fung, B. Qi, C. Chen, and H. K. Lo, "Quantum hacking: Experimental demonstration of time-shift attack against practical quantum-key-distribution systems," *Physical Review A*, vol. 78, no. 4, pp. 1–5, 2008.

[162] F. Xu, B. Qi, and H. K. Lo, "Experimental demonstration of phase-remapping attack in a practical quantum key distribution system," *New Journal of Physics*, vol. 12, 2010.

[163] L. Lydersen, C. Wiechers, C. Wittmann, D. Elser, J. Skaar, and V. Makarov, "Hacking commercial quantum cryptography systems by tailored bright illumination," *Nature Photonics*, vol. 4, pp. 686–689, Aug. 2010.

[164] L. B. Kish, "Totally secure classical communication utilizing Johnson (-like) noise and Kirchoff's law," *Physics Letters A*, vol. 352, pp. 178–182, Mar. 2006.

[165] J. Scheuer and A. Yariv, "Giant Fiber Lasers: A New Paradigm for Secure Key Distribution," *Physical Review Letters*, vol. 97, p. 140502, Oct. 2006.

[166] I. Kanter, E. Kopelowitz, and W. Kinzel, "Public Channel Cryptography: Chaos Synchronization and Hilbert's Tenth Problem," *Physical Review Letters*, vol. 101, p. 084102, Aug. 2008.

[167] K. Yoshimura, J. Muramatsu, P. Davis, T. Harayama, H. Okumura, S. Morikatsu, H. Aida, and A. Uchida, "Secure Key Distribution Using Correlated Randomness in Lasers Driven by Common Random Light," *Physical Review Letters*, vol. 108, p. 070602, Feb. 2012.

[168] A. Tonello, A. Barthelemy, K. Krupa, V. Kermene, A. Desfarges-Berthelemot, B. M. Shalaby, S. Boscolo, S. K. Turitsyn, and J. D. Ania-Castanon, "Secret key exchange in ultralong lasers by radiofrequency spectrum coding," *Light Sci. Appl.*, vol. 4, pp. e276–, Apr. 2015.

[169] R. Mingesz, Z. Gingl, and L. B. Kish, "Johnson(-like)-Noise-Kirchhoff-loop based secure classical communicator characteristics, for ranges of two to two thousand kilometers, via model-line," *Physics Letters A*, vol. 372, pp. 978–984, Feb. 2008.

[170] A. Zadok, J. Scheuer, J. Sendowski, and A. Yariv, "Secure key generation using an ultra-long fiber laser: transient analysis and experiment," *Optics Express*, vol. 16, p. 16680, Oct. 2008.

[171] D. Bar-Lev and J. Scheuer, "Enhanced key-establishing rates and efficiencies in fiber laser key distribution systems," *Physics Letters A*, vol. 373, pp. 4287–4296, Nov. 2009.

[172] J. Scheuer and O. Kotlicki, "Dark states ultra-long fiber laser (UFL) for practically secure key distribution," in *Asia Communications and Photonics Conference 2013*, (Beijing), p. AF1C.2, Optical Society of America, 2013.

[173] C. H. Bennett, "Quantum cryptography using any two nonorthogonal states," *Physical Review Letters*, vol. 68, no. 21, pp. 3121–3124, 1992.

[174] R. Mislovaty, E. Klein, I. Kanter, and W. Kinzel, "Public channel cryptography by synchronization of neural networks and chaotic maps.," *Physical review letters*, vol. 91, no. 11, p. 118701, 2003.

[175] V. Flunkert and E. Schöll, "Chaos synchronization in networks of delay-coupled lasers: Role of the coupling phases," *New Journal of Physics*, vol. 14, 2012.

[176] T. Horváth, L. B. Kish, and J. Scheuer, "Effective privacy amplification for secure classical communications," *Europhysics Letters*, vol. 94, p. 28002, Apr. 2011.

[177] R. M. Nguimdo, P. Colet, L. Larger, and L. Pesquera, "Digital Key for Chaos Communication Performing Time Delay Concealment," *Physical Review Letters*, vol. 107, p. 034103, July 2011.

[178] D. Huang, D. Lin, C. Wang, W. Liu, S. Fang, J. Peng, P. Huang, and G. Zeng, "Continuous-variable quantum key distribution with 1 Mbps secure key rate," *Optics Express*, vol. 23, no. 13, p. 17511, 2015.

[179] C. Bennett, G. Brassard, C. Crepeau, and U. Maurer, "Generalized privacy amplification," *IEEE Transactions on Information Theory*, vol. 41, no. 6, pp. 1915–1923, 1995.

[180] G. Brassard and L. Salvail, "Secret-key reconciliation by public discussion," *Eurocrypt1993*, pp. 410–423, 1994.

[181] Y. Watanabe, "Privacy amplification for quantum key distribution," *Journal of Physics A: Mathematical and Theoretical*, vol. 40, no. 3, pp. F99–F104, 2006.

[182] W. H. Kye, M. Choi, S. Rim, M. Kurdoglyan, C. M. Kim, and Y. J. Park, "Characteristics of a delayed system with time-dependent delay time," *Physical Review E*, vol. 69, p. 055202, May 2004.

[183] C. Briat, H. Hjalmarsson, K. Johansson, U. Jonsson, G. Karlsson, and H. Sandberg, "Nonlinear state-dependent delay modeling and stability analysis of internet congestion control," in *49th IEEE Conference on Decision and Control (CDC)*, pp. 1484–1491, IEEE, Dec. 2010.

[184] H. O. Walther, "On a Model for Soft Landing with State-Dependent Delay," *Journal of Dynamics and Differential Equations*, vol. 19, pp. 593–622, Nov. 2006.

[185] G. Kozyreff and T. Erneux, "Singular Hopf bifurcation in a differential equation with large state-dependent delay," *Proceedings of the Royal Society A: Mathematical, Physical and Engineering Sciences*, vol. 470, no. 20130596, pp. 97–117, 2014.

[186] M. C. Mackey, "Commodity price fluctuations: Price dependent delays and nonlinearities as explanatory factors," *Journal of Economic Theory*, vol. 48, pp. 497–509, Aug. 1989.

[187] T. Insperger, D. A. Barton, and G. Stépán, "Criticality of Hopf bifurcation in state-dependent delay model of turning processes," *International Journal of Non-Linear Mechanics*, vol. 43, pp. 140–149, Mar. 2008.

[188] T. Richard, C. Germay, and E. Detournay, "A simplified model to explore the root cause of stickslip vibrations in drilling systems with drag bits," *Journal of Sound and Vibration*, vol. 305, pp. 432–456, Aug. 2007.

[189] J. L. Mitchell and T. W. Carr, "Effect of state-dependent delay on a weakly damped nonlinear oscillator," *Physical Review E*, vol. 83, Apr. 2011.

[190] C. W. Eurich, M. C. Mackey, and H. Schwegler, "Recurrent inhibitory dynamics: the role of state-dependent distributions of conduction delay times.," *Journal of theoretical biology*, vol. 216, pp. 31–50, May 2002.

[191] J. Bélair, "Age-structured and two-delay models for erythropoiesis," *Mathematical Biosciences*, vol. 128, no. 1-2, pp. 317–346, 1995.

[192] J. M. Mahaffy, J. Bélair, and M. C. Mackey, "Hematopoietic model with moving boundary condition and state dependent delay: applications in erythropoiesis.," *Journal of theoretical biology*, vol. 190, pp. 135–146, Jan. 1998.

[193] W. G. Aiello, H. I. Freedman, and J. Wu, "Analysis of a Model Representing Stage-Structured Population Growth with State-Dependent Time Delay," *SIAM Journal on Applied Mathematics*, vol. 52, pp. 855–869, June 1992.

[194] H. O. Walther, "Algebraic-delay differential systems, state-dependent delay, and temporal order of reactions," *Journal of Dynamics and Differential Equations*, vol. 21, no. 1, pp. 195–232, 2009.

[195] J. Sieber, "Finding periodic orbits in state-dependent delay differential equations as roots of algebraic equations," *Discrete and Continuous Dynamical Systems - Series A*, vol. 32, no. 8, pp. 2607–2651, 2012.

[196] D. P. Rosin, D. Rontani, and D. J. Gauthier, "Synchronization of coupled Boolean phase oscillators," *Physical Review E*, vol. 89, p. 42907, Apr. 2014.

[197] P. Słowiński, B. Krauskopf, and S. M. Wieczorek, "Solution structure and dynamics of a semiconductor laser subject to feedback from two external filters," in *Semiconductor Lasers and Laser Dynamics IV*, vol. 7720, Proceedings of SPIE Europe, 2010.

[198] P. Słowiński, B. Krauskopf, and S. M. Wieczorek, "Mode structure of a semiconductor laser with feedback from two external filters," *Discrete and Continuous Dynamical Systems - Series B*, 2014.

[199] V. Pal, J. S. Suelzer, A. Prasad, G. Vemuri, and R. Ghosh, "Semiconductor laser dynamics with two filtered optical feedbacks," *IEEE Journal of Quantum Electronics*, vol. 49, no. 3, pp. 340–349, 2013.

[200] D. Brunner, X. Porte, M. C. Soriano, and I. Fischer, "Real-time frequency dynamics and high-resolution spectra of a semiconductor laser with delayed feedback.," *Scientific reports*, vol. 2, p. 732, Jan. 2012.

[201] R. Hui and M. O'Sullivan, *Fiber Optic Measurement Techniques*. Academic Press, 2009.

[202] M. Yousefi and D. Lenstra, "Dynamical behavior of a semiconductor laser with filtered external optical feedback," *IEEE Journal of Quantum Electronics*, vol. 35, no. 6, pp. 970–976, 1999.

[203] M. C. Soriano, F. Ruiz-Oliveras, P. Colet, and C. R. Mirasso, "Synchronization properties of coupled semiconductor lasers subject to filtered optical feedback," *Physical Review E*, vol. 78, no. 4, pp. 1–8, 2008.

[204] J. Martínez-Llinàs, X. Porte, M. C. Soriano, P. Colet, and I. Fischer, "Dynamical properties induced by state-dependent delays in photonic systems," *Nature Communications*, vol. 6, no. May, p. 7425, 2015.